INVESTIGATION OF CIRCUMFERENTIALLY-GROOVED GRINDING WHEELS FOR CREEP-FEED GRINDING

by

Al-Mokhtar Omran Mohamed

Submitted in partial fulfilment of the requirements
for the degree of Doctor of Philosophy

at

Dalhousie University
Halifax, Nova Scotia
December 2014

The work is dedicated to

my beloved mother,
my brothers Omar and Salem, and
my sisters Suaad and Reem

Table of Contents

List of Tables ..... **vii**

List of Figures ..... **viii**

Abstract ..... **xiv**

List of Abbreviations and Symbols Used ..... **xv**

Acknowledgements ..... **xviii**

Chapter 1. Introduction **1**

1.1 Motivation 2

1.2 Objectives 3

1.3 Thesis Outline 3

Chapter 2. Grinding Process **5**

2.1 Introduction 5

2.2 Grinding Wheels 5

2.3 Grinding Wheel Wear 9

2.4 Wheel Dressing Process 11

2.5 Grinding Kinematics 13

2.6 Grinding Forces & Energy 16

2.7 Grinding Fluids 19

2.8 Surface Finish in Grinding 21

2.9 Summary 22

Chapter 3. Grooving Grinding Wheels Review 23

3.1 Grooving Patterns 23

3.2 Review of Literature 24

3.3 Summary 31

Chapter 4. Experimental Procedure & Proof of Concept 32

4.1 Overview of Experimental Setup 32

4.1.1 Grinding Wheel Preparation 33

4.1.2 Grinding Fluid Delivery 34

4.2 Measurements Devices 38

4.3 Grinding & Repeatability Testing 42

4.3.1 Consumed Power vs. Wheel Diameter Experiments 43

4.3.2 Repeatability Experiments 45

4.4 Initial Wheel Grooving Proof of Concept 48

4.4.1 Wheel Grooving Method 48

4.4.2 Grinding Experiment Procedure 51

4.4.3 Results 53

4.4.4 Discussion 57

4.5 Summary 60

Chapter 5. Wheel Grooving Investigation 61

5.1 Introduction 61

5.2 Experimental Method 61
5.3 Results and Discussion 65
5.4 Summary 78

Chapter 6. A Novel Grooving Method: Design & Testing 80
6.1 Introduction 80
6.2 Wheel Grooving System Concept 81
6.3 Design Requirements 84
6.4 Wheel Grooving Setup 86
6.4.1 Control Boards 89
6.4.2 Motor & Power Supply 90
6.4.3 Linear Stage 90
6.4.4 Encoders 91
6.4.5 Limit Switches 95
6.5 Results and Discussion 96
6.6 Wheel Wear Experiments 109
6.6.1 Wheel Wear Results 110
6.7 Summary 112

Chapter 7. Non-grooved & Grooved Grinding Wheels Mechanics Comparisons .. 114
7.1 Kinematics & Effect of Grooving on Chip Formation 114
7.1.1 Chip Measurements Experiments 118
7.1.2 Chip Size Results 119
7.1.3 Effect of Grooving on Surface Finishes 123

7.2 Effect of Wheel Grooving on Grinding Forces & Power 131
7.2.1 Size Effect 132
7.2.2 Coolant Effect 137
7.2.3 Dry & Wet Grinding Experiments 140
7.3 Effect of Grooving on Fluid Flow 148
7.3.1 Flow Measurements Results 151
7.3.2 Flow Measurements Analysis & Discussion 152
7.4 Summary 159

Chapter 8. Conclusions 160
8.1 Recommendations for Future Work 163

References 165

Appendix A 171

Appendix B 172

Appendix C 173

Appendix D 174

List of Tables

Table 4.1: Dressing parameters 34

Table 4.2: Data acquisition equipment 39

Table 5.1: Grinding conditions 62

Table 5.2: Summary of groove parameters 63

Table 5.3: Summary of results 66

Table 6.1: Measured forces during grooving the grinding wheel 86

Table 6.2: Motor specification 90

Table 6.3: Proportional, integral, and derivative gains 98

Table 6.4: Measured spindle power in [kW] during grooving and re-grooving of the grinding wheel 101

Table 6.5: Comparison of resulted groove geometry of Test-1 104

Table 6.6: Average measured spindle power in [kW] as groove depth was gradually increased 106

Table 6.7: Comparison of resulted groove geometry of Test-2 107

List of Figures

Figure 1.1: U.S. economic impact for the grinding operation 2

Figure 2.1: Samples of various grinding wheels available at Dalhousie University 6

Figure 2.2: SEM micrograph of an 80-grit grinding wheel 7

Figure 2.3: Standard marking system for conventional abrasive wheel [6] 7

Figure 2.4: Elucidation of the wheel wear mechanism 10

Figure 2.5: Conventional grinding wheel dressing methods 11

Figure 2.6: Grinding kinematics 13

Figure 2.7: Trochoidal grain path 15

Figure 2.8: Force components in grinding process 16

Figure 2.9: Rubbing, ploughing, and cutting phases of grain-workpiece interaction 18

Figure 2.10: Coolant boiling phases 20

Figure 2.11: A profile of surface roughness 21

Figure 3.1: Wheel grooving patterns 24

Figure 3.2: Grooved and non-grooved surface areas 26

Figure 3.3: Axially-grooved wheel with cooling holes [29] 27

Figure 3.4: Schematic drawing of the grooved wheel used by Kwak and Ha [36] 29

Figure 3.5: Illustration of effective grains on axially-grooved grinding wheel [37] 29

Figure 4.1: A Blohm Planomat 408 creep-feed grinding machine 33

Figure 4.2: Coolant delivery layout. 35

Figure 4.3: Picture of typical refractometer 35

Figure 4.4: Brix% scale (a) clean fluid (b) dirty fluid 36

Figure 4.5: Coolant jet relative position to the grinding wheel & workpiece 37
Figure 4.6: Grinding fluid adjustment setup 38
Figure 4.7: Experimental setup 39
Figure 4.8: Calibration blocks 40
Figure 4.9: Results sample of Veeco Step High Standard 41
Figure 4.10: Results sample of Ambios Reference Standard for Thin Film Step Heights 42
Figure 4.11: Consumed power vs. grinding wheel diameter 44
Figure 4.12: Angled grinding cutting path 45
Figure 4.13: Using grinding wheel width for grinding two workpieces 46
Figure 4.14: Repeatability consumed power comparisons 47
Figure 4.15: Wheel grooving procedure 49
Figure 4.16: Illustration of circumferential groove 50
Figure 4.17: Initial circumferential pattern groove on aluminum oxide wheel 51
Figure 4.18: Experimental setup 52
Figure 4.19: Consumed power along workpiece length 54
Figure 4.20: Measured tangential and normal forces 55
Figure 4.21: Surface roughness along the workpiece's ground surface 56
Figure 4.22: Workpiece surface profile 57
Figure 4.23: Specific energy vs. depth of cut 58
Figure 4.24: Force ratio 59
Figure 5.1: Grooved grinding wheels with different groove geometries 63
Figure 5.2: Single-point diamond tip geometries 64

Figure 5.3: Consumed grinding power vs. depth of cut 66
Figure 5.4: Surface roughness vs. depth of cut 67
Figure 5.5: Measured workpiece surface profile 68
Figure 5.6: Comparisons of tangential and normal force results 69
Figure 5.7: Comparison of force ratio 71
Figure 5.8: Specific energy vs. material removal rate 72
Figure 5.9: Consumed power for wear study 74
Figure 5.10: Tangential and normal force for wear study 75
Figure 5.11: Surface roughness for wear study 76
Figure 5.12: Force ratio for wear study 77
Figure 6.1: Proposed wheel grooving concept 82
Figure 6.2: The synchronization concept of the wheel grooving system 83
Figure 6.3: Resulting groove factor vs. single-point diamond position error 84
Figure 6.4: Picture of the main parts of the grooving system 87
Figure 6.5: Schematic diagram of grinding wheel grooving system 88
Figure 6.6: Image of final grinding wheel grooving system 89
Figure 6.7: Linear stage (a HIWIN Single Axis Robot) 91
Figure 6.8: Splitting the encoder signal from the machine spindle' motor 92
Figure 6.9: Filtering and amplification circuit 93
Figure 6.10: Oscilloscope snapshots of signal treatment 94
Figure 6.11: Limit switches 95
Figure 6.12: Proportional gain tuning process 97

Figure 6.13: Derivative gain tuning process 97

Figure 6.14: System response during the PID controller tuning 98

Figure 6.15: Orientating the grooving setup to test the loading at different axes 99

Figure 6.16: Results of examining the effect of various loads on the position's steady state error 100

Figure 6.17: 3D grinding wheel surface topography measurement apparatus 102

Figure 6.18: Portion of grooved surface of grinding wheel 103

Figure 6.19: Groove profiles comparison when re-grooving the grinding wheel 104

Figure 6.20: Successful multi-grooving process with gradual increase of depth of cut .. 106

Figure 6.21: Comparison of the re-grooving accuracy when gradually increasing the groove depth 107

Figure 6.22: Sample groove patterns that the developed wheel grooving system is capable of 108

Figure 6.23: Consumed power vs. workpiece material removed for wear study 111

Figure 6.24: Surface roughness vs. workpiece material removed for wear study 112

Figure 7.1: Illustration of selected cross-sections for one complete groove rotation 116

Figure 7.2: Active grains spacing and chip thickness 118

Figure 7.3: SEM comparisons of chips sizes of (a) non-grooved and (b) grooved wheels 120

Figure 7.4: Illustration of thresholding process for extracted surfaces to obtain grain widths 122

Figure 7.5: Resulted surface finish (a) dry grinding and (b) wet grinding 124

Figure 7.6: Comparisons of workpiece burn degree 125

Figure 7.7: Burn or oxidation marks measurements 126

Figure 7.8: Workpiece surface profile measurements 127

Figure 7.9: Surface profiles across workpiece width 128

Figure 7.10: Surface profiles along workpiece length 129

Figure 7.11: An FFT analysis for non-grooved (a,b,c) and grooved (d,e,f) wheels 130

Figure 7.12: FFT results shown in respect to wave length 131

Figure 7.13: Specific energy verses specific removal rate (based on Malkin [7,54-56]) ... 133

Figure 7.14: A chart summaries the size effect property 134

Figure 7.15: Abrasive grain sharpness [57] 136

Figure 7.16: Rubbing, ploughing, and cutting phases 137

Figure 7.17: Effect of jet flowrate and wheel velocity on useful flowrate based on [57,58] 138

Figure 7.18: Coolant flow through grooves 139

Figure 7.19: Measured consumed power for (a) dry grinding and (b) wet grinding 141

Figure 7.20: Specific energy comparisons for (a) dry grinding and (b) wet grinding 142

Figure 7.21: Specific energy reductions when using grooved grinding wheel 143

Figure 7.22: Comparisons of tangential and normal forces for (a,b) dry and (c,d) wet grinding 145

Figure 7.23: Comparisons of force ratios for (a) dry grinding and (b) wet grinding 146

Figure 7.24: Contributions of adhesion and ploughing on over all coefficient of friction based on [46] 148

Figure 7.25: Grinding fluid's flow apparatus 149

Figure 7.26: Picture of fluid flow setup 150

Figure 7.27: Coolant exit geometry at workpiece wheel contact 151

Figure 7.28: Flow rate verses applied input pressure 152

Figure 7.29: The squared flow rate verses applied input pressure 154

Figure 7.30: Example of steps to obtain pressure drop 155

Figure 7.31: Resulted pressure drop at workpiece-wheel contact 156

Figure 7.32: Pressure drop at workpiece-wheel contact verses squared flow rate 157

Figure 7.33: Effect of loss coefficient per squired area 158

Abstract

This work investigates experimentally the use of a circumferentially-grooved grinding wheel on the creep-feed grinding process. The work was divided into three main objectives which are: investigating the performance of a grooved wheels in comparison to a regular non-grooved wheel, developing a practical method for wheel grooving, and exploring reasons why the grooved grinding wheel performed better. A single-point diamond dressing tool was used to cut shallow circumferential groove on an aluminum-oxide grinding wheel. The results showed that, for the creep-feed grinding conditions used in this research, a grooved wheel can reduce the consumed power by up to 61%, enable up to 37% more material to be removed while still maintaining workpiece surface roughness values below 0.3μm ("fine quality" surface finish), and enable up to 120% more material to be removed while still maintaining workpiece surface roughness values below 1.6μm ("average quality" surface finish). A wear study was also carried out to compare the performance of both the grooved and non-grooved grinding wheels. For the conditions used in this study, the results showed that a grooved wheel not only exhibits less wear than a non-grooved wheel but also can remove approximately twice as much workpiece material before failure occurs. A corresponding new grinding wheel grooving system was developed that is able to both groove as well as re-groove a grinding wheel using a single-point diamond tool. The re-grooving capability of the new system is achieved by synchronizing the grinding wheel angular position with the dressing tool translational position. This position synchronization enables the diamond dressing tip to repeatedly engage the grinding wheel at the same angular position around the wheel and then proceed to trace the existing groove pattern along the wheel surface to, for example, refresh a worn groove geometry. Furthermore, the proposed system can be mounted on either a conventional or a CNC grinding machines and can groove and re-groove the grinding wheel without the need to remove it from the grinding wheel spindle. The novel wheel grooving system was experimentally validated by creating helically shaped circumferential grooves on the grinding wheel surface. The developed grooving system is able to inscribe various groove patterns into the grinding wheel as well as dress the wheel. It was found that the grooved wheel performs better than regular non-grooved wheel because of an increase in the size effect as well as because more grinding fluid can be delivered into the contact zone. The grooved grinding wheel chips were approximately six to eight times wider than the chips removed by the regular wheel. Also, the grooved grinding wheel was, in comparison to the regular non-grooved wheel, able to deliver more than twice the volume of coolant fluid into the contact zone which lead to better lubrication and cooling.

List of Abbreviations and Symbols Used

Abbreviations

CNC	Computer Numerically Controlled
FFT	Fast Fourier Transformation
GDP	Gross Domestic Product
PID	Proportional, Integral, and Derivative gains
SEM	Scanning Electron Microscope
FFT	Fast Fourier Transformation

Symbols

a_d	Dressing depth (single-point-dressing)
a_e	Depth of cut
a_g	Groove or grooving depth
A_o	Total grinding wheel surface area
A_f	Flow area
A_g	Total surface area of grooves
b_c	Effective width of the abrasive grain
b_d	Effective cutting width (single-point dressing)
b_g	Groove or grooving width
b_w	Width of cut (width of contact)
d_g	Average diameter of abrasive grain
d_s	Grinding wheel diameter
e_c	Grinding specific energy
e_{ch}	Specific energy for chip formation (cutting)
e_p	Specific energy for ploughing
e_r	Specific energy for rubbing
e_r	Groove error
f_d	Dressing lead (dressing feed)
F_n	Normal force

$F_{n.ch}$	Normal force for chip formation
$F_{n,p}$	Normal force for ploughing
$F_{n,r}$	Normal force for rubbing
F_t	Tangential force
$F_{t,ch}$	Tangential force for chip formation
$F_{t,p}$	Tangential force for ploughing
$F_{t,r}$	Tangential force for rubbing
h	Instantaneous chip thickness
h_{cu}	Undeformed chip thickness (at effective width of abrasive grain)
h_{eq}	Equivalent chip thickness
h_m	Maximum uncut chip thickness
$h_{m,g}$	Maximum uncut chip thickness for grooved portion of the wheel
K	Lumped loss coefficient
K_s	Grinding wheel loss coefficient
K_{wp}	System losses upstream of the grinding wheel
l_c	Contact length
L	Active grains spacing
L_G	Active grain spacing between the leading & trailing edges of the groove
M	Abrasive grain size
P	Grinding power
P_1	Fluid pressure at location 1
P_2	Fluid pressure at location 2
P_{c_o}	Unknown pressure difference (no wheel)
P_{c_s}	Unknown pressure difference (with wheel)
P_{DROP}	Pressure drop at contact zone
Q_w	Material removal rate (unite volume per unite time)
$Q_w^{'}$	Specific material removal
r	Ratio of chip width to thickness
R_a	Workpiece surface roughness
S	Grinding wheel structure number
$\mathrm{t_d}$	System grooving (wheel-grooving tool) disengagement time
$\mathrm{t_e}$	System grooving (wheel-grooving tool) engagement time

t_i	System initiating time (for starting grooving program)
t_t	System triggering time (for starting motion)
v_d	Dressing cross-feed velocity or Axial tool traverse feed velocity
v_s	Grinding wheel peripheral velocity
v_w	Workpiece velocity (grinding feed)
U_d	Overlap ratio (single-point dressing)
V_1	Fluid velocity at location 1
V_2	Fluid velocity at location 2
V_b	Volumetric portion of abrasive grains
V_g	Volumetric portion of bond material
V_p	Volumetric portion of pores
z_1	Fluid height at location 1
z_2	Fluid height at location 2

Greek Symbols

η	Groove factor (%)
η_e	Resulting groove factor (%)
μ	Force ratio
μ_a	Adhesion friction
μ_p	Ploughing friction
ρ	Grinding fluid density
ψ	Slope (pressure-flow rate curve)

Acknowledgements

In the Name of Allah, the Most Gracious, the Most Merciful.

First of all, I thank Almighty Allah for all the blessing and guidance.

I would like to express the deepest appreciation to my supervisors, Dr. Andrew Warkentin and Dr. Robert Bauer. They continually and convincingly conveyed a spirit of adventure in regard to research and scholarship. I have been extremely lucky to have supervisors who cared so much about my work, who responded to my questions and queries so promptly; without them, Dr. Warkentin and Dr. Bauer, this dissertation would not have been possible. I wish also to thank my committee members, Dr. Marek Kujath and Dr. Zohier Farhat who were more than generous with their expertise and precious time. Their door was always open for my questions.

I owe my deepest gratitude to my friend Ray Newman, Peter John, and Angus MacPherson for their friendship and generous help throughout my years at Dalhousie University, and special thanks to Louis Desgrosseilliers for the valuable discussions.

I owe my sincere gratitude and very special thanks to my family: my mother, my brothers Omar and Salem, and my sisters Suaad and Reem. My words of thanks cannot express enough their contribution, yet with all humility I thank them for their noble gesture and splendid support.

Chapter 1. Introduction

The grinding operation is one of the oldest manufacturing processes and it is utilized in most manufacturing industries ranging from conventional machine shops to aerospace industries. The grinding process is very important due to its ability to grind or machine hard-to-machine materials such as ceramics and super alloys. The economic impact of the grinding process is staggering [1]. As determined by the United States Department of Commerce [2], the U.S. manufacturing sector accounted 14% of their Gross Domestic Product (GDP) and 20%-25% of all manufacturing expenditures are associated with the grinding operation as stated by Malkin and Guo [3] in 2008. In 2013, the U.S. GDP was $16.8 trillion [4], which indicates a conservative estimate of the economic impact for the grinding operation to be US$ 475 billion. An example of these conservative estimates for selected years between 2006 and 2013 are shown in Figure1.1.

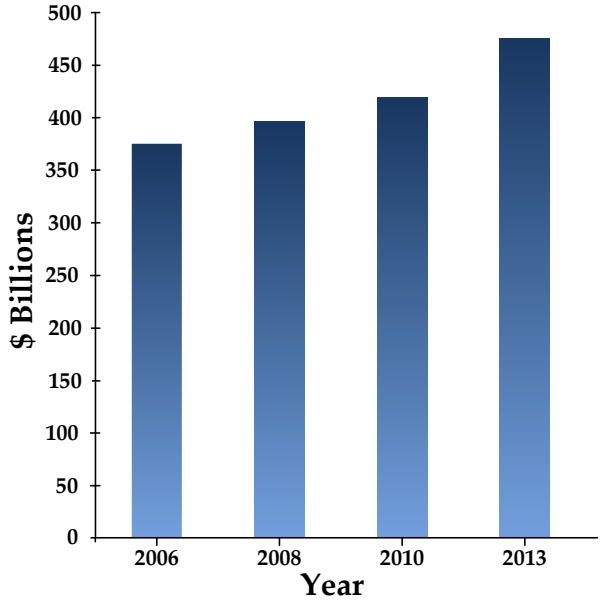

Figure 1.1: U.S. economic impact for the grinding operation

Because the grinding process plays such an important economic role, it is very critical to study this process and develop methods that help reduce the operational cost by ensuring that the manufactured part has the desired quality and the scrap (rejection) rates are reduced.

1.1 Motivation

There are some factors which limit the efficiency of this process. For instance, high grinding forces and high consumed power can cause grinding wheel break-down and/or workpiece thermal damage. The grinding process requires a very large energy input per unit volume of material removed. Most of this energy is converted into heat in the grinding wheel-workpiece contact region. A large portion of the generated heat is conducted to the workpiece and concentrated at the surface layers of the workpiece material causing a localized rise in grinding temperature. This has the potential to

create burn defects, surface oxidation, and a resulting change in workpiece material properties.

There are different approaches to improve the grinding process. For instance, the published literature suggested that the grinding wheels with slots or grooves may have the potential to improve grinding process efficiency and productivity. However, there was little recent concrete work in this area and existing grooving wheels methods seem impractical.

1.2 Objectives

The main objectives of this work are to:

- Investigate alternative/new groove patterns.
- Experimentally study different groove geometries and compare their results,
- Develop a practical method that can groove the grinding wheel quickly and repeatedly.
- Develop a better understanding of why grooved grinding wheels improve the grinding operation.

1.3 Thesis Outline

The contents of this thesis are arranged in the following sequence: Chapter 2 provides background of the grinding process including a description of grinding geometry and kinematics, grinding wheel specifications, and the dressing operation. Chapter 3 then presents a review of various grinding wheel grooving research that was found in the literature. Chapter 4 presents the experimental methodology which was followed. Also, this chapter includes an initial investigation that uses circumferential-groove pattern on the grinding wheel as a proof of concept case study. Then, in Chapter 5, experimental

investigations were conducted to assess the performance of grooving grinding wheels on the creep-feed grinding process. In these experimental investigations, different groove geometries are studied. Chapter 6 presents a novel and practical method of grooving and re-grooving the grinding wheel which was designed and tested. Chapter 7 then investigates the reasons why the grooved grinding wheel performed better than a regular non-grooved grinding wheel. Finally, Chapter 8 draws conclusions and makes recommendations.

Chapter 2. Grinding Process

2.1 Introduction

Grinding is a process by which materials is removed in the form of minute chips by the action of irregularly shaped hard abrasive particles [5]. These abrasive particles are bonded together to form a grinding wheel that operates at very high peripheral velocities. The grinding wheel, the grinding cutting parameters, and the grinding fluid are the main components of the grinding process. Therefore, in this chapter, a brief description of the grinding wheel, grinding kinematics, and grinding fluid are presented.

2.2 Grinding Wheels

A grinding wheel, as illustrated in Figure 2.1, is a ternary system that is composed of thousands of small hard, non-metallic, abrasive grains held together by a bonding material, and porosity. A Scanning Electron Microscope (SEM) micrograph of a typical

grinding wheel is shown in Figure 2.2, where the abrasive grits, bond material, and porosity (voids) are clearly visible. The bonding material is the glue that holds the abrasive grains together, the abrasive grains are responsible for material removal, and the voids provide chip cleaning and coolant transport into the grinding zone. The volumetric proportions of abrasive grains V_g , bond material V_b , and pores V_p can be expressed as:

$$V_g + V_b + V_p = 1.0 \tag{2.1}$$

The main parameters used to describe a grinding wheel are the abrasive type, the abrasive grain size, the wheel hardness (grade), the wheel structure, and the bond type. These parameters are specified in the marking system of a grinding wheel which is typically written on the side of the grinding wheel.

Figure 2.1: Samples of various grinding wheels available at Dalhousie University

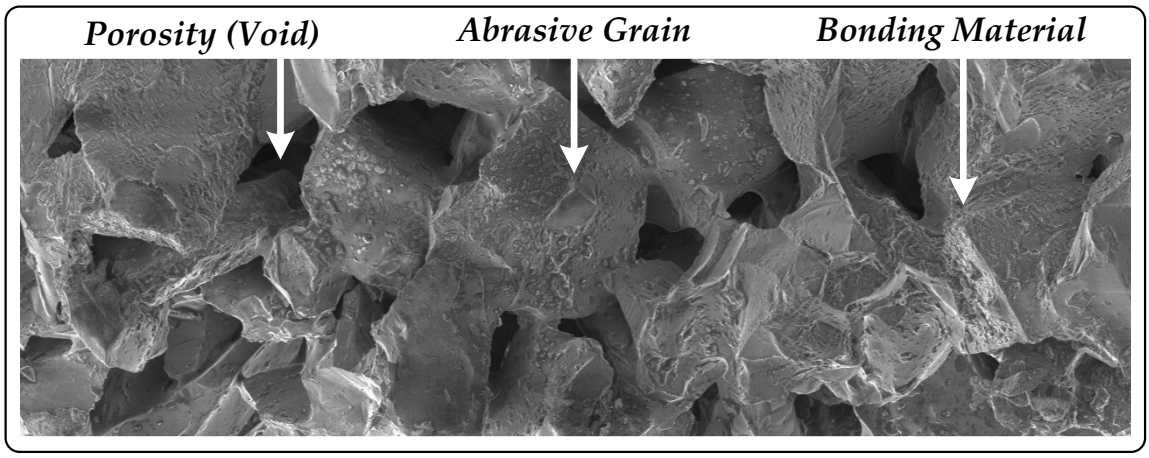

Figure 2.2: SEM micrograph of an 80-grit grinding wheel

The marking system for conventional abrasive wheels is defined by the American National Standards Institute [ANSI] by standard B74.13 – 1977 [6]. Figure 2.3 illustrates this marking standard that provide the user with key information regarding the construction of the grinding wheel. It starts with a prefix for the manufacture's symbol, which indicates the exact kind of abrasive, followed by the possible parameters of the wheel specification, and ends with a manufacture's private marking to identify a wheel.

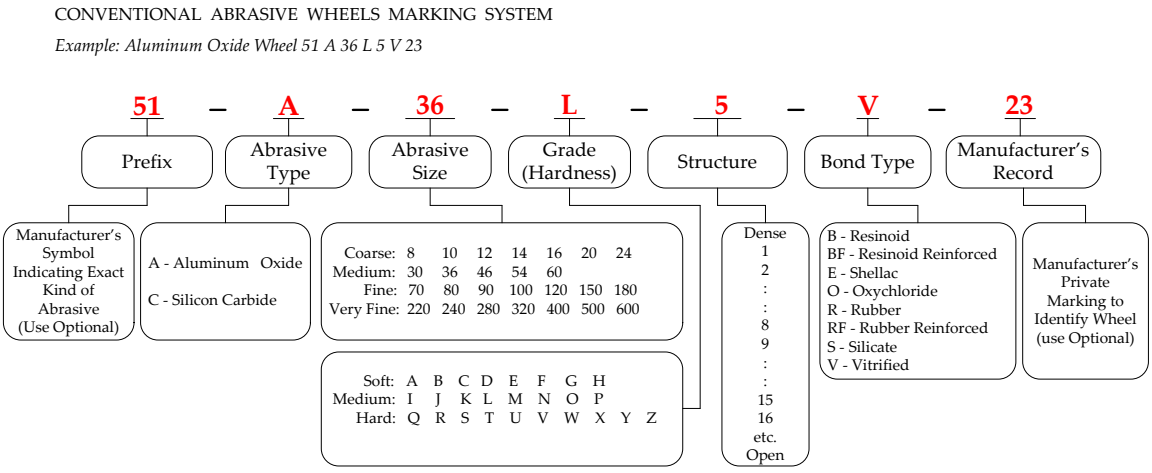

Figure 2.3: Standard marking system for conventional abrasive wheel [6]

The first parameter in the wheel marking system is the abrasive type. Aluminum oxide (Al_2O_3), which used for grinding most steels, and silicon carbide (SiC), which used for grinding cast irons and non-ferrous metals are the two most common abrasives used in production grinding. Super-abrasives such as cubic boron nitride (CBN) and diamond are generally reserved for demanding application where the workpiece material is very hard, such as ceramics and carbides. The second parameters used to characterize the grinding wheel is the abrasive grain size which is very important due to its influences on stock removal rate, chip clearance in the wheel, and surface finish of the grinding operation. A low abrasive grain size indicates large (coarse) grains which promotes higher material removal rates at the expense of surface finish while a high abrasive grain size indicates small (fine) grains which permits a smother surface finish at a lower material removal rates. Malkin [7] approximated the average diameter, in mm, of an abrasive grain d_g according to:

$$d_g = 15.2\, M^{-1} \tag{2.2}$$

where M is the abrasive grain size. The third parameter is the wheel grade which indicates the grinding wheel's bond strength in retaining the abrasive grits during cutting. The wheel grade is greatly dependent on the amount of bonding material present in the wheel structure – V_b in Equation (2.1). The abrasive grade is measured on a scale that ranges between soft and hard. The softest grade is indicated by the letter "A" and the hardest grade is indicated by the letter "Z". Softer wheels lose grains readily and are generally used for applications requiring low material removal rates and grinding of hard workpiece materials [8,9]. Harder wheels retain their abrasive grains and are typically used to achieve high stock removal rates and for grinding of relative soft work materials. The fourth parameter is the wheel structure which is measured on a scale that ranges between a dense structure and an open structure. A dense wheel structure is one in which the volumetric proportion of bond material V_b is relatively

small, and the volumetric proportion of abrasive grains V_g is larger, and it is used to obtain better surface finish and dimensional control. By contrast, an open structure is one in which V_b is relatively large, and V_g is relatively small, and it is generally recommended in grinding where clearance for chips must be provided. That is, there are more pores and fewer grains per unit volume. The relationship between the volumetric proportion of abrasive grains V_g and the structure number S is given in the following equation [7]:

$$V_g = 0.02(32 - S) \tag{2.3}$$

Finally, the fifth and last parameter in the wheel marking system is the bond type. The bond type is specified by the first letter of the material type. For example, V stands for "vitrified" which is used on more than 75 percent of grinding wheels [5]. One should say here that the conditions of the abrasive grains during grinding may change due to wear of the grinding wheel during grinding. Various grinding wheel wear mechanisms are explained next.

2.3 Grinding Wheel Wear

The wear of a grinding wheels affects the grinding process efficiency as well as the workpiece quality [10]. The wear cycle of a grinding wheel is an extremely complex process and is affected by many factors, such as: the initial condition of the grinding wheel, the workpiece material, the grinding process parameters, and the type and quantity of the cutting fluid used. Grinding wheel wear can be categorized into three modes [11,12]: bond fracture, grain fracture, and attritious wear, as shown in Figure 2.4. In bond fracture, the abrasive grain is broken away from the bond. Grain fracture occurs when the grain breaks and may create new sharp cutting edges – a process called self-sharpening. Both bond fracture and grain fracture occur when the cutting forces of a

dull abrasive grain exceed the fracture strength of the abrasive grain or bond material. Unfortunately, both fracture wear mechanisms tend to create an irregular wheel surface resulting in degradation of the workpiece surface finish. Attritious wear, on the other hand, is a gradual process of dulling the initially sharp grain and it refers to the growth of wear flats due to rubbing against the workpiece surface. This kind of wear leads to the increase in grinding forces and, consequently, grinding temperatures.

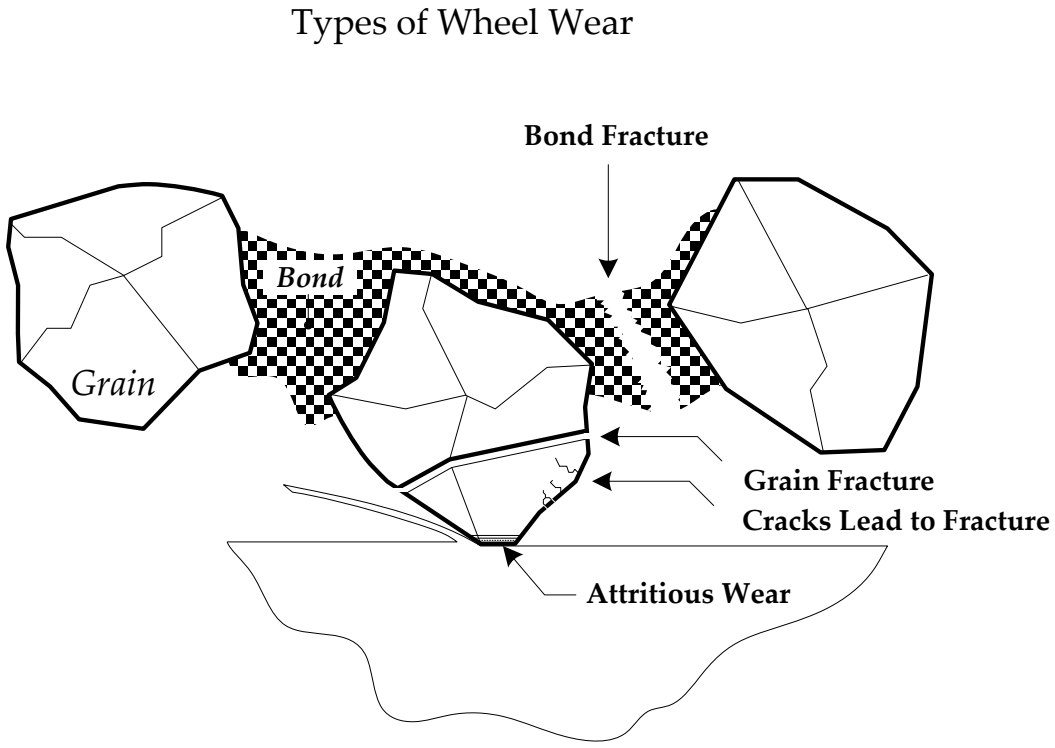

Figure 2.4: Elucidation of the wheel wear mechanism

Wheel wear causes a deterioration of the wheel surface which leads to damage of the workpiece surface and/or loss of accuracy. Therefore, reconditioning the grinding wheel surface by using a dressing operation is required to achieve the appropriate wheel surface with sharp and accurate cutting edges.

2.4 Wheel Dressing Process

Dressing is the process of conditioning the grinding wheel surface in order to reshape the wheel when it has lost its original form or has become dull due to wear. It restores and sharpens the grinding wheel topography which has a significant impact on the grinding wheel force, energy, temperatures, wheel wear, and surface finish [11]. Dressing is also performed as a method for removing chips that may become lodged in the grinding wheel. This clogging of the pores on the grinding wheel surface is called grinding wheel loading which decreases the cutting efficiency of the grinding wheel.

There are different methods used for dressing the grinding wheel, such as diamond roll dressing and single-point diamond dressing as illustrated in Figure 2.5.

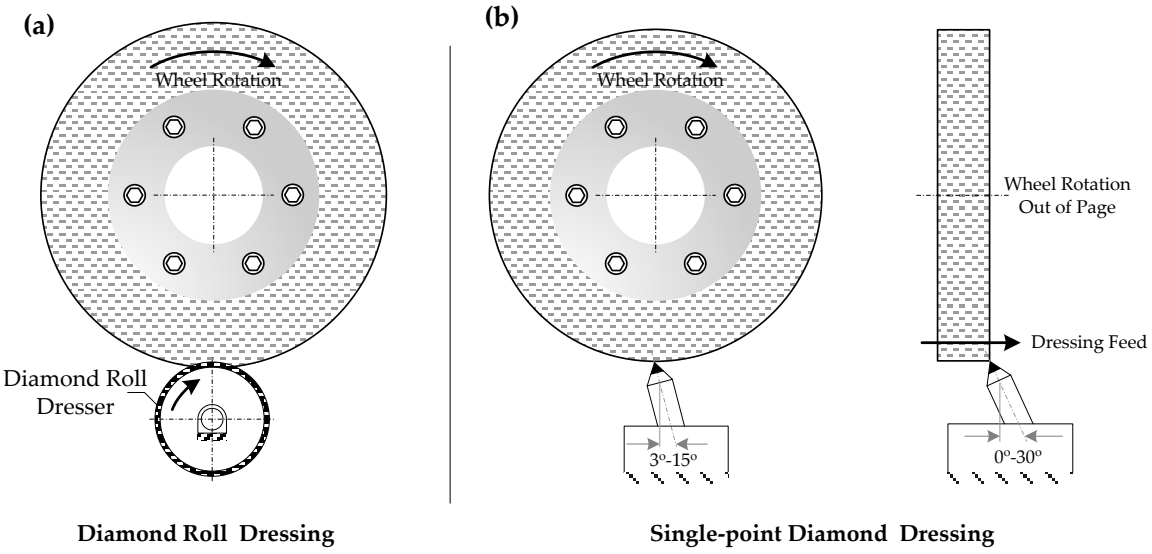

Figure 2.5: Conventional grinding wheel dressing methods

Diamond roll dressing, which is also called rotary dressing as shown in Figure 2.5(a), is a method that uses a cylindrical tool with diamond particles embedded in the periphery. In this method, the rotating grinding wheel is a fed into the rotating diamond roll to a specific depth. Single-point diamond dressing is the most common method of dressing

grinding wheels. As shown in Figure 2.5(b), this method employs a single-point diamond that is set at an angle with the periphery and the face of the grinding wheel [13]. The dressing is accomplished by feeding a grinding wheel having a diameter d_s and rotating with a peripheral velocity v_s toward the diamond's tool tip at a certain cross-feed velocity v_d and depth of cut a_d. The axial feed of the dressing tool per wheel revolution is called the dressing lead/feed f_d which can be calculated by the following equation:

$$f_d = \frac{\pi \cdot d_s \cdot v_d}{v_s} \tag{2.4}$$

In single-point dressing, the effective cutting width b_d depends on the dressing depth a_d and the tool geometry. The ratio of the cutting width and the feed f_d is called the overlap ratio U_d [8]:

$$U_d = \frac{b_d}{f_d} \tag{2.5}$$

Small overlap ratios indicates fast cross-feed velocities which cause coarse wheel surfaces used for rough grinding processes, while large overlap ratios correspond to slow cross-feed velocities which generate fine wheel surfaces used for fine surface finishes. In this thesis work, both rotary dressing and single-point dressing were applied. The former dressing method was used for removing a desired depth from the grinding wheel and the latter method was used prior to each grinding experiment to condition the wheel surface.

2.5 Grinding Kinematics

Analysing the grinding cutting geometry provides information on the cutting path and the contact behavior between a grinding wheel and a workpiece. Figure 2.6 illustrates the basic grinding operation. As can be seen from this figure, an abrasive wheel of diameter d_s rotating with a peripheral velocity v_s takes a depth of cut a_e from the workpiece as it translates at velocity v_w [7]. The width of contact between the abrasive wheel and workpiece during the grinding process is b_w. The curve that defines the contact between the grinding wheel and the workpiece is known as the contact length l_c and is calculated as [7-9]:

$$l_c = \left(a_e \cdot d_s\right)^{1/2} \tag{2.6}$$

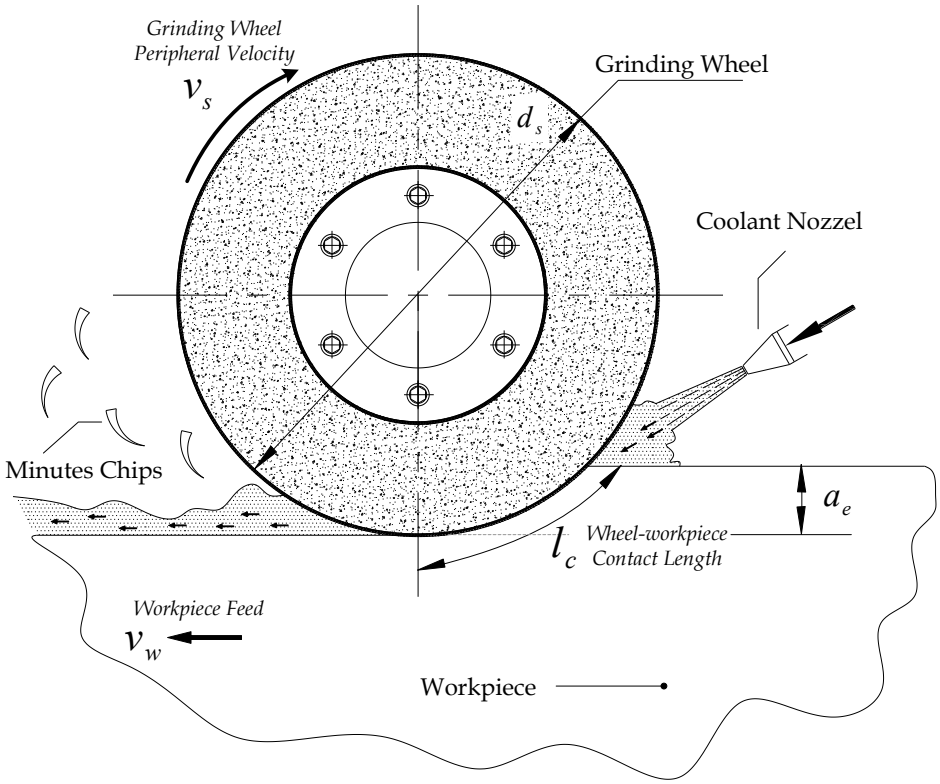

Figure 2.6: Grinding kinematics

The volume of workpiece material removed per unite time is known as the material removal rate Q_w and is found from:

$$Q_w = b_w \cdot a_e \cdot v_w \tag{2.7}$$

During the cutting interaction between the grinding wheel and the workpiece, the abrasive grain follows a path which is a complicated trochoidal motion that results from the simultaneous rotational motion of the grinding wheel and the translational motion of the workpiece. Figure 2.7 depicts the result of the abrasive grain motion simplified for a single grain. A grain in imminent contact with the workpiece is shown embedded in a grinding wheel at time t^n when the relative position between the grinding wheel and workpiece is at point O as represented in Figure 2.7. At time t^{n+1} when the relative position between the grinding wheel and workpiece is at point O', the abrasive grain has exited the workpiece and removed the shaded material shown in the figure. Evidently, the thickness of the removed material changes with the position of the acting grain along the cutting path and is symbolized as the instantaneous chip thickness h in Figure 2.7. The maximum grain engagement with the workpiece produces the maximum un-cut chip thickness h_m which can be calculated using the following equation [7-9]:

$$h_m = 2L\frac{v_w}{v_s}\left(\frac{a_e}{d_s}\right)^{0.5} \tag{2.8}$$

where L is the spacing or distance between adjacent abrasive grains.

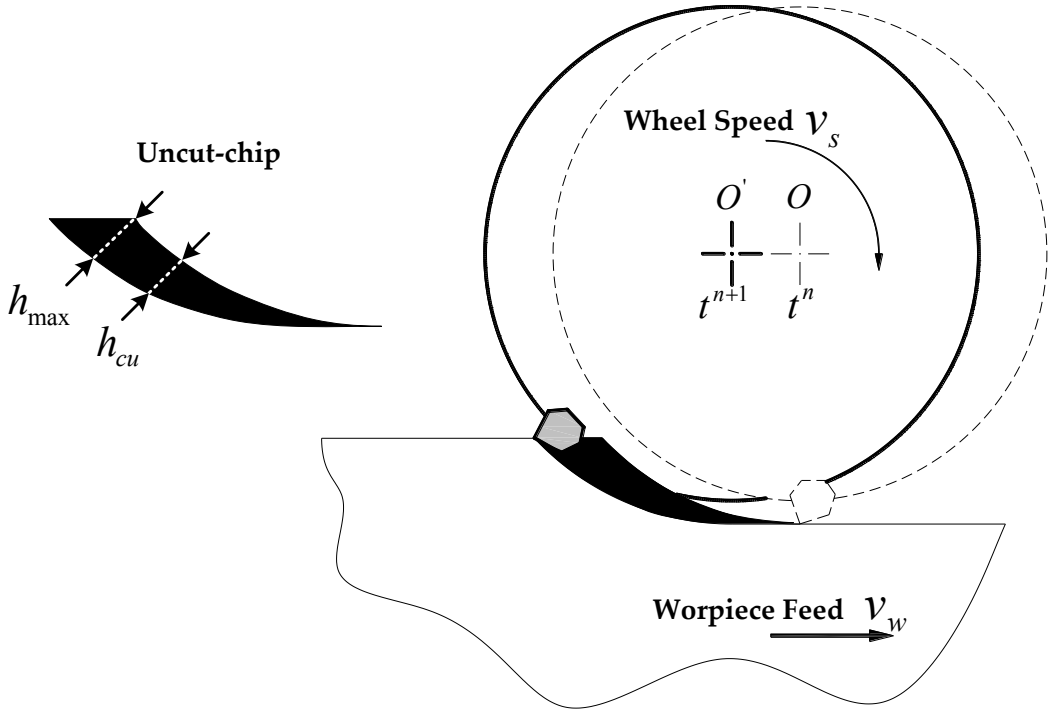

Figure 2.7: Trochoidal grain path

The equivalent chip thickness h_{eq} is widely used in describing the undeformed chip because of its simplicity and is defined as [7-9]:

$$h_{eq} = a_e \cdot \frac{v_w}{v_s} \tag{2.9}$$

It is obvious from Equations (2.8) and (2.9) that the uncut chip thickness is in direct relation with both the spacing between active grains and depth of cut. The increase in the uncut chip thickness tends to result in more efficient grinding in energy terms [8] – a phenomenon known as the size effect.

2.6 Grinding Forces & Energy

Grinding forces and grinding energy are important grinding performance measures since they are directly related to grinding wheel wear, grinding temperatures, and surface integrity [14]. Grinding forces and spindle power are commonly measured to characterize the grinding process and evaluate grinding wheel performance. The main two force components acting between the abrasive grinding wheel and workpiece during grinding are the tangential force F_t and the normal force F_n as shown in Figure 2.8. The tangential force component is proportional to the grinding power, which in turn is directly related to the temperature generated in the grinding contact zone and possible thermal damage to the workpiece [15]. The grinding power P is associated with the tangential force F_t and the grinding wheel peripheral velocity v_s and can be found from the following equation [7-9]:

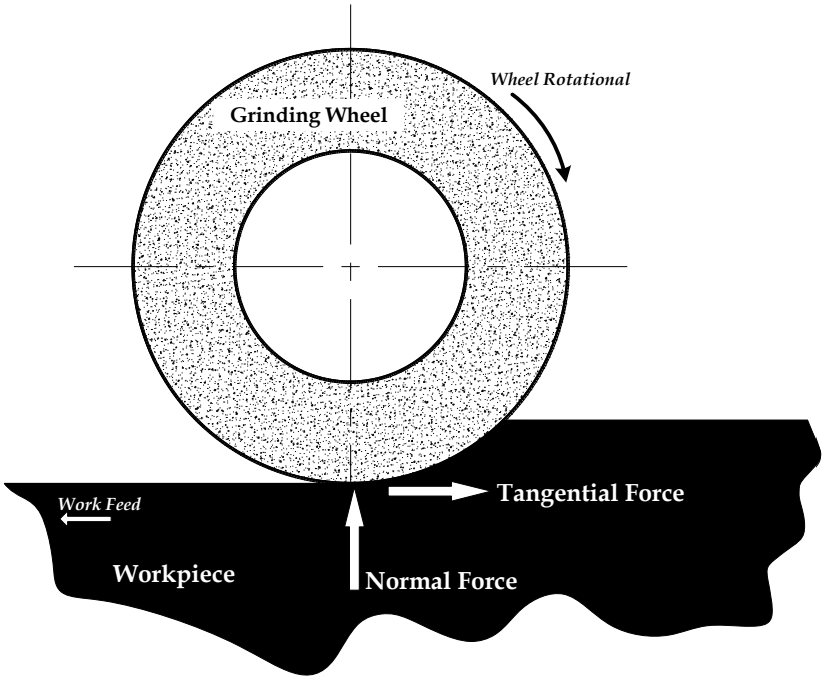

Figure 2.8: Force components in grinding process

$$P = F_t \cdot v_s \tag{2.10}$$

The power in grinding is often represented as the energy per unit volume of removal material which is often known as the specific energy e_c. This specific energy can be obtained by combining Equations (2.7) and (2.10) as [7-9]:

$$e_c = \frac{P}{Q_w} \tag{2.11}$$

Specific energy is an inverse of grinding process efficiency. The lower the specific energy, the more efficient the process. Specific energy is affected by the difficulty to grinding or machine a workpiece material as well as wheel wear [8,16]. There are various factors that can be considered to reduce the specific grinding energy; for example: a well lubricated process, large uncut chip thickness, and sharp abrasive grains.

An increase in specific energy during grinding is, as proposed by Hahn [17], a result of the increased rubbing between the abrasive grains and the workpiece. Additionally, as shown in Figure 2.9, Hahn [18] perceived three distinct stages during the abrasive grain's interaction with the workpiece: rubbing, ploughing, and cutting. Rubbing takes place at low depth of cuts when the uncut chip thickness is in the range of $0 \le h \le \delta_r$. This stage consists of elastic deformation and heat generation through friction and is considered an energy waste stage as no material removal occurs [1]. At slightly greater depths of cut, when the uncut chip thickness increases to the range of $\delta_r \le h \le \delta_p$, the ploughing stage occurs causing plastic deformation of the material on the surface of the workpiece. The workpiece material tends to bulge ahead of the abrasive grain to form a ploughed lip followed by side flow as the motion progresses. The ploughing phase is considered inefficient as well since there is no material ejected from the workpiece. The cutting stage happens at large depths of cut once the uncut chip thickness increases to

the range of $\delta_p \le h \le \delta_c$ causing material removal. The cutting phase tends to be efficient as there is little energy wasted in the form of elastic deformation.

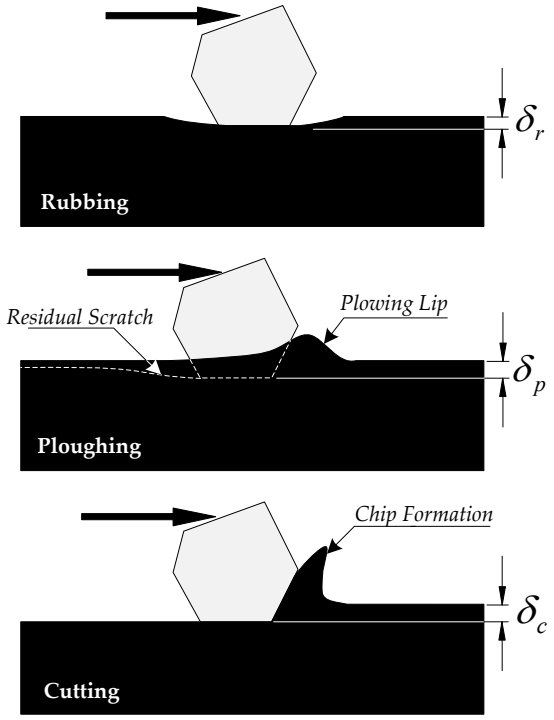

Figure 2.9: Rubbing, ploughing, and cutting phases of grain-workpiece interaction

It was suggested by Kannapan and Malkin [19] that the specific energy in grinding could be divided into three components that correspond to three mechanisms proposed by Hahn [18]. Therefore, the total specific energy is the summation of the specific energy for rubbing e_r, the specific energy for ploughing e_p, and the specific energy for cutting or chip formation e_{ch} as expressed by the following [7,8]:

$$e_c = e_r + e_p + e_{ch} \tag{2.12}$$

The tangential and normal forces are each split into three components according to the three values of grinding energy. These grinding forces are composed of a sliding force, ploughing force and, chip formation force, so [7,8]:

$$F_t = F_{t,r} + F_{t,p} + F_{t,ch} \tag{2.13a}$$

$$F_n = F_{n,r} + F_{n,p} + F_{n,ch} \tag{2.13b}$$

where $F_{t,r}$ and $F_{n,r}$ are the tangential and normal forces associated with the sliding or rubbing stage, $F_{t,p}$ and $F_{n,p}$ are the tangential and normal forces for the ploughing phase, and $F_{t,ch}$ and $F_{n,ch}$ are the tangential and normal forces for the cutting or chip formation phase. There are some parameters that affect the grinding forces and consequently the grinding energy. For instance, the grinding fluid as well as the abrasive grain spacing. An effective lubrication can result in minimizing the tangential force and grinding power due to the reduction in friction occurring in the sliding phase. An increase in grinding wheel spacing between active grains results in increase in the uncut chip thickness and, consequently, decreases the grinding energy.

2.7 Grinding Fluids

Grinding fluids are an important component in the grinding process and are traditionally used as an external means to improve the process performance by providing lubrication and cooling at the grinding wheel-workpiece interface [20,21]. Yet, the effectiveness of the grinding fluid depends upon many factors, such as: placement of the coolant jet, flow velocity, quantity of flow, direction of application, and design of the nozzle [22]. The main purposes of utilizing grinding fluids include: to lubricate the abrasive contacts, to cool the wheel-workpiece contact zone, and to remove and transport the debris away. Grinding fluid could be either water based or oil based. In this research, a water based grinding fluid is utilized.

During grinding operation, the coolant absorbs a fraction of the heat generated in the grinding contact zone between the grinding wheel and workpiece. The rise in grinding temperature causes an increase in the fluid temperature which can lead to a change of

fluid phases from non-boiling, to nucleate boiling, to film boiling (Figure 2.10). In the non-boiling case, the coolant temperature is below the boiling point. In the nucleate boiling case, the temperature is at the boiling limit where bubbles occur at the heated surfaces causing a higher rate of heat transfer than that in the non-boiling case [23,24]. With the increased heat transfer, a vapour film forms near the heated surface behaving as an insulator preventing further heat convection and causing a temperature spike.

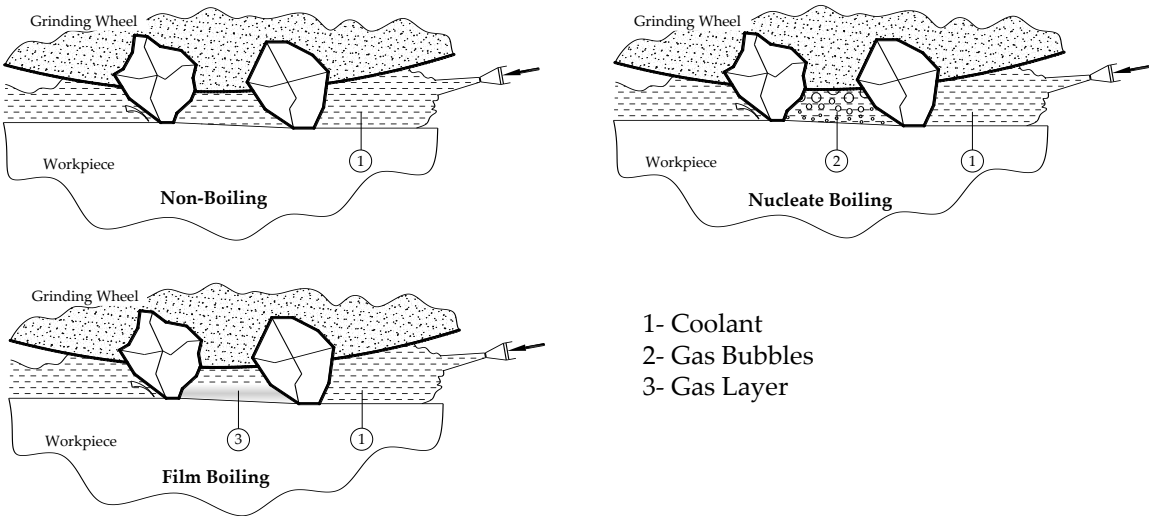

Figure 2.10: Coolant boiling phases

The occurrence of a temperature spike is considered to be one of the grinding process failure modes. Such a temperature spike could be monitored during grinding by seeing or measuring a sudden rise in the grinding spindle power. Therefore, in this work, any thermal damage that occurred due to a failure in fluid delivery was considered to be a grinding process limitation. The fluid delivery system utilized in this research is described in the coming chapter.

2.8 Surface Finish in Grinding

The term surface finish generally refers to the overall description of the machined or ground surface. The surfaces produced by machining and grinding, in particular, are generally irregular and complex. The principal elements of surfaces have been defined by the American Society of Mechanical Engineers in ASME B46.1-2002. The roughness parameter measured and used in this thesis work is the arithmetic mean surface roughness symbolized as R_a. Figure 2.11 represents the profile of a surface highly magnified. A centerline, x-axis, is drawn through the profile representing the average plane of the surface. The ordinates h_1, h_2, …, h_n show the variations of the profile from the centerline at equal intervals. The average surface roughness parameter is found as:

$$R_a = \frac{1}{l}\int_0^l |f(x)|\,dx \tag{2.14}$$

The digital approximation of the average surface roughness is [25]:

$$R_a = \frac{1}{n}\sum_{i=i}^{i=n} |h_i| \tag{2.15}$$

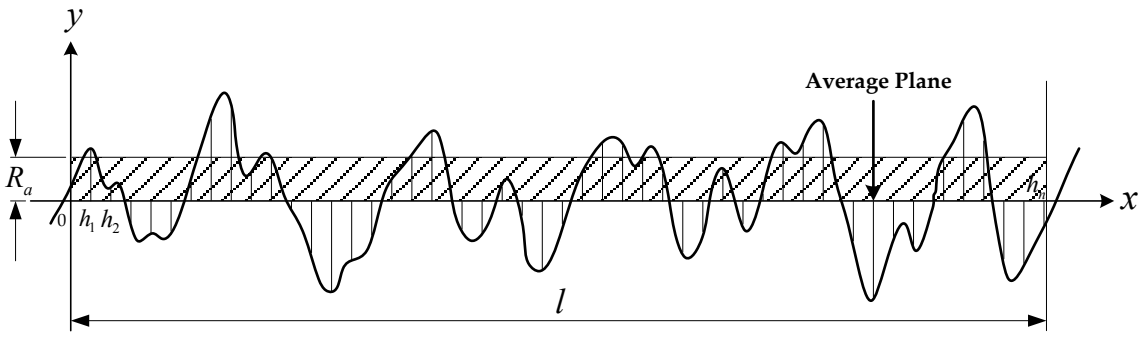

Figure 2.11: A profile of surface roughness

The surface roughness in this research is considered to be a quality measure of the grinding process; therefore, it was measured for every grinding experiment in this thesis work.

2.9 Summary

This chapter has briefly introduced the grinding process and outlined the important of the kinematic relationship that affects the grinding process and that are relevant to this work. Of note was the trochoidal motion of the abrasive grain through the workpiece and the resulting increase in the uncut chip. It was also shown that grinding forces and specific energy are affected by kinematic parameters of grinding as well as the grinding wheel surface topography.

Chapter 3. Grooving Grinding Wheels Review

The state of the surface of a grinding wheel affects the performance of the grinding operation. Therefore, researchers have investigated different parameters that would assist in improving the performance of the grinding process. For instance, it appears from the literature that grinding wheels with grooves or slots tend to improve the grinding process. The following sections describe the grooves and their potential benefits found in literature.

3.1 Grooving Patterns

A groove pattern refers to the geometry of how the grooves were formed on the grinding wheel surface. Figure 3.1 illustrates various grooved grinding wheels with different surface grooving patterns (except Figure 3.1(a) which depicts a non-grooved regular grinding wheel for a comparison purposes). As can be seen from this figure, three groove patterns are introduced as follows. Firstly, a helical-groove pattern (see

Figure 3.1(b)) where the grooves are formed on the grinding wheel surface at an angle called the helix angle. Secondly, an axial-groove pattern where the grooves are parallel to the wheel axis as shown in Figure 3.1(c). This second groove pattern is similar to the first in that it has a helix angle which is equal to zero. Thirdly, as illustrated in Figure 3.1(d), a circumferential-groove pattern which is further developed and presented in this thesis work with more details in the forthcoming chapters.

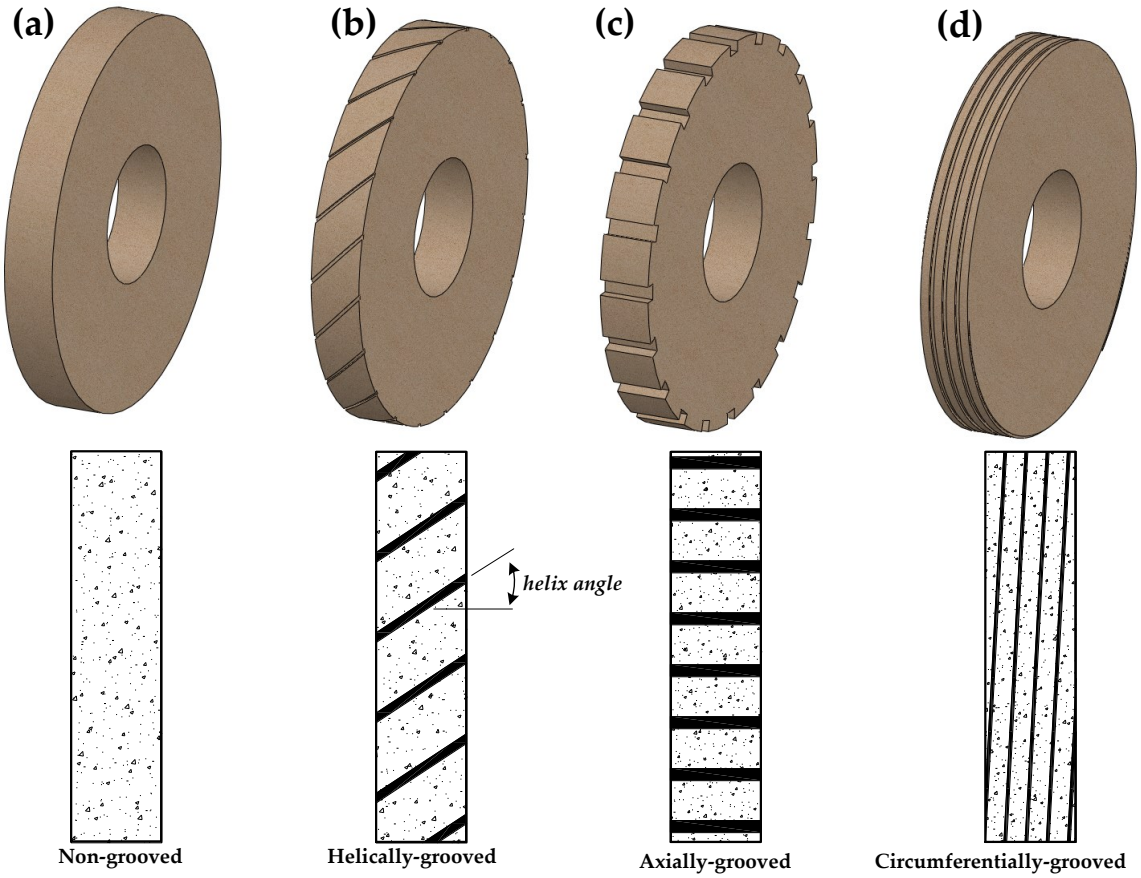

Figure 3.1: Wheel grooving patterns

3.2 Review of Literature

The earliest published research investigating the use of a grooved grinding wheel is the work of Nakayama *et al.* [26] in 1977. In their work, a grooved grinding wheel (WA 46 J

6 V) was tested on the surface grinding process. Helical grooves, as depicted in Figure 3.1(b), were formed on the surface of the grinding wheel using a screw-shaped crushing roll made of hardened carbon steel. The groove width was 2.5 mm. The authors reported a 30% reduction in the grinding forces and consumed energy when using this grooved wheel.

In 1979, Verkerk [27] also studied a helically-grooved grinding wheel (NA 100 K7 VA) on the cylindrical grinding process. In addition to creating 1 mm to 1.2 mm wide grooves on the wheel using a crushed roll approach similar to Nakayama *et al.* [26], Verkerk [27] used a grinding wheel (NWA 80 N 8 VA) with premanufactured helical slots (60 slots) with width and depth of 3.5 mm and 65 mm, respectively. He recommended that the slots be narrow to avoid measurable traces of the slots on the workpiece surface, and that the slots be at an angle with the wheel axis to reduce grinding force fluctuations. Verkerk [27] also introduced the term groove factor (η) that can be used to describe the remaining non-grooved surface area of the grinding wheel after it has been grooved and it can be calculated as follows:

$$\eta = \frac{A_o - A_g}{A_o} \times 100\% \tag{3.1}$$

where A_o, as illustrated in Figure 3.2(a), is the total wheel surface area (mm^2), and A_g, as illustrated in Figure 3.2(b), is the total groove area (mm^2). A grinding wheel without any grooves would, therefore, have a 100% groove factor.

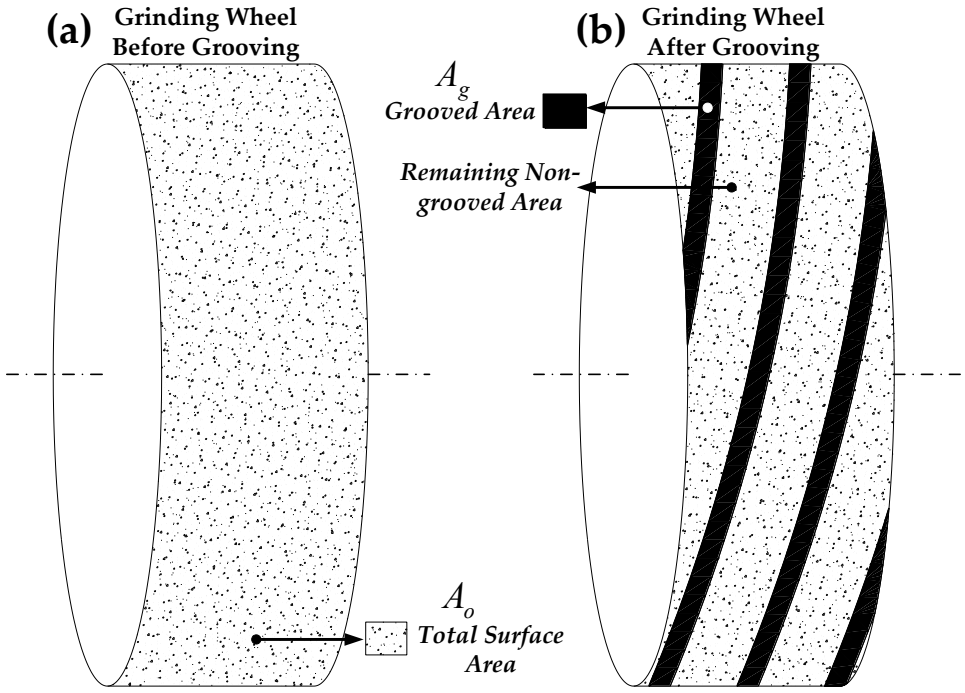

Figure 3.2: Grooved and non-grooved surface areas

Matsui *et al.* [28], in 1986, used an axially grooved (segmented) grinding wheel (WA 60E 7V) with 6, 12, and 24 pieces which were removed from the upper layer of a conventional grinding wheel. These pieces were then attached to the outer circumference of an aluminum holder. This segmented axially-grooved wheel showed a reduction in both grinding forces and grinding temperature. However, it could be said that the construction strategy of the segmental wheel was very complex and is impracticable to use for ordinary machining workshops.

In 1990, Suto *et al.* [29] developed an axially-grooved grinding wheel with cooling holes perforated in the wheel working surface as shown in Figure 3.3(a). They stated that the specific worn area of the active abrasive grains at the leading edge and at the trailing edge of every segment as shown in Figure 3.3(b) were 0.70% and 0.95% respectively. It was suggested that the abrasive grains on the leading edge experience micro scale fracture on their tips. However, the grains on the trailing edge are rubbing and thus

form wear flats more quickly. Zhang *et al.* [30], in 1995, used the same developed wheel by Suto *et al.* [29] and reported that the axially-grooved wheel with a cooling-hole structure possesses advantages in grinding metallic material, can avoid wheel loading, and provides a more effective and efficient coolant supply method.

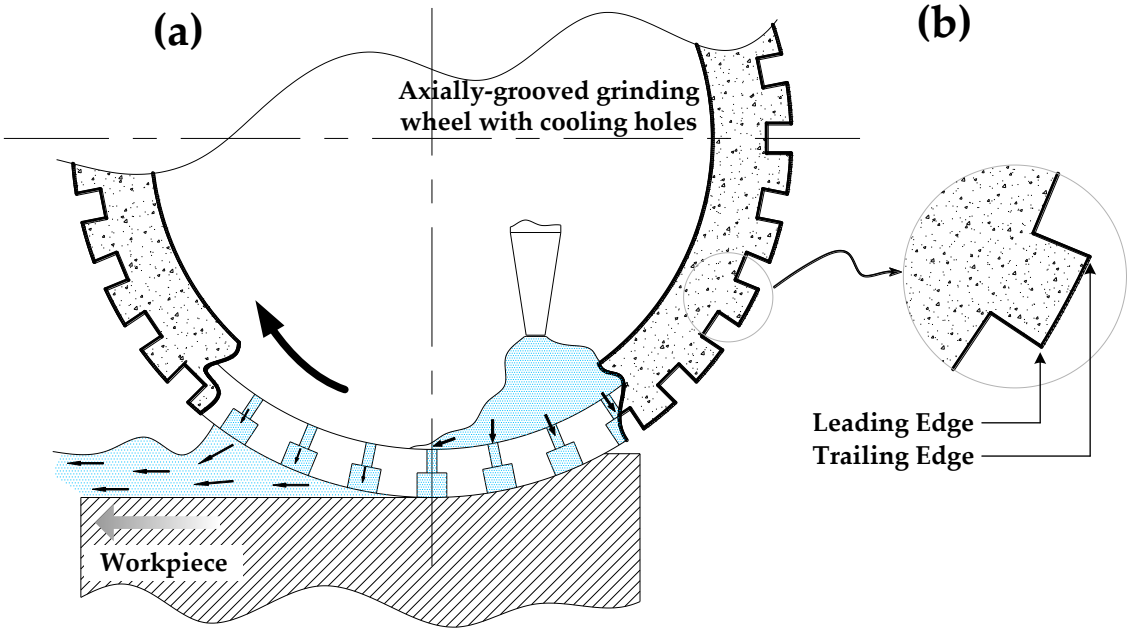

Figure 3.3: Axially-grooved wheel with cooling holes [29]

Okuyama *et al.* [31], in 1993, studied the effect of axially-grooved grinding wheels on the surface grinding process. The axial grooves studied by Okuyama *et al.* [31] had a width and depth of 3.0 mm and 0.5 mm, respectively. These researchers examined the use of 4, 12, and 36 grooves around the periphery of the grinding wheel and reported that the maximum heat transfer coefficient increases with the number of grooves. In addition to this grooved-wheel research, in 1994, Zheng and Gao [32] developed an analytical thermal model for axially-grooved wheels showing how groove geometry influences the grinding temperature and can reduce workpiece thermal damage. The developed thermal model is based on the Jaeger [33] and DesRuisseaux [34] thermal models. The developed model [32] was verified experimentally and results showed that grinding

temperatures were less when using the grooved wheel than when using the regular wheel; however, the grooved wheel temperatures were fluctuating in a periodic fashion.

In 1997 Kim *et al.* [35] noted that, while grooved wheels show promising results, implementing grooved wheels in practice is problematic because the groove depth is limited and requires frequent re-dressing and grooving of the wheel as it wears. These authors focused their research on axially-grooved wheels and developed a moulding technique to produce grinding wheels with very deep axial-groove geometries (such that the groove depth spans the working radius of the wheel). Their solution overcomes the need for redressing axial grooves on the wheel as the wheel wears while still achieving the improved grinding performance observed when using axial grooves.

Kwak and Ha [36], in 2001, introduced a simulation model using the SIMULAB program for predicting the grinding forces. The model was verified experimentally utilizing axially-grooved wheels that have 6, 12, and 24 grooves with a groove width of 6 mm. On an aluminum oxide wheel (WA 100 L MV), these axial grooves were cut by using a diamond wheel in the tool grinder and inclined from the radial direction. Figure 3.4 depicts a schematic drawing of this wheel. They reported that as the number of axial grooves increase the grinding temperature decreased and the value of surface roughness increased resulting in a worse surface finish.

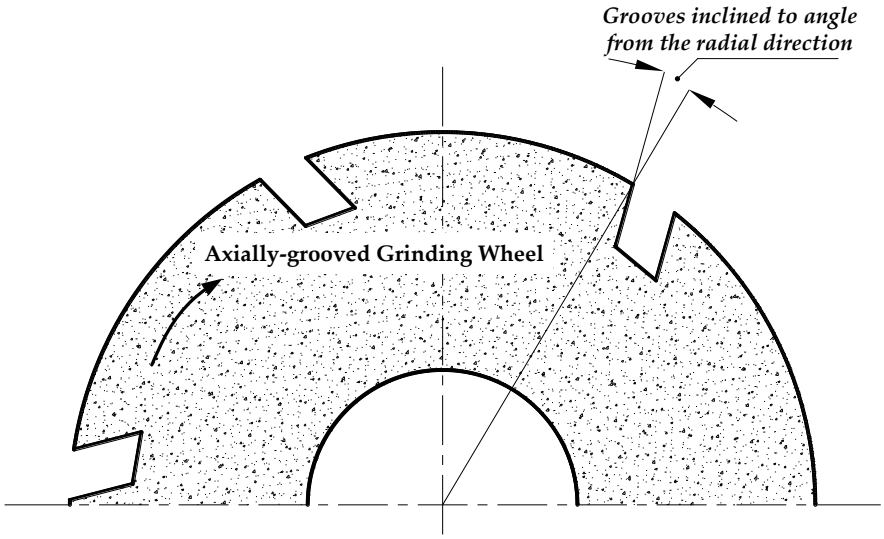

Figure 3.4: Schematic drawing of the grooved wheel used by Kwak and Ha [36]

Fu *et al.* [37], in 2002, presented an optimization model for wheel topography. They designed and fabricated a slotted CBN grinding wheel with 144 axial grooves to optimize the model and to verify it experimentally using the fabricated axially-grooved wheel. The model accounts for the spacing between two effective abrasive gains which, in the case of the grooved wheel, are located at the edges of the groove as shown in Figure 3.5.

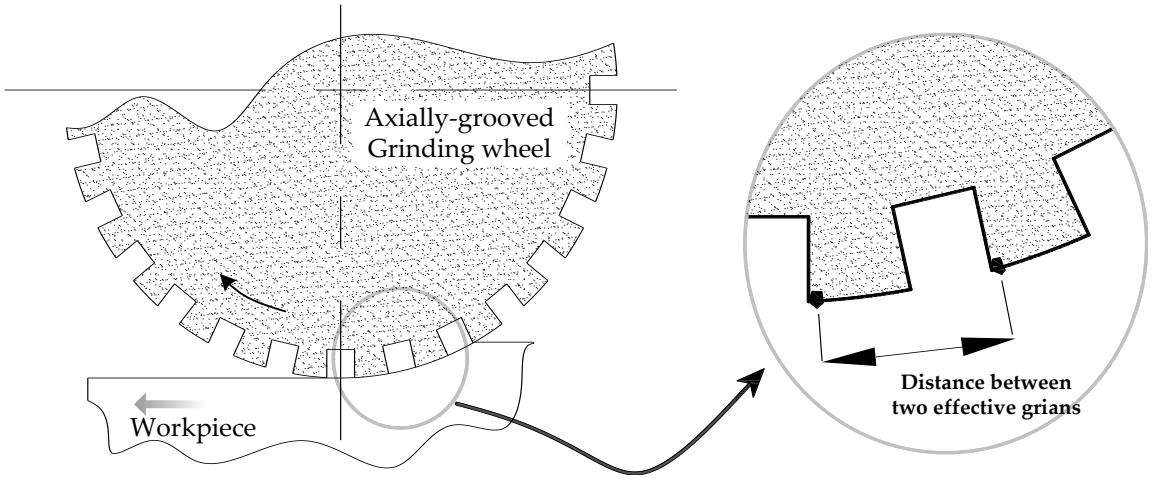

Figure 3.5: Illustration of effective grains on axially-grooved grinding wheel [37]

In 2005, Nguyen and Zhang [38,39] incorporated radial coolant jets into an axially slotted (segmented) grinding wheel via a fluid chamber system which forces the coolant to penetrate into the grinding zone. They also developed a model to predict and understand the relationship between coolant flow rate and fluid mist formation when using the developed grinding wheel. In their later research, Nguyen and Zhang [40,41] concluded that the developed wheel assists in reducing the ploughing and rubbing during grinding and as well as in improving in better chip cleaning.

Jackson [42], in 2008, developed a finite element model to study radial and circumferential stresses for segmented (axially-grooved) grinding wheels. He stated that increasing the number of segments and reducing the depth of the abrasive segments can reduce the radial and circumferential stress levels.

In 2012, Köklü [43] experimentally investigated the cylindrical grinding process for different steel materials using a helically-grooved aluminum oxide wheel (127 TS 291-3 EKR 60K6V). 24 helical grooves were formed on a grinding wheel using a cut-off disc where the groove width and depth were 2.6 and 3 mm, respectively. The helical grooves were cut at three angles 15^o, 30^o, and 45^o. Köklü [43] stated that the helically-grooved wheel, especially the wheel with the 45^o grooves, improved the workpiece ground surface finish, the workpiece roundness, and the residual stress.

In 2014, Fang and Xu [44] established an analytical model to calculate the temperature distribution in surface grinding with an intermittent wheel that has axial grooves. Their experimental results validated the model and showed that the contributions of segment and groove-engaging states to the temperature profiles were of a big difference.

3.3 Summary

As was found in the literature, grinding wheels with grooves or slots appear to have the potential to improve the grinding process. Axially and helically-grooved grinding wheels were utilized in previous research work. The procedures used to form these grooves, however, were unpractical and difficult to reproduce. Therefore, the forthcoming chapters introduce the development of a novel and practical wheel grooving device and demonstrate the effect of circumferentially-grooved grinding wheels on the creep-feed grinding process.

Chapter 4. Experimental Procedure & Proof of Concept

From the previous literature review chapter, it was found that axial and helical grooves with wide and deep grooves have been studied. However, circumferentially-grooved grinding wheels with shallower groove geometries have never been investigated. This chapter describes the experimental procedure for the grinding experiments followed by a description of some initial experimentations used to prove that performing grinding with sallow circumferentially-grooved grinding wheels is effective. Finally, this chapter is ended with a summary.

4.1 Overview of Experimental Setup

This thesis work was based on extensive grinding experimental investigations. Therefore, a great deal of care was performed on monitoring and controlling the grinding parameters such as the conditions of the grinding wheel and the grinding fluid, etc.

4.1.1 Grinding Wheel Preparation

Figure 4.1 shows a picture of a Blohm Planomat 408 creep-feed grinding machine which was used for all the grinding experiments performed for this thesis work. Prior to proceeding the grinding experiments, the grinding wheels utilized in this thesis study were initially trued and then a precise static balancing was performed. The procedure of the grinding wheel balancing is shown in Appendix A. Additionally, to condition the grinding wheel cutting surface, a single-point diamond dresser was implemented for all experiments presented in this thesis work. A medium dressing condition, as summarized in Table 4.1, with a fixed depth of cut of 0.1 mm and overlap ratio of three was applied on the grinding wheel.

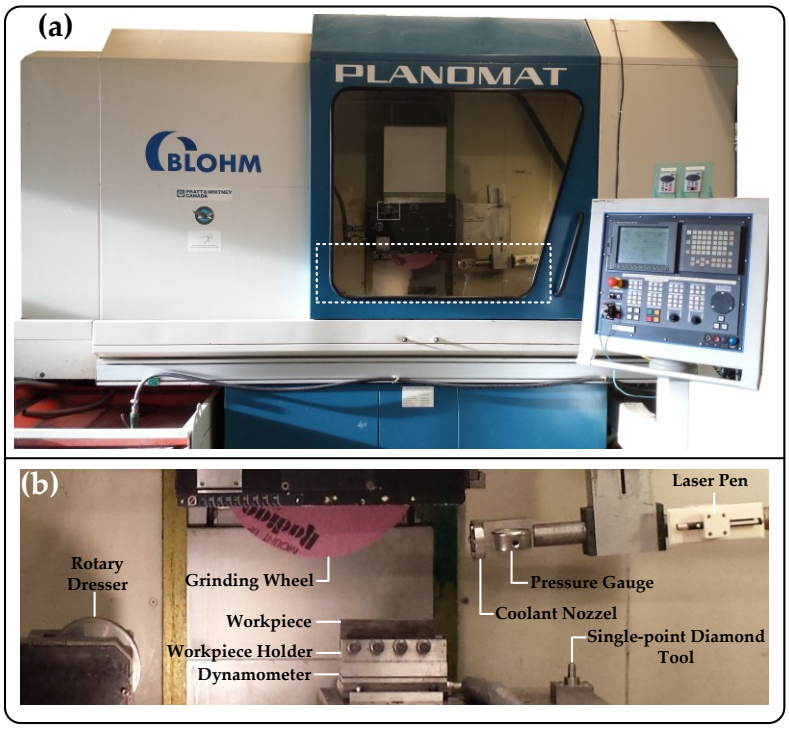

Figure 4.1: A Blohm Planomat 408 creep-feed grinding machine

Table 4.1: Dressing parameters

Parameter	Value
Style	Single-point diamond dresser
Depth of dressing	0.01 mm
Grinding wheel surface speed	22.35 m/sec
Dressing overlap ratio	3
Dressing cross-feed	Variable

4.1.2 Grinding Fluid Delivery

Figure 4.2 depicts the grinding fluid delivery system layout used in this research work. As can be seen, a tank which contains approximately 950 liters of the grinding fluid was used in the grinding experiments. A CIMTECH 310 metal working fluid, which is recommended for creep-feed grinding processes on non-ferrous or ferrous metals, was mixed with water so the mix concentration was 5.1% (the minimum recommended percentage for grinding operation). The grinding fluid concentration was monitored and measured before and in-between every grinding experiment using a refractometer shown in Figure 4.3. The mix concentration in percent was obtained by multiplying the refractometer factor which is here a 1.7 by the scale reading (Brix %) obtained from the refractometer scale.

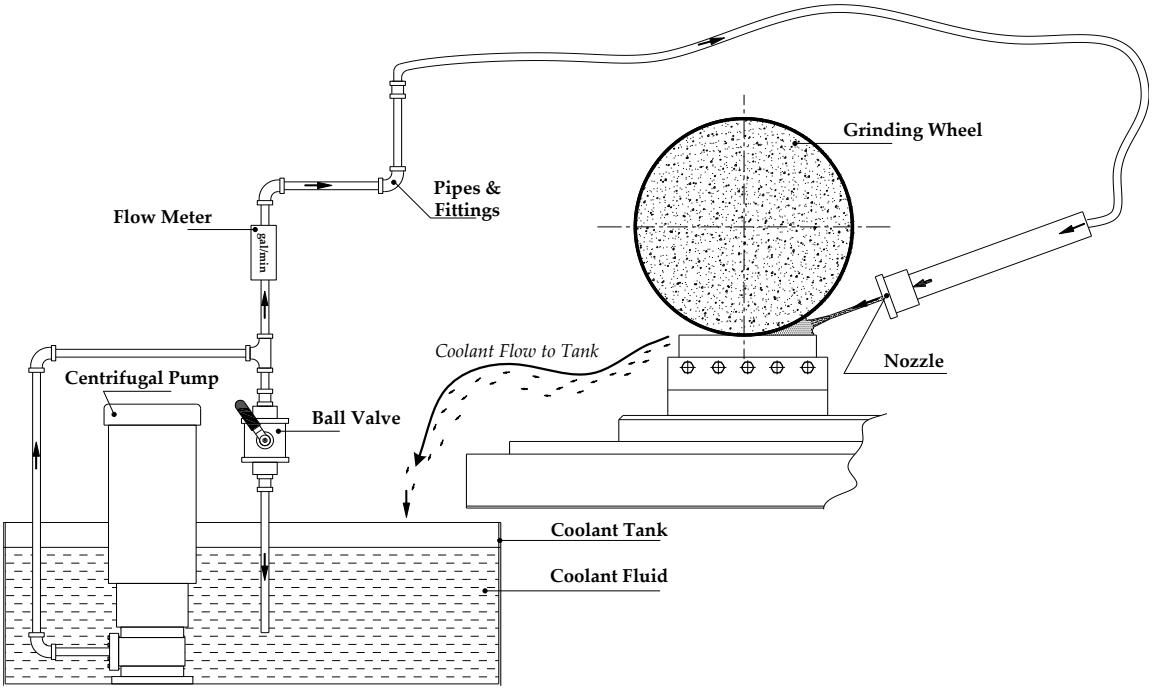

Figure 4.2: Coolant delivery layout.

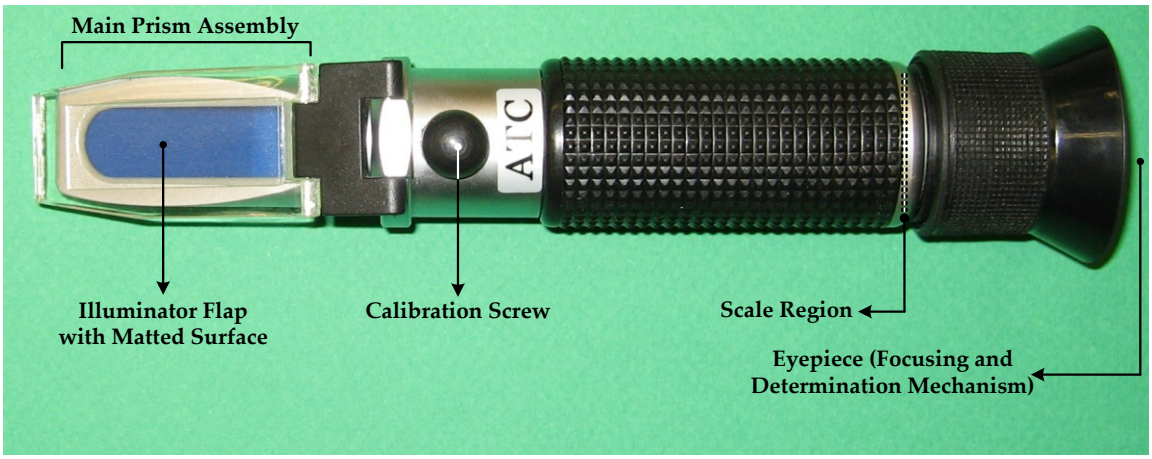

Figure 4.3: Picture of typical refractometer

A continuous filtration of the grinding fluid was performed using two parallel filter medias Cyclotron HF125-3 and Cyclotron HF225-3 of rating 10 and 20 micron, respectively; and produced by Cyclotron Products, Inc. This important maximum filtration procedure was performed to ensure the grinding fluid was always in good condition. The refractometer utilized in measuring the fluid mix concentration was also used for checking the grinding fluid quality. For example, a display of a sharp line, as shown in Figure 4.4(a), indicates a clean fluid and a display of fuzzy or blurred line, as shown in Figure 4.4(b), indicates a dirty or old fluid.

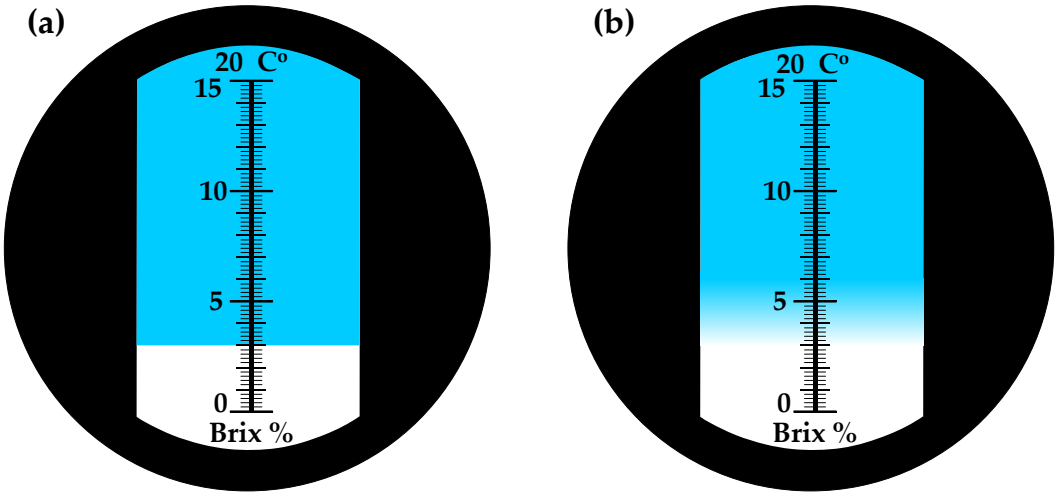

Figure 4.4: Brix% scale (a) clean fluid (b) dirty fluid

Besides the regular check of the grinding fluid concentration and filtration, a precise positioning of the fluid nozzle was achieved. An 8 mm nozzle diameter was used to cover the entire workpiece width as illustrated in Figure 4.5. The nozzle distance from the centre of the grinding wheel was 242 mm. A small reduction in the grinding wheel diameter happens when the grinding wheel is dressed or cleaned and consequently this would result in changing the jet spot position or direction. Therefore, it was necessary to implement a coolant delivery methodology to ensure that the relative position of the

coolant jet with respect to the grinding wheel and the workpiece was always maintained the same.

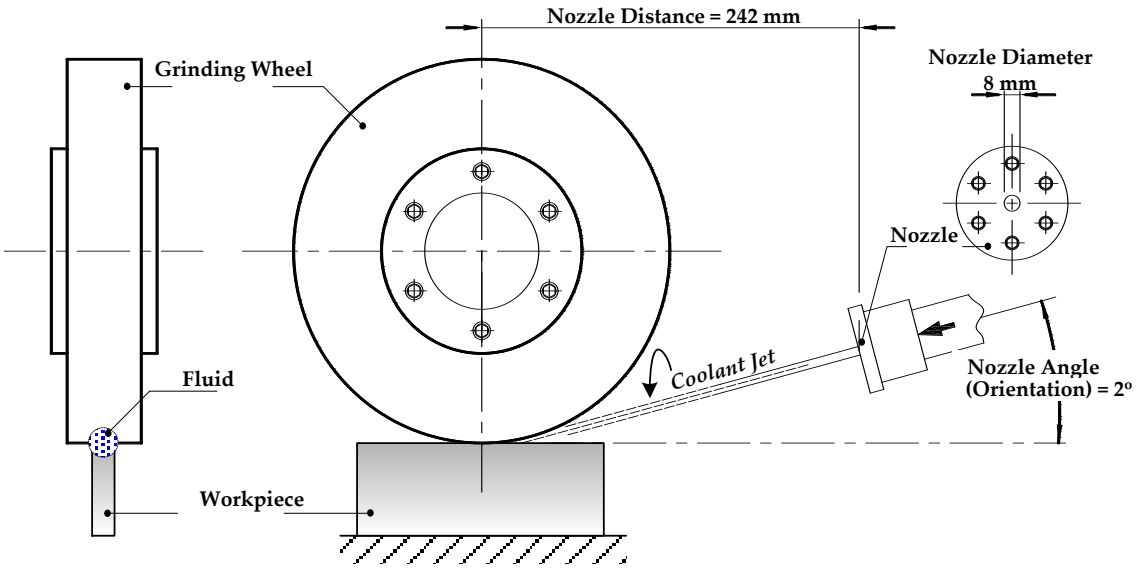

Figure 4.5: Coolant jet relative position to the grinding wheel & workpiece

Figure 4.6 shows a drawing of a procedure developed for adjusting the fluid jet position with any change in the grinding wheel diameter. As can be seen, a laser pen was mounted on the pipe utilized in delivering the grinding fluid. With the availability of the accurate machine axes positioning, a G-code program was written and used so the fluid jet positioning was always updated when any change in the grinding wheel diameter occurred. Then, the exact spot of the fluid jet was adjusted using the laser beam that passes through a hole on a target mounted on the grinding machine table as it can be seen from Figure 4.6. When all the adjustment procedure were set, the fluid positioning system was tightened.

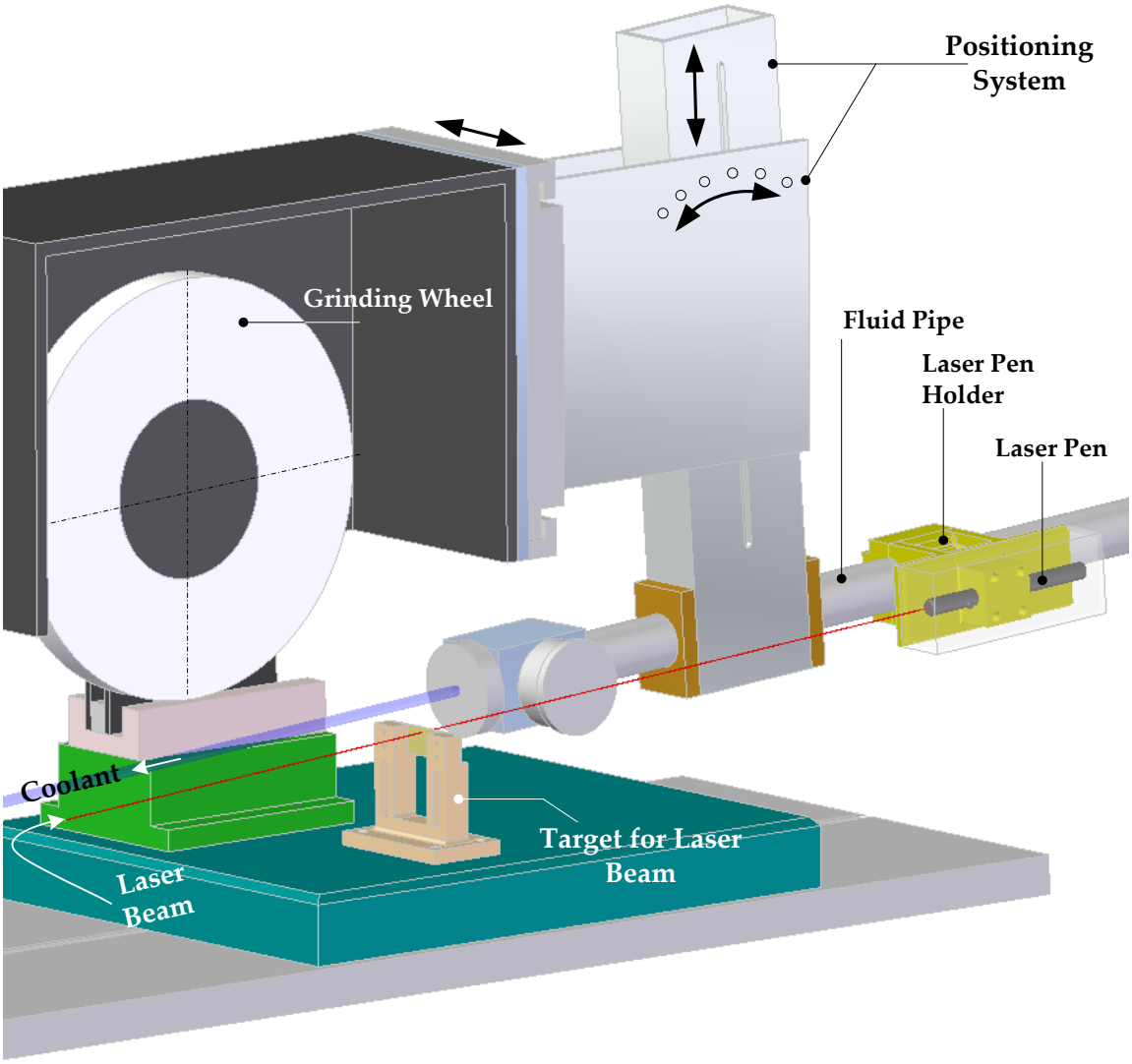

Figure 4.6: Grinding fluid adjustment setup

4.2 Measurements Devices

Figure 4.7 illustrates the experiment setup used during all grinding experiments. As can be seen, consumed grinding power and forces were acquired. The grinding power was measured indirectly by measuring the voltage and current supplied to the spindle motor

using a power transducer and the grinding forces were measured by using a force dynamometer–Kistler 3 component dynamometer.

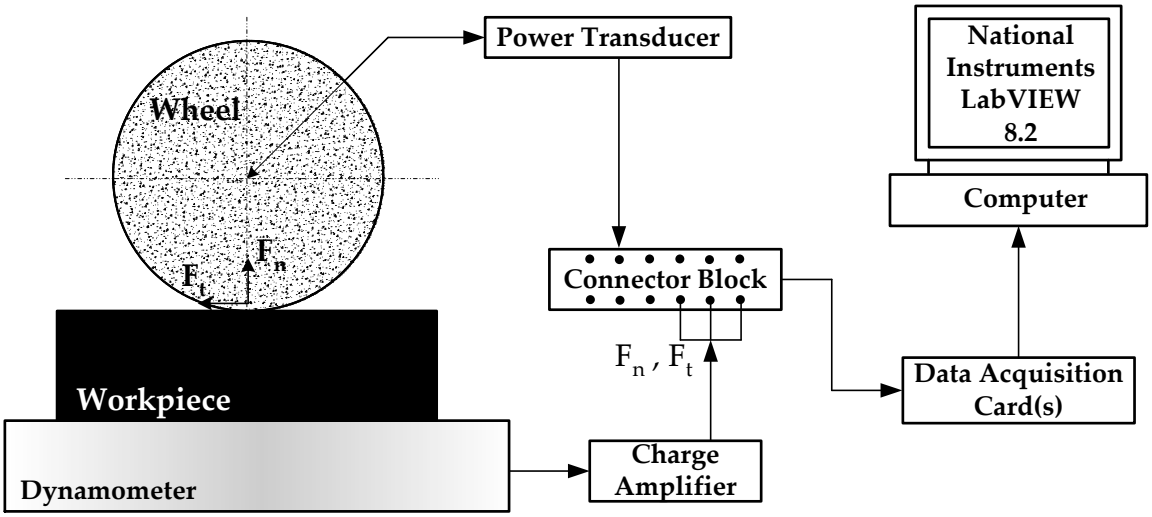

Figure 4.7: Experimental setup

The data acquisition utilized for the experimental work is detailed in Table 4.2. A LabView code was developed to acquire and save the consumed power and forces measurements.

Table 4.2: Data acquisition equipment

Component	Make and Model
Spindle Power Meter	Load Control Inc. PH-3A Power Cell Power Transducer
Force Dynamometer	Kistler: 3 Component Dynamometer – Type 9257B
Charge Amplifier	Kistler: Multi Channel Charge Amplifier – Type 5019
Connector Block	National Instruments BNC 2120
Data Acquisition Card	National Instruments PCI-MIO-16XE-10
Acquisition Computer	Desktop PC
Analysis Software	National Instruments LabVIEW 8.2

Besides acquiring the forces and consumed power data during grinding experiments, the workpiece ground surface was measured. First, a precise high measurement was taken using a height gauge with an accuracy of 0.001 mm to ensure the specific desired depth of cut was achieved. Any sign that the depth of cut was less than the desired value could be an indication of wheel wear or wheel breakdown. Visual inspection of the grinding wheel cutting surface was also performed after each grinding experiment to examine if there were any signs of visible abrasives breakages. Second, the surface roughness along the ground workpiece surface was measured using a MahrFedral Inc. Pocket Surf. The surface roughness measured is the arithmetic average of the absolute values of the roughness profile ordinates (R_a) which is the most widely used one-dimensional roughness parameter. Third, a surface profile scanning measurements were also acquired utilizing a Nanovea CHR white light chromatic sensor with a 1200 µm optical pen. The scanning system was validated using two calibration blocks shown in Figure 4.8.

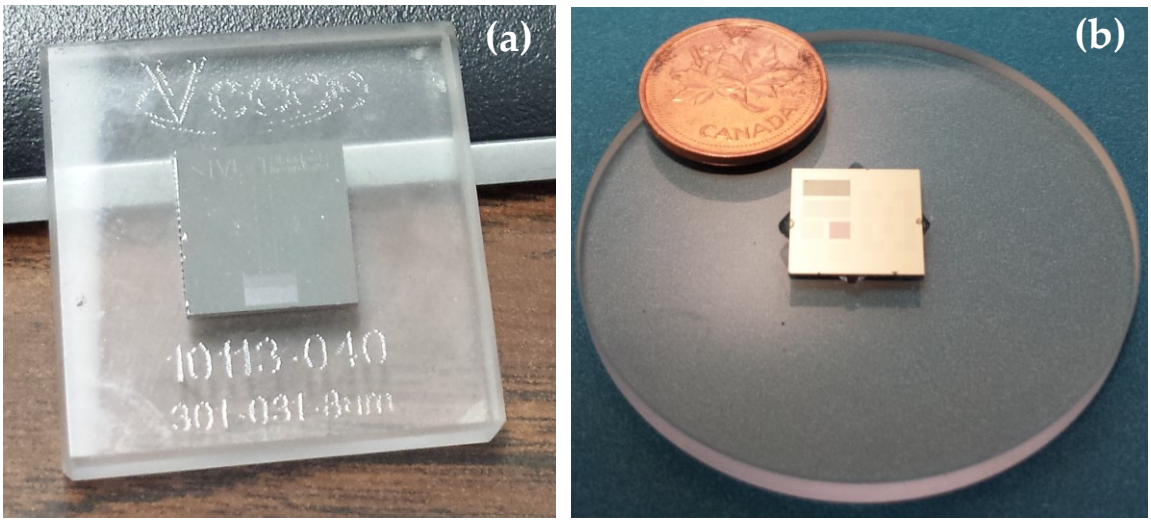

Figure 4.8: Calibration blocks

The first calibration block, Figure 4.8(a), was a Veeco Step High Standard (Veeco Part #: 301-031-8.0µm) from VLSI Standards incorporated and the second calibration block, Figure 4.8(b), was an Ambios Reference Standard for Thin Film Step Heights. Samples of the calibration results are illustrated in Figure 4.9 and Figure 4.10.

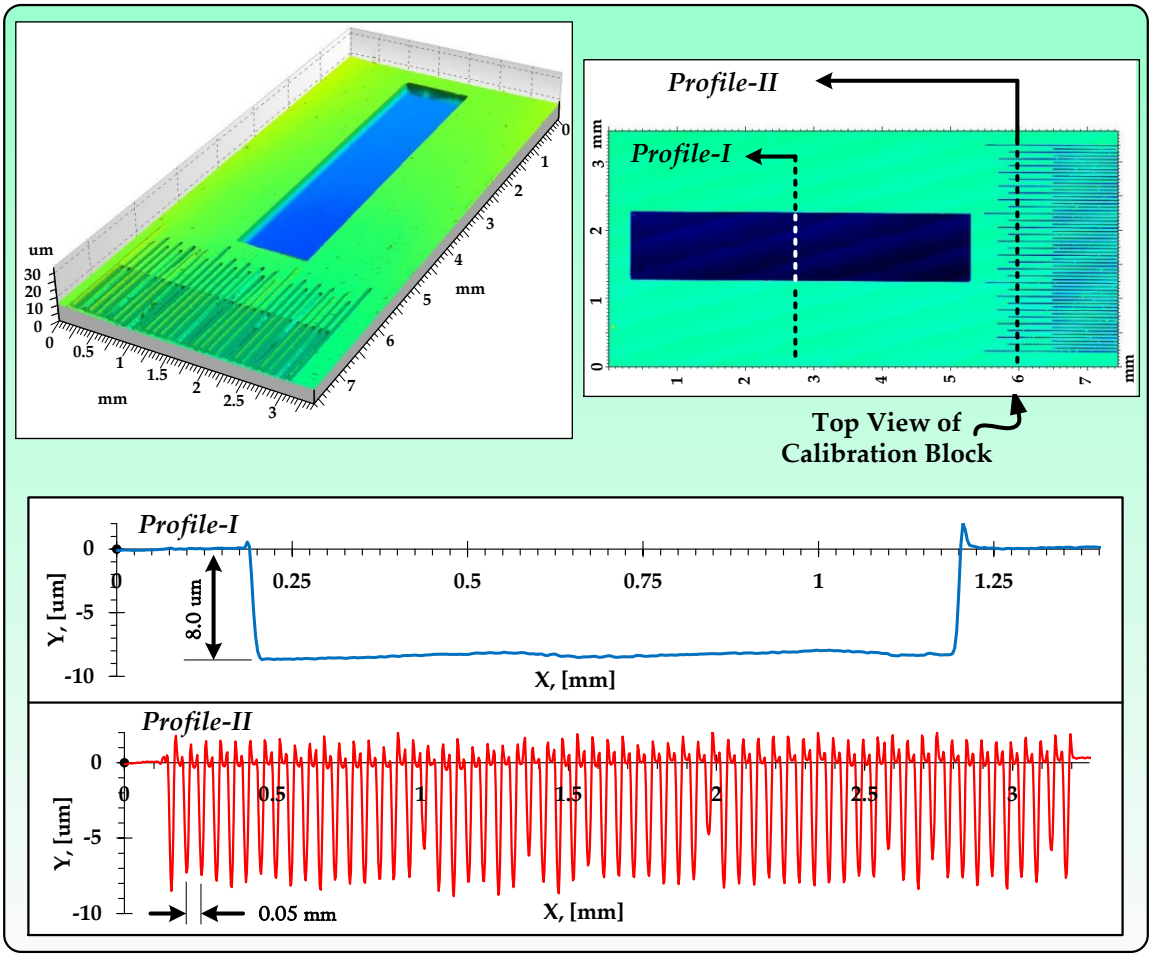

Figure 4.9: Results sample of Veeco Step High Standard

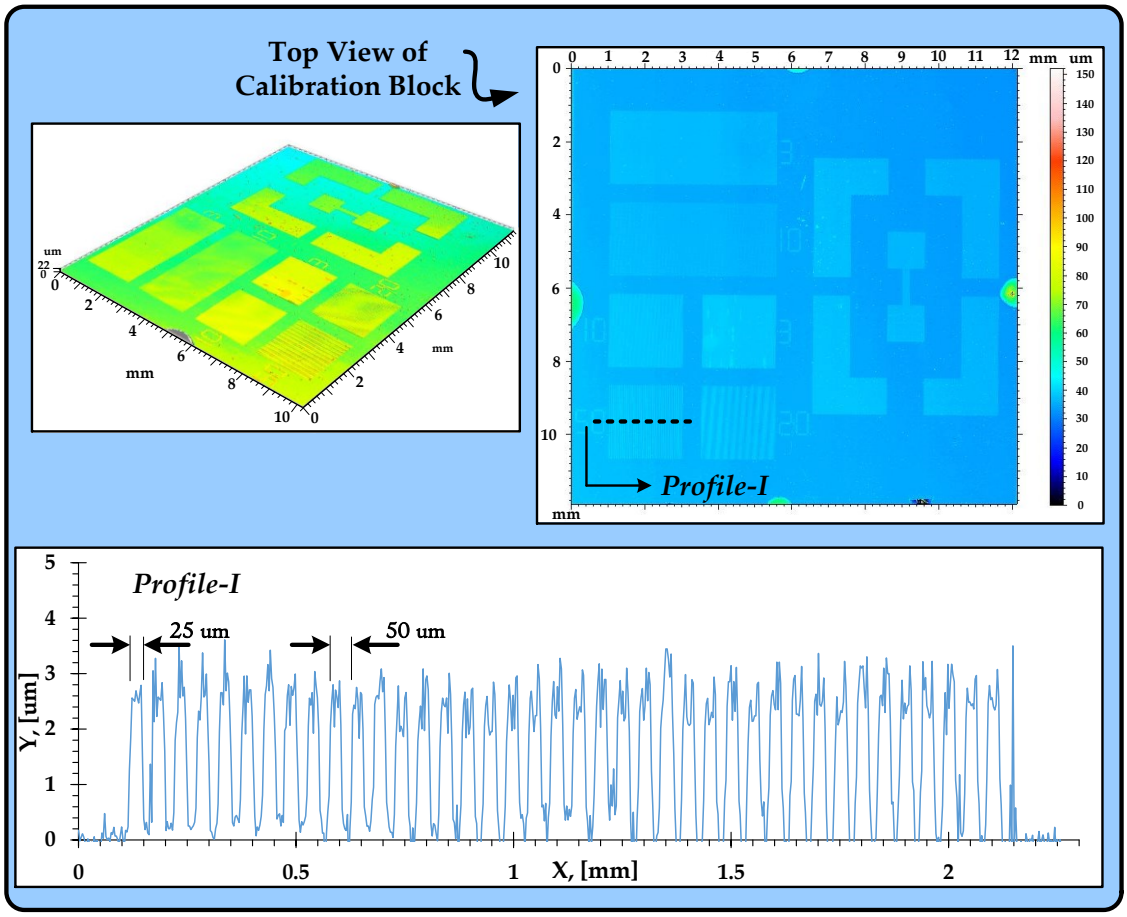

Figure 4.10: Results sample of Ambios Reference Standard for Thin Film Step Heights

4.3 Grinding & Repeatability Testing

In this section, two main grinding experiments were applied. The first experiment was set to examine the change in the consumed power with the change of the grinding wheel diameter. This experiment was considered as it was anticipated to groove and remove the groove from the grinding wheel and thus this would result in a decrease in the

grinding wheel diameter. The second grinding experiment was set to examine the repeatability of the grinding experiments and to ensure the controllability of the grinding fluid delivery and other grinding parameters.

4.3.1 Consumed Power vs. Wheel Diameter Experiments

In this set of experiments, creep-feed grinding experiments were conducted on a Blohm Planomat 408 creep-feed grinding machine utilizing an aluminum oxide Al_2O_3 grinding wheel (WRA 60-J5-V1) and an AISI 4140 steel workpiece material (152 mm × 50 mm × 6.35 mm). The depth of cut, feed rate, and wheel speed grinding parameters were held constant for all experimental samples and set to 1.25 mm, 1.7 mm/sec, and 23 m/sec, respectively. In order to experiment various grinding wheel diameters, the grinding wheel was reduced in radius, using rotary dresser, by 0.570 mm in every experiment (rotary dresser used gradually by 0.095 mm in six passes to achieve 0.570 mm reduction in the grinding wheel radius). Then, to maintain a constant sharp wheel condition after each wheel reduction, the wheel was dressed with a single-point diamond dresser prior to each grinding experiment using the dressing parameters listed in Table 4.1.

Figure 4.11 shows the measured grinding consumed power results verses the grinding wheel diameter. It can be noticed from the figure that the consumed power decreased as the grinding wheel diameter decrease. The maximum change in consumed power was approximately 10% when the grinding wheel diameter decreased by up to 13 mm. The rate of change of the consumed power with wheel diameter reduction was 0.027 kW/mm.

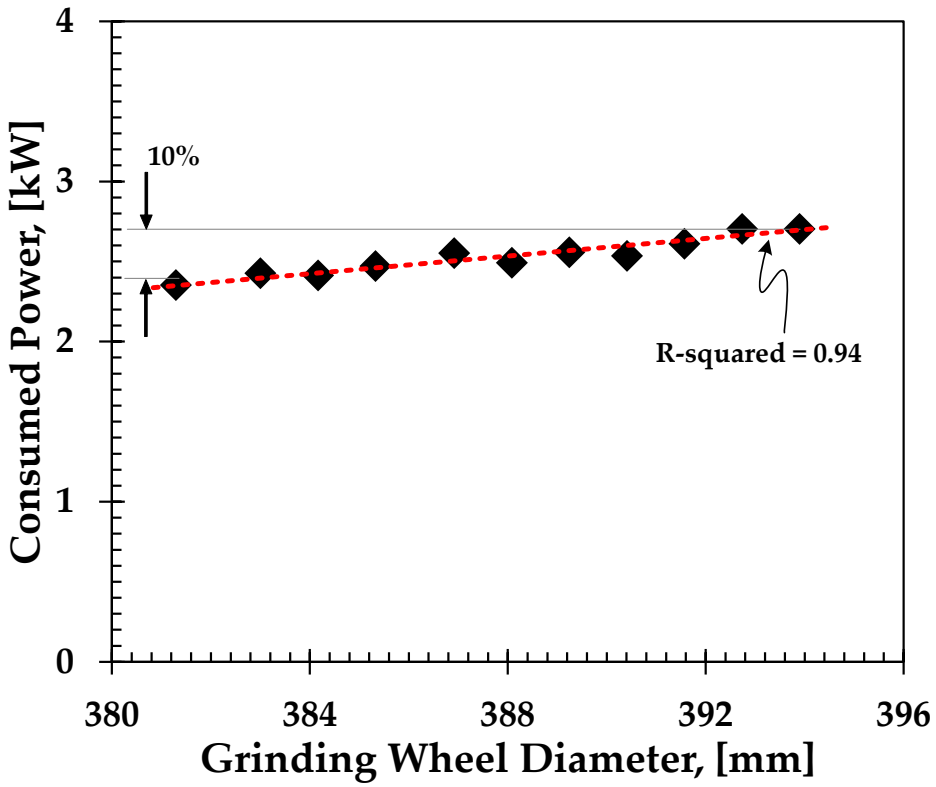

Figure 4.11: Consumed power vs. grinding wheel diameter

It is obvious from the above figure that the results have a linear relationship trend. The R-squared value is 0.94. This resulting trend was expected due to the linearly reduction in the contact area between the workpiece and the grinding wheel as the grinding wheel diameter decreased. More importantly is that the result of this experiment was a supporting evidence that when pursuing the grooving experiments and with the use of shallower grooves resulting in decreasing the wheel diameter in smaller difference than shown in this study, the effect of change in wheel diameter, due to grooving and groove removing, on the resulting measured power would be very small.

4.3.2 Repeatability Experiments

These experiments were performed to test how consistent the grinding operation was. A creep-feed grinding experiments were performed on the Blohm Planomat 408 creep-feed grinding machine utilizing an aluminum oxide Al_2O_3 grinding wheel (WRA 60-J5-V1) and an AISI 4140 steel workpiece material. The grinding cutting path performed at an angle (as shown in Figure 4.12) using a G code program written and used for these experiments. As the grinding progressed along the workpiece, the depth of cut increased. The angle of cut was very small (0.2^o) to obtain precisely the critical depth of cut where a workpiece burn occurred. The initial depth of cut was 1.6 mm. The grinding wheel cutting speed and the workpiece feed remained constant for all experiments and were set to 22.352 m/sec and 1.693 mm/sec, respectively. The grinding fluid was delivered at 50.4 L/min.

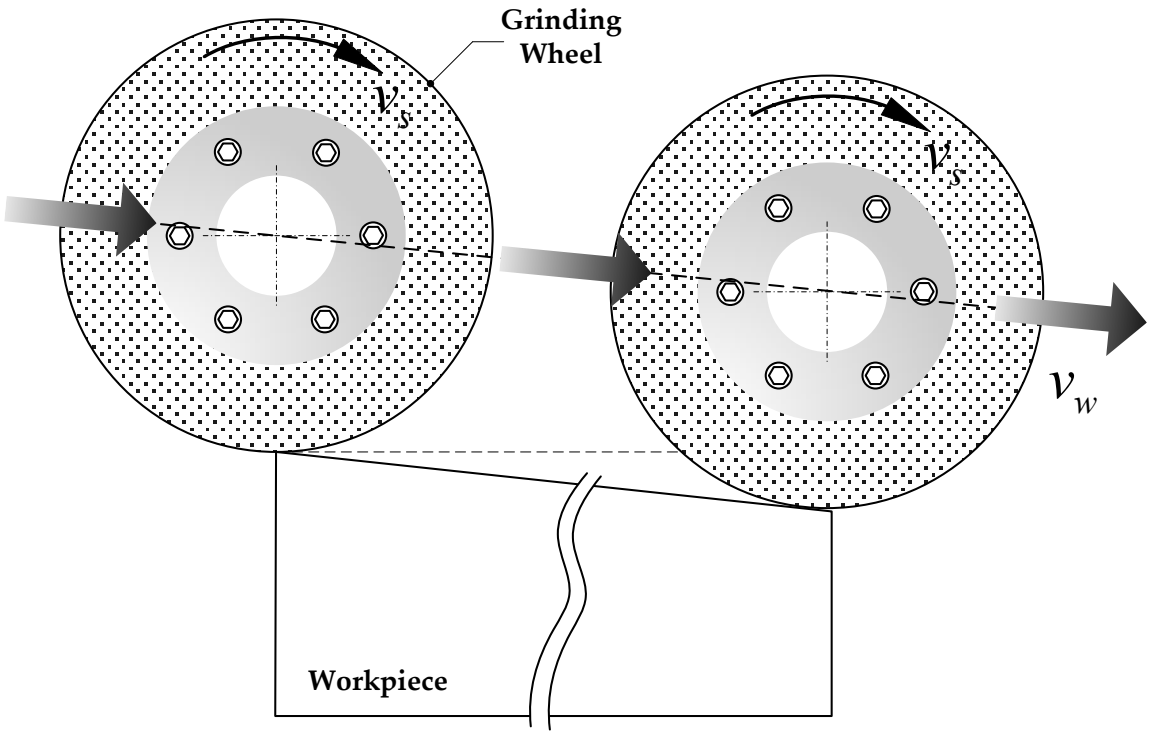

Figure 4.12: Angled grinding cutting path

A procedure was developed to grind two workpieces in two separate grinding passes using the same grinding wheel diameter as illustrated in Figure 4.13. The grinding wheel width was symmetrically divided into two sides. The first side was used to grind the first workpiece, which is workpiece (a) shown in Figure 4.13(a), and the second side was used to grind the second workpiece, which is workpiece (b) shown in Figure 4.13(b). This technique was developed so that: 1- two workpiece samples can be ground with the same grinding wheel diameter; and 2- one side of the wheel can be used for grinding a workpiece using the non-grooved wheel and then the other side can be used for grinding a workpiece using the grooved wheel after grooving it.

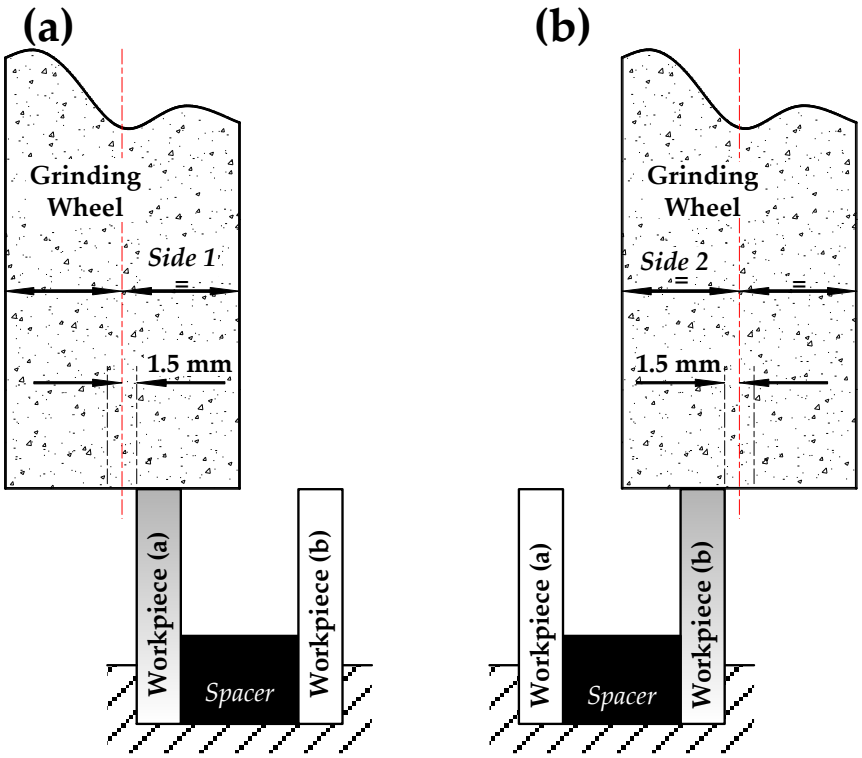

Figure 4.13: Using grinding wheel width for grinding two workpieces

Figure 4.14 depicts the consumed power measured along the workpiece. As can be seen, the consumed power increases as the depth of cut increased and all measured consumed power approximately matched indicating grinding repeatability. The spikes seen at the

end of the curve are where a workpiece burn occurred. It appears, from Figure 4.14, that the burn spikes changes its position and yet the maximum variation of the depth of cut was only 0.028 mm (±0.014 mm) with maximum change in consumed power of 2.9%.

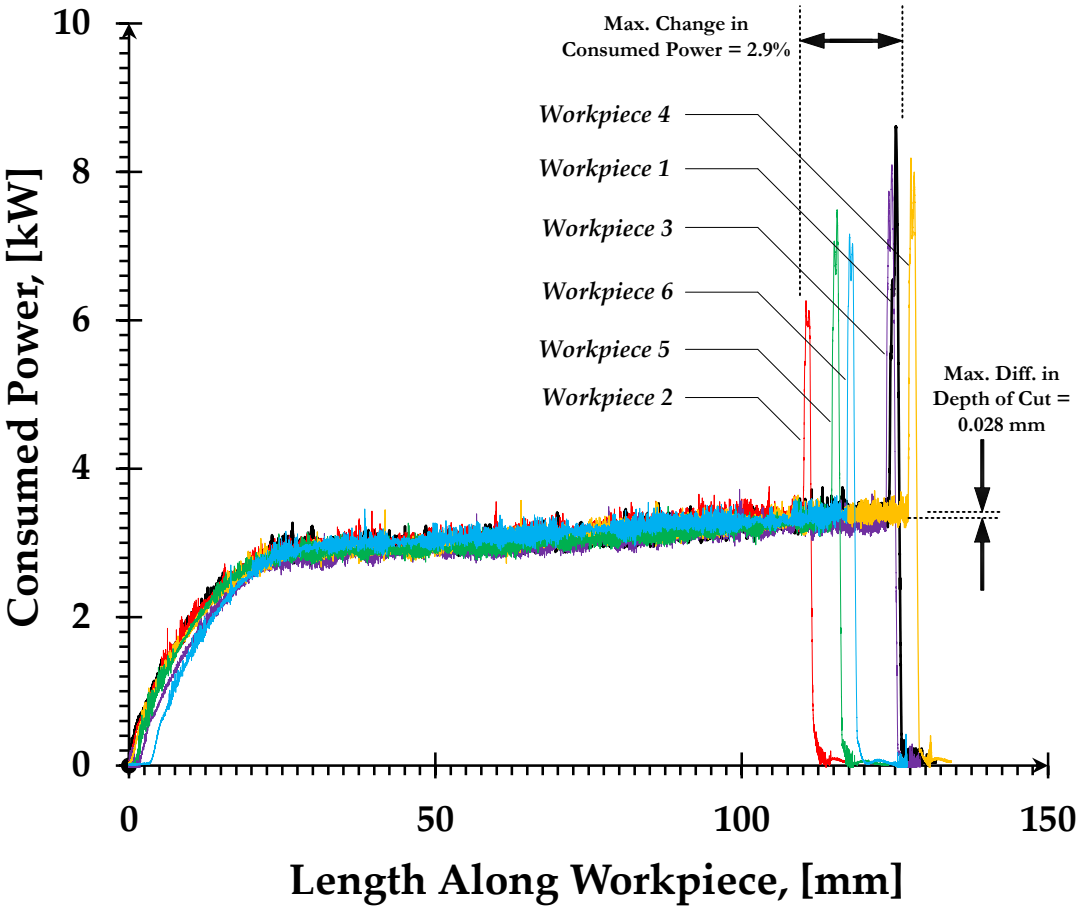

Figure 4.14: Repeatability consumed power comparisons

The results presented in the above two set of experiments indicate that great controllability and repeatability of the grinding parameters can be achieved using the developed technique.

4.4 Initial Wheel Grooving Proof of Concept

In this section, a grinding study was made to investigate whether or not grooving the grinding wheel would improve the performance of a regular a grinding wheel. First, an explanation of how the wheel was grooved is presented and then initial grinding results and comparisons are presented.

4.4.1 Wheel Grooving Method

Figure 4.15 illustrates a novel, inexpensive, and straightforward method to cut circumferential grooves on a grinding wheel surface was performed using a single-point diamond dresser. The grooving was, as seen from Figure 4.15 and Figure 4.16, applied by traversing a rotating grinding wheel across a single-point diamond mounted on the grinding machine table. The resulting groove geometry is shown in Figure 4.16. The spiral-shaped groove on the working surface of the grinding wheel has a groove depth of a_g and a groove width of b_g.

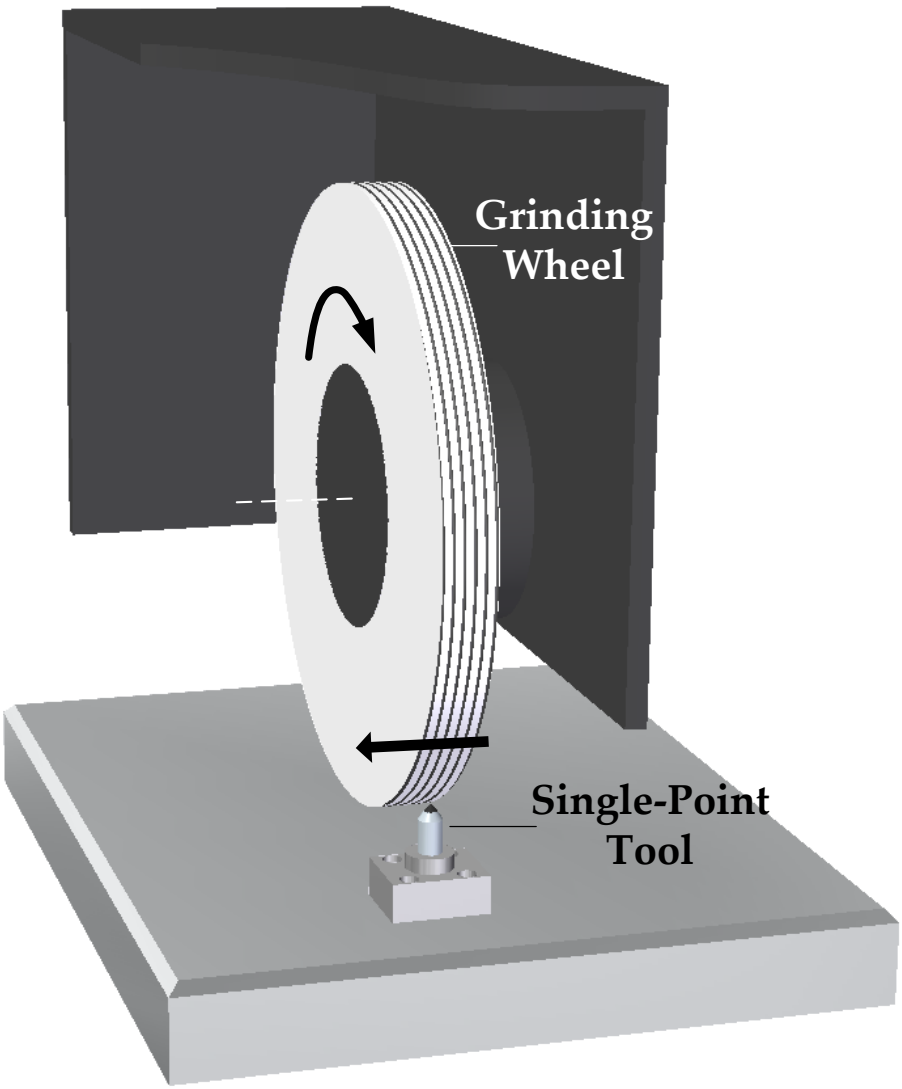

Figure 4.15: Wheel grooving procedure

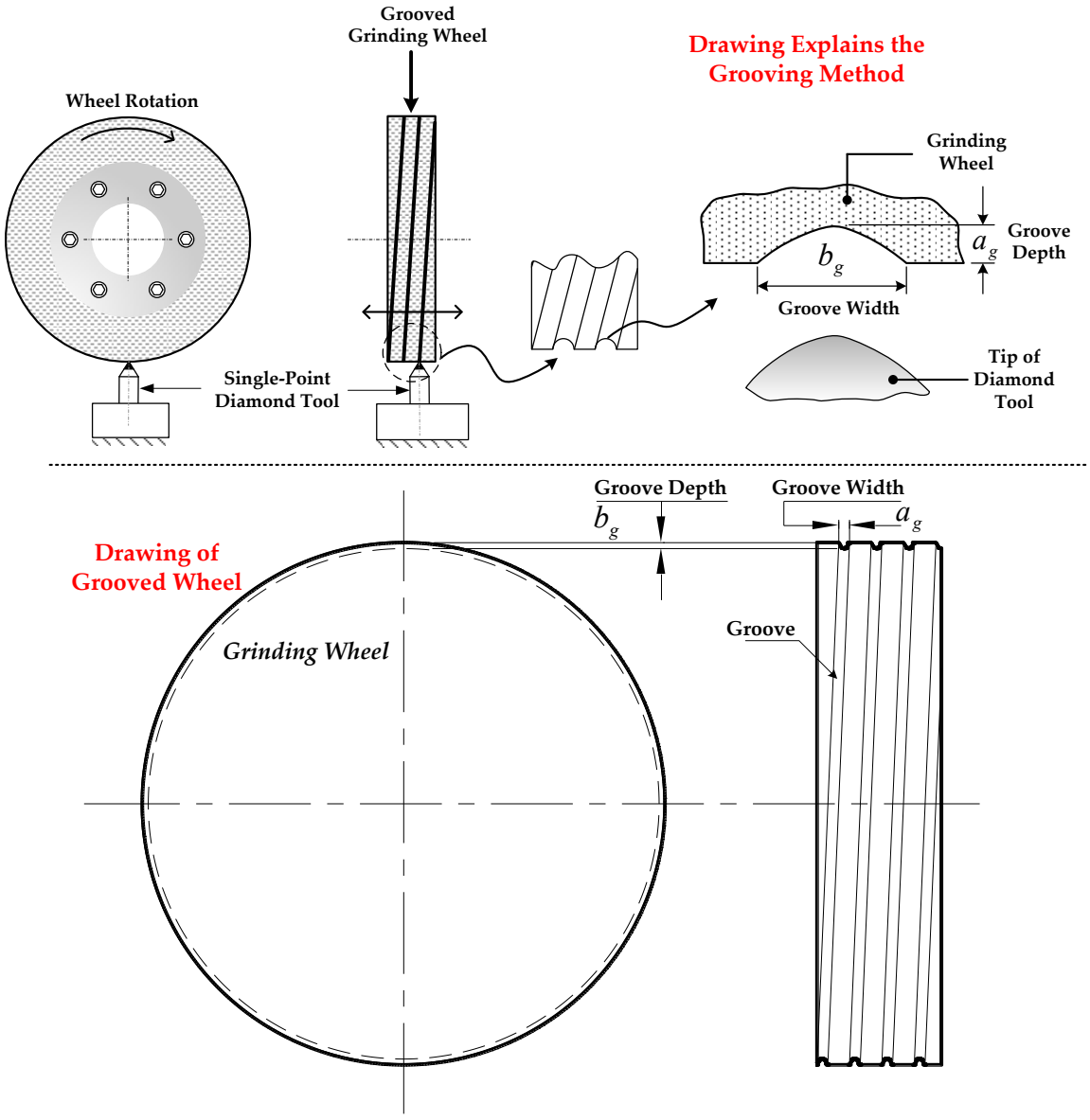

Figure 4.16: Illustration of circumferential groove

Figure 4.17 shows a picture of a grooved grinding wheel (Norton 38A46HVBE) utilized in this study.

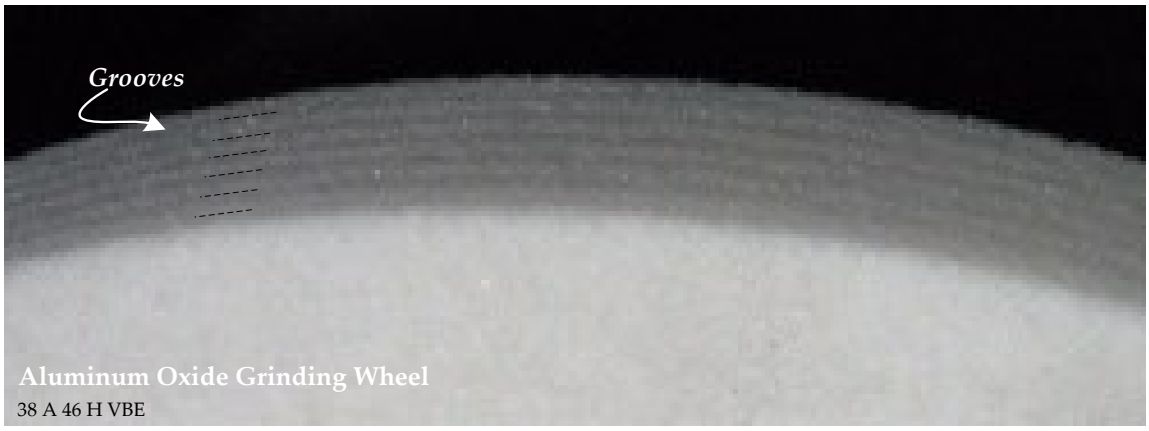

Figure 4.17: Initial circumferential pattern groove on aluminum oxide wheel

4.4.2 Grinding Experiment Procedure

The experimental setup used in this study is shown in Figure 4.18. This experimental investigation was performed on a Blohm Planomat 408 creep-feed grinding machine. An aluminum oxide Al_2O_3 wheel, Norton 38A46HVBE, was used on AISI 1018 workpiece (152 mm × 50 mm × 6.35 mm) with constant grinding parameters. The grinding wheel speed and workpiece feed parameters were 22.35 m/sec and 1.7 mm/sec respectively. In the grinding experiments, power, forces, and workpieces surface finishes were measured. Besides these measured data, a visual inspection was performed on the workpiece and the grinding wheel surfaces to determine whether any surface damage occurred. In this study, two sets of grinding experiments were conducted where each set of experiments consists of the use of a non-grooved wheel and a grooved wheel.

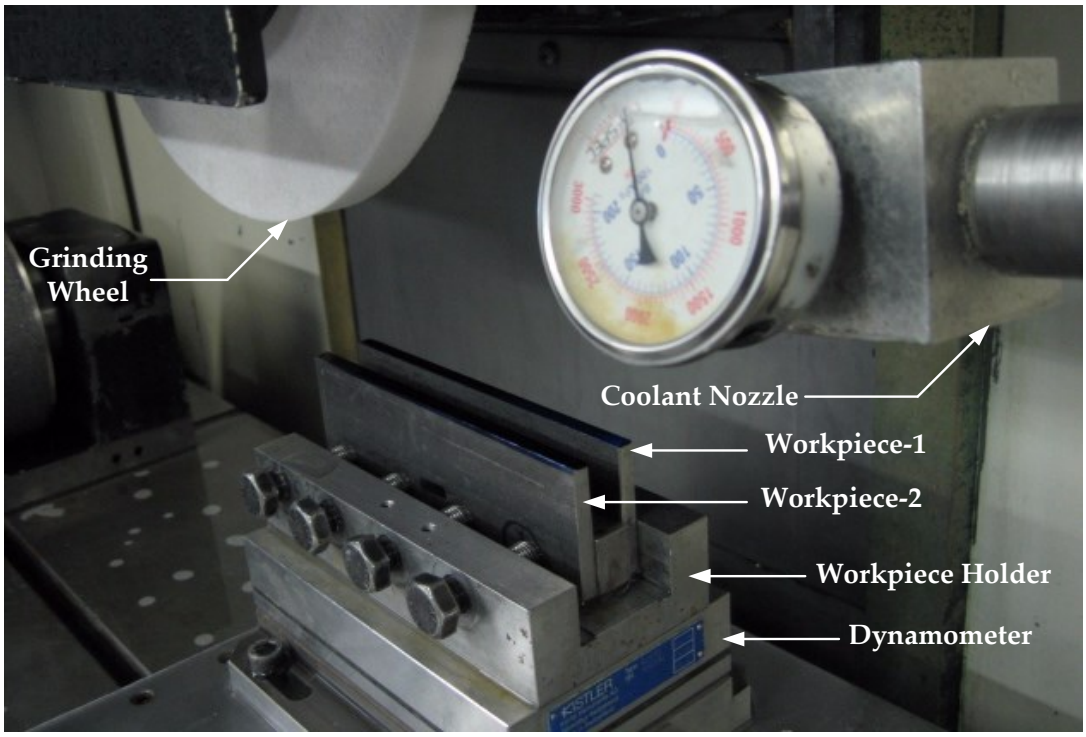

Figure 4.18: Experimental setup

Prior to the grinding experiments, the workpieces were trued and then the grinding wheel was dressed using a single-point dresser. In order to examine both a non-grooved wheel and a grooved wheel using the same grinding wheel diameter for each set of experiments, the grinding wheel working surface was divided into two areas (this method was explained in Figure 4.13). The grinding was first performed on one workpiece using one grinding wheel edge. When the non-grooved wheel experiment was completed, the grinding wheel was grooved to the desired groove geometry and then the grinding experiment was performed on the other workpiece using the other side of the grinding wheel.

In order to examine various depths of cut during a single grinding cutting pass, the grinding machine was programed to take a constant angled grinding path (the cut path angle was 2^{o}). Therefore, this setup enables the depth of cut to continuously increase starting from initial depth of cut of zero. Figure 4.12 depicts schematically the angled grinding cut path which was performed in this study. During the grinding operation along the workpiece, the machine power was monitored. A sudden rise in the consumed power appearing as a power spike indicates the occurrence of workpiece burn.

4.4.3 Results

- ***Consumed Power & Forces Results***

Figure 4.19 shows the resulting consumed power profiles for both the non-grooved and grooved grinding wheels experiments, where the measured spindle power is plotted as a function of the distance travelled by the wheel along the workpiece (lower axis) and depth of cut (upper axis). It can be seen from this figure that, as grinding progressed along the workpiece length, the consumed power increased due to the continuous increase in the grinding depth of cut. As shown in Figure 4.19, the non-grooved wheel was able to grind to a maximum depth of cut of 1.5 mm which was the point or the depth of cut limit where a workpiece thermal damage occurred (as indicated in the figure by the measured power spike). When using a grooved wheel, however, the maximum depth of cut increased to approximately 4.0 mm. Furthermore, the consumed spindle power decreased by about 54% when compared with the non-grooved wheel case.

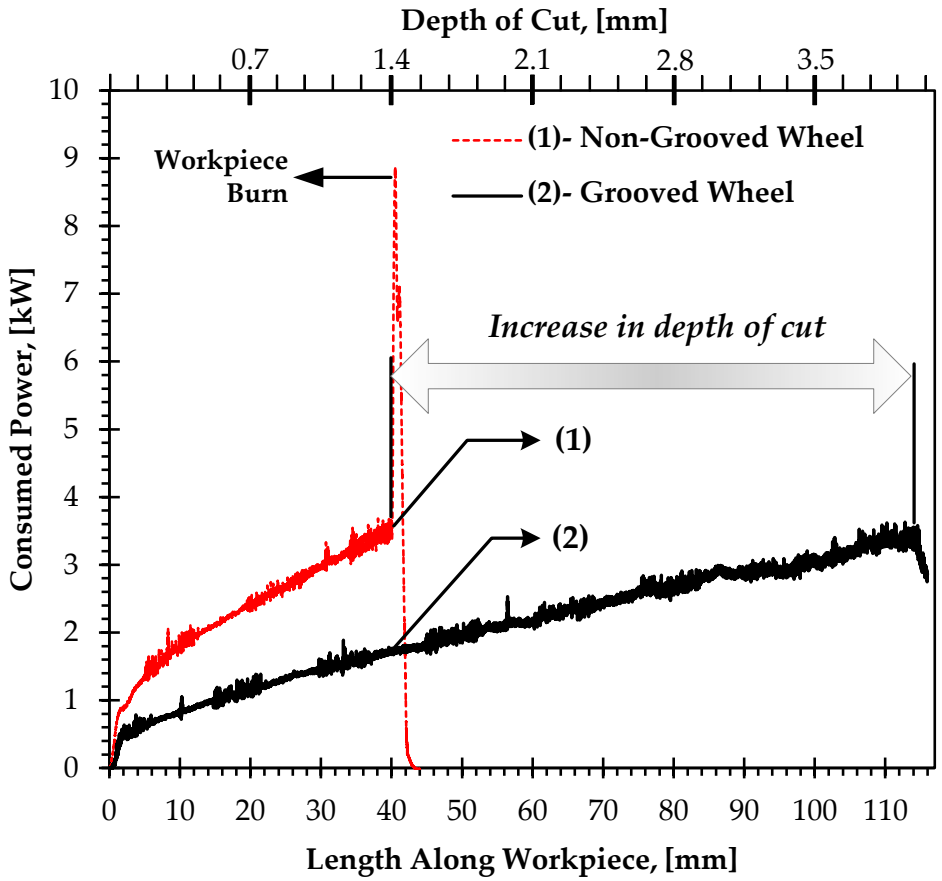

Figure 4.19: Consumed power along workpiece length

Similar trends were also observed with the measured tangential and normal grinding forces as shown in Figure 4.20. The observed drop in spindle power and grinding forces when using the grooved wheel is likely due to a combination of the following two factors: First, the grooved wheel may allow more cutting fluid to be delivered into the contact zone between the workpiece and the grinding wheel enabling more lubrication and cooling than the non-grooved wheel case. Second, grooving the grinding wheel may increase the spacing between active cutting grains on the wheel surface thereby effectively increasing in the average uncut chip thickness and improving grinding efficiency.

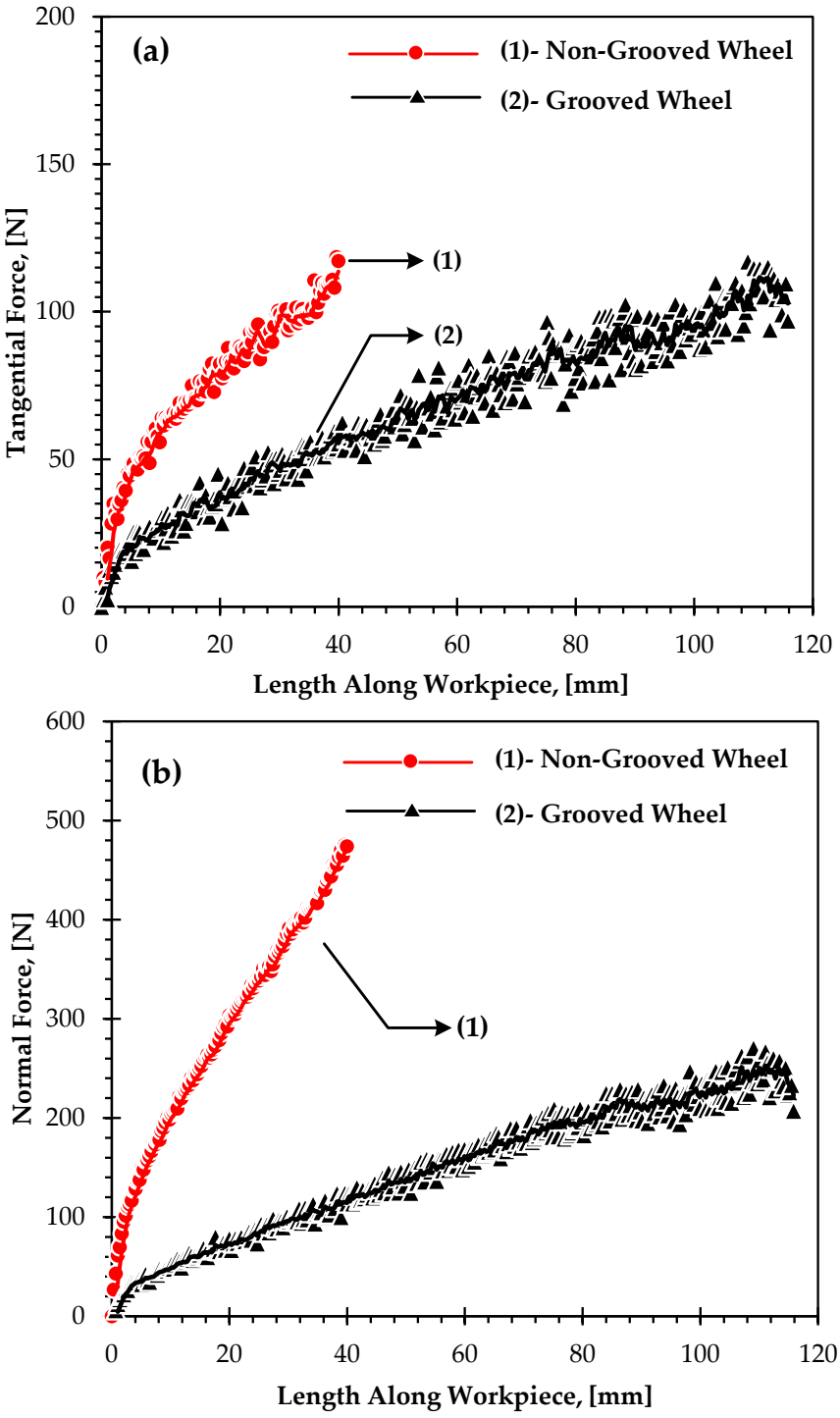

Figure 4.20: Measured tangential and normal forces

- *Surface Finish Results*

Figure 4.21 plots the measured average surface roughness along the length of the ground workpiece for both the non-grooved and grooved wheel cases. As can be noticed from the figure, the grooved wheel resulted in slightly rougher workpiece surfaces. This increase in surface roughness may indicate that grooving the grinding wheel generates a sharper wheel surface – an observation consistent with the hypothesis that grooving the grinding wheel may increase the spacing between the active cutting grains. It should be pointed out, however, that the resulting increase in surface roughness is still below the 1.6 μm surface roughness associated with Average Quality surface finish [45].

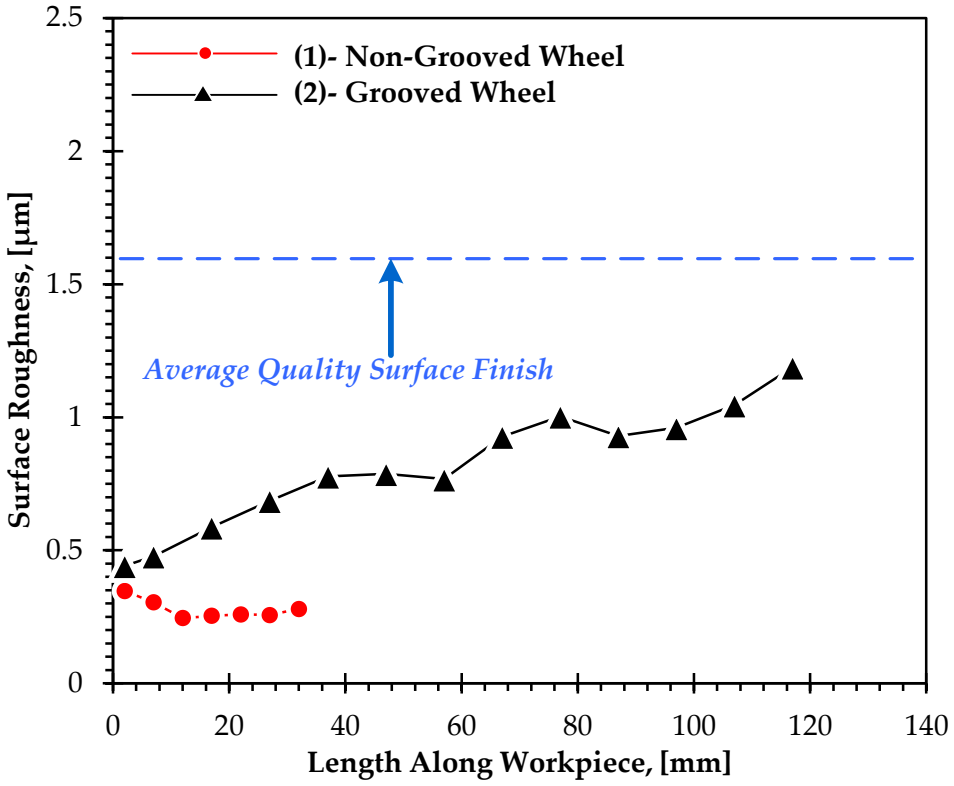

Figure 4.21: Surface roughness along the workpiece's ground surface

Additional workpiece surface measurements were taken using a Nanovea PS-50 Surface Profilometer to determine whether or not the use of the grooved wheel leaves any trace of groove marks on the workpiece ground surface. Figure 4.22 shows an example of the measured surface profile across the width of the workpiece for both the non-grooved wheel and grooved wheel cases. As can be seen in this figure, there was no indication of any groove marks left on the ground surface.

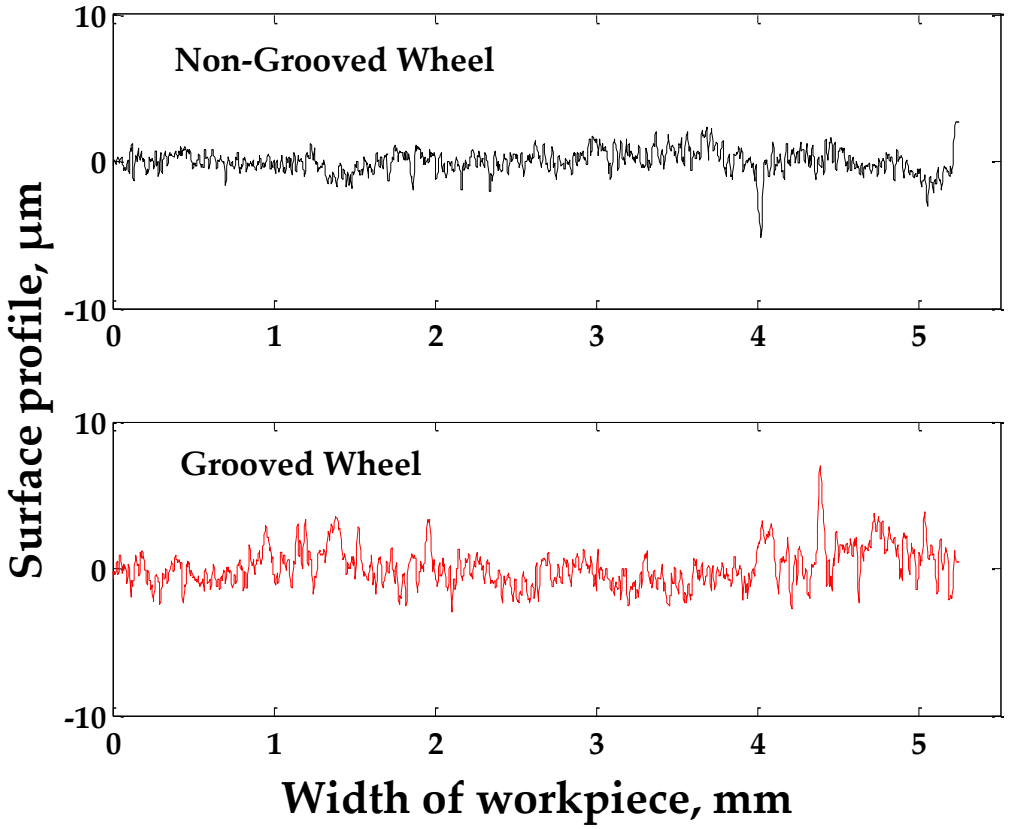

Figure 4.22: Workpiece surface profile

4.4.4 Discussion

It was shown from the above figures, the consumed power figure and forces figure, that the mechanism of cutting of the grooved grinding wheel is different in comparison to

the regular non-grooved grinding wheel. Two main parameters that assist in describing the prevailing mechanism of the abrasive cutting. These parameters are the specific energy and the force ratio. The specific energy results from this experiment is shown in Figure 4.23. As can be seen, the specific energy decreases as the depth of cut increased when the grinding progressed along the workpiece. More, the specific energy of the grooved wheel is less than the non-grooved case. This observation might be due to the energy consumed in the grinding using the grooved grinding wheel was spent more on deforming and cutting and less on sliding than the regular wheel.

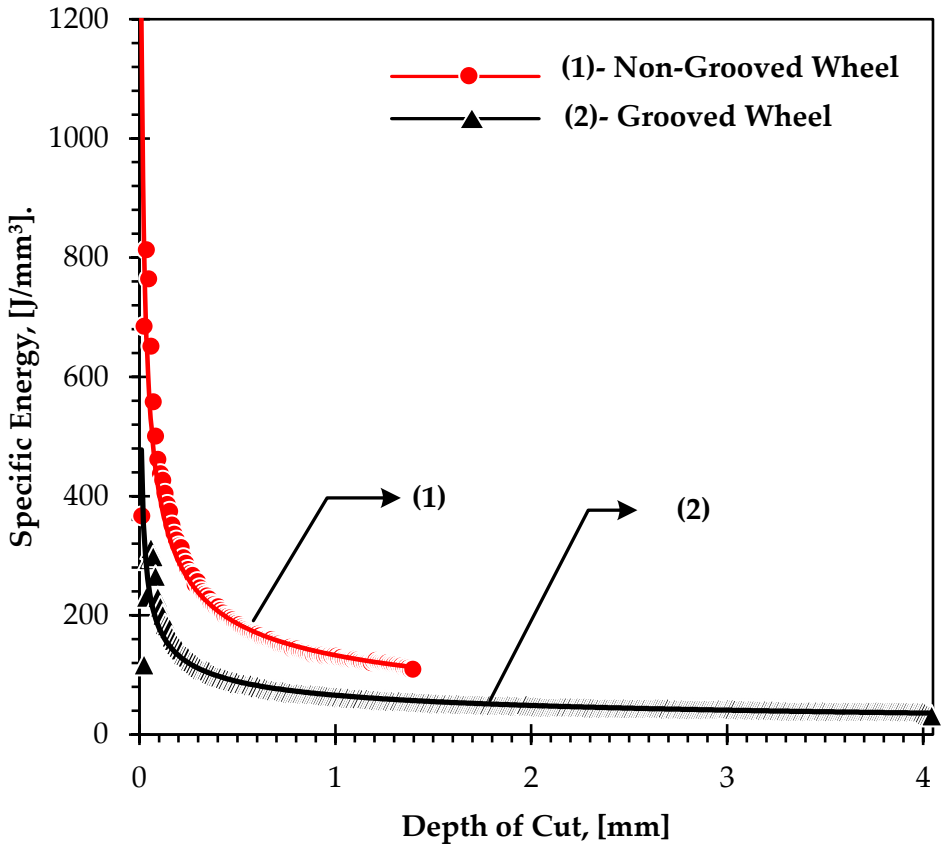

Figure 4.23: Specific energy vs. depth of cut

The force ratio, which is the tangential force divided by the normal force, is illustrated in Figure 4.24. From the figure, it appears that the force ratio is higher when grinding with

the grooved wheel. This might be an evidence for a change in the friction forces during grinding. Therefore, there is less friction when using grooved wheel due to the decrease in the number of grains, which was caused by grooving the wheel, in the contact zone.

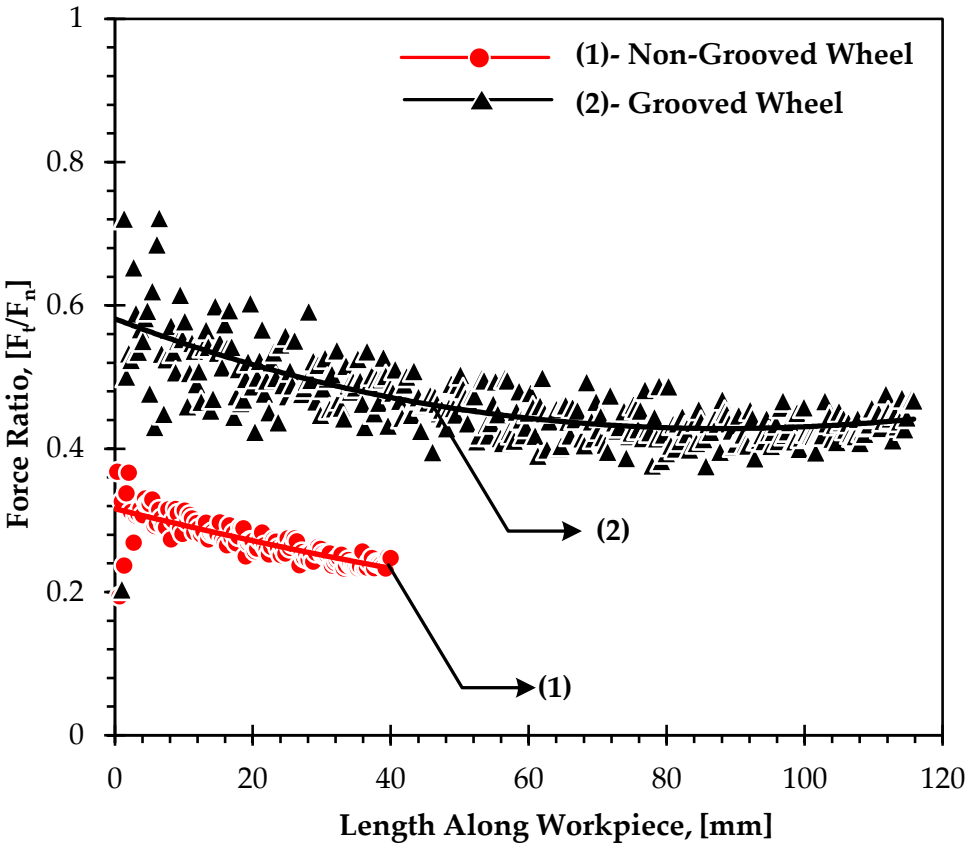

Figure 4.24: Force ratio

It was found from this proof of concept experiment that the new grooving method works and outcomes in better results. However, this proof of concept did not study various groove geometries and groove factors. The groove geometry is assumed to take the cross-section interaction between the grinding wheel and the grooving tool tip and, as described previously, the groove factor is based on the remaining cutting surface area of the grinding wheel after grooving it which can be calculated from:

$$\eta = \frac{A_o - A_g}{A_o} \% \tag{4.1}$$

For that, the forthcoming chapter, chapter 5, studies various groove factor and geometries. The study will consider the use of another aluminum oxide grinding wheel with different grits specification. Additionally, more examination of why the grooved grinding wheel behaves better or different than the regular non-grooved grinding wheel is explored carefully in later chapter, chapter 7.

4.5 Summary

In this chapter, it was presented how all experimental procedure was under precise control. Also initial investigation of wheel grooving showed a potential improvement of the grinding operation. It was found that circumferentially-grooved grinding wheel can remove more than twice as much material as a non-grooved wheel before workpiece burn occurs. Furthermore, it was found that the consumed power dropped by approximately 54% when using a grooved wheel. The resulted surface finish was slightly higher in the grooved wheel case than the non-grooved wheel case. This promising results leads to more grooving experiment investigation which is presented in the following chapter, Chapter 5.

Chapter 5. Wheel Grooving Investigation

5.1 Introduction

An initial investigation of wheel grooving, which was called proof of concept, presented in the previous chapter proofed that grooving the grinding wheels with circumferential groove have a potential improvement to the creep-feed grinding process. Therefore, in this chapter, wider exploration of the use of shallow circumferential grooved grinding wheels to the creep-feed grinding is explored. Various groove factors and geometries are studied in this chapter.

5.2 Experimental Method

In this study, a Radiac Abrasives WRA 60-J5-V1 aluminum oxide (Al_2O_3) wheel was utilized to investigate further the performance of the newly implemented circumferentially-grooved wheels. This grinding wheel had different specifications, such as grit size and hardness, than the once used in the previous chapter for the proof

of concept study. The grinding conditions are similar to the described in the previous chapter. However, the following table, Table 5.1, summaries these grinding conditions.

Table 5.1: Grinding conditions

Condition	Description
Grinding Process	Creep-feed Grinding
Grinding Wheel	aluminum oxide (Al_2O_3) wheel (Radiac Abrasives WRA 60-J5-V1)
Workpiece	AISI 4140 – 46 HRC – (152.4 mm × 6.23 mm × 30 mm)
Wheel Speed	22.4 m/sec
Feed Rate	1.7 mm/sec
Results Measured	Forces, Consumed Powers, Surface Roughness
Dressing	dressing feed of 0.04 mm/rev and a dressing depth of 0.01 mm
Fluid Flow	50.4 L/min

Experiments were initially carried out using a regular (non-grooved) grinding wheel in order to establish a benchmark for comparing the performance of the grooved wheels. Referred to throughout this chapter as Case 1, these benchmark creep-feed grinding experiments gradually increased the depth of cut from 0.75 mm until either workpiece burn or grinding wheel breakdown occurred.

Similar experiments were then carried out with three circumferentially-grooved wheels, referred to in this chapter as Cases 2, 3 and 4, to compare their performance against this benchmark. As summarized in Table 5.2 and illustrated in Figure 5.1, Cases 2 and 3 used two different groove factors (70% and 50%, respectively) while keeping the groove width and depth constant at 1.08 mm and 0.10 mm, respectively. For these experiments, the two different groove factors were achieved by changing the single-point diamond dressing lead from 3.60 to 2.16 mm per wheel revolution (referred to as groove lead in Table 5.2). The experiments conducted for Case 4 investigated the effect of reducing the groove width from 1.08 mm to 0.50 mm, while keeping the groove factor and groove depth the same as in Case 3. Note that in order to change the groove width without changing the groove depth, two different single-point diamond dressing tools were required. Figure 5.2 illustrates the measured tip geometry for the two diamonds used in

this research. Diamond tips were selected such that, for the given depth of cut of 0.1 mm, the width changed by approximately a factor of two (from 1.08 mm for Cases 2 and 3, to 0.50 mm for Case 4).

Table 5.2: Summary of groove parameters

Case #	**1**	**2**	**3**	**4**
Groove Factor - η	100%	70%	50%	50%
Groove Width - b_g (mm)	--	1.08	1.08	0.50
Groove Depth - a_g (mm)	--	0.10	0.10	0.10
Groove Lead (mm/rev)	--	3.60	2.16	1.00
Groove Shape	--	Figure 5.1(a)	Figure 5.1(b)	Figure 5.1(c)

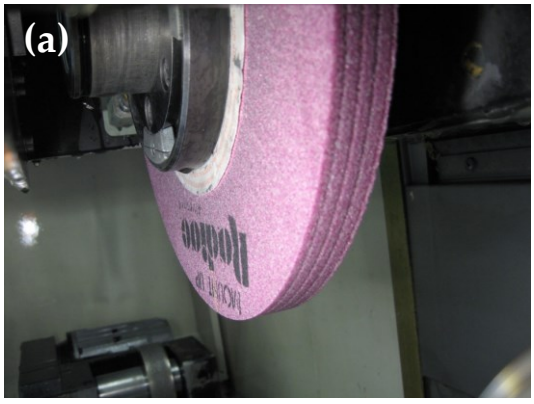

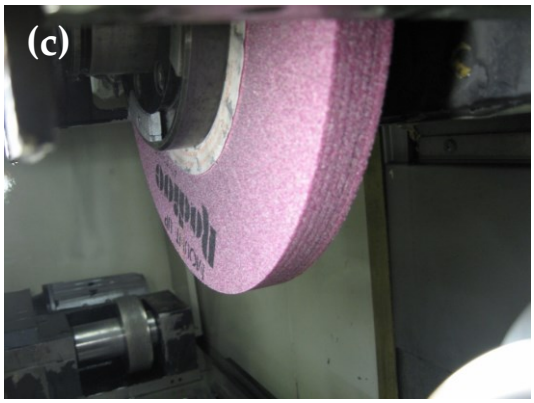

	(a) Case 2	**(b) Case 3**	**(c) Case 4**
η	70%	50%	50%
a_g	0.1 mm	0.1 mm	0.1 mm
b_g	1.08 mm	1.08 mm	0.50 mm

Figure 5.1: Grooved grinding wheels with different groove geometries

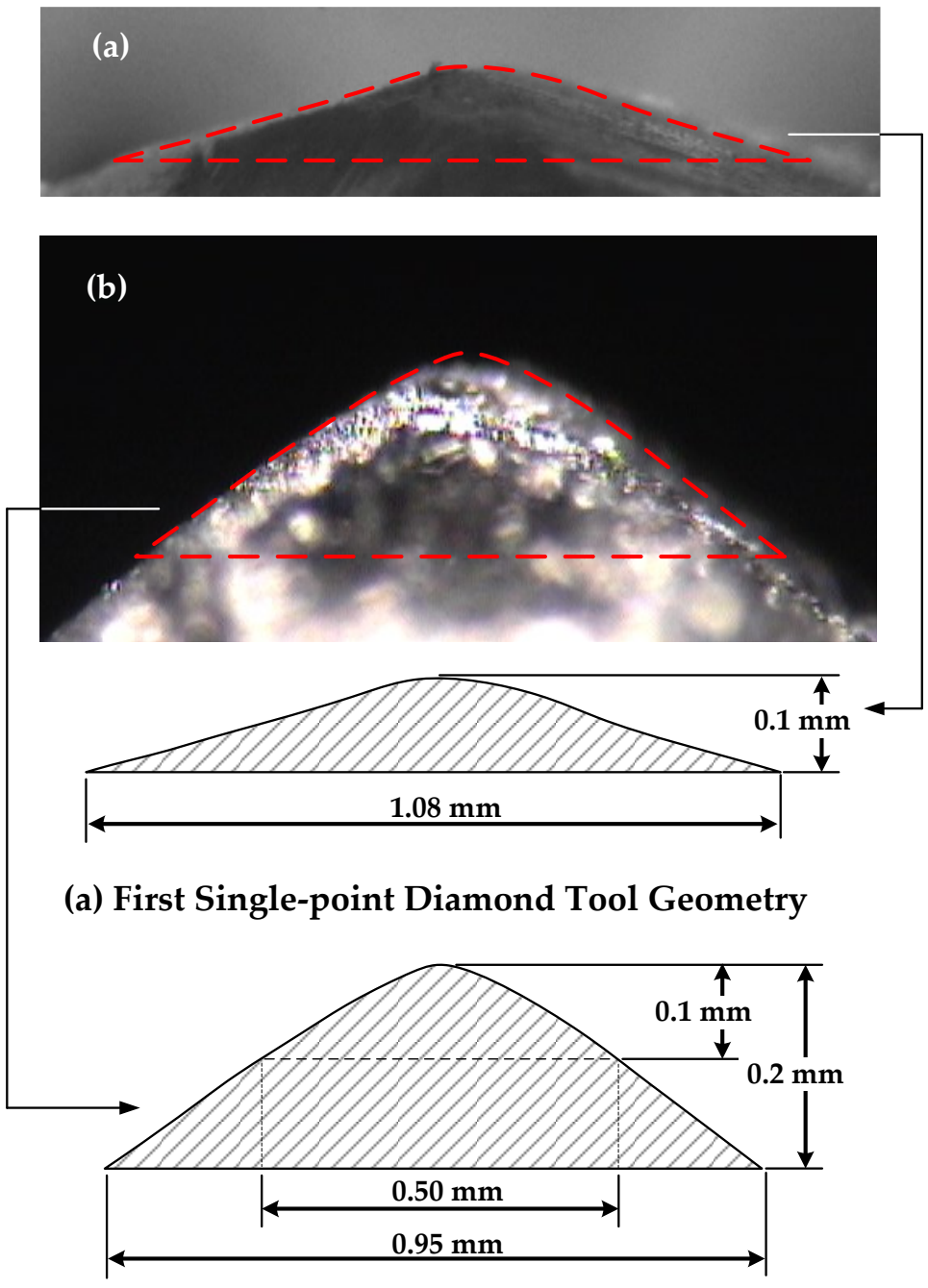

Figure 5.2: Single-point diamond tip geometries

5.3 Results and Discussion

Figure 5.3 compares the measured creep-feed grinding spindle power as a function of increasing grinding depth of cut for all four cases (regular non-grooved wheel and three grooved wheel cases). It can be seen in Figure 5.3 that, as the grinding depth of cut increases, the consumed power increases as expected; however, this figure also shows that, in all cases, the grooved grinding wheels required less power than the non-grooved wheel and enabled larger grinding depths of cut before workpiece burn or wheel breakdown occurred. As summarized in the upper portion of Table 5.3, compared with a non-grooved grinding wheel, there was an average reduction in the consumed power by 34% when using a grooved wheel having a 70% groove factor, and an average reduction in the consumed power by 42 to 61% when using a grooved wheel having a 50% groove factor. Figure 5.3 also shows that the maximum grinding depth of cut for the non-grooved wheel (Case 1) was approximately 1.82 mm, after which point workpiece burn occurred and power spike was recorded. The maximum depth of cut achieved using the grooved wheel with a 70% groove factor was 2.75 mm, after which point workpiece burn occurred. This increase in depth of cut represents an improvement of 51%. Furthermore, the maximum depth of cut achieved using the grooved wheels with 50% groove factor was between 3.75 and 4.00 mm before signs of grinding wheel breakdown began to occur – an improvement of between 106 and 120%.

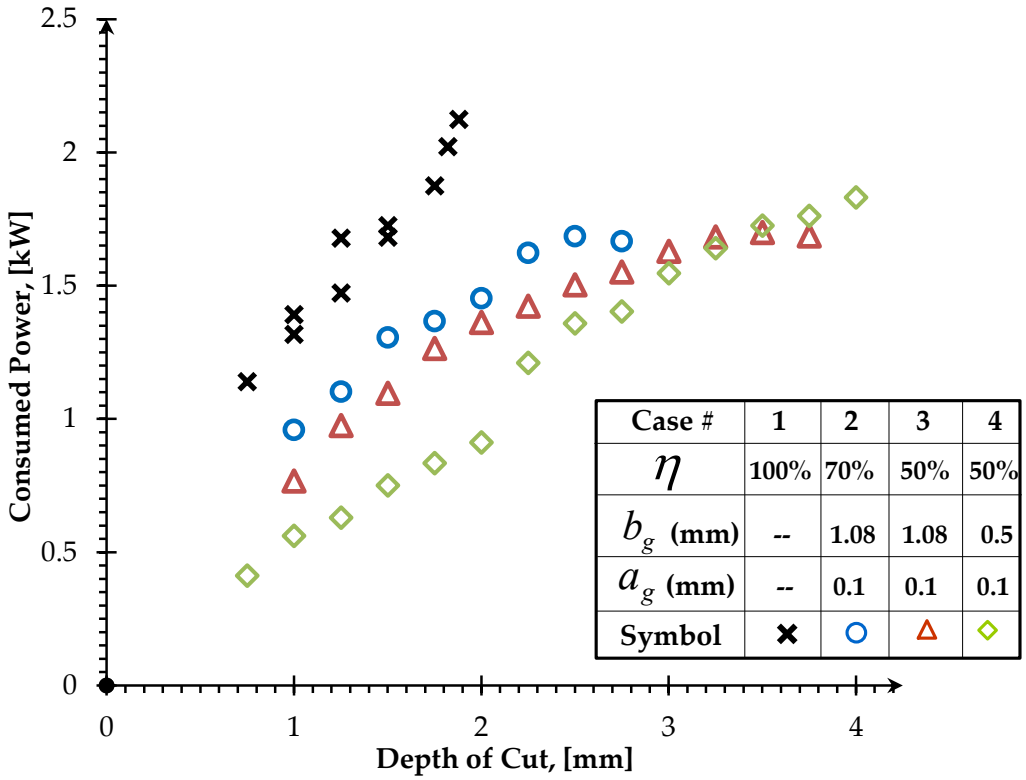

Figure 5.3: Consumed grinding power vs. depth of cut

Table 5.3: Summary of results

Case #	1	2	3	4
Groove factor	100%	70%	50%	50%
Max. depth of cut (mm)	1.82	2.75	3.75	4.00
Depth of cut increase	--	51%	106%	120%
Power reduction	--	34%	42%	61%
Max. depth of cut for fine surface finish (mm)	1.82	2.50	2.25	1.75
Depth of cut increase	--	37%	24%	–4.0%
Max. depth of cut for average quality surface finish (mm)	1.82	2.75	3.75	4.00
Depth of cut increase	--	51%	106%	120%

The resulting average workpiece surface roughness for all four cases was measured and plotted as a function of grinding depth of cut in Figure 5.4. To place the results into perspective, dashed lines were superimposed on this figure to represent "fine quality" surface finishes (as defined by roughness values up to approximately 0.30 μm [45] and "average quality" surface finishes (as defined by maximum roughness values between 0.30 and 1.6 μm [45]. In the case of the non-grooved wheel (Case 1), the resulting workpiece surface roughness remained within the fine quality surface finish standard; however, this case was limited to a maximum depth of cut of 1.82mm (due to workpiece burn). As summarized in the lower portion of Table 5.3, the grooved wheel cases remained within the fine quality surface finish standard up to depths of cuts of 2.50, 2.25, and 1.75 mm for Cases 2, 3 and 4, respectively. Furthermore, although the surface roughness appears to increase as the grinding depth of cut continues to increases, the grooved wheel cases still achieved average quality surface finishes at depths of cut as high as 2.75, 3.75 and 4.00 mm for Cases 2, 3 and 4, respectively.

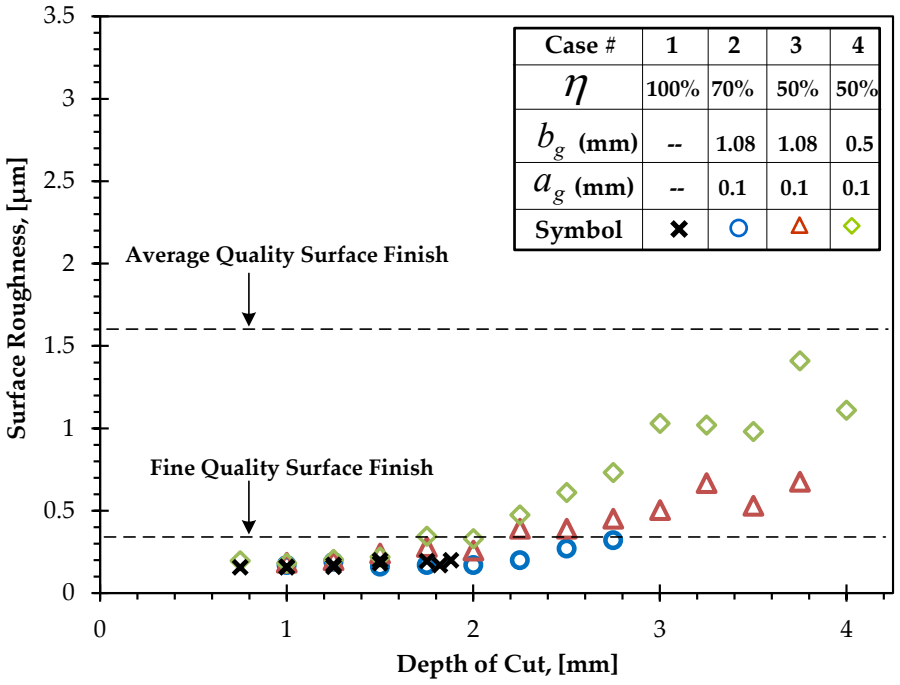

Figure 5.4: Surface roughness vs. depth of cut

To ensure that there are no traces of the grooved wheel on the resulting workpiece surface, a Nanovea PS50 – 3D Non-Contact Profilometer was used to determine if the grinding wheel groves left any grooves or ridges on the workpiece surface. Figure 5.5 shows a sample of the measured workpiece surface topography over a 5mm×6mm area achieved with a grooved wheel at a grinding depth of cut of 3.50 mm. The 5 mm length was selected to ensure that more than one full revolution of the grooved wheel was represented along the measured surface. It is evident from Figure 5.5 that the workpiece surface does not exhibit any sign of the circumferential grooves embedded in the grinding wheel.

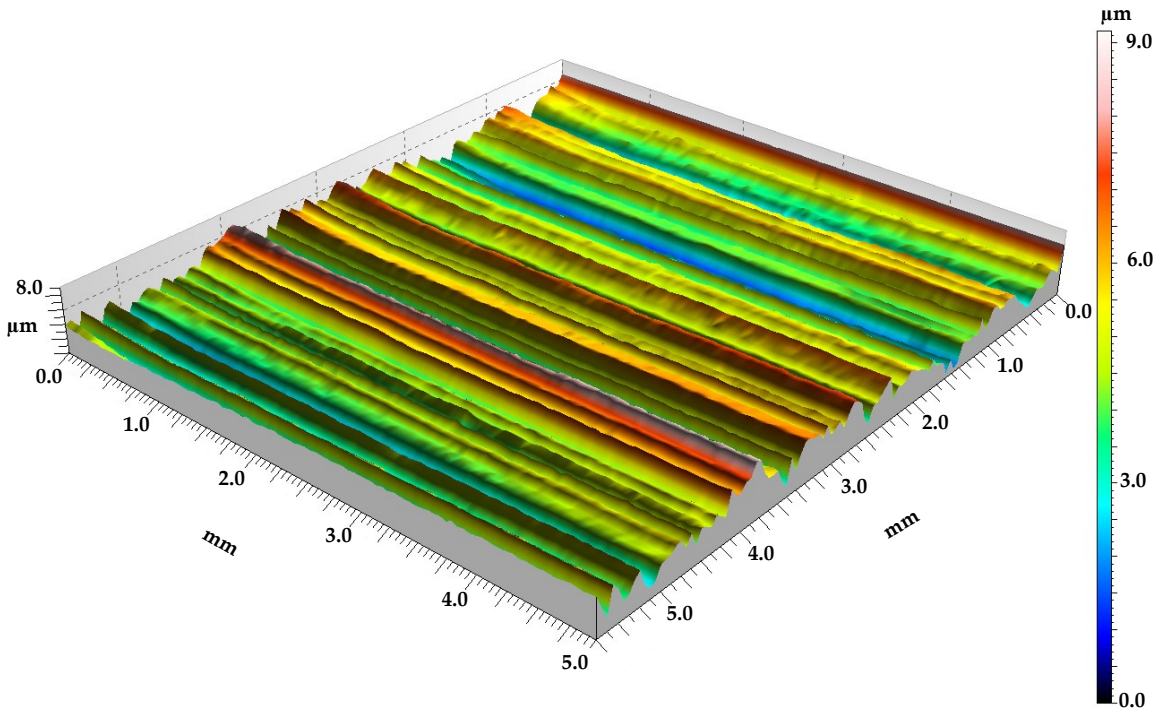

Figure 5.5: Measured workpiece surface profile

Figure 5.6 plots the tangential and normal grinding forces as a function of depth of cut for all four cases studied in this work. It is clear from this figure that the grinding forces generally appear to increase with depth of cut and that grooving the wheel decreases the forces such that the lower the groove factor, the smaller the forces.

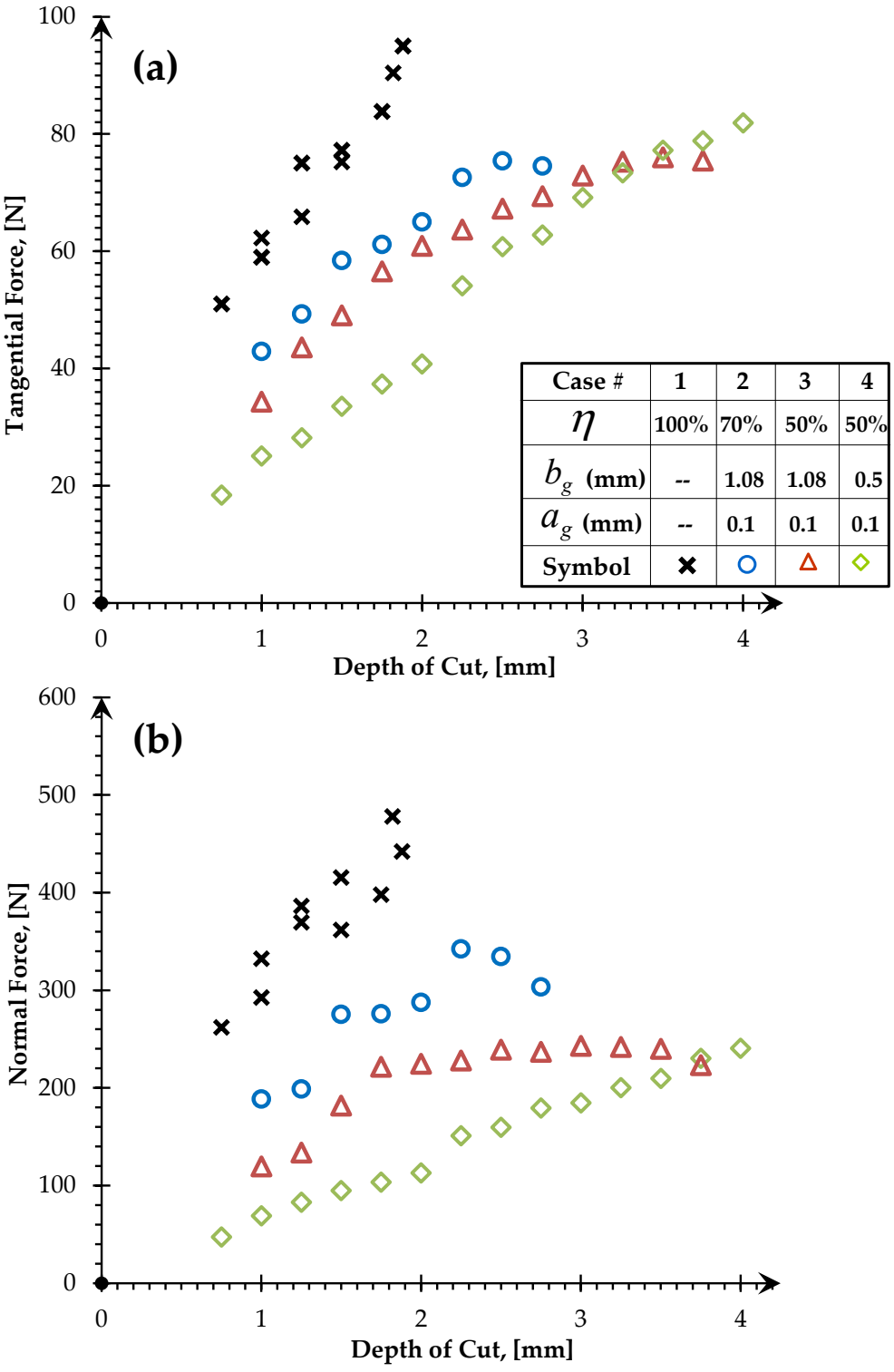

Figure 5.6: Comparisons of tangential and normal force results

The corresponding force ratio μ can be calculated by dividing the tangential force F_t by the normal force F_n as follows [7,8]:

$$\mu = \frac{F_t}{F_n} \tag{5.1}$$

Figure 5.7 plots the force ratio as a function of depth of cut for all four cases studied. It can be observed that, for a given wheel groove case, the force ratio is relatively constant over all grinding depths of cut tested – suggesting a linear relationship between F_t and F_n. More importantly, however, the force ratio tends to increase as the groove factor decreases. Anderson *et al.* [46] used a combination of experiments and finite element simulations to show that the force ratio has both a frictional component and a cutting mechanics component for a single abrasive. Given that the frictional component is a material property which can be assumed to be constant in the present case, the remaining component represents the cutting force divided by the normal force. A higher force ratio, therefore, implies that more of the applied tangential force is being used for cutting rather than for overcoming friction which, in turn, suggests a more efficient grinding process. Referring to Figure 5.7, the higher force ratios associated with grooved wheels suggests that decreasing the groove ratio increases the resulting grinding efficiency.

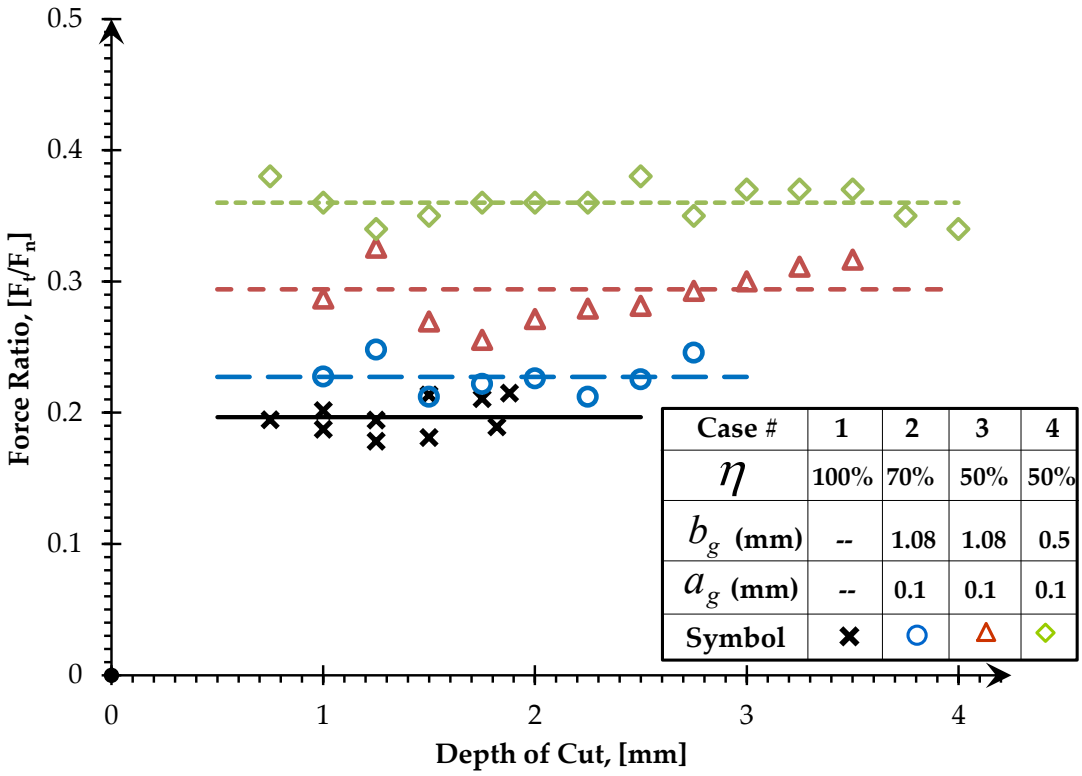

Figure 5.7: Comparison of force ratio

To quantitatively evaluate the efficiency of the grinding process one can use the grinding specific energy e_c which is a measure of the amount of energy required to displace a unit volume of material and can be calculated as follows [7,8]:

$$e_c = \frac{P}{Q_w} \tag{5.2}$$

where P is the consumed power and Q_w is the material removal rate.

Figure 5.8 plots the grinding specific energy as a function of the material removal rate for the four different cases studied. The figure clearly shows that creep-feed grinding with a grooved wheel is more efficient (having lower specific energies) than grinding with a non-grooved wheel. This result is consistent with the higher force ratios

observed in Figure 5.7. Furthermore, the pronounced negative slopes observed in Figure 5.8 indicate that there is a size effect whereby increases in the uncut chip thickness further improve the efficiency of the grinding process. This increase in the uncut chip thickness might be reasoned to the increase in the spacing of the active grains which generated by grooving the grinding wheel. For the conditions used in this research, the efficiency of the grinding wheel having a 70% groove factor improved by about 30% over a non-groove wheel, while the efficiency of the grinding wheels having a 50% groove factor improved by approximately 50 to 60%.

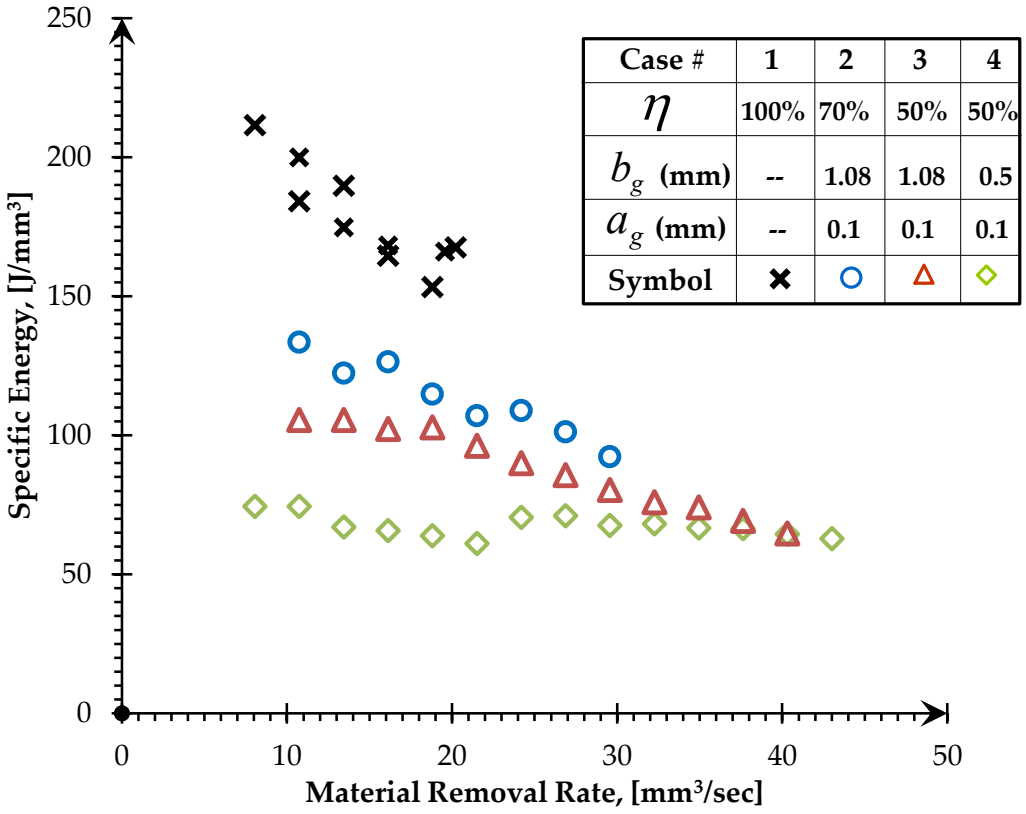

Figure 5.8: Specific energy vs. material removal rate

In addition to these experiments, a wear study was performed to determine whether or not wheel grooving would result in accelerated wear. These wear experiments were conducted for both a non-grooved grinding wheel as well as the grooved wheel

corresponding to Case 3. Throughout all of these experiments, the grinding depth of cut, wheel speed, and workpiece speed were kept constant at 1.0 mm, 22.4 m/sec, and 1.7 mm/sec, respectively. To carry out the wear study, the workpieces were continuously ground without dressing the grinding wheel surface, and the grinding forces, consumed power and workpiece surface roughness were measured continuously. As this work did not measure the wear occurred at the grain level, the measured forces and power data were utilized to determine the type of wheel wear mechanism occurred during grinding. Generally, grinding wheel wear is classified into three mechanisms: attritious wear, grain fracture, and bond fracture [7,11-12]. Only the attritious wear results in increasing the grinding forces due to the growth in wear flats.

Figures 5.9 and 5.10 plot the corresponding average consumed power, tangential forces and normal forces as a function of workpiece material removed for both the non-grooved and grooved wheels. As expected, the power and forces tend to increase as more workpiece material is removed indicating the growth of wear flats. It can also be observed in these figures that the grooved wheel exhibits less power and lower forces than the non-grooved case – results which are consistent with Figure 5.3 and Figure 5.6. It is interesting to note that the rate of increase in grinding power and forces is higher for the non-grooved case than it is for the grooved case. This important result suggests that grooving the wheel does not accelerate the wheel wear process and may in fact slow down wheel wear.

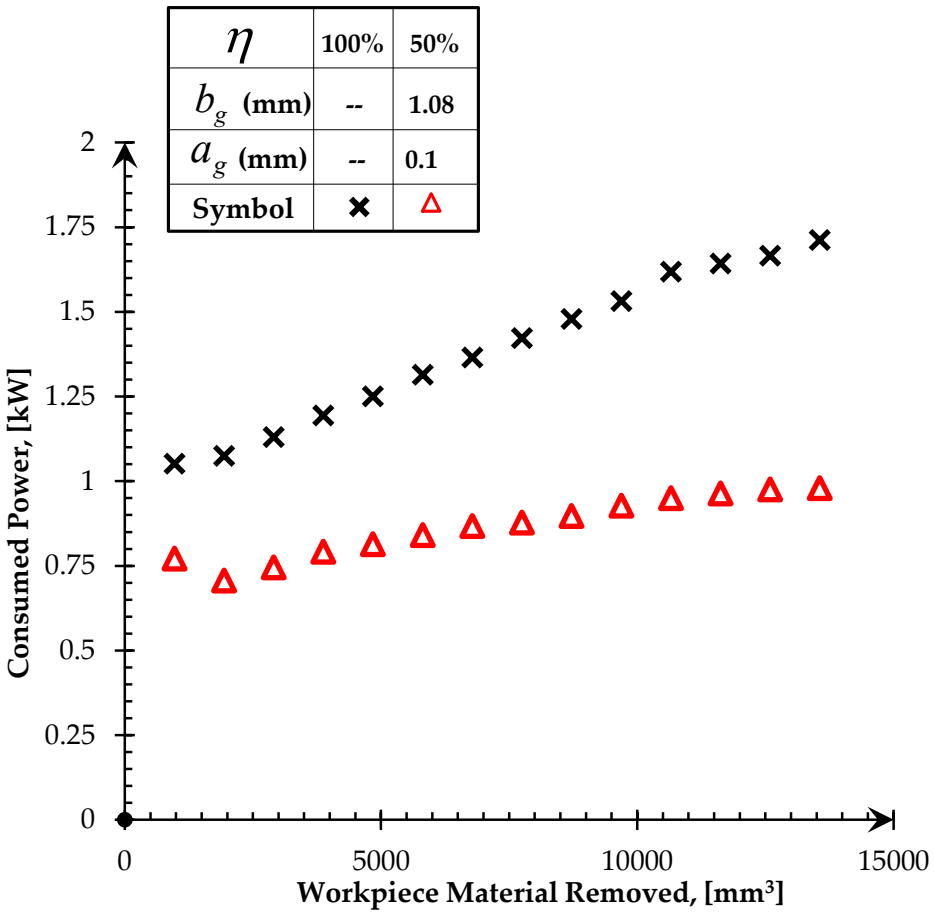

Figure 5.9: Consumed power for wear study

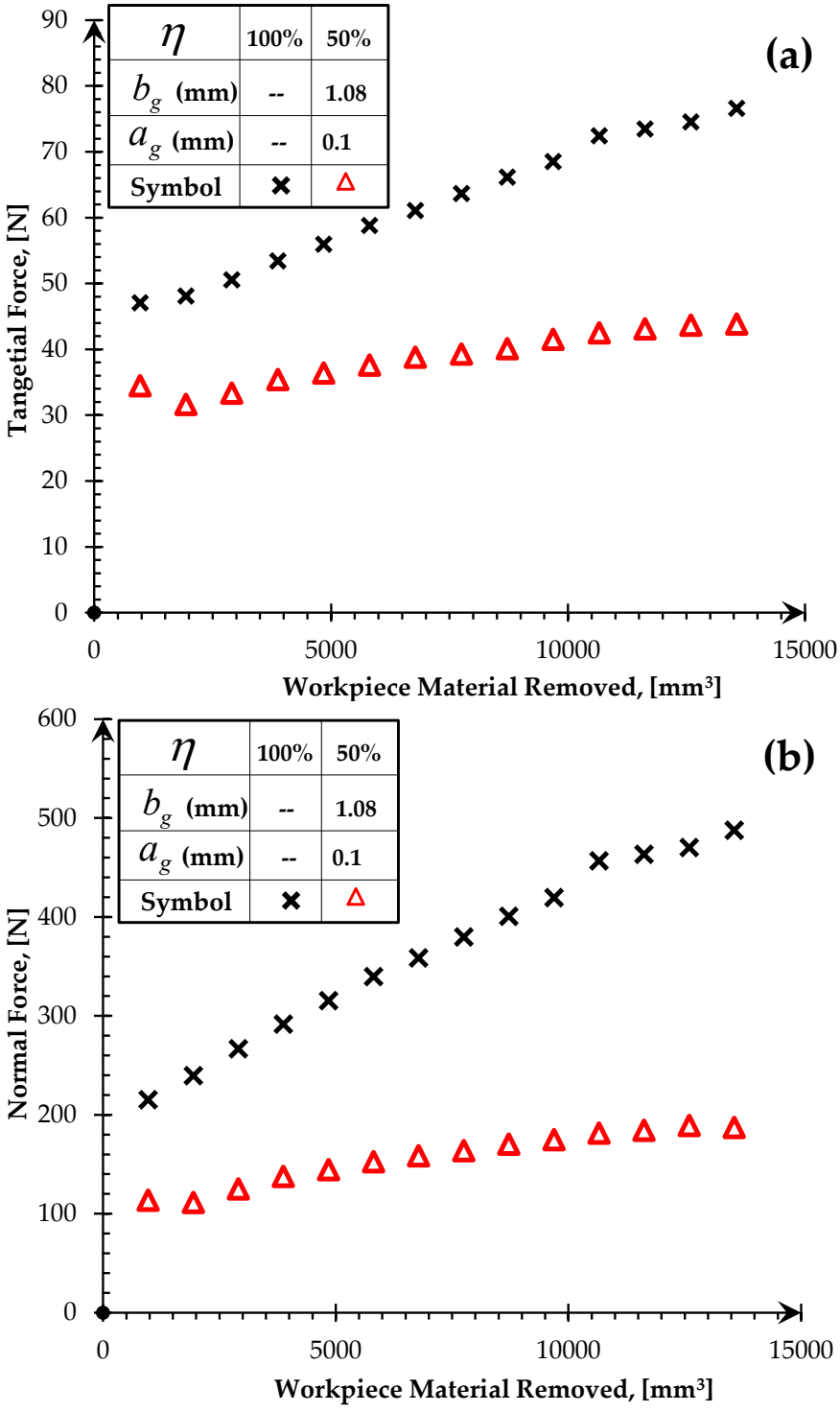

Figure 5.10: Tangential and normal force for wear study

Figure 5.11 plots the resulting workpiece surface roughness as a function of workpiece material removed for both the non-grooved and grooved wheels. Although the grooved wheel produces a slightly rougher workpiece surface than the non-grooved wheel, both wheels are able to maintain a "fine quality" surface finish over the course of the wear study. Furthermore, the relatively constant roughness values observed during the wear study support the observation that grooving the wheel does not accelerate the wheel wear process.

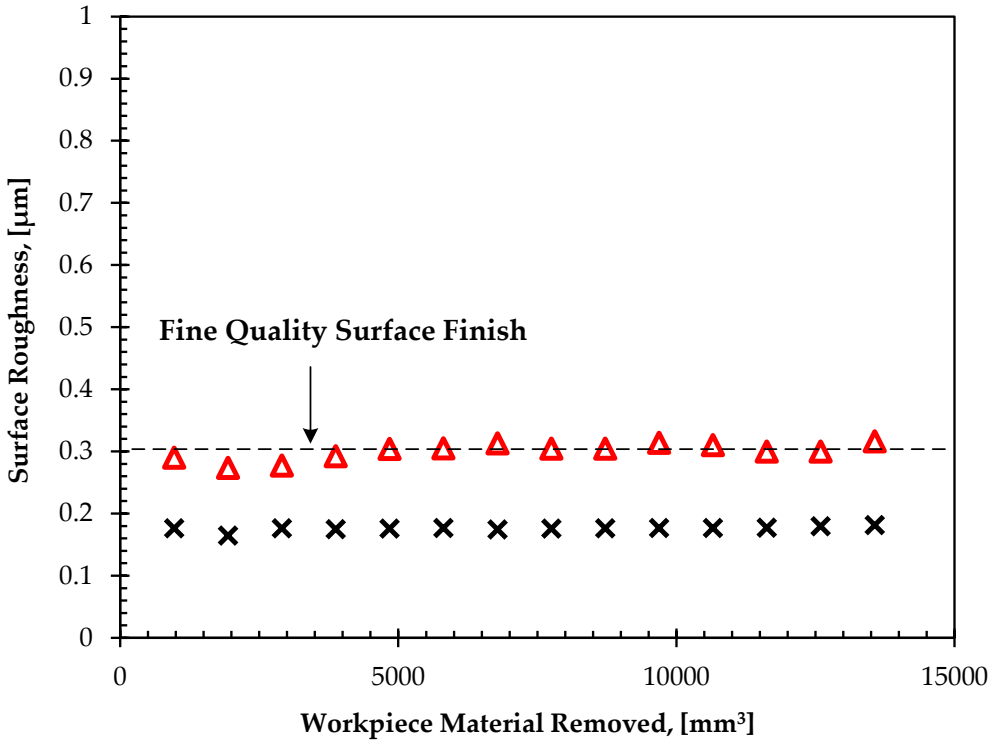

Figure 5.11: Surface roughness for wear study

Figure 5.12 plots the force ratio as a function of workpiece material removed for both the non-grooved and grooved wheels. In both cases, the force ratio decreases as the wheel wears indicating that the cutting edges are becoming less sharp and grinding efficiency is decreasing. The grooved wheel case, however, is consistently higher than the non-grooved wheel case – an advantage of grooved wheels which is consistent with Figure

5.7. Furthermore, the rate at which the force ratio changes is approximately the same in both cases suggesting, again, that grooving the wheel does not accelerate the wheel wear process.

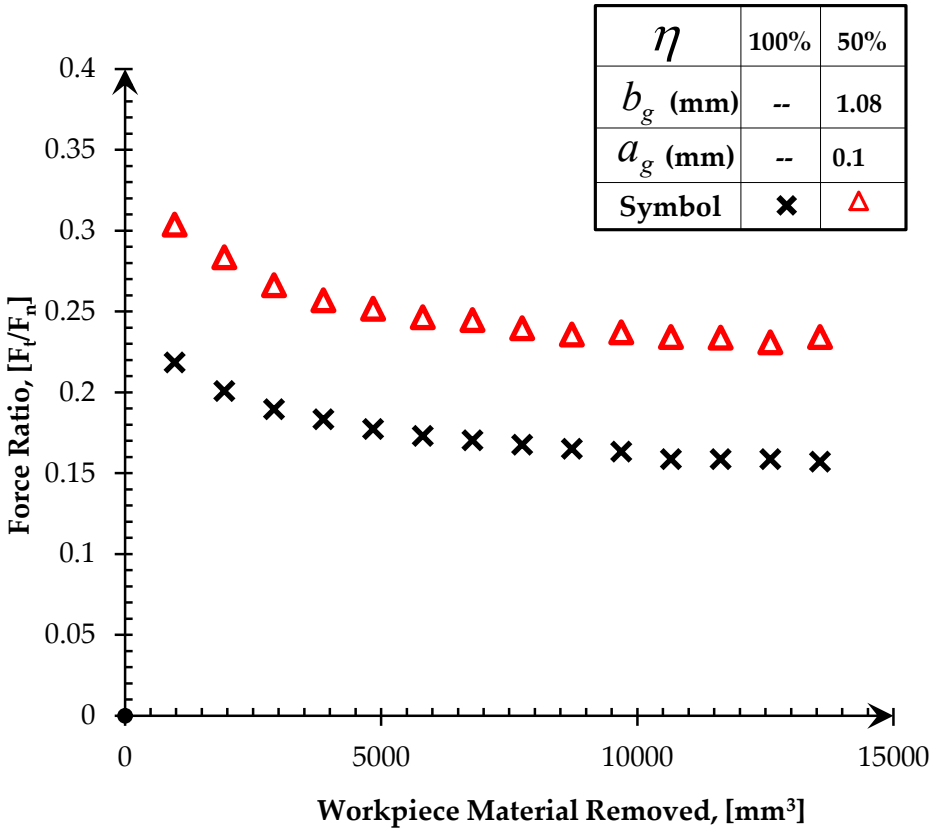

Figure 5.12: Force ratio for wear study

It is interesting to note that, while Verkerk [27] characterizes grooved wheels using the groove factor, the different results observed in this research for the 50% groove factor (Cases 3 and 4) suggest that other groove characteristics, such as groove width, also play an important role. For example, the 50% groove factor (Cases 3 and 4) in Figures 5.3, 5.6 and 5.8, show that a 0.5 mm groove width is more efficient as it yields lower consumed power, tangential and normal forces, and specific energy – all of which tend to reduce the chances of workpiece burn. The 1.08mm groove width (50% groove factor), on the other hand, yields a better workpiece surface finish at higher depths of cut (Figure 5.4).

Ultimately, the improvements observed in creep-feed grinding using a grooved wheel are likely due to, by virtue of the grooves, more cutting fluid being able to pass through, lubricate and cool the grinding zone, and a larger average uncut chip thickness which creates more efficient cutting via the size effect. Such reasoning supports the result that the groove geometry (in addition to the groove factor) has a strong influence on the resulting grinding performance.

5.4 Summary

This chapter has investigated grooved grinding wheels with different groove factors and groove geometries and compared their results with grinding using a regular non-grooved wheel results. It was shown that, for the conditions tested in this research, a grooved wheel has the potential to increase the achievable depth of cut by up to 120% and reduce the power required by up to 64% (when compared with a non-grooved wheel) while still maintaining an "average quality" surface finish. Furthermore, the maximum depth of cut that yielded a "fine quality" surface finish for a non-grooved wheel was 1.82um while, for a grooved wheel, was up to 2.5um (an increase of 37%). By studying the specific power and force ratio, it was concluded that the lower the groove factor, the more efficient the grinding process became. In addition to the groove factor, the groove geometry (such as groove width) strongly influences the grinding performance. It was also observed that grooving does not appear to accelerate the wheel wear process. One can suggest that the resulting improvements observed when using a grooved wheel in the creep-feed grinding process are likely due to the different in the grinding mechanism of the grooved wheel. Therefore, a hypotheses and discussions of why the grooved wheel improved the creep-feed grinding process is investigated and presented in chapter 7. Finally, one can say that the grooving method investigated and presented showed two main facts which are: first, grooving the grinding wheel circumferentially benefited the creep feed grinding process and second, the method

cannot be used to re-groove the grinding wheel when it is worn. Therefore, a practical method of wheel grooving was developed and is presented in the coming chapter.

Chapter 6. A Novel Grooving Method: Design & Testing

6.1 Introduction

While grooving a grinding wheel has been shown in the literature, introduced in the previous chapter, to have the potential to be highly beneficial, a practical method of grooving and then re-grooving a grinding wheel has not been found in the literature. Previous researchers have created grooved grinding wheels using complicated grooving techniques requiring the wheel to be removed from the machine spindle. It was found that the grooving methodology was performed on the grinding wheel while it was not mounted on its machine spindle by the use of complicated grooving techniques or was manufactured by applying moulding processes. Additionally, the straight forward approach of using the single-point dressing tool developed in the previous two chapters where a circumferential groove formed on an aluminum oxide grinding wheel is incapable of re-grooving the existing groove as the grinding wheel wears. Therefore, this chapter presents the design, development, and testing of a novel and practical wheel

grooving method that can carry out this re-grooving process without removing the wheel from the grinding machine spindle and can readily be retrofitted onto existing traditional, conventional and CNC grinding machines.

This novel system enables grooves on the grinding wheel to be precisely re-grooved so that the desired groove geometry can be maintained as the wheel wears without having to first remove the worn groove through a dressing operation which wastes both time and wheel material. Using the developed grooving system, this chapter validate the new grooving system, re-examines the wear characteristics of the resulting grooved grinding wheel, and compares the wear results with a non-grooved wheel.

The following sections describe the novel wheel grooving system that was designed and developed to enable the single-point diamond's motion to be controlled so that it could engage and re-groove the grinding wheel by following the same trajectory taken by the diamond tip's previous grooving pass.

6.2 Wheel Grooving System Concept

In the previous chapters, the grooving tool, which is a single-point diamond, was stationary and mounted on the grinding machine table. The concept of the new grooving system, as shown schematically in Figure 6.1, is to drive the single-point diamond in a linear manner and, at the same time, synchronize its linear motion with the rotational motion of the grinding wheel. To achieve this synchronization, the system monitors a reference point which is an index pulse signal from an encoder mounted on the motor of the grinding wheel spindle.

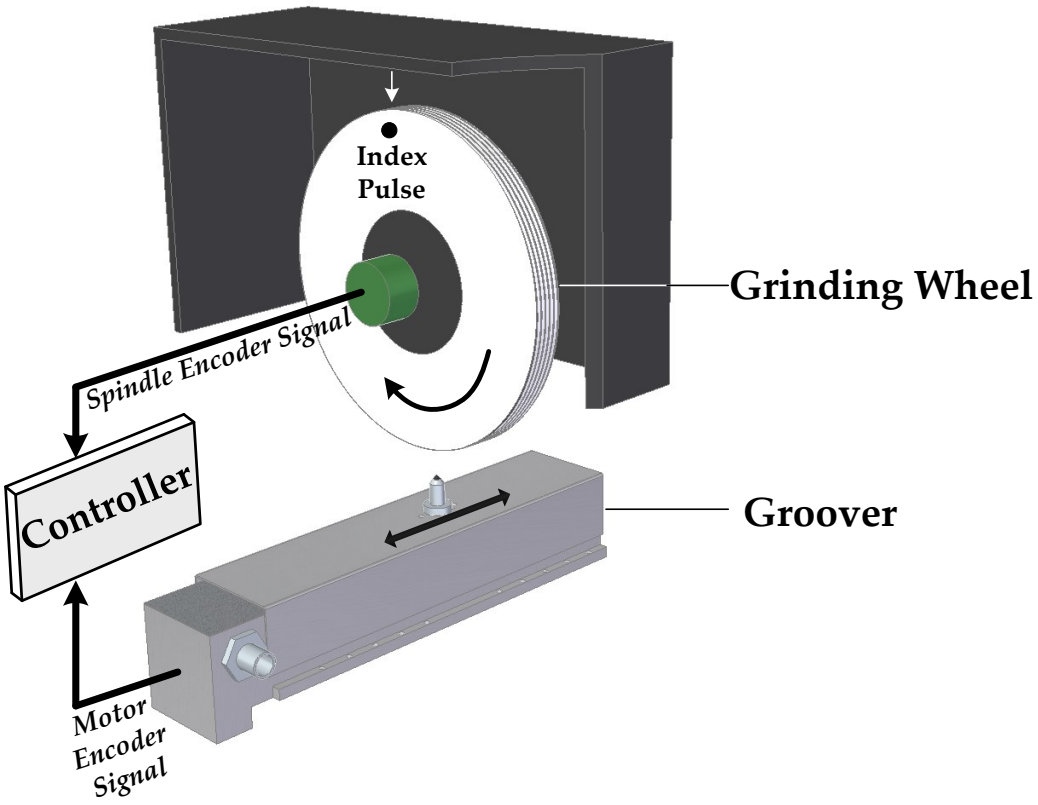

Figure 6.1: Proposed wheel grooving concept

Figure 6.2 shows an illustration of the motion synchronization which is desired from the proposed wheel grooving system. The figure shows an illustration of the position of a point on a rotating grinding wheel as a function of time, the grinding wheel's encoder index pulse cycle occurring once for each revolution of the grinding wheel, and the linear velocity curve of the grooving tool as a function of time. It can be seen that at time t_i a C-program code for grooving is initiated so the system monitors a pulse signal from the grinding spindle encoder to trigger the grooving system. Immediately, when the encoder pulse signal is detected, it triggers the linear motion of the grooving tool at time t_t and the grooving tool (single-point diamond) accelerates to reach a constant velocity before the engagement between the grinding wheel and grooving tool occurred. The single-point diamond tool tip engages with the grinding wheel to start to form the

circumferential groove at time t_e and then it disengages the grinding wheel at time t_d. To perform the re-grooving process to track the present groove on the grinding wheel, the same sequence of events shown in Figure 6.2 occur. Note that the difference between the initiating time and the triggering time ($t_t - t_i$) of the system are not always the same (depending on what the angular position of the grinding wheel is when the grooving sequence of events is initiated); however, the linear stage speed and wheel phase curves shown in Figure 6.2 should always match. As a result, the engagement and disengagement of the grooving tool should occur at the same locations on the grinding wheel. The following section outlines the design requirements of the proposed grooving system.

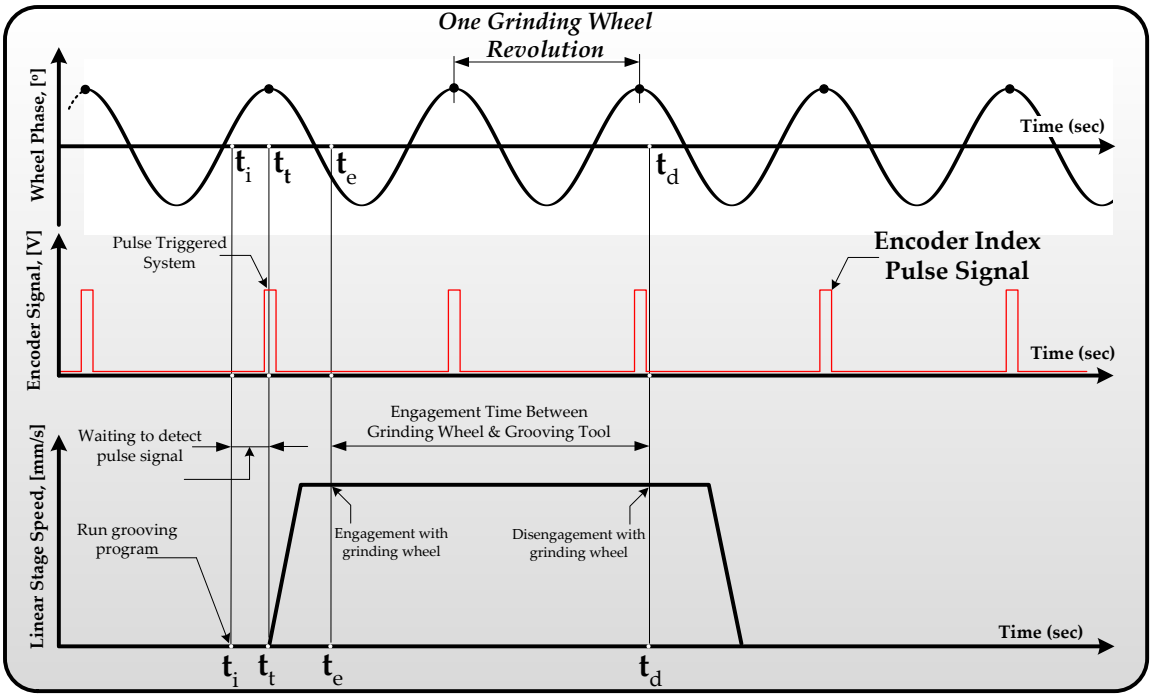

Figure 6.2: The synchronization concept of the wheel grooving system

6.3 Design Requirements

Key to the success of the proposed wheel grooving system was to establish the required accuracy of the motion of the single-point diamond tip throughout its engagement with the grinding wheel.

During the re-grooving processes, any deviation in the position of the diamond dressing tip as it attempts to re-trace the existing groove pattern along the wheel surface will effectively increase the groove width b_g and reduce the resulting groove factor. To help determine the required position accuracy of the proposed wheel grooving system, Figure 6.3 plots the resulting groove factor η as a function of error in the position of the single-point diamond tip e_r during re-grooving. As shown in this figure, a groove factor of 100% corresponds to a non-grooved wheel, while a groove factor of η represents the desired groove factor for a re-grooving operation. Any error in the position of the single-point diamond will result in a decrease in the resulting groove factor η_e.

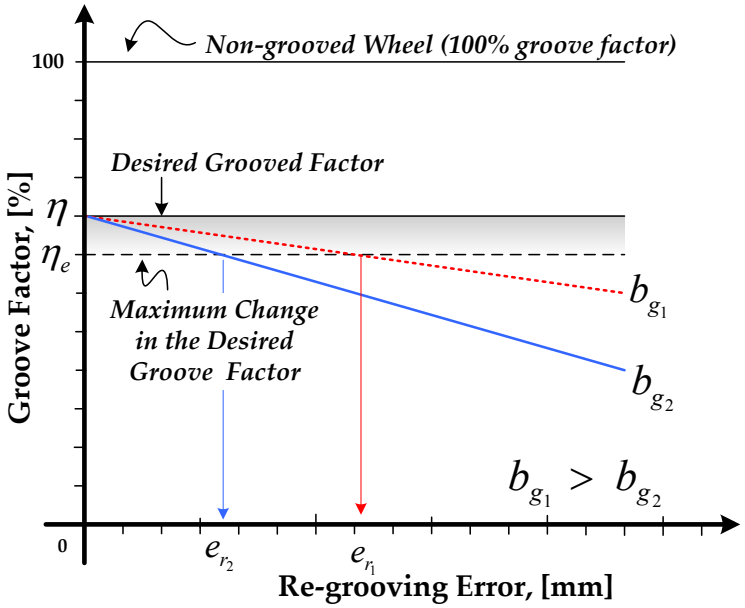

Figure 6.3: Resulting groove factor vs. single-point diamond position error

For a given groove width b_g, the single-point diamond position error e_r can be related to the corresponding change in the groove factor ($\eta - \eta_e$) using the following equation:

$$e_r = \left(\frac{\eta - \eta_e}{100 - \eta} \right) \cdot b_g \tag{6.1}$$

where η_e is the resulting groove factor for a given re-grooving position error e_r, and b_g corresponds to the desired groove width. Referring to Figure 6.3, if a relatively wide groove corresponding to b_{g_1} was used to achieve a desired groove factor η, then a single-point diamond position error of e_{r_1} would result in a decrease in the resulting groove factor from η to η_e. If, however, a narrower groove corresponding to b_{g_2} was used to achieve the desired groove factor η, then less diamond tip position error e_{r_2} could be tolerated for the same decrease in the resulting groove factor from η to η_e. In general, as it can be seen from both Figure 6.3 and Equation (6.1), the larger the groove width used to achieve a desired groove factor, the larger the allowable single-point diamond position error can be for a given maximum allowable decrease in groove factor. Here, the maximum acceptable change in groove factor was assumed to be 2% (a drop in groove factor from 50% to 48%) and the desired groove width ranged from 0.5 to 1.5 mm. Therefore, using Equation (6.1), the maximum re-groove position error that can be tolerated during a re-grooving operation (corresponding to the smallest groove width of 0.5mm) was determined to be 0.02 mm.

In order to design the wheel grooving system, estimates of the tool forces and cutting speeds were required. A single-point diamond dressing tool was mounted on the force dynamometer in the Blohm Planomat 408 CNC creep-feed grinding machine. Experiments were conducted on an aluminum oxide (Al_2O_3) wheel (Radiac Abrasives WRA 60-J5-V1). The results, summarized in Table 6.1, show that the tangential and normal forces increase as the wheel speed increases and that the axial force is relatively

small. Note that the wheel speed was significantly smaller than typically used in dressing and trueing operations in order to keep the forces on the single point diamond relatively small to avoid damage to the grinding wheel and to enhance the controllability of the grooving operation. Results presented later in this chapter will show that these speeds produced an acceptable groove profile. Given the results of these tests, the proposed wheel grooving system needs to be designed to meet the single-point diamond tip position requirements in the presence of normal, tangential and axial load conditions of 100 N, 80 N, and 10 N, respectively, for wheel velocities up to 7.5 m/sec and axial speeds of 35 mm/sec.

Table 6.1: Measured forces during grooving the grinding wheel

Wheel RPM	Wheel Velocity (m/sec)	Axial Speed (mm/sec)	Normal Force (N)	Tangential Force (N)	Axial Force (N)
90	1.764	8.50	77.3	57.5	3.1
180	3.528	17.0	93.5	76.2	6.0
385	7.560	36.4	96.0	69.7	0.5

6.4 Wheel Grooving Setup

Figure 6.4 shows a picture of the main components of the grooving system. Figure 6.5 presents a schematic diagram of the grinding wheel grooving system while Figure 6.6 shows an image of the final wheel grooving device mounted on the grinding machine. As can be seen from Figure 6.4 and Figure 6.5, the wheel grooving system consists of the following main components: control boards, power supply, brushed DC motor, linear stage that carry and drive a single-point diamond tool, encoders, and limit switches. The following is a brief description of the setup components.

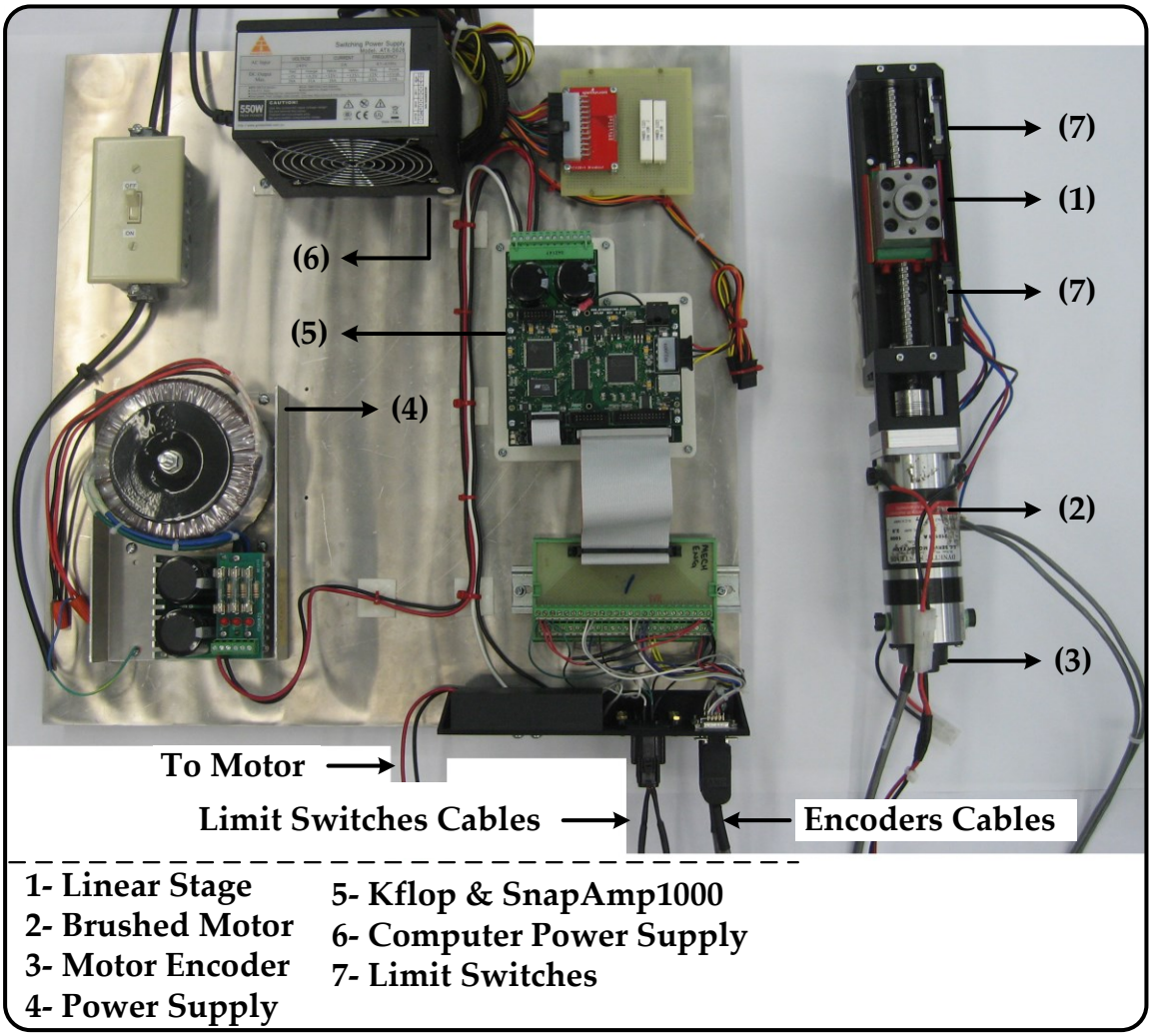

Figure 6.4: Picture of the main parts of the grooving system

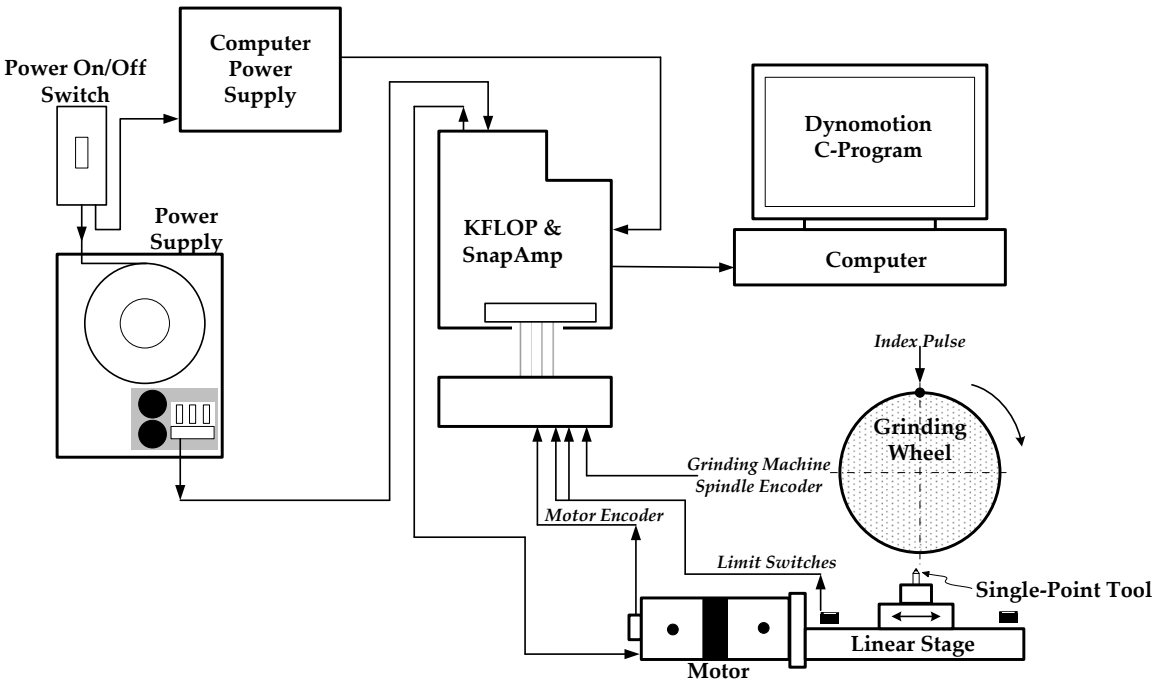

Figure 6.5: Schematic diagram of grinding wheel grooving system

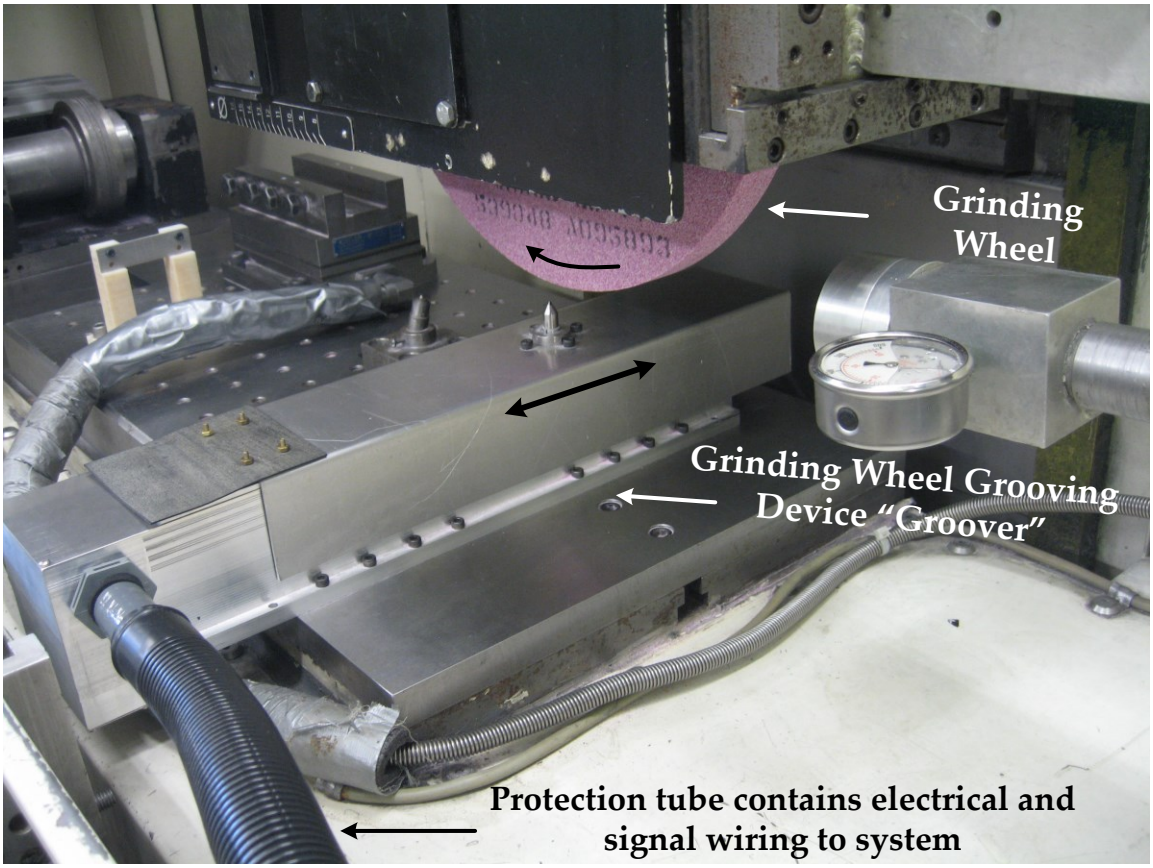

Figure 6.6: Image of final grinding wheel grooving system

6.4.1 Control Boards

A high performance 8-axis motion controller Board (KFLOP: Dynomotion, Inc. – Processor: TMS320C67-200MHz DSP 1.2GFLOP and 90 μsec servo sample rate was used. This KFLOP board provides low-latency, guaranteed, real-time deterministic response and offers 45 Bi-directional I/O bits. Along with KFLOP Board, a multi-purpose amplifier (SnapAmp: Dynomtion, Inc. – max. supply of 80 Voltage and peak current of 25 Amps) is connected to KFLOP. The SnapAmp adds four PWM full bridge amplifiers and a single PWM/Full bridge is required for a brushed motor.

6.4.2 Motor & Power Supply

A brushed DC servo motor (Dynetic Systems: MS22 series – model: MS2215-38/GI-392) was used to drive the single-point diamond grooving tool. This motor specification is listed in Table 6.2. The power supply used is AnTek Inc.–PS-4N38 with two capacitors of 10000 μF and its power, output voltage, and current are 400W, 38V, and 10.5Amps consequently.

Table 6.2: Motor specification

Motor Type	Brushed DC Motor
Max Speed (Operating Limit)	8000 RPM
Rated Voltage D.C.	38 DC Volts
Rated Current	2.9 Amps
Rated Torque	22 oz-in
Rated Speed	5700 RPM
Rated Power Out	92 Watts
No Load Speed	6400 RPM

6.4.3 Linear Stage

The linear stage is the device that carries the single-point diamond tool mounted on a holder and driven by the brushed DC servo motor. The linear stage which was utilized is HIWIN Single Axis Robot (model: a HIWIN KK60 05 P 100T9-1192) with ballscrew lead of 5.0 mm as shown in Figure 6.7. It provides a high stiffness and a high accuracy linear motion of ±0.003 mm with maximum speed limit of 550 mm/sec. The basic static and dynamic load of the linear stage ballscrew are 6243N and 3744N, respectively; and the basic static and dynamic load rating of the linear stage guideway are 13230N and 21462N respectively.

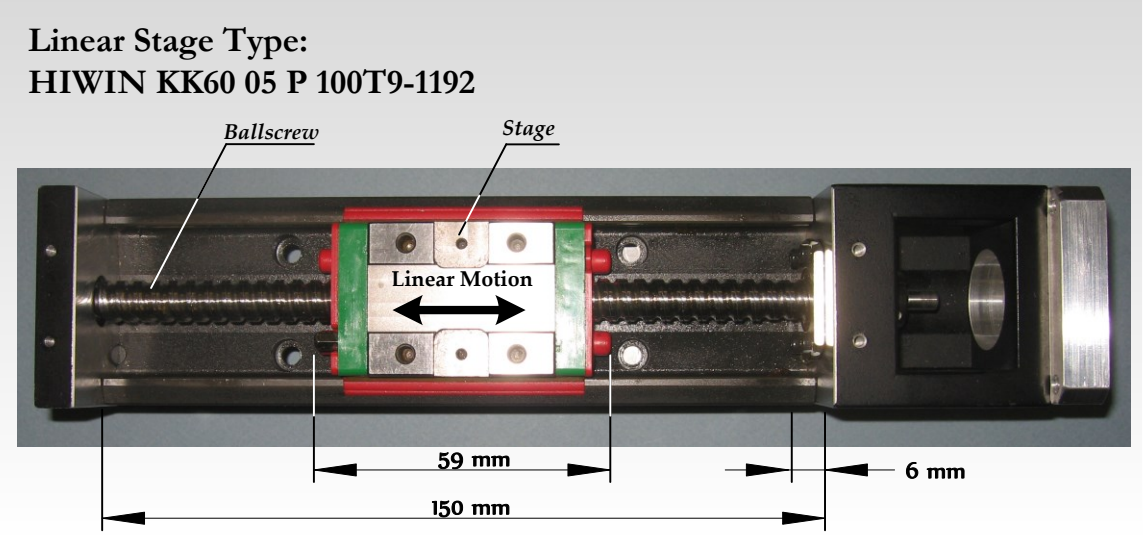

Figure 6.7: Linear stage (a HIWIN Single Axis Robot)

6.4.4 Encoders

Two encoder sensors were required for the wheel grooving setup in order to track the position of the wheel grooving (single-point dressing) tool and synchronize its movement with the rotating grinding wheel as described previously in Section 6.2. The first encoder (US-Digital: E5-1250-IE D-E-GB) is mounted on the brushed DC servo motor that drives the linear stage. This encoder provides 5000 pulses per one revolution and one index pulse per one revolution. Since the one revolution of the linear stage results in 5mm linear motion, then one pulse of the encoder represents 1×10^{-3} mm of the linear motion. Besides knowing the linear motion position of the wheel grooving tool, this encoder is used for homing the wheel grooving system with the assistance of a limit switch signal.

The index pulse signal of a second encoder mounted on the grinding wheel spindle motor is utilized by the control system to trigger and synchronize the precise movement of the linear stage. The encoder is a high speed MZ encoder which was incorporated into the CNC grinding machine spindle's motor (FANUC AC spindle motor series α

15/8000). The encoder provides signals A, A*, B, B*, Z, and Z* and the last two are related to the index pulse being used. In order to use this machine encoder signal, a GE Fanuc breakout board was installed to split the signal into two parallel lines as shown in Figure 6.8. As can be seen, a signal line remains connected to the machine spindle amplifier and the second parallel signal line is connected to the control board of the wheel grooving setup.

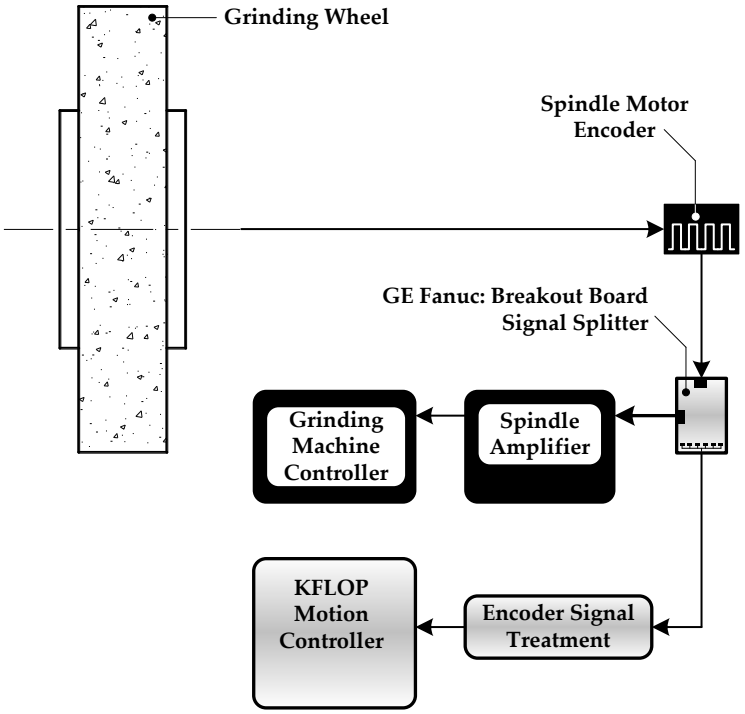

Figure 6.8: Splitting the encoder signal from the machine spindle' motor

It was found that the split signal was noisy and its amplitude was lower than the minimum 3.0V limit required by the control system. Therefore, first order low pass filter and instrumentation amplifiers were implemented and built as shown in Figure 6.9. Figure 6.9(a) shows a schematic drawing of the developed signal conditioning circuit, Figure 6.9(b) displays the breadboard circuit utilized for initial testing of this circuit, and Figure 6.9(c) presents the final circuit board that was utilized in the control system of the wheel grooving setup. Figure 6.10 presents snapshots from an oscilloscope showing the

steps used to condition the signal. Figures 6.10(a) and 6.10(b) show samples of noisy signal and low voltage signal, respectively.

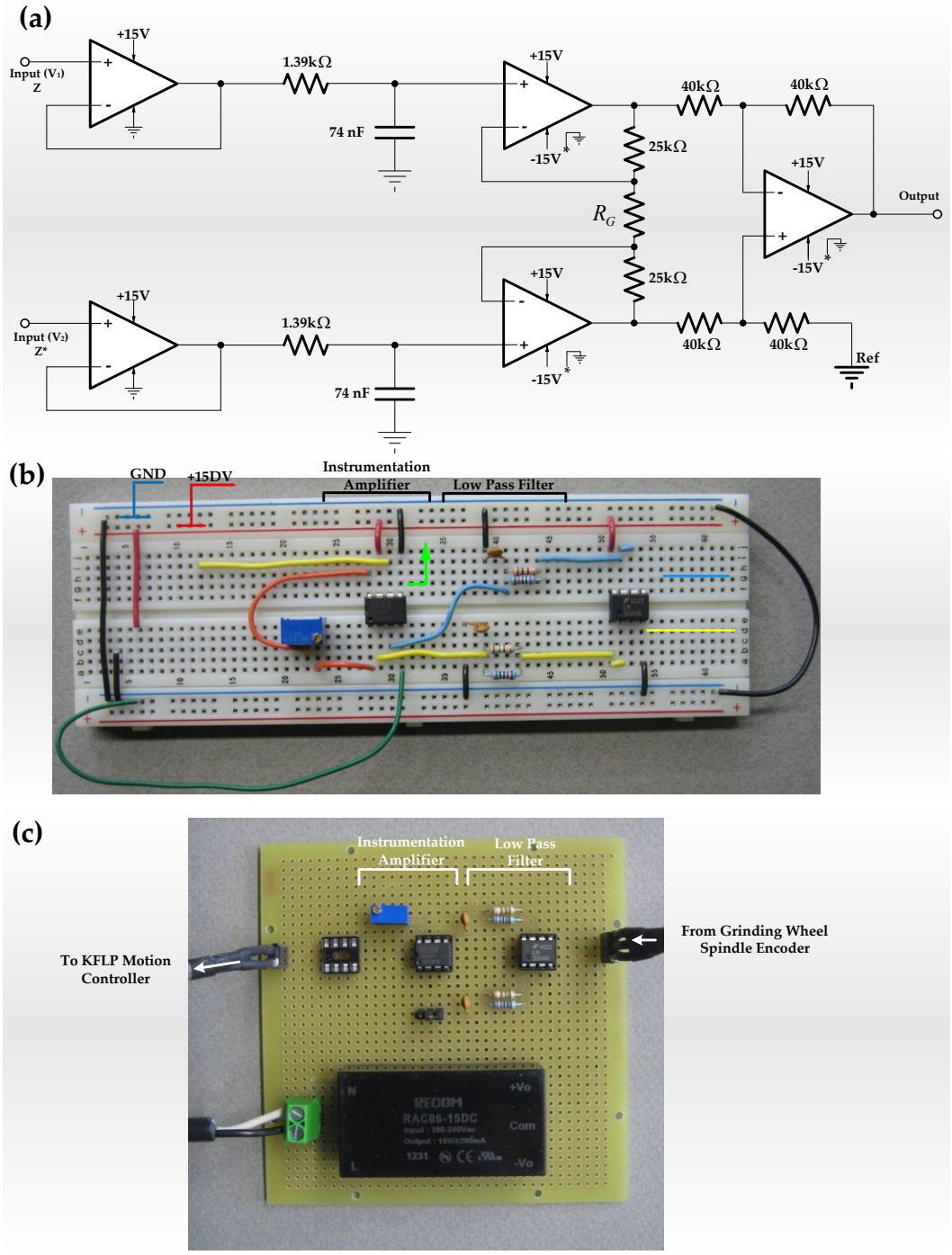

Figure 6.9: Filtering and amplification circuit

It can be seen from the schematic drawing shown in Figure 6.9(a) that both encoder inputs (V_1 and V_2) that represent Z and Z* were first connected to operational amplifiers (op amps) that acted as voltage followers (buffers) in order to keep both inputs stable without any losses so that the parallel encoder signals remain steady. Then both voltages (V_1 and V_2) were connected to a first order low pass filter to eliminate the high frequency noise. A sample of the resulting filtered signal is shown in Figure 6.10(c). Now, both filtered voltages (V_1 and V_2) were amplified utilizing a low power differential instrumentation amplifier and a sample of the resulting amplified signal is shown in Figure 6.10(d) which appears as a clean sinusoidal pulse. Since the positive cycle is the desired input to the control system, the bias voltages were changed from ($+V_{cc}$, $-V_{cc}$) to ($+V_{cc}$, 0) and a sample of the resulting signal is shown in Figure 6.10(e). Finally, the gain value was adjusted via a variable resistor to obtain +3.0V, as shown in Figure 6.10(f), so that the system controller was able to detect the encoder index pulse signal.

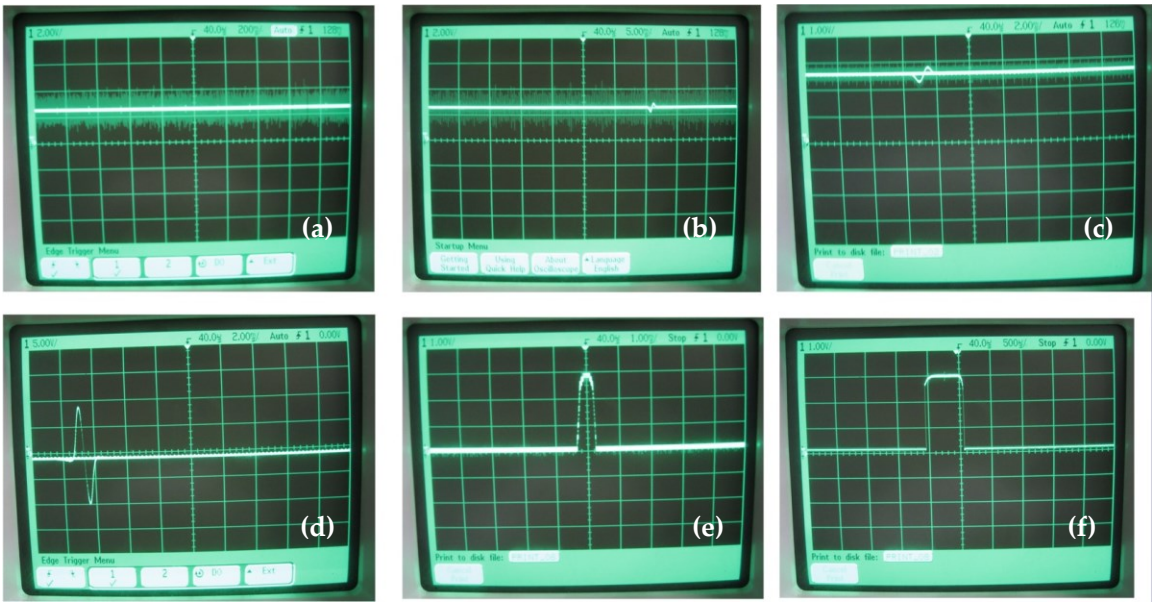

Figure 6.10: Oscilloscope snapshots of signal treatment

6.4.5 Limit Switches

There are two limit switches (Omron Electronics Inc-EMC Div: D2VW-01L2A-1MS), as shown in Figure 6.11(a), which are used in the wheel grooving setup. Each limit switch was mounted at one end of the linear stage. For safety purposes, these switches also trigger the control system to stop the linear stage should it travels too close to the ends of the stage. These limit switches are also used for homing purposes so that the linear stage is always initialized at the same position. It can be seen from Figure 6.11(b) that a normally open connection was used with a pull-up resistor configuration to ensure a well-defined logical level.

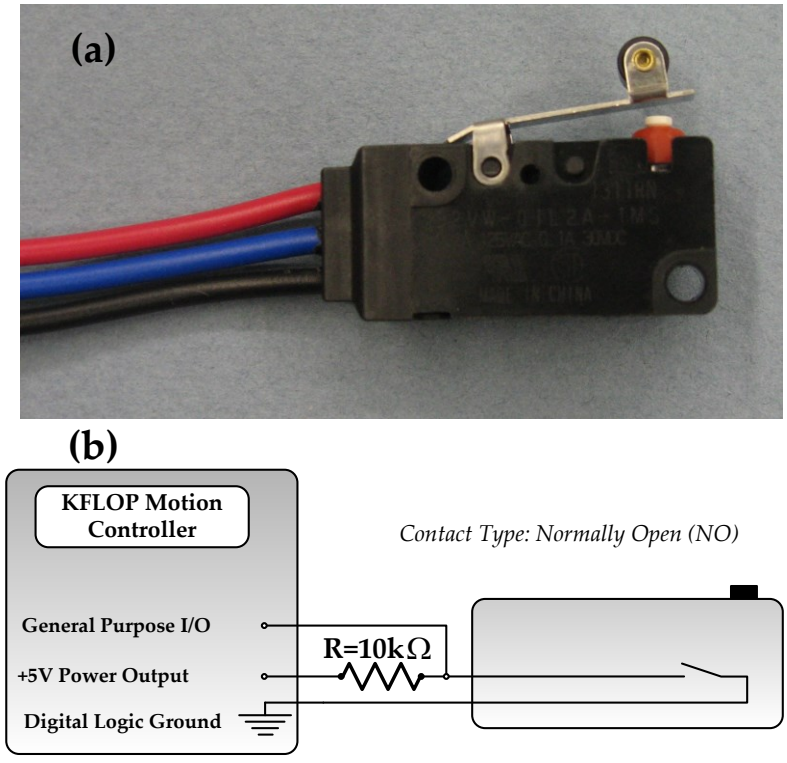

Figure 6.11: Limit switches

For the note, two C programs were written for homing the wheel grooving system and grooving the grinding wheel. A G-code program was also written to place the grinding wheel at the same position whenever grooving and re-grooving is required. After assembling the wheel grooving setup and precisely installing it on the grinding machine table, experiments were performed to test the system's repeatability and accuracy. Details of these experiments are shown in the following section.

6.5 Results and Discussion

The PID controller gains were manually tuned using a ramp response. First, the proportional gain was tested by increasing its value starting from zero. The minimum steady state error was at proportional gain value of 3.25 as shown in Figure 6.12. The selected proportional gain was held constant while varying the other gains. When setting the integral gain to a non-zero value, the system became unstable and the steady state error increased; therefore, the integral gain was kept at a value of zero. Repeating the same procedure for the derivative gain, better results were achieved when the derivative gain value was at 0.005 as shown in Figure 6.13. Table 6.3 summaries the final PID gains values.

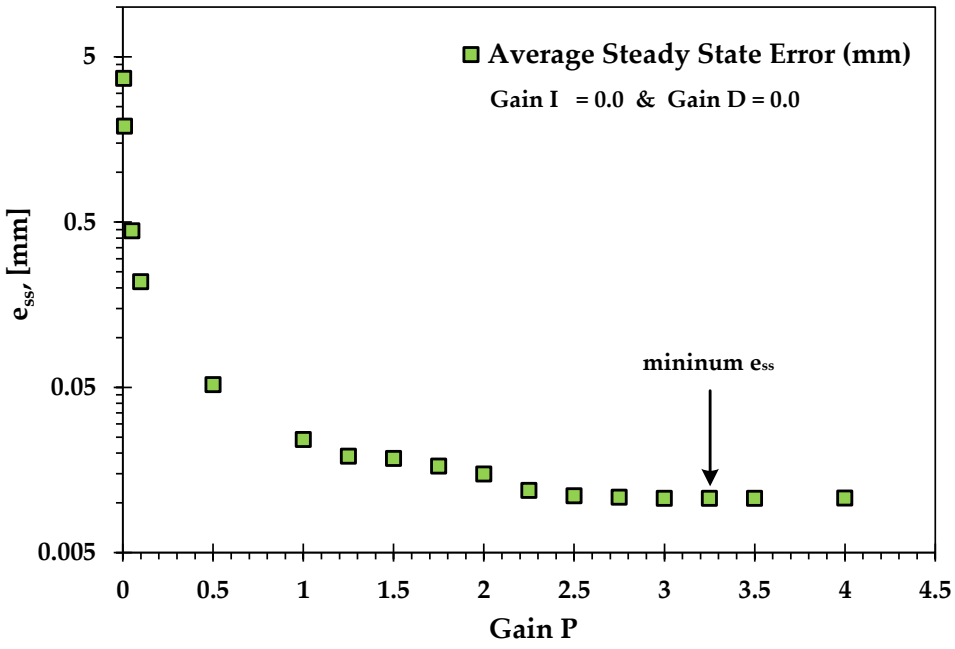

Figure 6.12: Proportional gain tuning process

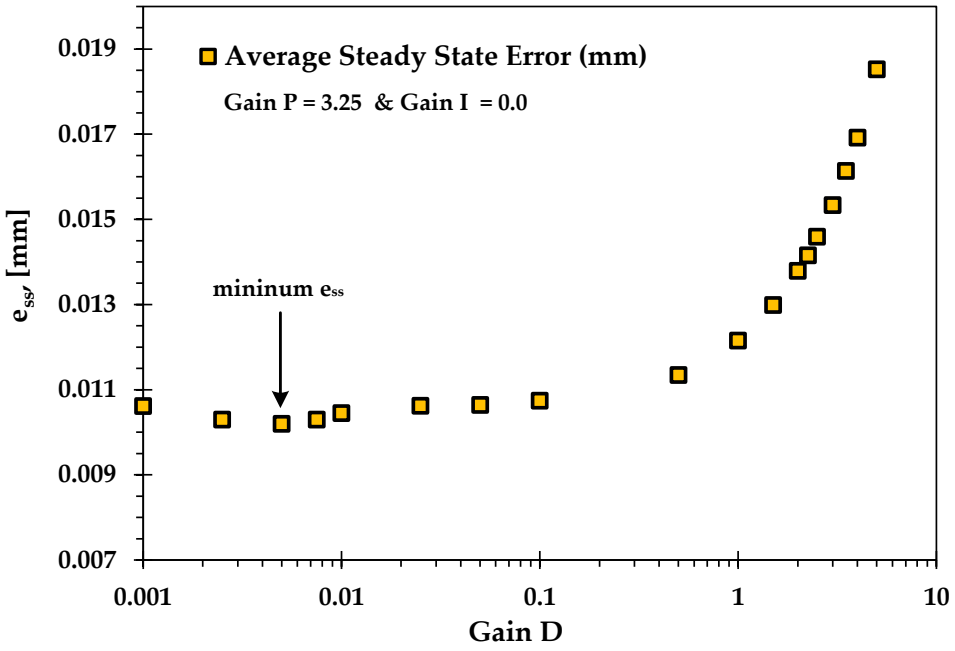

Figure 6.13: Derivative gain tuning process

Table 6.3: Proportional, integral, and derivative gains

Gain	Proportional	Integral	Derivative
value	*3.25*	*0*	*0.005*

Figure 6.14 shows the final no-load ramp response and corresponding position error using these controller gains. It can be seen from this figure that the stage can follow a ramp input with an average steady state error of 0.01 mm when the wheel grooving system was tested without any loading at a speed of 40 mm/sec and an acceleration of 7×10^3 mm/sec^2. As desired, this error is less than the 0.02 mm maximum error requirement established in the previous section.

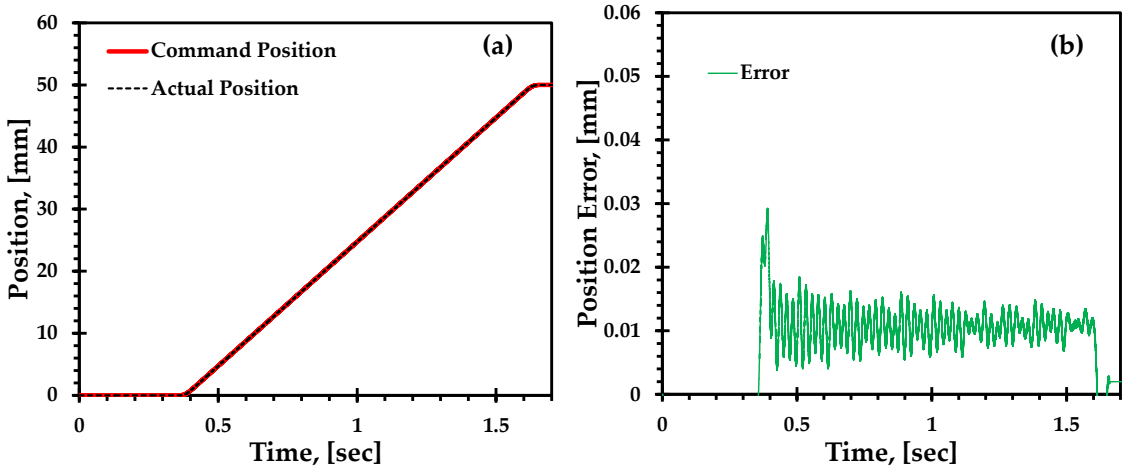

Figure 6.14: System response during the PID controller tuning

In order to examine the effect of grooving forces on the motion accuracy and performance of the wheel grooving system, a variety of external loads were applied to the stage, as shown in Figure 6.15, in the normal, tangential, and axial directions while the stage was commanded to follow the ramp input shown in Figure 6.14. The resulting steady state errors for a ramp input are plotted as a function of the applied load in Figure 6.16 for a linear stage speed of 40 mm/sec. The normal (Figure 6.16(b)) and tangential (Figure 6.16(c)) applied loads resulted in steady state position errors of 0.0088mm and 0.0102mm, respectively, when the maximum normal and tangential

forces were applied. Moreover, it can be seen from Figure 6.16(d) that the steady state error increases linearly as the axial load increases and a 50N maximum axial load would result in a position error of 0.02mm. It can also be seen that, in all cases, the position errors are under the required accuracy by at least a factor of 10 under the worst-case loading conditions.

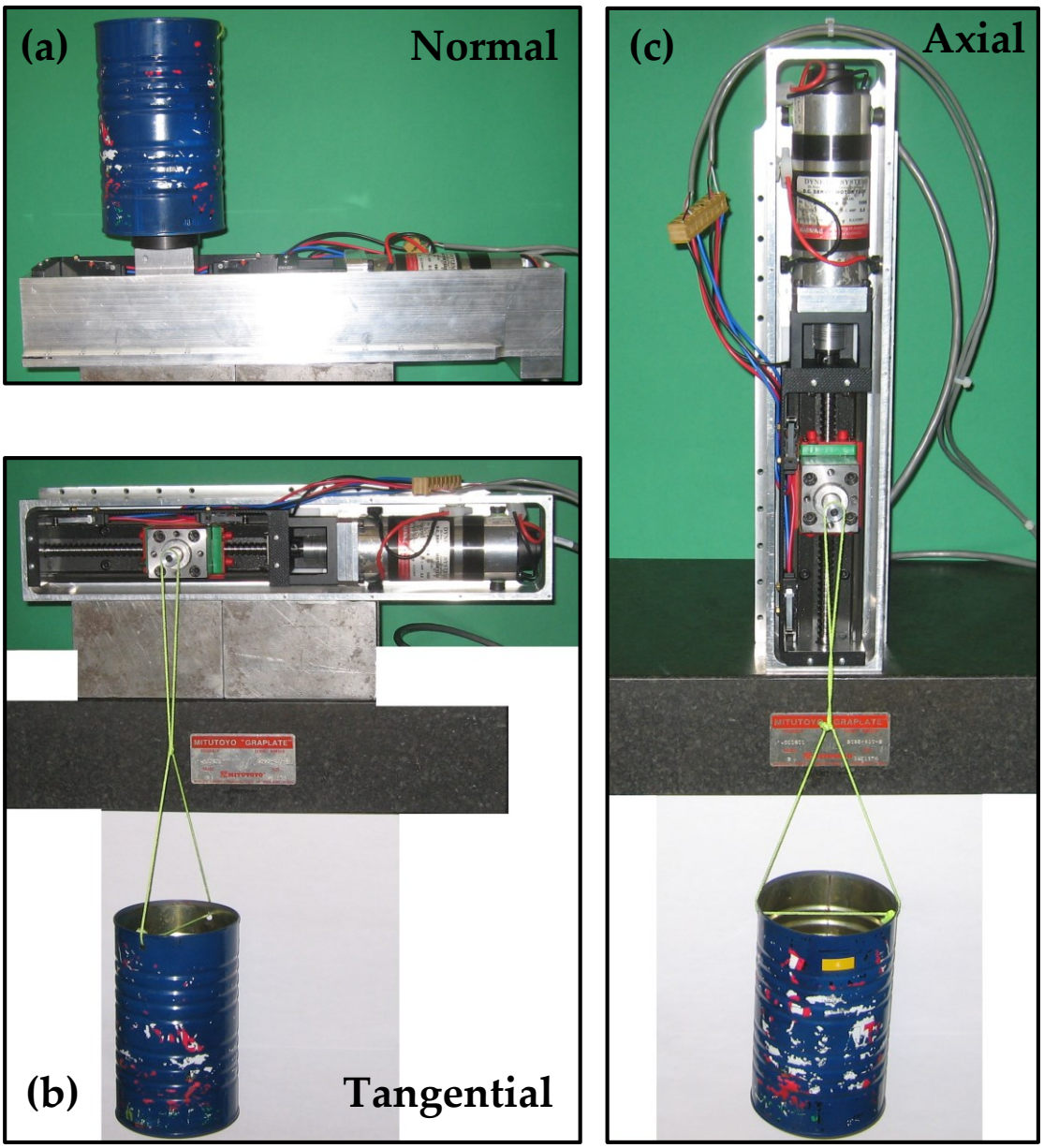

Figure 6.15: Orientating the grooving setup to test the loading at different axes

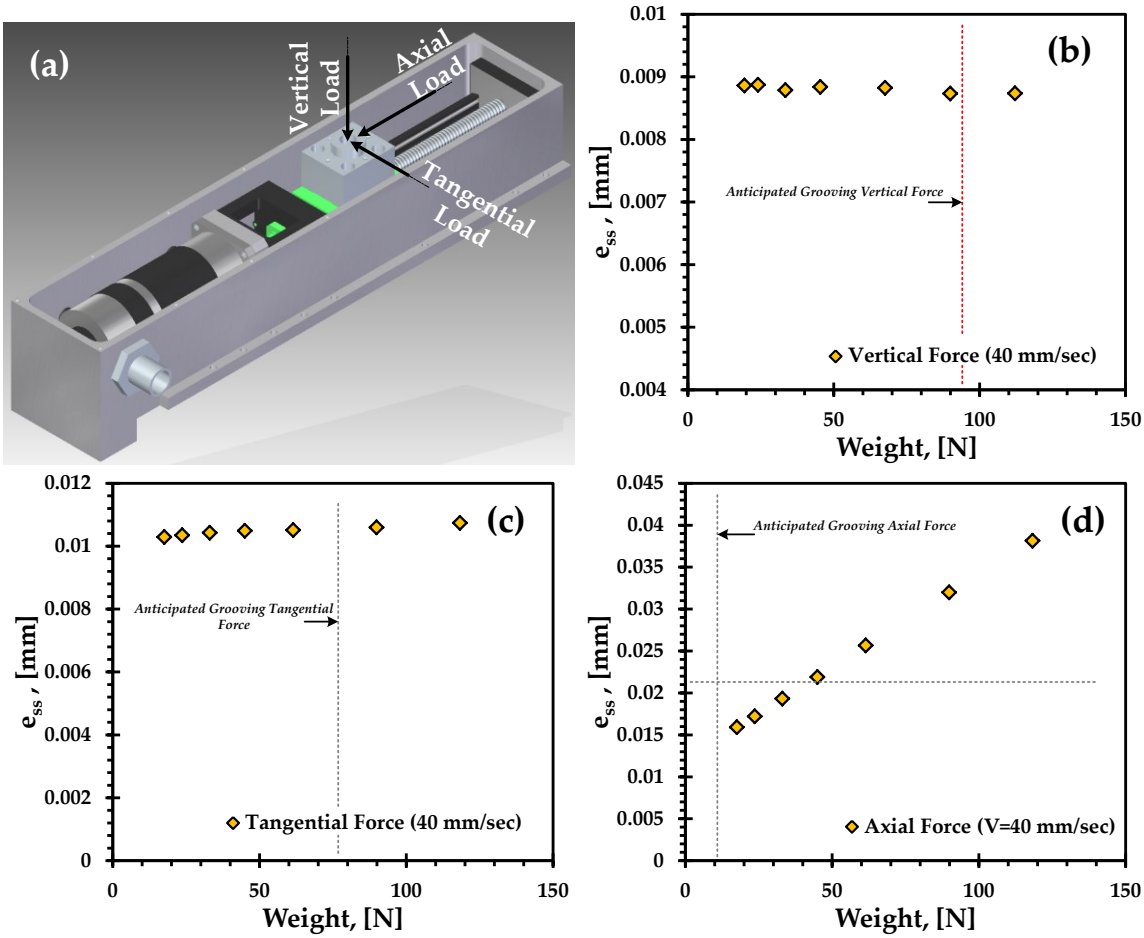

Figure 6.16: Results of examining the effect of various loads on the position's steady state error

In order to validate the wheel grooving system's accuracy and performance, experiments were conducted at constant wheel speed and constant linear stage speed which were 155 rev/min and 10.935 mm/sec, respectively. The first set of experiments, which is referred to as Test 1, consists of three experiments. The first experiment (Test 1-a) commanded the wheel grooving system to carry out one grooving pass having a 0.1 mm groove depth. The second experiment (Test 1-b) repeated (Test 1-a) and then carried out three subsequent passes without increasing the groove depth. The third experiment (Test 1-c) was similar to the previous experiment except that instead of only

three passes, six subsequent passes were carried out without increasing the groove depth.

For each of these three experiments, the spindle power during wheel grooving and re-grooving was measured using a Load Controls Inc. PH-3A Power Cell Transducer and the results are presented in Table 6.4. It can be seen in this table that, for all three experiments, the measured spindle power for the first wheel grooving pass was approximately the same with an average of 0.113 kW. It can also be noticed that the measured power for all subsequent re-grooving passes (which were performed without increasing the depth of cut) was, on average, only 0.00580 kW – which is very similar to the average measured spindle power when a grinding wheel is freely rotating and not engaged with the grooving system's single-point diamond (0.00586 kW). Looking at how close these averages are in Table 6.4, it is evident that, within the sensitivity of the spindle power sensor, there were no detectable changes in power between a freely spinning grinding wheel and a re-grooving pass. This important result lends credibility to the new re-grooving system's ability to accurately re-trace the same grooving path generated from the first grooving pass.

Table 6.4: Measured spindle power in [kW] during grooving and re-grooving of the grinding wheel

	Grooving	Re-grooving					
Pass #	1	2	3	4	5	6	7
Test (1-a)	0.113	-	-	-	-	-	-
Test (1-b)	0.105	*0.0076*	*0.0058*	*0.0063*	-	-	-
Test (1-c)	0.121	*0.0043*	*0.0048*	*0.0051*	*0.0064*	*0.0049*	*0.0070*
Average grooving power over Tests a), b) and c):		*0.113*					
Average re-grooving power over Tests a), b) and c):		*0.00580*					
Average power when grinding wheel is freely rotating:		*0.00586*					

To further validate the re-grooving system, the resulting groove profiles on the grinding wheel's surface were measured using the 3D grinding wheel surface topography measurement apparatus shown in Figure 6.17. This setup consists of a Nanovea

CHR150 white light chromatic sensor with a 1200 μm optical pen. This sensor gives the wheel scanning systems a measurement range of 1200 μm, a depth accuracy of ± 200nm, a depth resolution of ±25 nm, a maximum planer resolution of 1 μm, and a range of sampling rates between 30 and 1000 Hz. The grinding wheel scanning system uses the horizontal, vertical, and rotary stages shown in Figure 6.17 to position the optical pen and rotate the grinding wheel as desired [47,48]. Figure 6.18 depicts surface topography measurements of a grooved grinding wheel as well as a selected cross-section profile.

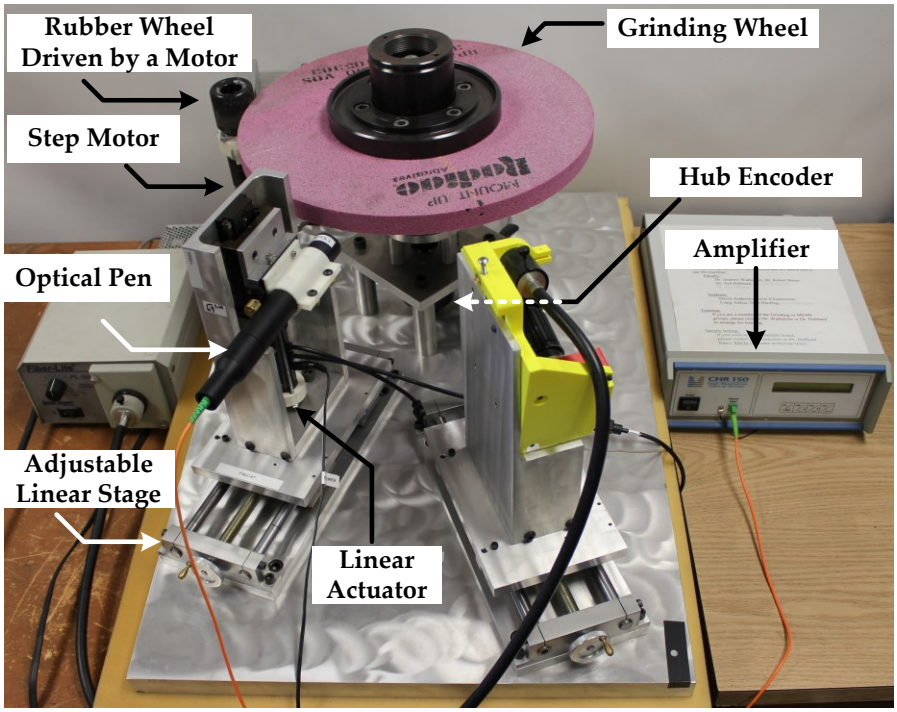

Figure 6.17: 3D grinding wheel surface topography measurement apparatus

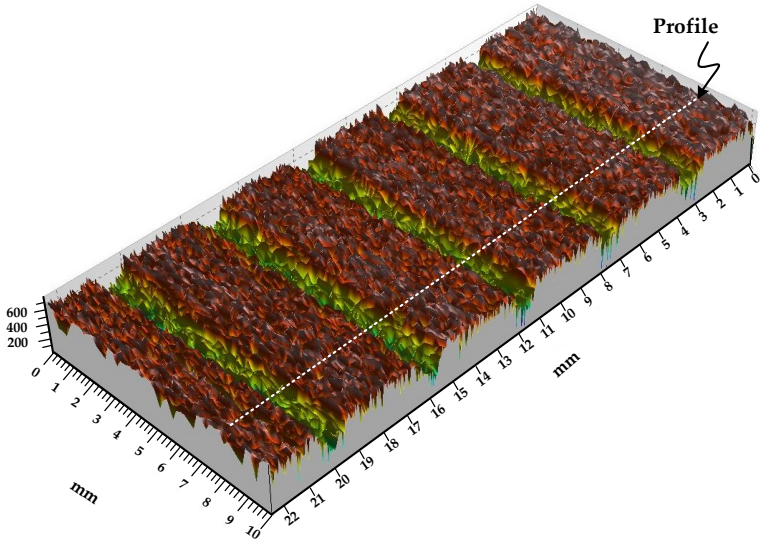

Figure 6.18: Portion of grooved surface of grinding wheel

Figure 6.19 shows the resulting grinding wheel groove profiles taken along a line parallel to the grinding wheel axis. It can be seen from this figure that the measured profiles of the resulting grooves generated from the Test 1-a), b) and c) experiments are very similar. This observation is confirmed in Table 6.5 which uses manual measurements of Figure 6.19 to summarize the corresponding groove width, groove depth, and groove lead for this set of experiments. The maximum deviation in the groove width was only 0.015 mm. The maximum difference of the groove depth was only 0.013 mm. This small difference is likely due to the brittle fracture mechanism of the abrasive grits. It can also be seen in Figure 6.19 that the resulting groove lead was 4.233 mm which is very close to the desired 4.25 mm.

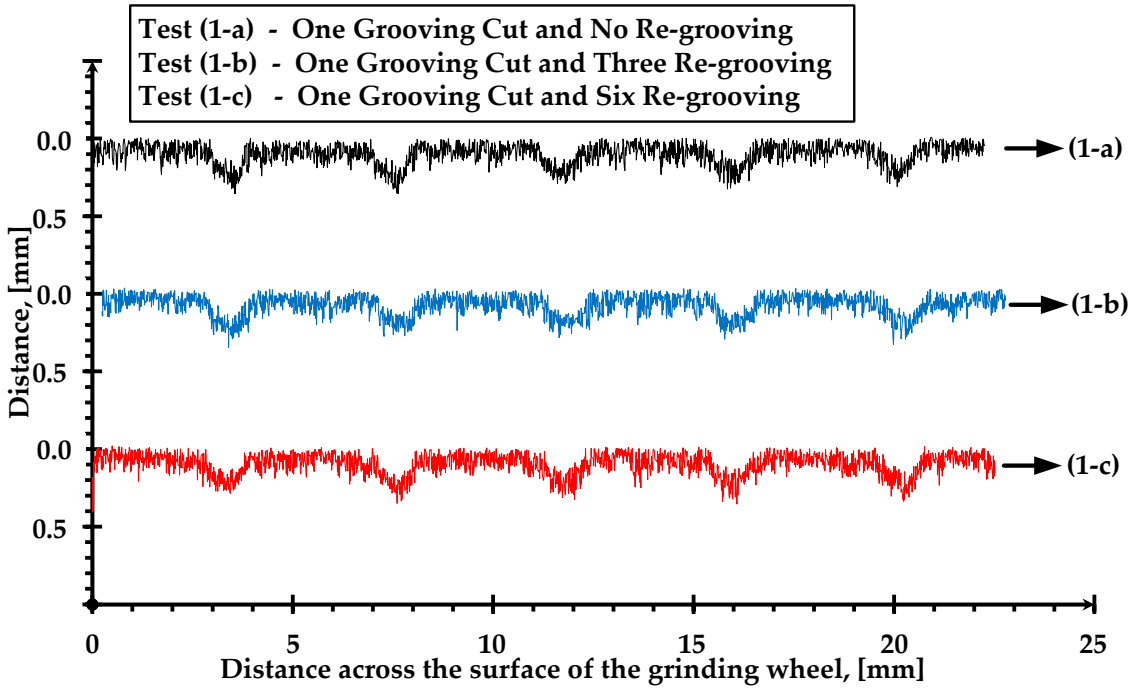

Figure 6.19: Groove profiles comparison when re-grooving the grinding wheel

Table 6.5: Comparison of resulted groove geometry of Test-1

	Groove width b_g [mm]	Groove depth, a_g [mm]	Groove lead [mm]
Test (1-a)	0.925	0.110	4.25
Test (1-b)	0.940	0.113	4.25
Test (1-c)	0.935	0.109	4.25

A second set of experiments was carried out to further validate the proposed wheel grooving system. Identified as Test-2, this set of experiments also contains three experiments; however, unlike Test-1, the grooving depth of cut was gradually increased for each subsequent pass. Test-2 was carried out because it was envisioned that this

system might be used to cut very deep grooves using a series of shallow cuts. The first experiment (Test 2-a) consists of one grooving pass with a 0.1 mm groove depth. The second experiment (Test 2-b) started with a 0.1 mm groove depth, and was followed by two grooving passes which incrementally increased the depth of cut by 0.05 mm resulting in a final predicted groove depth of 0.2 mm. The third experiment (Test 2-c) also started with a 0.1 mm groove depth, but it was followed by five grooving passes which incrementally increased the depth of cut by 0.05 mm resulting in a final predicted groove depth of 0.35 mm. Figure 6.20 shows a picture of grooved grinding wheel which resulted from the multi grooving passes of the third experiment (Test 2-c).

The average spindle power measurements for Test 2-a), b) and c) are presented in Table 6.6. It can be seen in this table that the average measured power for the first wheel grooving pass for each of the three experiments was approximately the same with an average of 0.114 kW. The grooving depth of cut for subsequent passes was incrementally increased by 0.05mm and the results show that the average measured power for these re-grooving passes resulted in approximately the same average power of 0.061 kW. The similar power measurements for the first pass as well as the similar power measurements for all subsequent passes attest to the ability of the wheel grooving system to consistently groove and re-groove the grinding wheel.

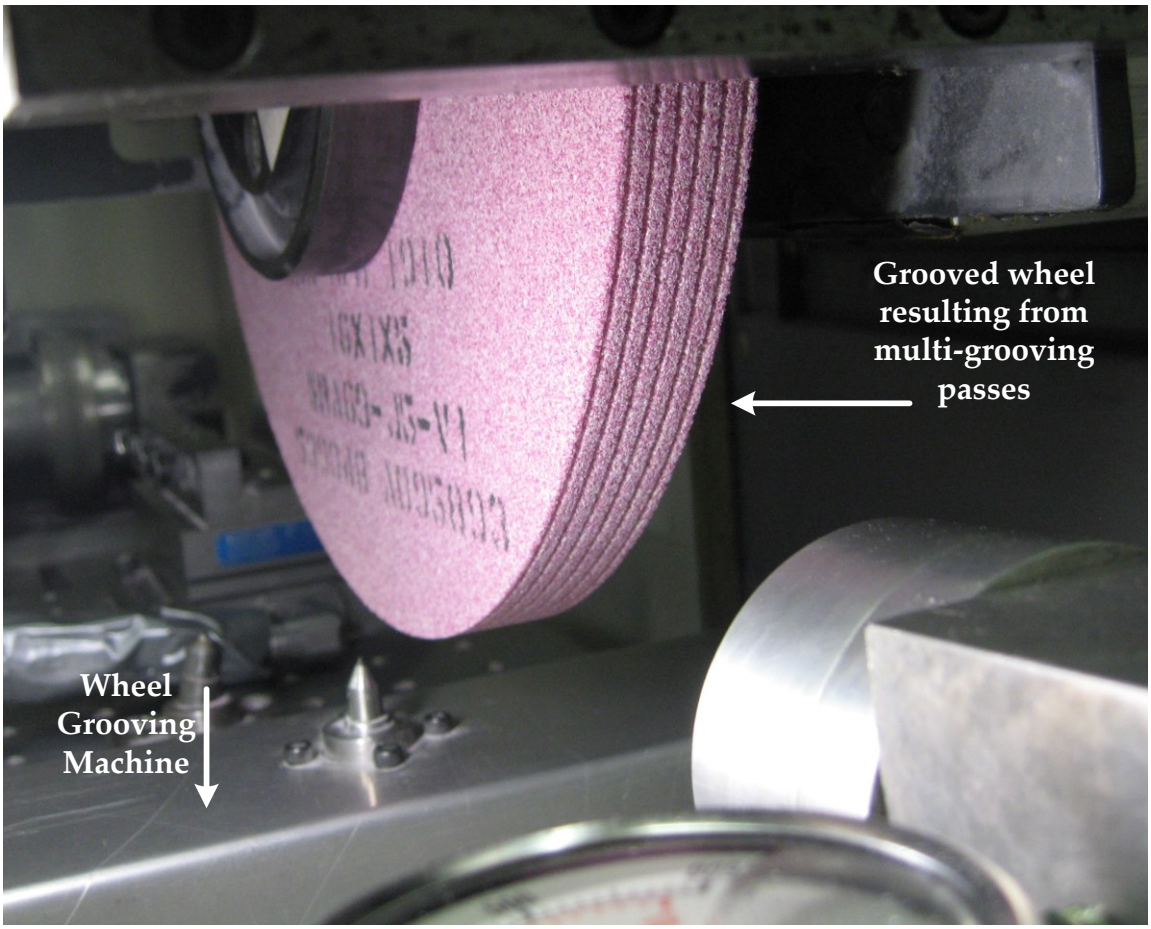

Figure 6.20: Successful multi-grooving process with gradual increase of depth of cut

Table 6.6: Average measured spindle power in [kW] as groove depth was gradually increased

	0.1 mm depth	Incremental increases in re-groove depth by 0.05 mm				
Pass #	1	2	3	4	5	6
Test (2-a)	0.130	-	-	-	-	-
Test (2-b)	0.111	*0.0499*	*0.0703*	-	-	-
Test (2-c)	0.100	*0.05735*	*0.0667*	*0.0721*	*0.0536*	*0.05735*
Average 0.1mm grooving power over Tests a), b) and c):				*0.114*		
Average 0.05mm grooving power over Tests a), b) and c):				*0.061*		

Figure 6.21 shows the corresponding surface profile measurements for the Test 2-a), b) and c) experiments where the grooving depth of cut was gradually increased in different

cutting passes. To quantitatively compare the resulting groove width, groove depth, and groove lead for these experiments, Table 6.7 summarizes the resulting measurements. The results shown in Figure 6.21 and Table 6.7 support the observation that the wheel grooving system works well. It should also be pointed out that gradually increasing the groove depth to create a deep groove will likely reduce the chances of damaging the wheel or single-point tool compared to using only one deep groove cut.

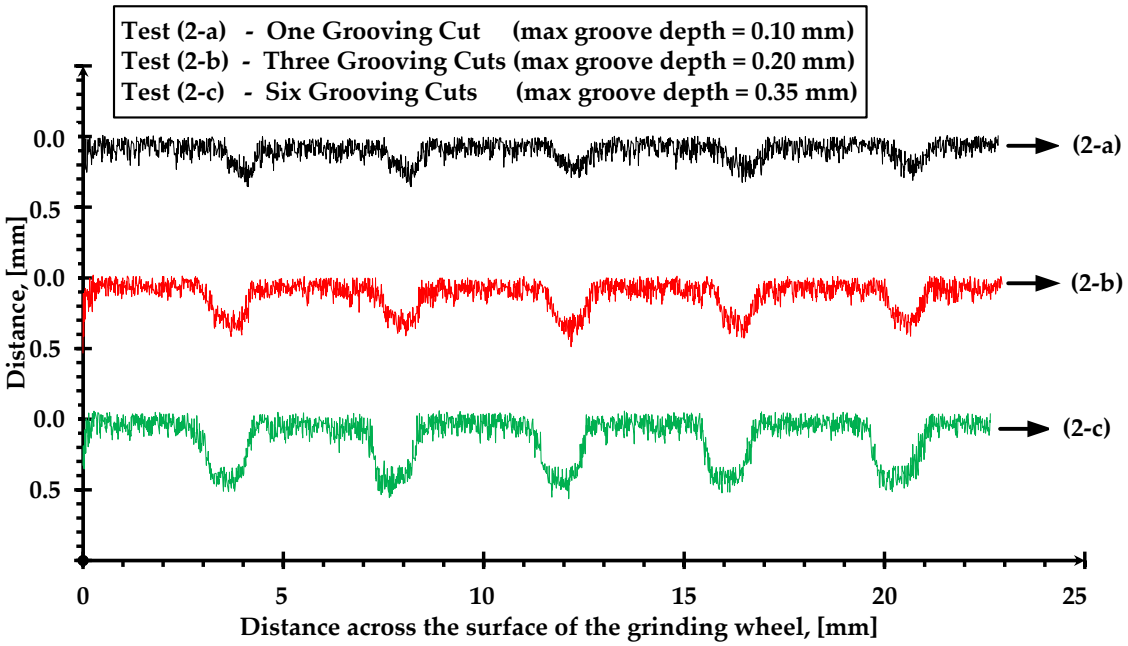

Figure 6.21: Comparison of the re-grooving accuracy when gradually increasing the groove depth

Table 6.7: Comparison of resulted groove geometry of Test-2

	Groove width b_g [mm]	Groove depth, a_g [mm]	Groove lead [mm]
Test (2-a)	0.925	0.116	4.25
Test (2-b)	1.360	0.209	4.25
Test (2-c)	1.605	0.364	4.25

Figure 6.22 shows that the new wheel grooving system is also capable of producing different groove patterns in addition to the spiral-shaped circumferential groove pattern studied in this paper. For the groove patterns (a), (b), and (c) shown in Figure 6.22, re-grooving tests were performed four times in order to accomplish the desired final

groove depth of 0.150 mm, while the sinusoidal groove shown in Figure 6.22(d) was performed using one grooving cut which was 0.0889 mm in depth.

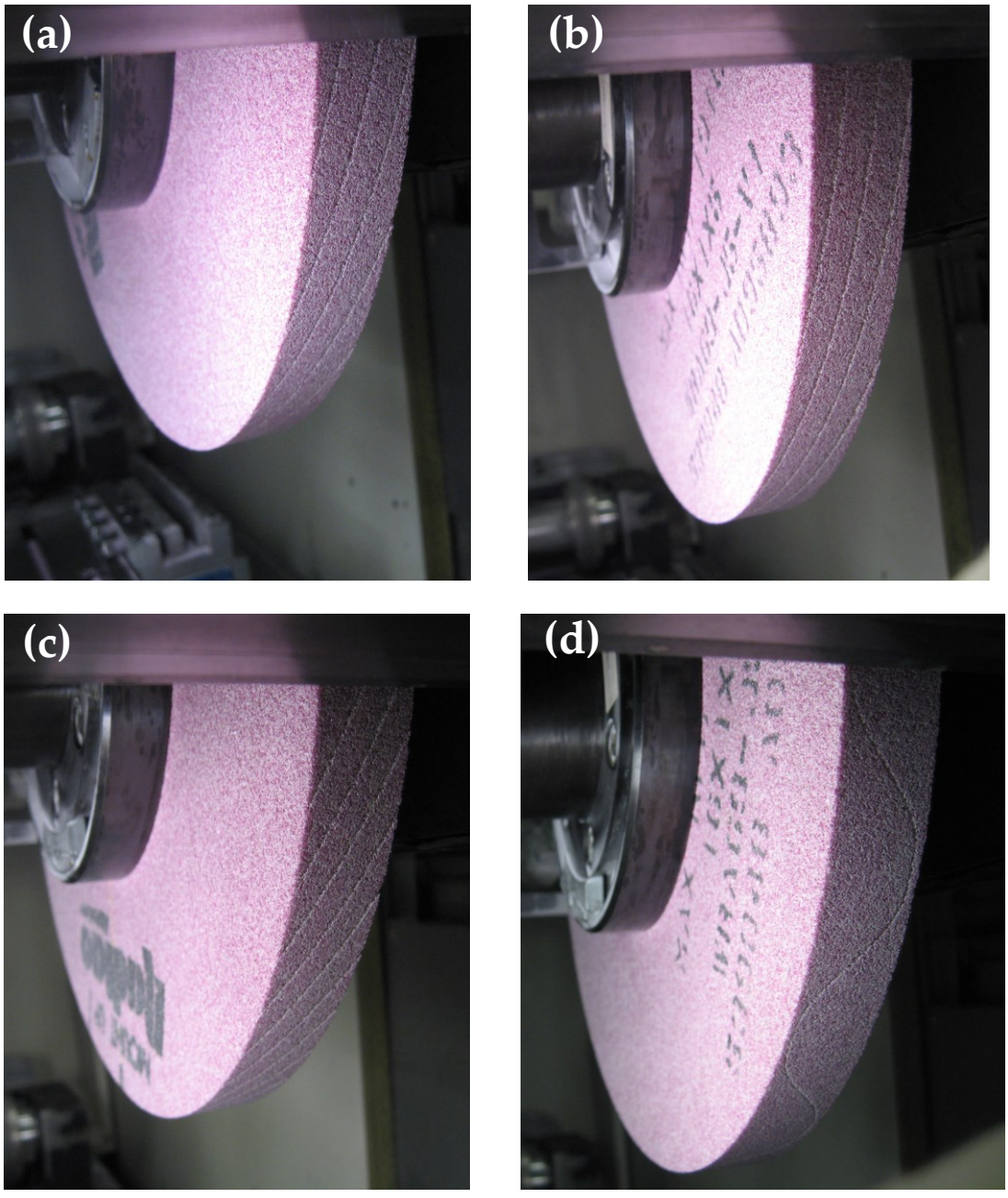

Figure 6.22: Sample groove patterns that the developed wheel grooving system is capable of

6.6 Wheel Wear Experiments

Grinding experiments were then carried out to study the wear performance of these circumferentially-grooved wheels formed by the developed setup. Creep-feed grinding experiments were conducted on the Blohm-Planomat 408 creep-feed grinding machine utilizing an annealed AISI 4140 steel workpiece with the same material poroperties and dimensions introduced in the previous chapter, and an aluminum oxide (Al_2O_3) wheel (Radiac Abrasives WRA 60-J5-V1). Throughout all of these wear experiments, the grinding depth of cut, wheel speed, and workpiece speed were kept constant at 1.0 mm, 22.4 m/sec and 1.7 mm/sec, respectively. Prior to the creep-feed grinding experiments, the grinding wheel was dressed using a single-point diamond dresser having a dressing feed of 0.04 mm/rev and a dressing depth of 0.01 mm. Grinding wheel wear experiments were first conducted using a non-grooved grinding wheel and then a grooved grinding wheel was used under the same grinding conditions. In the grooved wheel case, the grinding wheel was grooved according to the following parameters: groove factor of 50%, groove depth of 0.0889 mm, and groove width of 1.4 mm. These parameters were selected because of the different groove geometries explored in the previous chapter, this groove geometry performed best. In calculating the groove factor, the geometry of the groove was assumed to take the same geometry of the diamond tip engaged with the grinding wheel during the grooving operation.

Grinding forces and consumed power results were acquired using the force dynamometer and power transducer. The resulting grinding forces and consumed power were measured at a sampling frequency of 500Hz. The arithmetic mean surface roughness R_a of the resulting ground workpiece was measured directly using a MahrFedral Inc. Pocket Surf. The cutting-fluid concentration and flow maintained similar to the experiments in the previous chapter at 5.1%and 50.4 L/min, respectively.

6.6.1 Wheel Wear Results

Figure 6.23 plots the consumed power as a function of the volumetric workpiece material removed. As can be seen from this figure, the consumed power increased as more workpiece material was removed, due to grinding wheel wear. Generally, grinding wheel wear is classified, as discussed in the background chapter: Chapter 2, into three mechanisms: attritious wear, grain fracture, and bond fracture [11,12]. Attritious wear occurs by the rubbing of the grains on the workpiece which, over time, dulls the cutting edges and results in higher consumed grinding power. It can also be observed in Figure 6.23 that the rate of increase in grinding power is higher for the non-grooved case than it is for the grooved case. This important result suggests that grooving the wheel does not accelerate the wheel wear process and may in fact slow down wheel wear. Additionally, it can be seen from Figure 6.23 that in the non-grooved wheel case, the amount of workpiece material removed was limited by the occurrence of workpiece burn – likely due to an increase of rubbing between the workpiece and the grinding wheel. The grooved grinding wheel, on the other hand, was able to remove approximately twice as much workpiece material as the non-grooved wheel case. Instead of workpiece burn, grinding wheel breakdown ultimately limited the amount of workpiece material that could be removed. This wheel breakdown can be identified by a slight drop in the consumed power just before failure occurred where grain fracture likely existed.

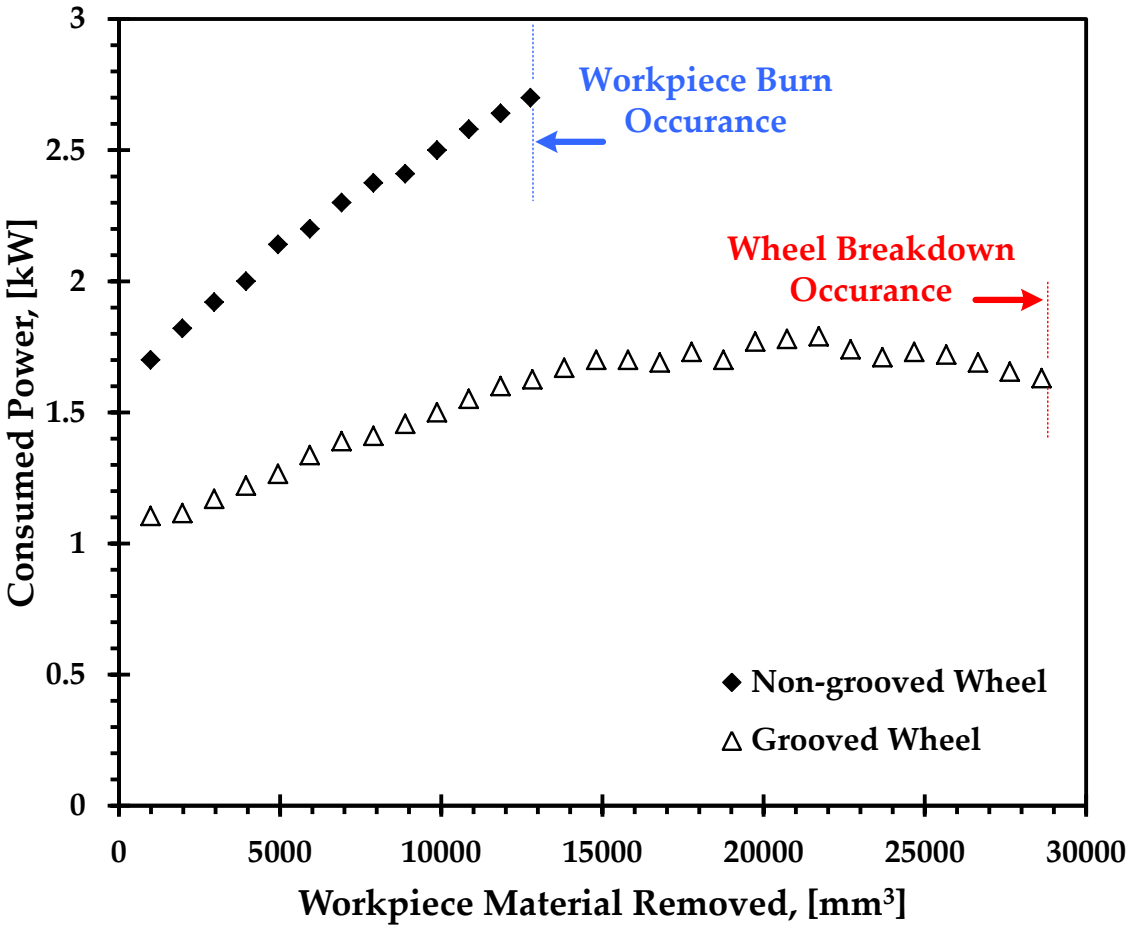

Figure 6.23: Consumed power vs. workpiece material removed for wear study

Figure 6.24 plots the corresponding average measured workpiece surface roughness as a function of the volumetric workpiece material removed. It can be seen from this figure that the average surface roughness using the grooved grinding wheel was only slightly higher than when a non-grooved wheel was used and was in the range of 0.30 μm which corresponds to a "fine quality" surface finish and was well within the 1.6 μm range which corresponds to an "average quality" surface finish [45].

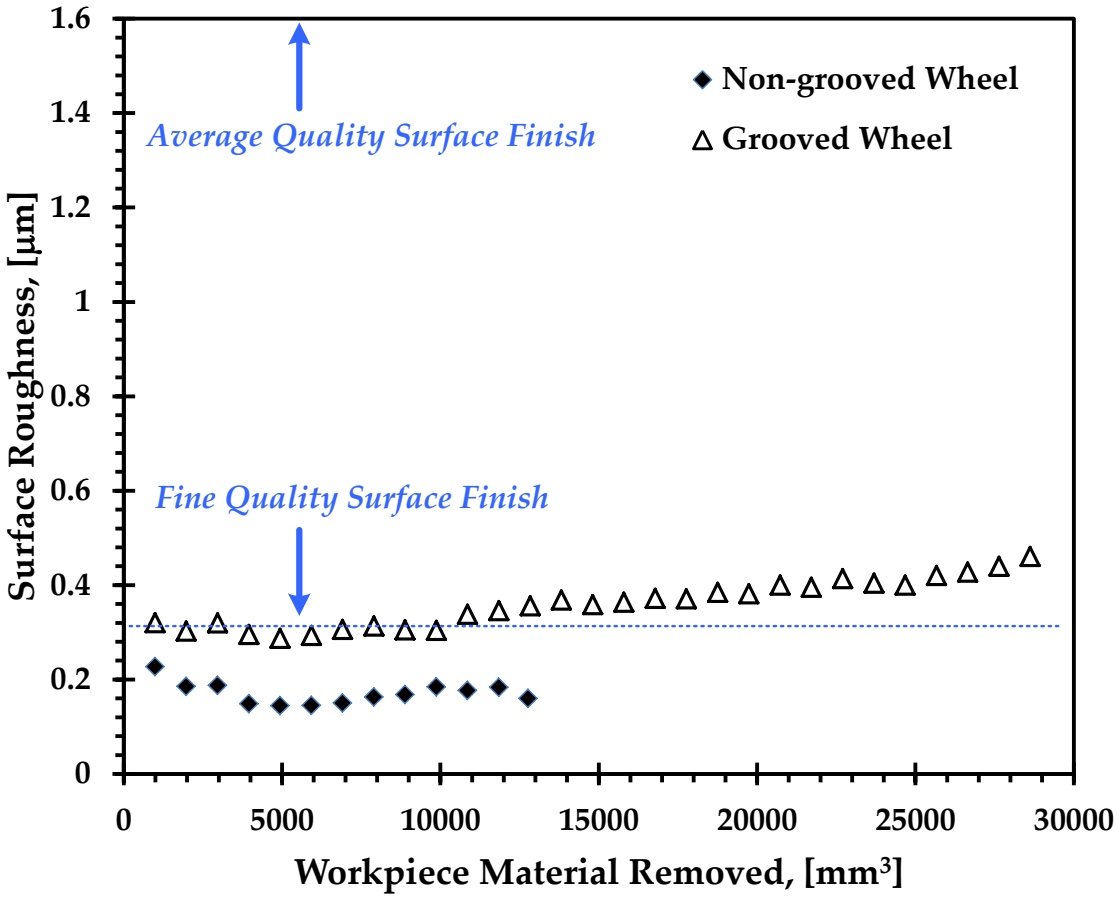

Figure 6.24: Surface roughness vs. workpiece material removed for wear study

6.7 Summary

A novel wheel grooving system was successfully designed, developed, and experimentally validated. The resulting system exhibited a high degree of repeatability, with a maximum difference in groove width and depth of 0.015 mm and 0.013 mm, respectively, for 10 consecutively cut grooves. These small discrepancies are likely due to the brittle fracture mechanism of the aluminum oxide grits. The wheel grooving system has the ability to groove and re-groove a wide variety of groove patterns including circumferential, helical, and sinusoidal patterns. For the conditions used in

this research, a wear study showed that circumferentially-grooved wheels can remove twice as much material as the non-grooved wheel case. Furthermore, these wear results showed that wheels with grooves wear slower than a non-grooved wheel.

Chapter 7. Non-grooved & Grooved Grinding Wheels Mechanics Comparisons

This chapter investigates why circumferentially-grooved grinding wheels are able to improve the performance of the grinding process when compared with non-grooved wheels by examining the roles that chip formation and coolant play on the resulting grinding wheel cutting mechanics.

7.1 Kinematics & Effect of Grooving on Chip Formation

This section provides an explanation of the kinematics of the circumferentially-grooved grinding wheel and how its chips are formed. Figure 7.1 delineates the mechanism of how a circumferentially-grooved grinding wheel interacts with the workpiece during the grinding operation. The right hand of the figure represents a grooved grinding

wheel with a 50% groove factor* and the left hand of the figure shows a serious of slices; series of slices are taken for one groove spiral for one lead. If one takes a single slice of the grinding wheel, such as slice (1) in Figure 7.1, it can be seen that there is an equal amount of grooved and non-grooved wheel surfaces, as represented by the solid red and dotted black lines, respectively. By taking equally spaced slices of the wheel across its width, for example from slice (1) to slice (9) in the cross-section A-A shown in Figure 7.1, it can be seen that the grooved and non-grooved portions rotate clockwise one complete cycle for every rotation of the wheel. This cycle then repeats if one is to continue taking slices across the wheel.

* Groove factor is the percentage of the remaining surface area of the grinding wheel after grooving it. The lead of the groove is the distance that the groove advances across the grinding wheel width.

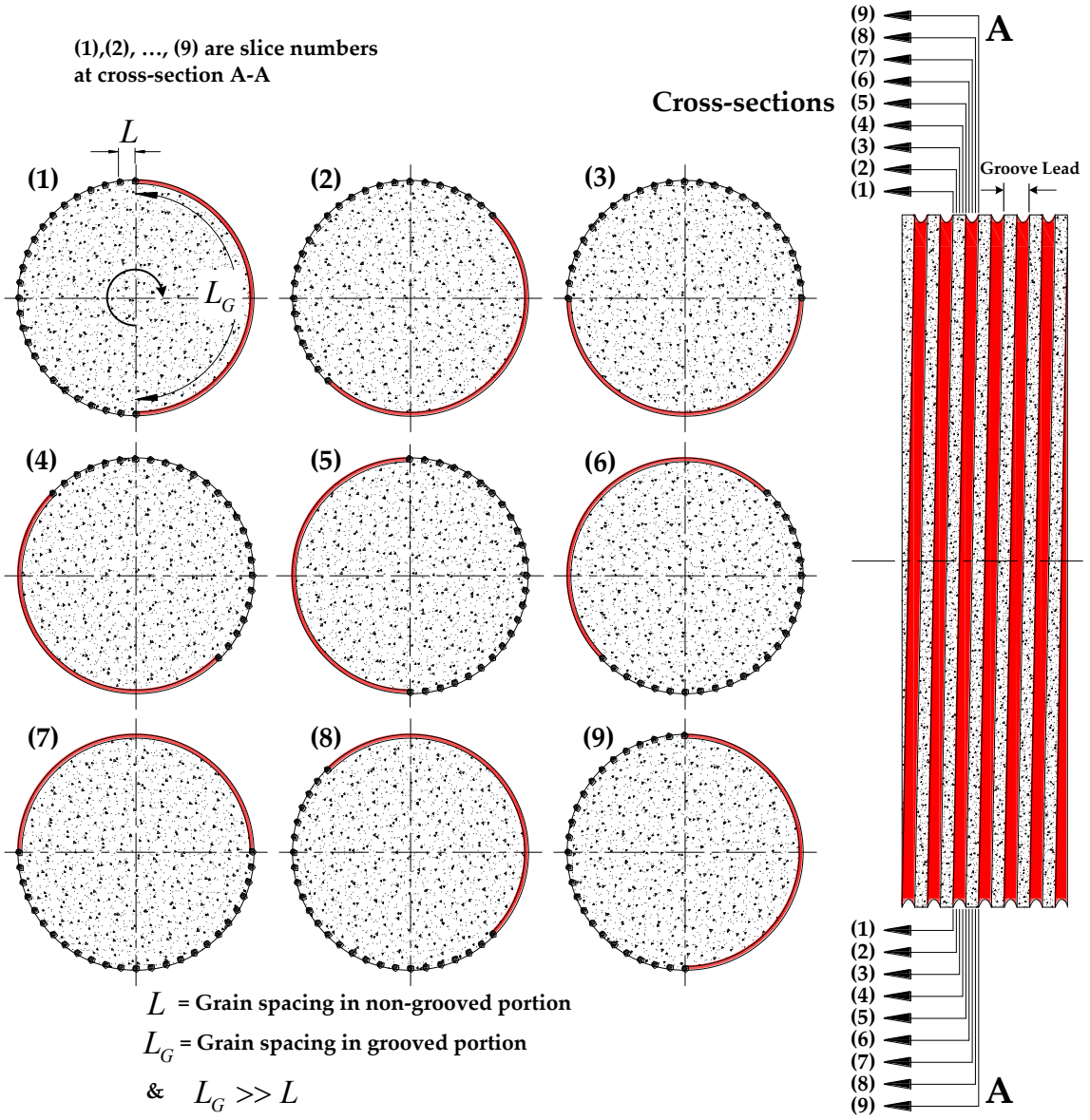

Figure 7.1: Illustration of selected cross-sections for one complete groove rotation

The grain spacing in the groove portion L_G is much greater than the grain spacing in the non-groove portion L (see slice 1 in Figure 7.1). This large spacing results in the large undeformed chip thickness. To help observe this phenomenon more clearly, Figure 7.2 shows the effect of wheel grooving and abrasive grain spacing on chip formation and chip thickness. As can be seen from the figure, the spacing between active abrasive grains for the non-grooved portion of the grooved grinding wheel is represented by the symbol L which results in a mean undeformed chip thickness of h_m that can be calculated as [7,8]:

$$h_m = \frac{v_w}{v_s} \cdot L \cdot \left(\frac{a_e}{d_s} \right)^{0.5} \tag{7.1}$$

For the grooved portion of the grinding wheel, the spacing of cutting edges L_G (which are located at the leading and trailing edges of the groove) and the resulting undeformed chip thickness $h_{m,g}$ are shown in Figure 7.2. The undeformed chip thickness for the grooved portion of the grinding wheel $h_{m,g}$ can also be calculated by Equation (7.1). Since L_G is larger than L, then $h_{m,g}$ will be proportionally larger than h_m.

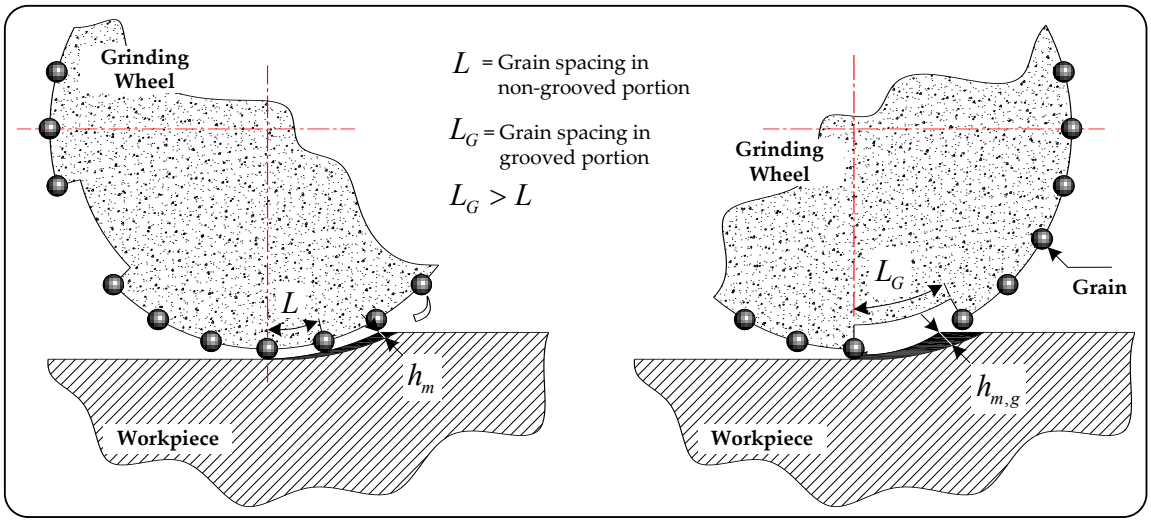

Figure 7.2: Active grains spacing and chip thickness

As a result, the overall average chip thickness for the entire grooved wheel will be effectively larger than a non-grooved wheel. To validate the kinematics explained in Figures 7.1 and 7.2, experiments were carried out to examine the resulting chip sizes generated from both grooved and non-grooved grinding wheels.

7.1.1 Chip Measurements Experiments

In order to compare grinding chip sizes generated from the use of a regular non-grooved grinding wheel and a circumferentially-grooved grinding wheel, grinding experiments were conducted to collect and examine the resulting chips. Prior to each grinding experiment, the grinding machine was cleaned to ensure that only chips from the desired experiment were collected. In these experiments, an aluminum oxide wheel (Al_2O_3 Radiac Abrasives WRA 60-J5-V1) was utilized to grinding 4140 annealed steel. First, a grinding operation was performed using a non-grooved wheel. The grinding wheel speed, workpiece feed, and depth of cut were 22.35 m/sec, 1.70 mm/sec, and 1.00 mm, respectively and the grinding fluid was delivered at 50.4 L/min. At the end of this experiment, all of the grinding chips were collected and dried. Then, a

circumferentially-grooved grinding wheel with a 50% groove factor was tested under the same grinding conditions utilized for the non-grooved wheel case. In a similar manner to the non-grooved case, all grinding chips were collected and dried.

7.1.2 Chip Size Results

The collected chips were examined using a scanning electron microscope (SEM) and the resulting images are shown in Figure 7.3. Figure 7.3(a) is an SEM image of the grinding chips collected after using the regular non-grooved grinding wheel, and Figure 7.3(b) is an SEM image of grinding chips collected after using the grooved grinding wheel. Evidently, a significant chip size difference can be seen in these figures. Most chips shown in Figure 7.3(a) are same sizes while chips shown in Figure 7.3(b) vary in size. Using the provided scale on the images, the average chip width for the non-grooved wheel case is between approximately 5 and 8 μm while the average chip width for the grooved wheel case is between approximately 42.5 and 55 μm – an increase of approximately 7.5 times. Figure 7.3(b) shows that there are also some chips which have similar sizes to the ones seen in Figure 7.3(a) which is evidence that the cutting mechanisms associated with the non-grooved portion and grooved portion of the grooved wheel were both involved in grinding (as predicted from Figures 7.1 and 7.2). Extra figures of large chips that the grooved grinding wheel formed are shown in Appendix D.

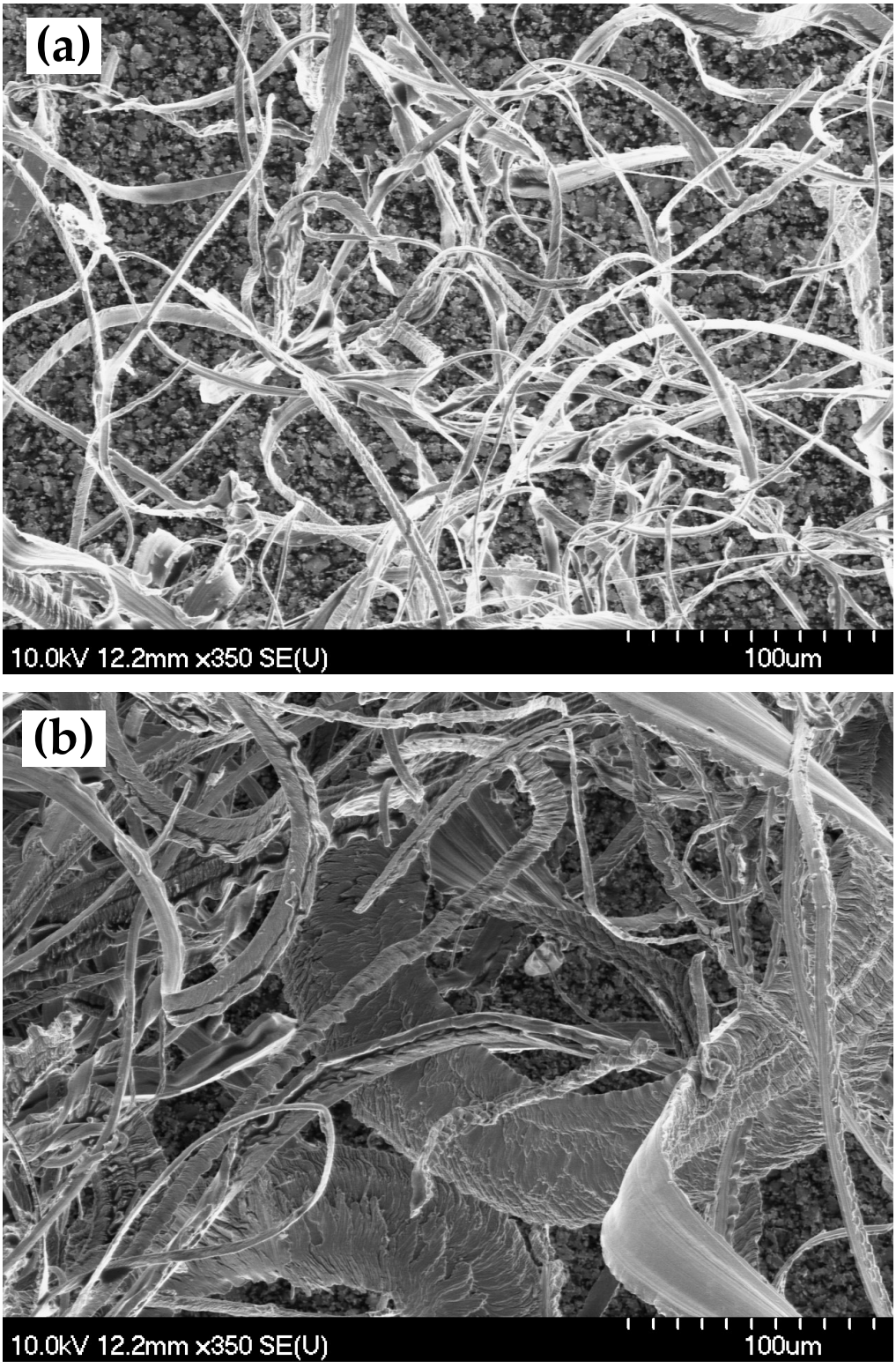

Figure 7.3: SEM comparisons of chips sizes of (a) non-grooved and (b) grooved wheels

The increase in the chip width seen in Figure 7.3(b) must be related to chip thickness. Both the chip thickness and chip width are a result of the abrasive grain width that acting when it penetrate into the workpiece during the chip formation. To help further explain this phenomenon why an increase in chip width occurred when using a circumferentially-grooved grinding wheel, an exaggerated schematic drawing illustrating the variation of the effective width of the abrasive grain as it interacts with the workpiece is shown in Figure 7.4. As can be seen in the figure, different wheel surfaces can be extracted by taking slices of the wheel along threshold planes at increasing depths into the grinding wheel (i.e., h_{cu_1}, h_{cu_2}, h_{cu_3}, and h_{cu_4}). Figure 7.4 demonstrates how, the deeper the abrasive grains penetrate into the workpiece during the metal removal process, the wider the effective widths are. For example, depth h_{c_4} causes a greater effective width of b_{c_4} than depth h_{cu_1} which only results in an effective width of b_{c_1}. Backer *et al.* [49] suggested that the effective width b_c can be assumed to be proportional to the average undeformed chip thickness h_{cu}:

$$b_c \propto h_{cu} \tag{7.2a}$$

$$b_c = \frac{1}{2 \cdot r} h_{cu} \tag{7.2b}$$

where r is the ratio of chip width to thickness at any point.

Therefore, the greater the effective width is, the greater the average undeformed chip thickness will be.

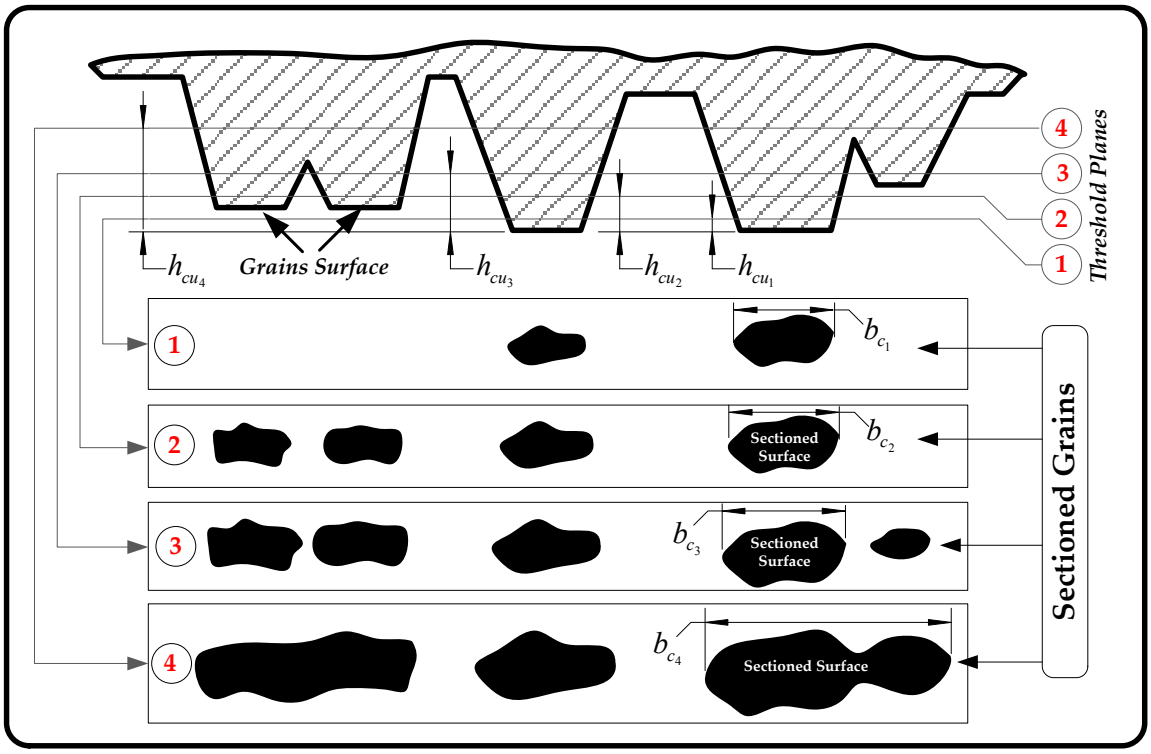

Figure 7.4: Illustration of thresholding process for extracted surfaces to obtain grain widths

Due to the kinematic motion between the grinding wheel rotational speed and the linear translation of the workpiece feed, it requires time for the active grain at the edge of the groove to interact with the workpiece as it penetrates deeper than the grains in the non-grooved portion of the wheel. This increase in the interaction time results in an increase in the depth of penetration causing a higher effective width and, consequently, a higher average undeformed chip thickness.

Clearly, as seen from the above discussion, a grooved wheel results in an increase in the chip size or volume. The following section investigates the effect of grooving on the resulting workpiece surface finish.

7.1.3 Effect of Grooving on Surface Finishes

To investigate the effect of grooving the grinding wheel on the workpiece surface finishes, dry and wet grinding experiments were carried out. The resulting surface roughness of the ground workpiece is depicted in Figure 7.5. It can be seen from this figure that the grooved grinding wheel produced workpiece surface finishes that were slightly rougher than the regular non-grooved grinding wheel. In addition, both dry and wet grinding cases produced workpieces having surface roughness values that were approximately in the same range. In the dry grinding experiments, the resulting average surface roughness for the regular non-grooved and the grooved wheel cases were 0.69 μm and 0.76 μm, respectively. In the wet grinding experiments, the resulting average surface roughness for the regular non-grooved and grooved wheel cases were 0.66 μm and 0.74 μm, respectively. Note that all experiments resulted in what is considered to be a fine surface finishes suggesting that the loss of surface finish was not problematic.

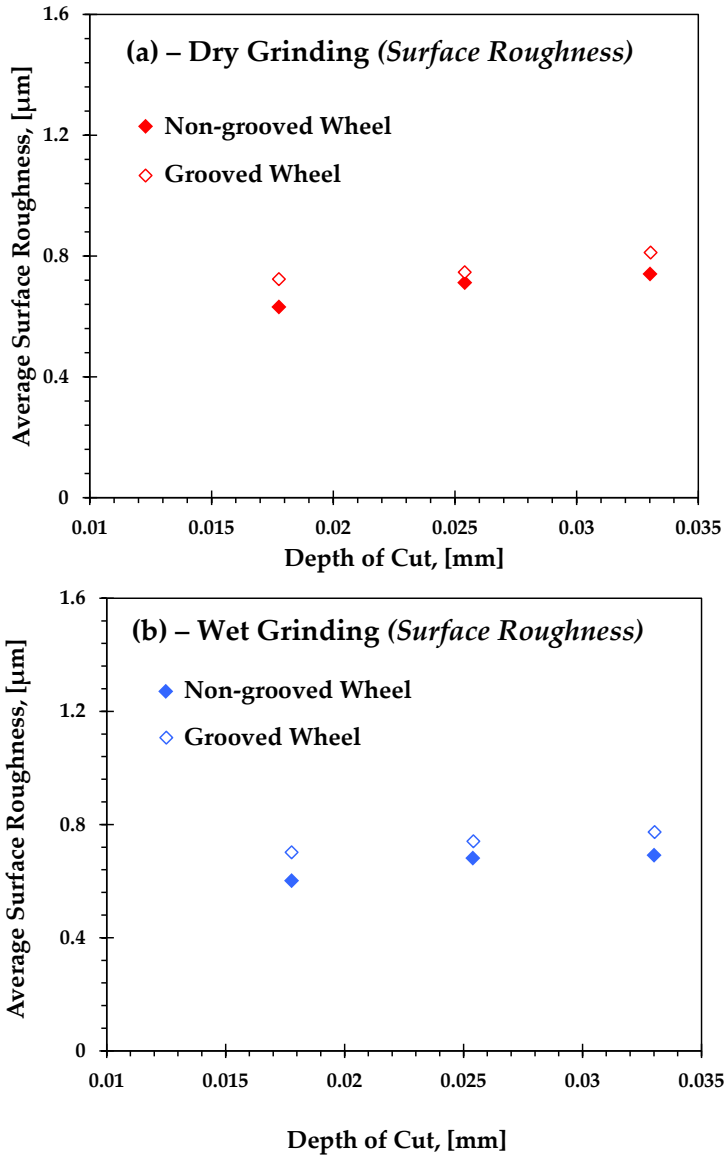

Figure 7.5: Resulted surface finish (a) dry grinding and (b) wet grinding

When performing wet grinding experiments, there were no signs of workpiece burn or surface oxidation due to the availability of the grinding fluid; however, in the dry grinding experiments, workpiece burn occurred. Figure 7.6 depicts pictures of the workpiece ground surface resulting from performing these dry grinding experiments where the first row of images shows the results for the non-grooved wheel experiments and the second row of images shows the results for the grooved wheel experiments. It

can be seen from the figure that different degrees of oxidation or burn occurred during these grinding tests. For both the regular non-grooved and grooved wheels, the degree of burn increased with depth of cut. It is also apparent that the grooved grinding wheel resulted in less discoloration or burn in comparison to the non-grooved wheel confirming that a grooved wheel can remove more material before workpiece damage occurs. In addition, for the grooved wheel, the burn occurred in a periodic manner. It is likely that the non-burned areas were due to the grooves and the burned areas were due to the non-grooved portion of the wheel.

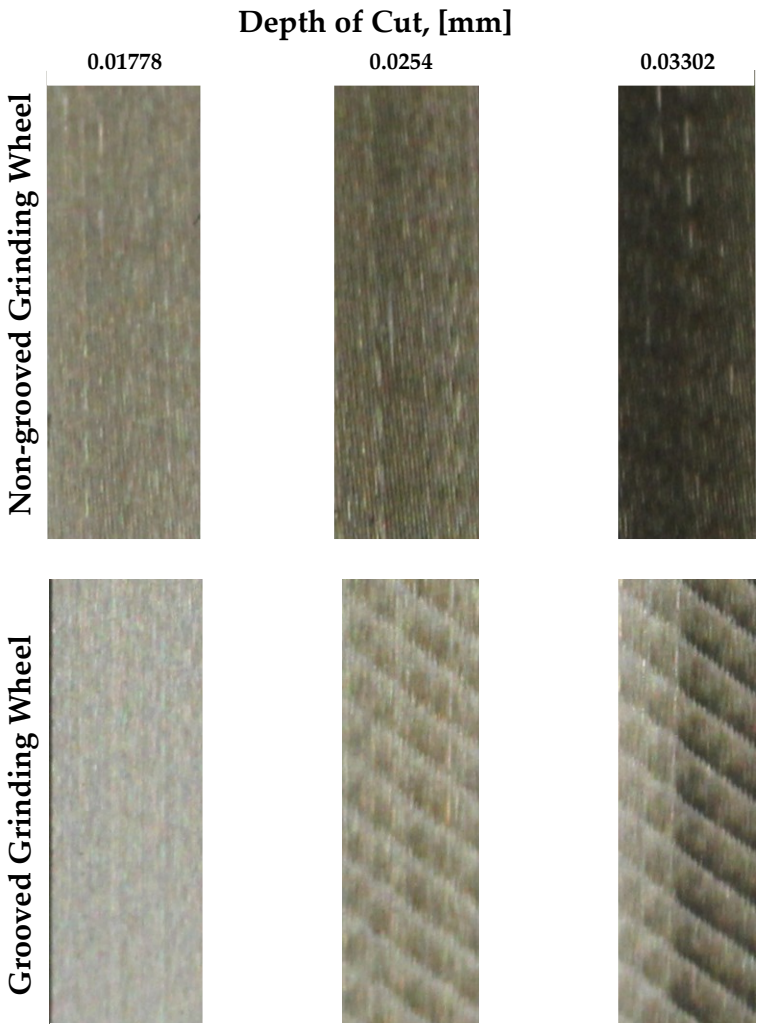

Figure 7.6: Comparisons of workpiece burn degree

Furthermore, these marks have a certain angle relative to the direction of grinding when using a circumferentially-grooved grinding wheel. To explain these angled marks, the kinematics of the grooved grinding wheel was analysed. For this set of experiments, the wheel speed and workpiece feed were 22.35 m/sec and 38.1 mm/sec, respectively. The resulting grinding wheel rotation was approximately 1048 rpm which is one revolution per 0.0572 sec. Therefore, the workpiece advances approximately 2.18 mm per grinding wheel revolution. It can be seen from Figure 7.7 that the period of burn markings occurred approximately every 2 mm, which is consistent with the distance the grinding wheel advances per revolution. Since the circumferential grooves are in the shape of a helix, wrapped around the axis of the grinding wheel with a pitch of 2.8 mm/turn, the resulting helix angle is 37.9° which is close to the measured value of 36.8° on the workpiece shown in Figure 7.7. Therefore, there is an excellent agreement between the kinematic calculations and the measurements of the burn pattern.

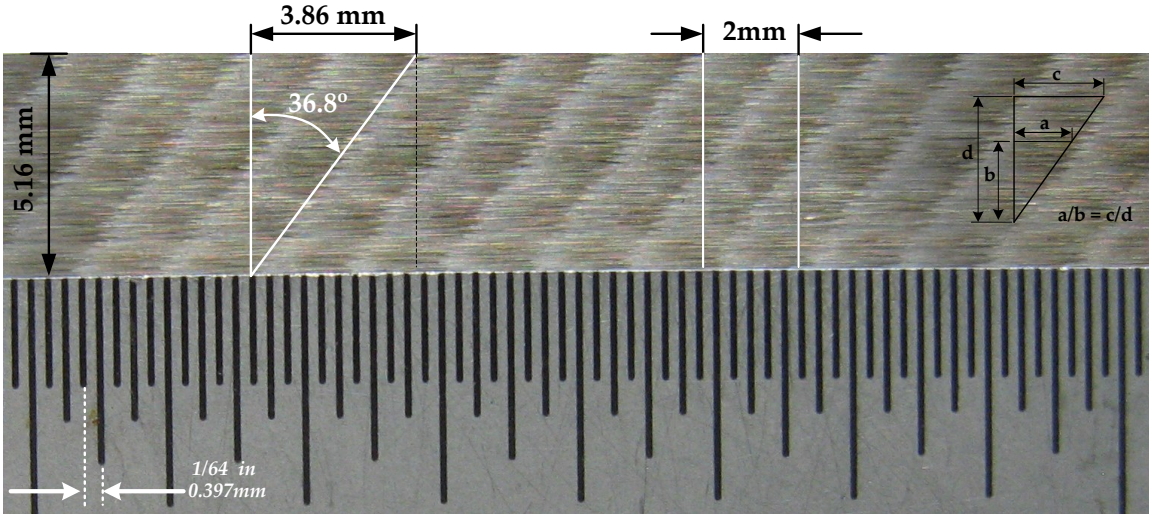

Figure 7.7: Burn or oxidation marks measurements

Given the different burn patterns observed on the workpiece surfaces, precise profiles of the ground surface were measured across the workpiece and along the workpiece as shown in Figure 7.8(a) using a Nanovia Surface Profilometer – PS50 shown in Figure

7.8(b) to ensure that the circumferentially-grooved grinding wheel was not creating any surface waviness on the ground surface of the workpiece.

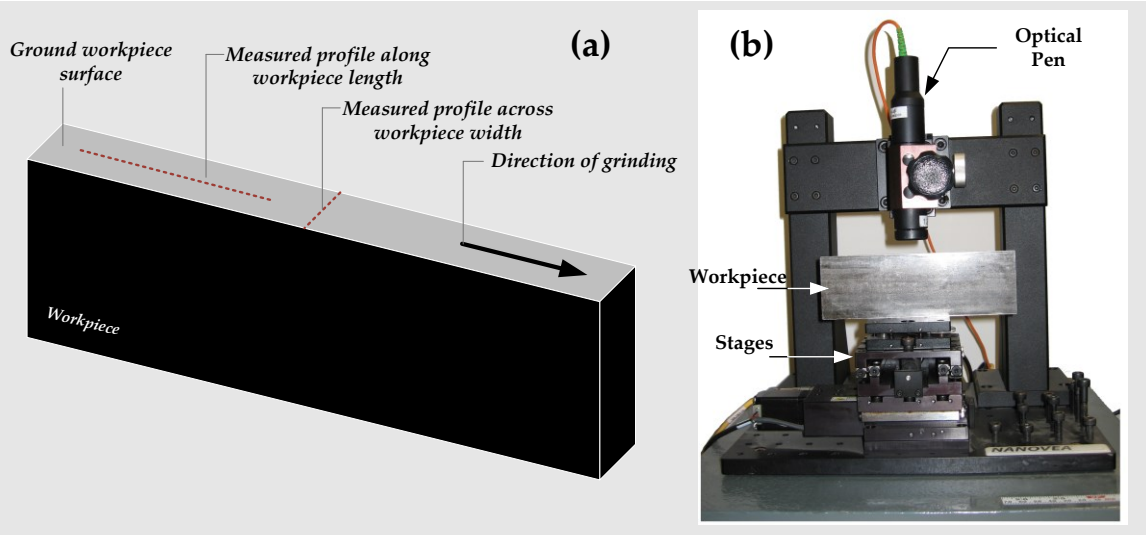

Figure 7.8: Workpiece surface profile measurements

Figure 7.9 presents the resulting profile measurements of the ground surface across the workpiece width and Figure 7.10 shows the profile measurements of the ground surface along the workpiece length in the direction of the grinding for both the non-grooved and grooved grinding processes. It can be seen that the surface profiles resulting from the circumferentially-grooved grinding wheel are very similar to the surface profiles generated from the regular non-grooved wheel.

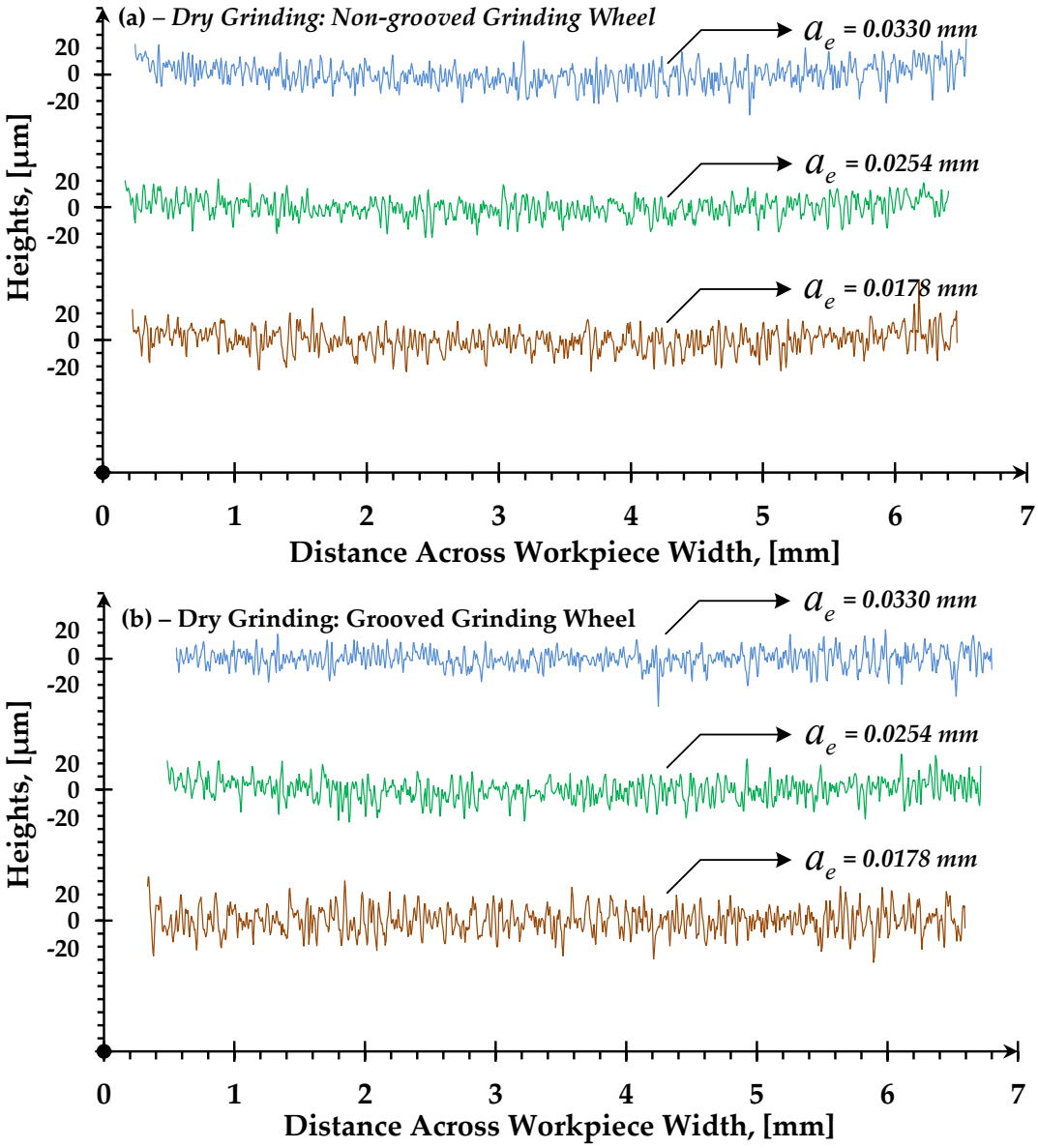

Figure 7.9: Surface profiles across workpiece width

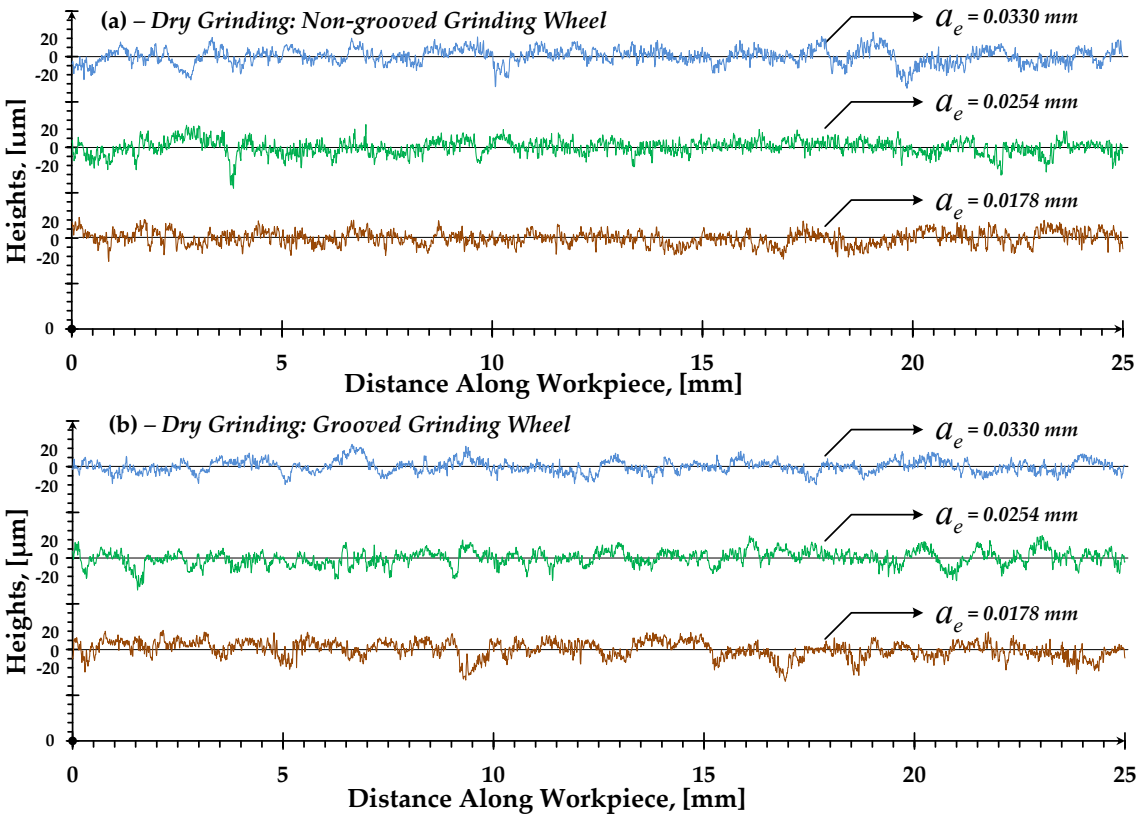

Figure 7.10: Surface profiles along workpiece length

In order to affirm that there are no signs of dominant surface frequencies caused by the circumferentially-grooved grinding wheel, a Fast Fourier Transformation (FFT) Analysis using MATLAB software was performed on the measured profiles for both the non-grooved and grooved grinding processes. Figure 7.11 plots the results of the FFT in the frequency domain (1/mm) for the measured profile taken along the workpiece length and Figure 7.12 plots the same FFT results with respect to wave length in (mm). It can be seen from both figures that the FFT analysis resulting from the profiles measured from the grinding experiments using the circumferentially-grooved wheel are similar to the ones generated from the profiles measured from the grinding experiments using the regular non-grooved wheel. Clearly, for the grooved wheel set of result, there is no dominant frequency to indicate the presence of any surface waviness.

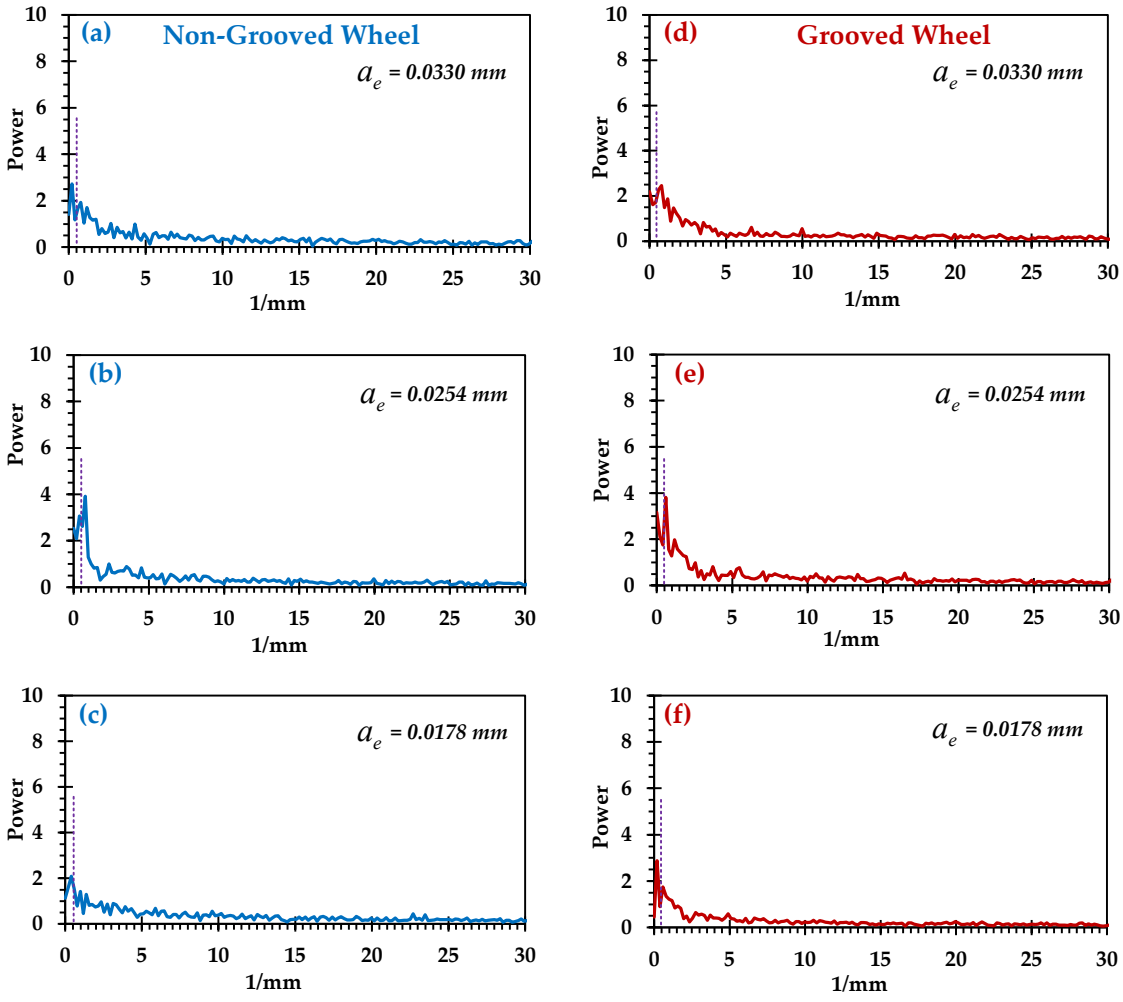

Figure 7.11: An FFT analysis for non-grooved (a,b,c) and grooved (d,e,f) wheels

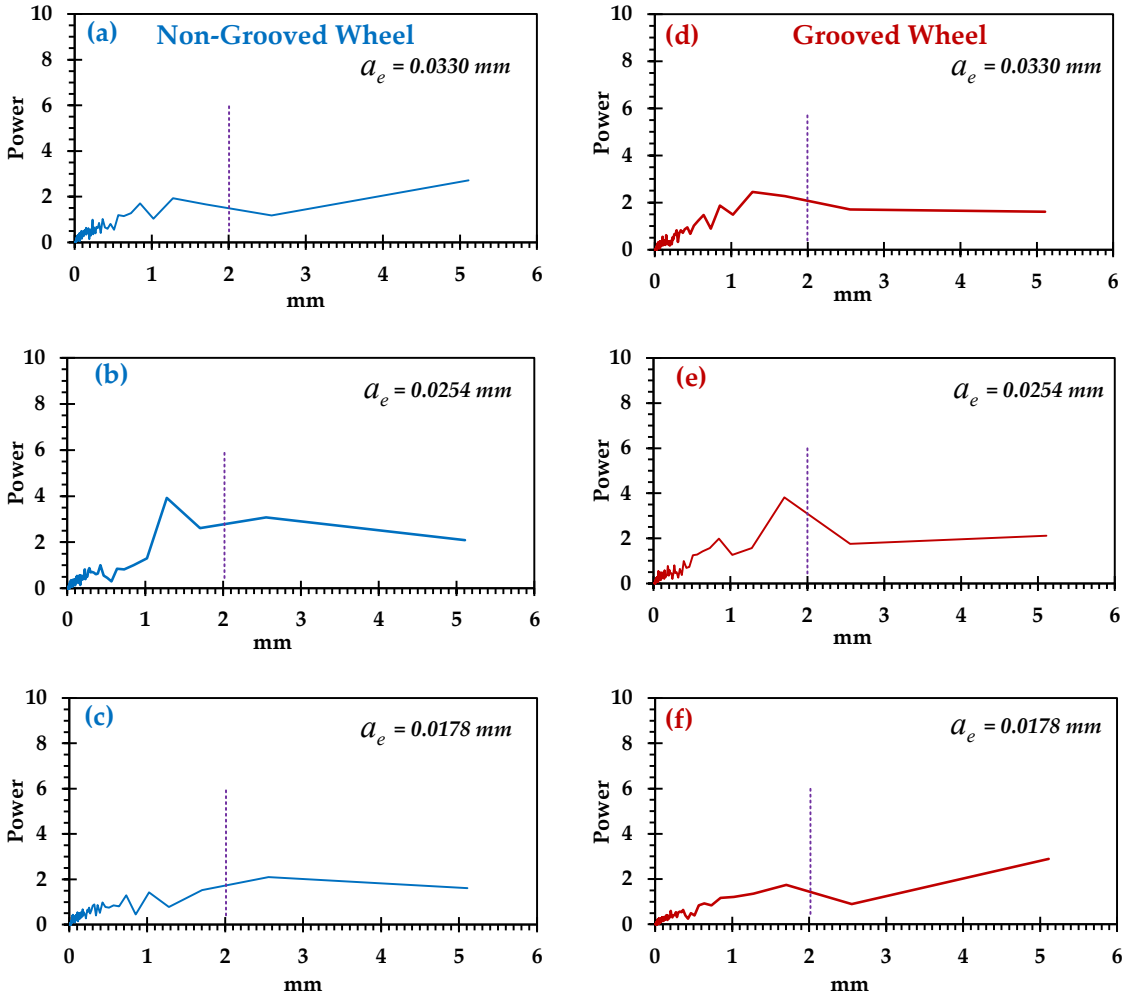

Figure 7.12: FFT results shown in respect to wave length

7.2 Effect of Wheel Grooving on Grinding Forces & Power

From the previous section, it was found that the kinematics of a grooved wheel resulted in proportionally larger chips than that from a regular non-grooved wheel. This, consequently, affects the performance of the grinding process. In this section, the effect of wheel grooving on the resulting grinding forces and power is explained.

It is known that there are various grinding variables affect the grinding forces and power of the grinding operation such as the grinding wheel type, wheel structure [50] wheel dressing condition [51] and grinding fluid delivery parameters [52]. The dressing process and wheel type affect the grinding wheel surface topography and both play a role in the grinding fluid delivery to the wheel-workpiece contact zone. Since wheel grooving is a methodology of restructuring the grinding wheel surface topography and since the grinding wheel topography directly affects the undeformed chip thickness and the ability of coolant to flow through the grinding zone, it is likely that one or both of these factors is/are responsible for the improved performance observed with the grooved grinding wheels. These two factors will be referred to as the "size effect" and the "coolant effect" hypotheses.

7.2.1 Size Effect

The size effect is an important property that relates the undeformed chip thickness in grinding [53] to the process efficiency [7]. Rowe and Chen [53] stated that the power consumption per unit volume of material removed increases as the undeformed chip thickness decreased. The undeformed chip thickness is directly related to the material removal rate. This relationship can be seen in Figure 7.13 which plots the experimentally determined specific energy verses the specific material removal rate [7,54-56]. As can be seen from this figure, there is a pronounced decrease in the specific energy e_c as the specific removal rate $Q_w^{'}$ increases [7,8], hence:

$$e_c = \frac{P}{Q_w} = \frac{P}{b_w \cdot Q_w^{'}} = \frac{F_t \cdot v_s}{b_w \cdot a_e \cdot v_w} \tag{7.3}$$

The undeformed chip thickness (or measured equivalent chip thickness h_{eq}) is proportional to the specific removal rate as follows [8]:

$$h_{eq} = \frac{Q_w^{'}}{v_s} = a_e \cdot \frac{v_w}{v_s} \tag{7.4}$$

As a result, the specific energy decreases with an increase in the undeformed chip thickness as shown by the following relation [7,8]:

$$e_c \propto \frac{1}{h_{eq}} \tag{7.5a}$$

$$e_c = \frac{F_t}{b_w \cdot h_{eq}} \tag{7.5b}$$

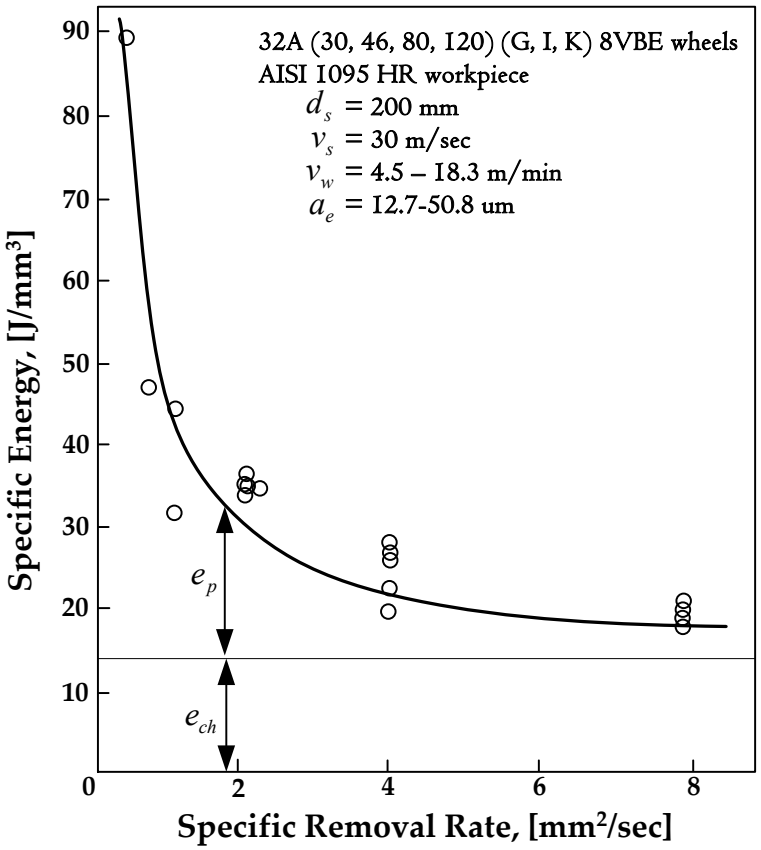

Figure 7.13: Specific energy verses specific removal rate (based on Malkin [7,54-56])

Studying the size effect is very important as it reveals conclusions about factors controlling efficiency, wear, and surface finish. Rowe [57] and Marinescu *et al.* [8] have listed several possible contributions (physical reasons) to the size effect as shown in Figure 7.14. These reasons are: 1- threshold force effect, 2- surface area effects, 3- grain sharpness effect, and 4- rubbing, ploughing and cutting differences. The following provides a brief description of how each of these physical reasons contributes to the size effect [8,57]:

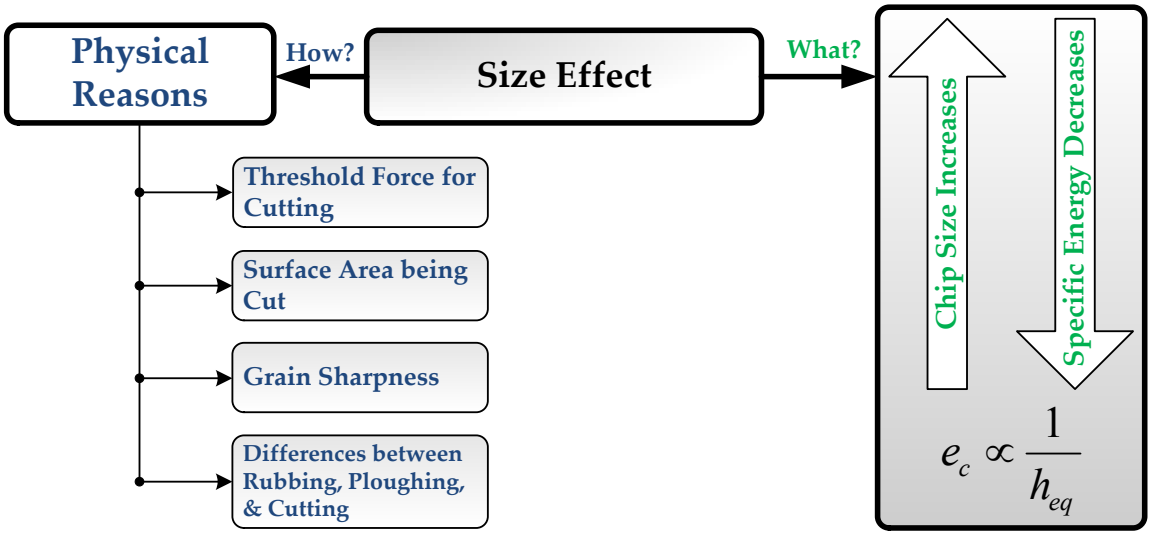

Figure 7.14: A chart summaries the size effect property

• **Threshold Force Effect:** Hahn [18] observed that there is a threshold force required before significant material removal takes place to overcome the elastic effects of the workpiece. If the depth of cut value is almost zero, then the specific energy is infinite as no material is removed. When the depth of cut increases, the abrasive grains penetrate into the workpiece material resulting in less finite material removal; consequently, the specific energy becomes finite [8,57].

• **Surface Area Effects**: the surface area here is related to the surface area of the undeformed chips. The surface area being cut is also considered as a measure of the

energy required. There are some parameters that affect the surface area; these parameters are the grinding depth of cut, grinding feed and active grain density. For the grinding depth of cut parameter, as it increases, the new surface area of the undeformed chip increases resulting in a reduction of the specific energy. Regarding the grinding feed parameter (also known as the workpiece speed), increasing it for a constant depth of cut results in cutting larger chip area for each single active grain and this, consequently, reduces the specific energy. And, for the cutting grain density, as the active grains per unite area increases, the specific energy decrease and vice versa [8,57]. To explain the surface area effects, Rowe and Chen [53] presented a sliced bread analogy to explain the size effect phenomenon. They stated that the thinner a loaf is sliced, the more energy is needed to finish slicing the loaf because a greater surface area is ultimately cut. For example, cutting a loaf into twenty slices will consume approximately twice as much energy as cutting a loaf into ten slices. This analogy, when applied to the grinding process, suggests that the energy required to remove material is reduced when the size of the chips produced is increased.

- **Abrasive Grain Sharpness:** cutting edge sharpness is described by the ratio of the depth t that the abrasive grain penetrates into the workpiece over the contact diameter d_g as shown in Figure 7.15. An increase in the depth-to-diameter ratio indicated that the abrasive grain is sharp (i.e Figure 7.15(a)) and can easily cut the workpiece, while a reduction in the depth-to- diameter ratio indicates that the abrasive grain is blunt (i.e Figure 7.15(b)) and energy is consumed more in rubbing than material removed [8,57].

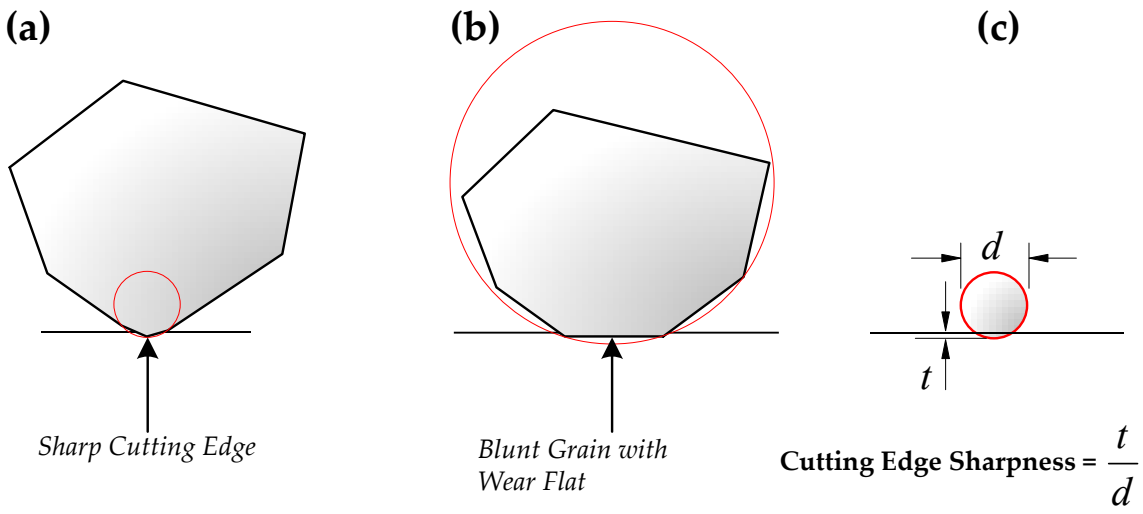

Figure 7.15: Abrasive grain sharpness [57]

• **Rubbing, Ploughing, and Cutting:** these three chip formation phases were introduced in Chapter 2; however, Figure 7.16 is reproduced here for convenience. As can be seen in Figure 7.16(a), during the chip formation along the contact zone, the abrasive grain experiences three phases which are rubbing, ploughing, and cutting. In the rubbing phase shown in Figure 7.16(b), friction is apparent and material removal is insignificant. This phase is associated mainly with elastic deformation. In the ploughing phase shown in Figure 7.16(c), the abrasive grain penetrates more and plastic deformation of the workpiece material occurs and starts to build up in front of the abrasive grain. As the interaction depth between the abrasive grain and workpiece increases, the cutting phase, shown in Figure 7.16(d), starts to occur where forces are sufficient to shear the workpiece material into a chip which is removed from the workpiece. Each of these stages is associated with it is specific energy; rubbing energy, ploughing energy and cutting energy. These energies vary as the depth of cut increases or the abrasive grain penetrates deeper. For instant, when the depth of cut increases, the rubbing energy decreases as the rubbing stage gets smaller. Also, the reduction of the ploughing energy can be a significant contribution in the size effect and this was seen clearly in Figure 7.13. Larger wear flats causes more rubbing during the chip formation and this results an

increase in the specific energy [8,57]. Generally, it can be stated that the cutting is more efficient as abrasive grain acts in the chip formation stage in the early stage when it engages with the workpiece that it acts in rubbing stage.

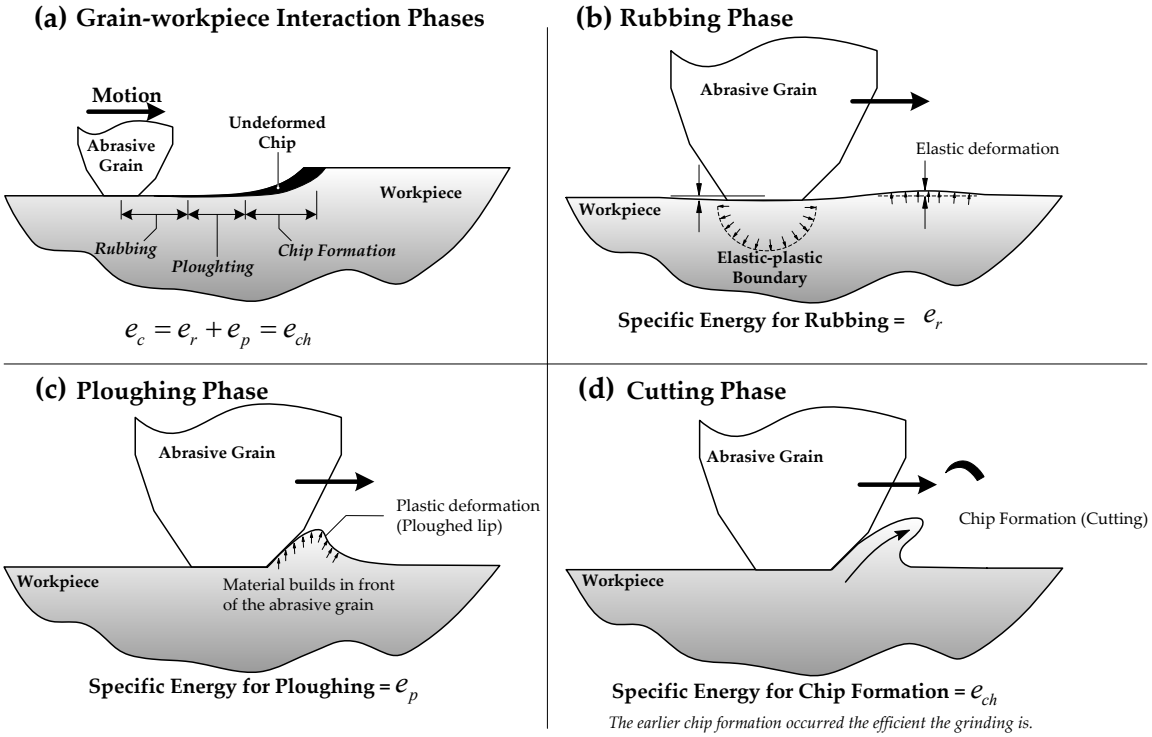

Figure 7.16: Rubbing, ploughing, and cutting phases

7.2.2 Coolant Effect

Grinding fluid also plays an important role on the performance of the grinding process. Its main purposes are to reduce grinding temperatures and to lubricate the grinding process in the contact zone. The amount of grinding fluid that can be transported through the contact area (also called the "useful flow") is mainly limited by variables such as the jet flowrate, grinding wheel speed, and the structure of the grinding wheel. Guiniashvilli *et al.* [58] and Rowe [57] found that the useful flow rate increases with the jet flowrate and the wheel speed, as illustrated in Figure 7.17. There are two main mechanisms that describe the flow of coolant through the grinding zone. The first

mechanism is the flow through the channels between the abrasive grains [59,60] and the clearance between the grinding wheel and workpiece [61]. This mechanism also considers the macro channels produced by the grinding wheel dressing process as found in Engineer *et al.*'s [62] work. Engineer *et al.* [62] stated that dressing severity affects the amount of fluid passing through the grinding zone. They observed that fine dressing of the grinding wheel resulted in less fluid flow in the contact zone than when coarse dressing was applied. The second mechanism of the fluid flow through the grinding zone considers the grinding wheel surface structure [62,63] when the porous surface of a grinding wheel traps and carries grinding fluid through the contact zone as it rotates. It is reasonable to assume that this "pumping" action is proportional to the rotation and porosity of the grinding wheel surface.

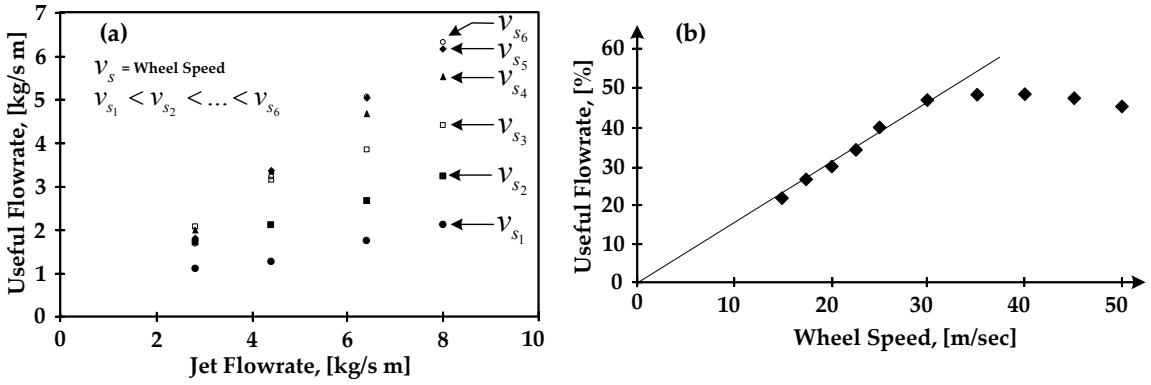

Figure 7.17: Effect of jet flowrate and wheel velocity on useful flowrate based on [57,58]

Grooving a grinding wheel circumferentially effectively increases the porosity of the grinding wheel surface and the grooves form miniature tubes that, as seen in Figure 7.18, can deliver more coolant to the contact zone. Therefore, one would expect that a grooved grinding wheel would enhance coolant flow.

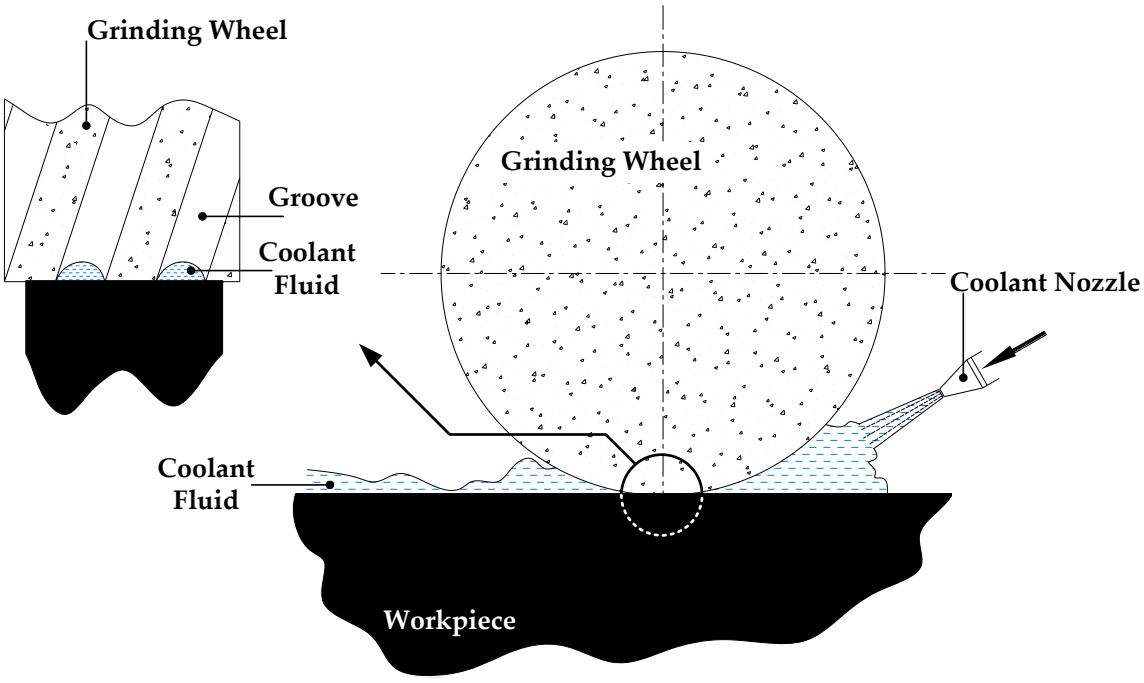

Figure 7.18: Coolant flow through grooves

7.2.3 Dry & Wet Grinding Experiments

Dry shallow grinding experiments (without grinding fluid) were first performed to examine whether or not the "size effect" contributed to improving the grinding process when using a grooved wheel. Then, wet shallow grinding experiments (with grinding fluid) were performed to investigate the "coolant effect" on the grinding process. In both dry and wet grinding experiments, regular non-grooved and circumferentially-grooved grinding wheels (Al_2O_3 Radiac Abrasives WRA 60-J5-V1) were utilized to grind 4140 anneled steel at three depths of cut of (0.0178, 0.0254, and 0.0330 mm) and then their results were compared. The grinding speed and feed remained constant at 22.35 m/sec and 38.1 mm/sec, respectively. The grooved wheel parameters were as follows: groove factor of 50%, groove width of 1.4 mm, and groove depth of 0.1 mm. In wet grinding the fluid flow was 50.4 L/min through an 8 mm diameter nozzle exit. Both wheels were initially conditioned using single-point diamond dressing with an overlap ratio of 3.0.

Figure 7.19 shows the resulting consumed power as a function of the applied depth of cuts for both dry and wet grinding experiments. As can be seen from the figure, the consumed power increased as the depth of cut increased for dry and wet grinding. After grooving the grinding wheel, the consumed power decreased in comparison to the regular non-grooved wheel results for both dry and wet experiments. The average percentage decrease in the consumed power when using a grooved wheel for the dry grinding experiments was 30.5% and the average percentage decrease in the consumed power when using a grooved wheel for the wet grinding experiments was 40%.

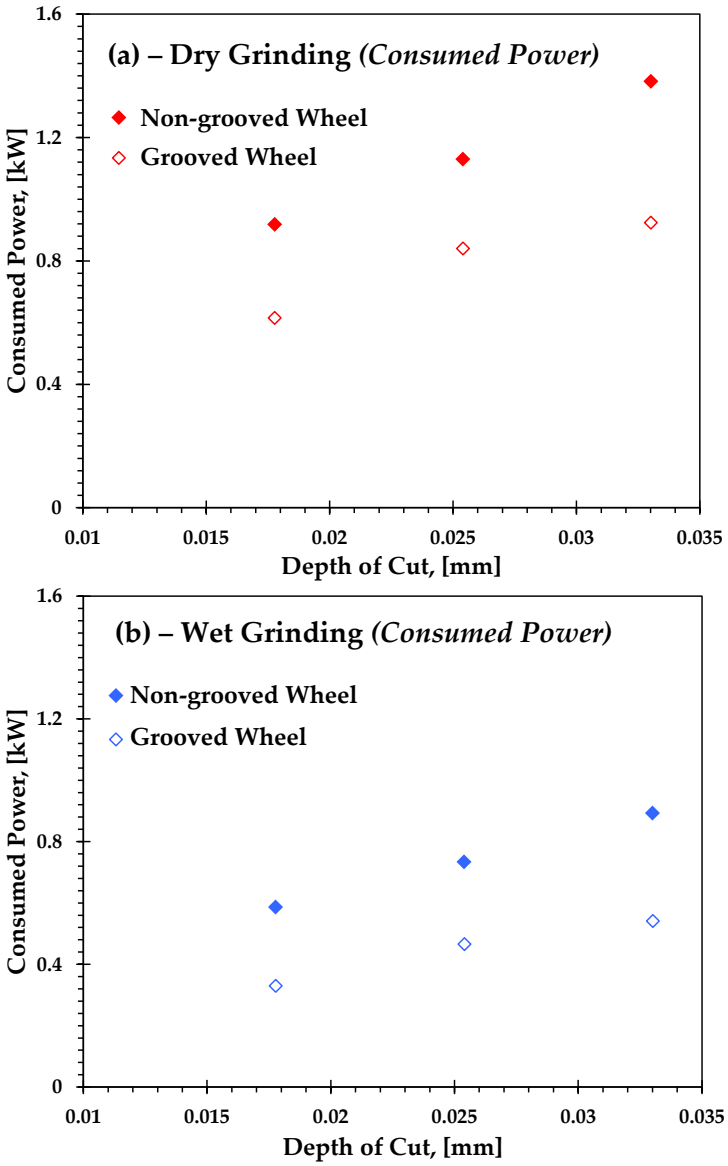

Figure 7.19: Measured consumed power for (a) dry grinding and (b) wet grinding

One of the measures to evaluate and characterize the grinding performance is the specific energy which is defined as the energy expended per unit volume. The experimental specific energy can be calculated with the use of the grinding process parameters and the consumed power which is a function of the tangential forces as follows:

$$e_c = \frac{\text{Consumed Power } (P)}{\text{Material Removal Rate}} = \frac{F_t \cdot v_s}{Q_w} \tag{7.6}$$

The grinding specific energy for this investigation study is shown in Figure 7.20. This figure shows that the specific energy declines with an increase in grinding depth of cut and, consequently, with an increase in undeformed chip thickness.

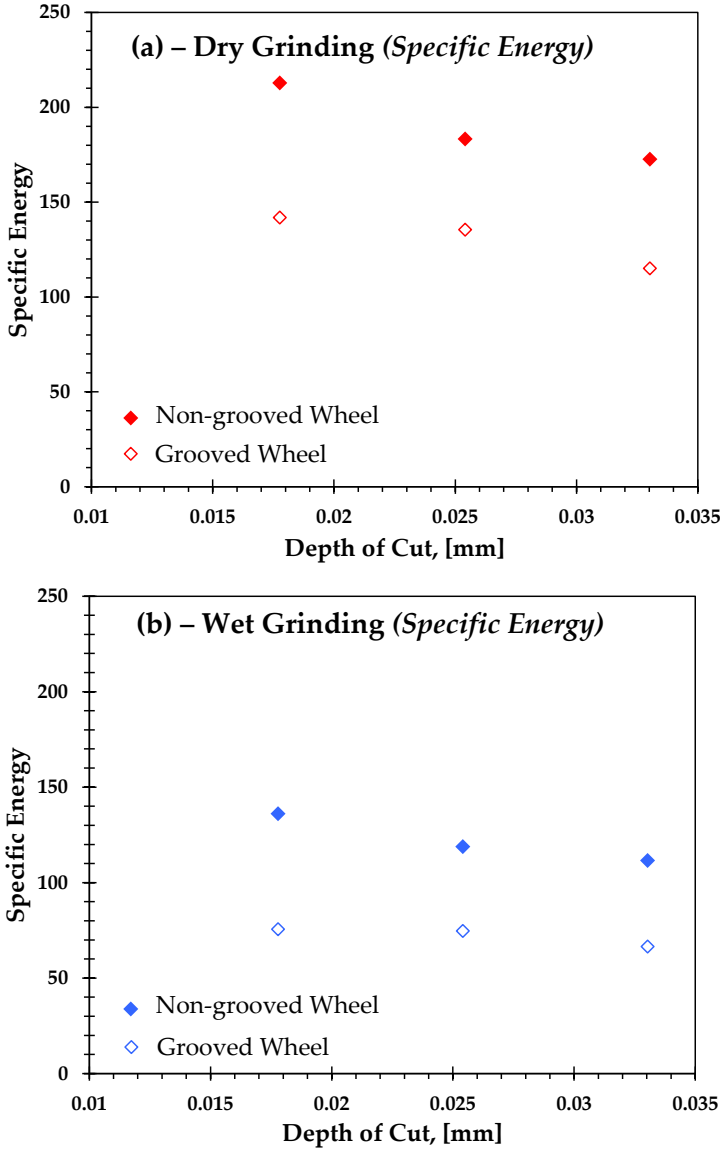

Figure 7.20: Specific energy comparisons for (a) dry grinding and (b) wet grinding

From these results, it can be clearly seen that the grooved grinding wheel improved the grinding process when performing both dry grinding and wet grinding. By comparing the specific energy differences for each depth of cut, as can be seen in Figure 7.21, one can conclude that there is a variation in the specific energy reduction between dry grinding experiments and wet grinding experiments. First, the average reduction in the specific energy when using a grooved wheel in the dry case is 30.6%. As no grinding fluid was applied in dry grinding experiments, this reduction in the specific energy was most likely consequence of the size effect. Second, the average reduction in the specific energy when using a grooved wheel in the wet grinding case was 41.3%. In this situation, the observed improvement is likely due to a combination of the size effect and the coolant effect where the additional 10.7% reduction of the specific energies is attributed to the coolant effect and lubrication.

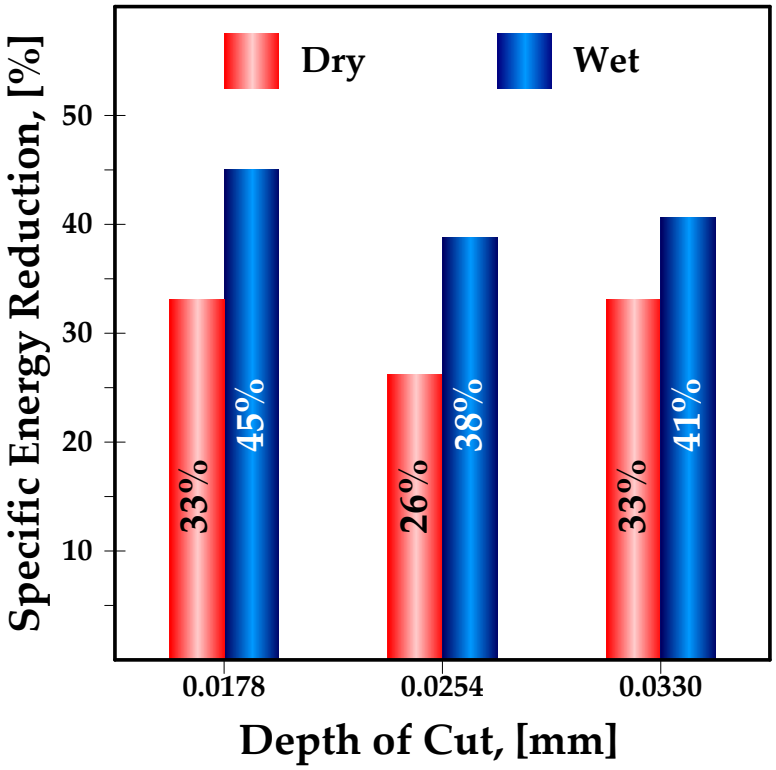

Figure 7.21: Specific energy reductions when using grooved grinding wheel

Studying the grinding forces also assists in understanding more about the behavior of the grinding process. The measured tangential forces and normal forces are shown in Figure 7.22. Figures 7.22(a) and (b) show the forces resulting from the dry grinding experiments and Figures 7.22(c) and (d) show the forces resulting from the wet grinding experiments. As can be seen in these figures, the trend of the force results is similar to the trend of the consumed power results. The average percentage decreases in the tangential and normal forces when using the grooved grinding wheel, in the dry grinding experiments, were 39% and 49%, respectively; while the average percentage decreases in the tangential and normal forces when using a grooved wheel, in the wet grinding experiments, were 45.8% and 57.7%, respectively.

To further discuss the force results, one can investigate the force ratio behavior. The calculated force ratios F_t / F_n are presented in Figure 7.23 where Figure 7.23(a) presents the forces ratios for the dry grinding experiments and Figure 7.23(b) presents the forces ratios for the wet grinding experiments. In both dry and wet grinding experiments, it appears that, when using the grooved grinding wheel, the force ratio is slightly higher than when using the regular non-grooved grinding wheel. Additionally, it can be seen from the figure that when wet grinding was performed, the force ratios decreased for the non-grooved and grooved wheels. In the dry grinding experiments, the average force ratio for the regular non-grooved and grooved grinding wheels are 0.59 and 0.66, respectively; and in the wet grinding experiments, the average force ratio for the regular non-grooved and grooved grinding wheels are 0.44 and 0.53, respectively.

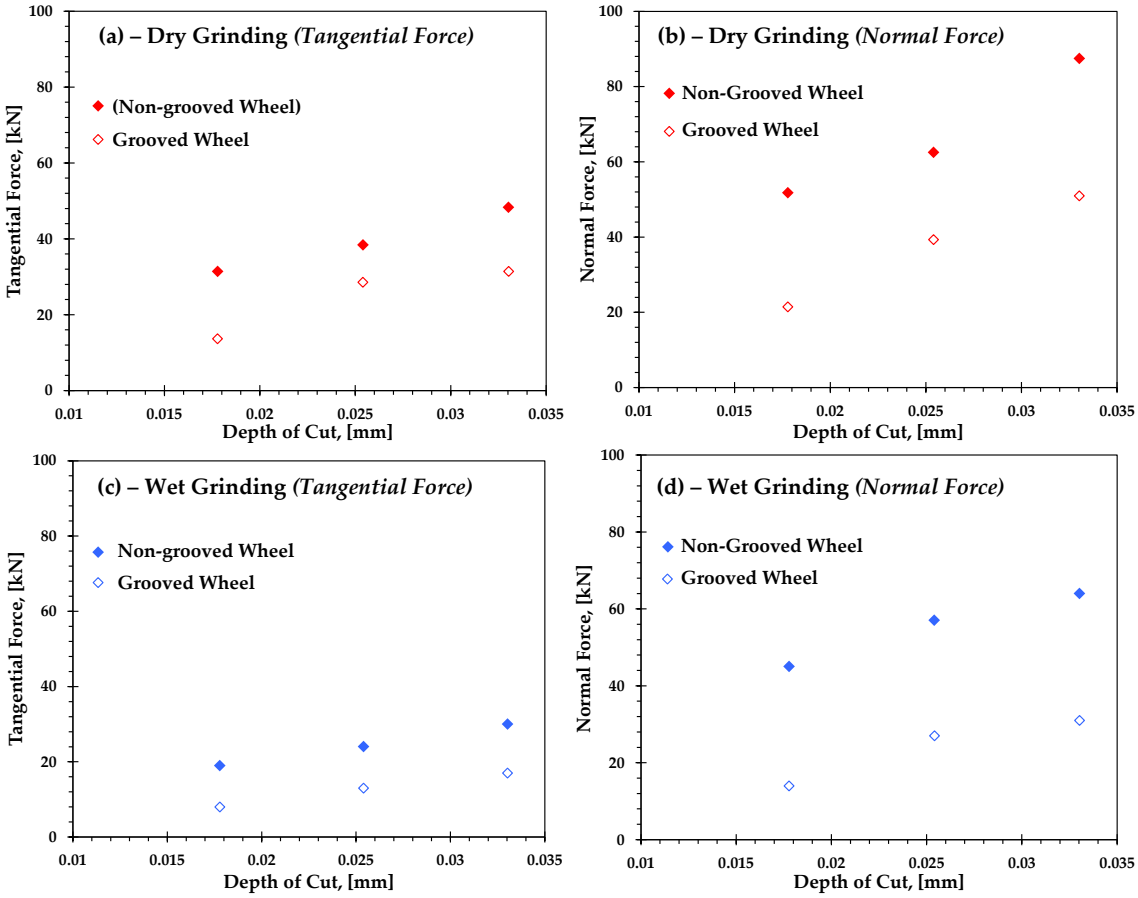

Figure 7.22: Comparisons of tangential and normal forces for (a,b) dry and (c,d) wet grinding

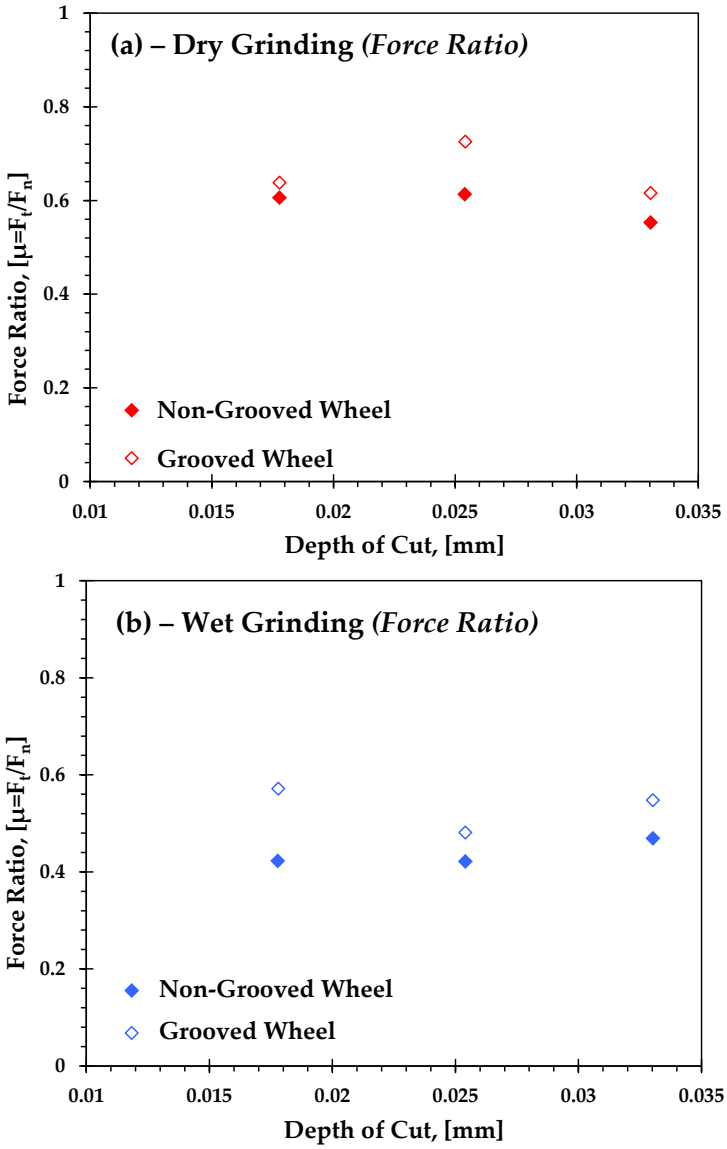

Figure 7.23: Comparisons of force ratios for (a) dry grinding and (b) wet grinding

The increase in the force ratio for the grooved grinding wheel case occurred because the tangential force did not decrease as quickly as the normal force. This suggests that there is perhaps large amount of built up martial in front of the abrasive grains which makes them to be more efficient. The force ratio μ, as proposed by Subhash and Zhang [64], is the sum of adhesion friction μ_a and ploughing friction μ_p. Adhesion friction is a

result of the tool sticking or rubbing to the workpiece, whereas ploughing friction is the result of workpiece material ahead of the tool (abrasive grain) providing resistance to the abrasive grain motion. Anderson *et al.* [46] and Cai *et al.* [65] looked into changes in the force ratios as a function of grinding cutting speed. They found that the force ratio increased with reduction of the cutting speed. It is apparent that a decrease of the grinding cutting speed increases the undeformed chip thickness and this, consequently, might vary the occurring periods of chip formation phases (rubbing, ploughing, and cutting). Anderson *et al.* [64] found that, as shown in Figure 7.24, the adhesion friction μ_a decreased with cutting speed and the ploughing friction μ_p remained constant for all cutting speeds. For each cutting speed, as the grain engaged with the workpiece and interacted deeper, the adhesion friction remained constant and the ploughing friction increased. Their result was important as it confirms that adhesion friction was only affected by the rubbing between the abrasive grain and workpiece while ploughing friction was a result of the abrasive grain geometry (the abrasive grain sharpness) interacting with the workpiece. So, at low undeformed chip thickness, pure rubbing occurred, and as the undeformed chip thickness increased the proportion of rubbing decreased while ploughing increased. As the undeformed chip thickness was further increased cutting started and rubbing and ploughing were reduced [46]. In another work, Anderson *et al.* [66] reported an increase in the force ratio as the grain size was decreased. They examined numerically and experimentally the behavior of various single grain sizes to cut different depth of cuts. Obviously, the depth to diameter ratio increased as size of the grain got smaller; consequently, the small grain is sharper. Anderson *et al.* [66] found that more ploughing and more material were piled up ahead of the grain that was smaller in size causing the specific energy to decrease and the force ratio to increase. This was explained in the previous section for the cutting mechanics of the grooved wheel. Therefore, one can state that the increase in the force ratio indicates the present of the size effect when using a grooved grinding wheel. Furthermore, a decrease in force ratio was observed in the wet grind experiments for both wheel cases

which supports the second hypothesis that coolant also plays a role in improving the performance of grinding with grooved wheels.

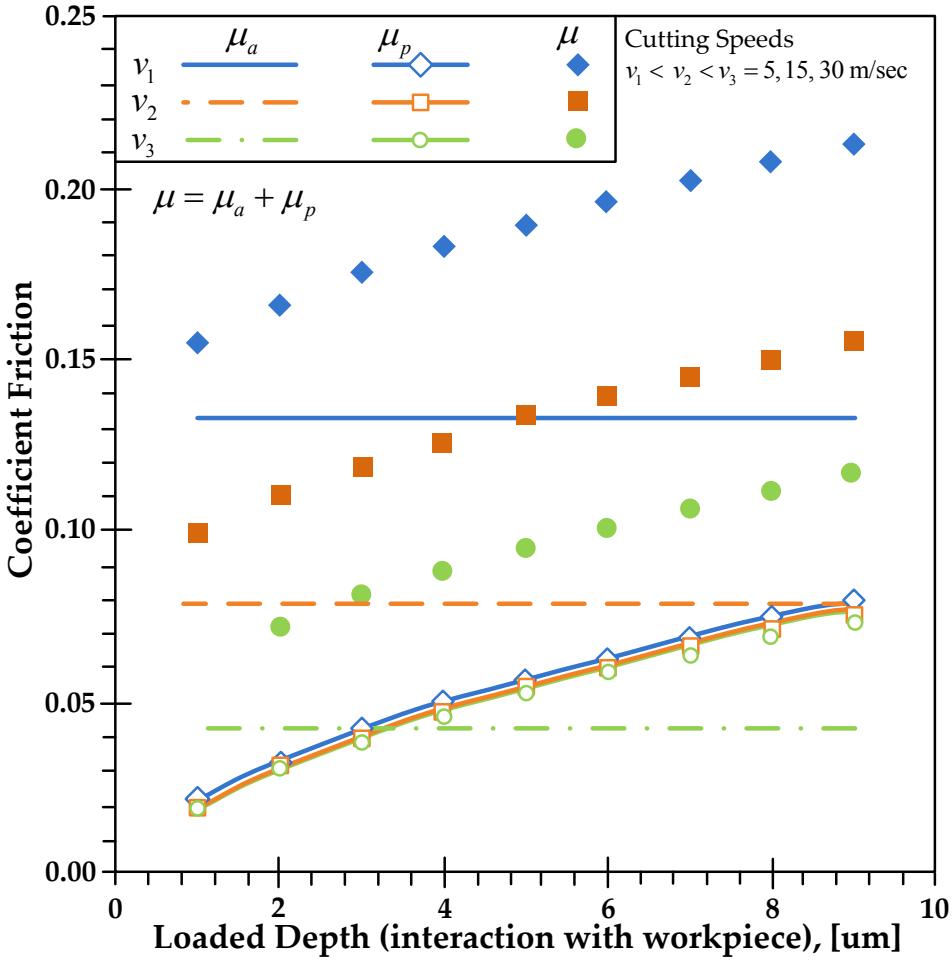

Figure 7.24: Contributions of adhesion and ploughing on over all coefficient of friction based on [46]

7.3 Effect of Grooving on Fluid Flow

It was shown, in the previous section, that both the size effect and grinding fluid play an important role in improving the grinding operation when using a circumferentially-grooved grinding wheel in comparison to a non-grooved wheel. In this section, an

experimental investigation is presented to examine differences in coolant flow when using both non-grooved and circumferentially-grooved grinding wheels.

The experimental setup utilized for this study is presented schematically in Figure 7.25 while Figure 7.26 shows a picture of the setup. As can be seen from both figures, a tank that contains 12.65×10^{-3} m^3 of grinding fluid was used to deliver the grinding fluid at different applied pressures. The desired air pressure inside the tank was kept constant via the use of a precise air pressure regulator. The experiments were first conducted using a regular non-grooved grinding wheel first and then a circumferentially-grooved grinding wheel with a 50% groove factor was tested. A set of five air pressures (0, 34.48, 68.95, 103.42, and 137.90 kPa) and four different grinding wheel speeds (0, 10, 23.35, and 35 m/sec) were investigated for each grinding wheel type. Finally, the results of the flow performance for both the regular non-grooved and grooved grinding wheels were analysed and compared.

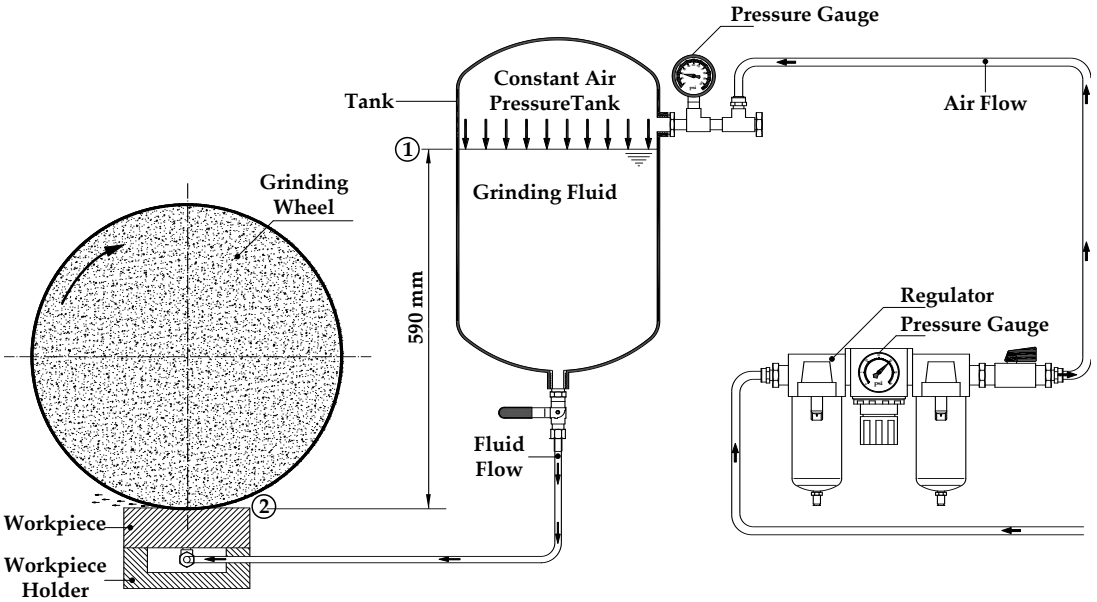

Figure 7.25: Grinding fluid's flow apparatus

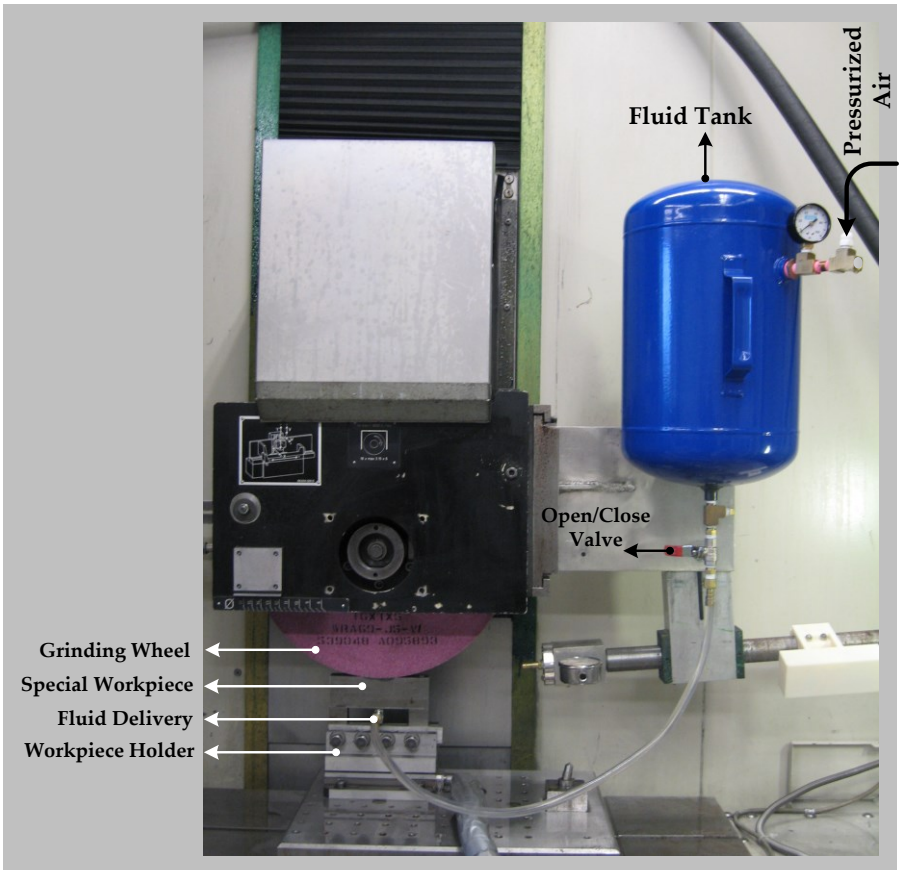

Figure 7.26: Picture of fluid flow setup

A special workpiece setup as shown in Figure 7.27 was prepared for this study. The workpiece was designed in such a way that coolant could enter the grinding zone via a grinding fluid exit slot. The workpiece had the same width as the grinding wheel width of 25.4 mm and the grinding fluid exit slot had a cross sectional area of 51.4 mm^2. As can be seen in Figure 7.27, the fluid's exit slot on the workpiece was not machined across the entire workpiece width to prevent any side flow of the fluid out of the grinding zone. Prior to the measurements, the grinding wheel was gradually fed down onto the workpiece in order to grind an arc on the workpiece that exactly matched the grinding wheel.

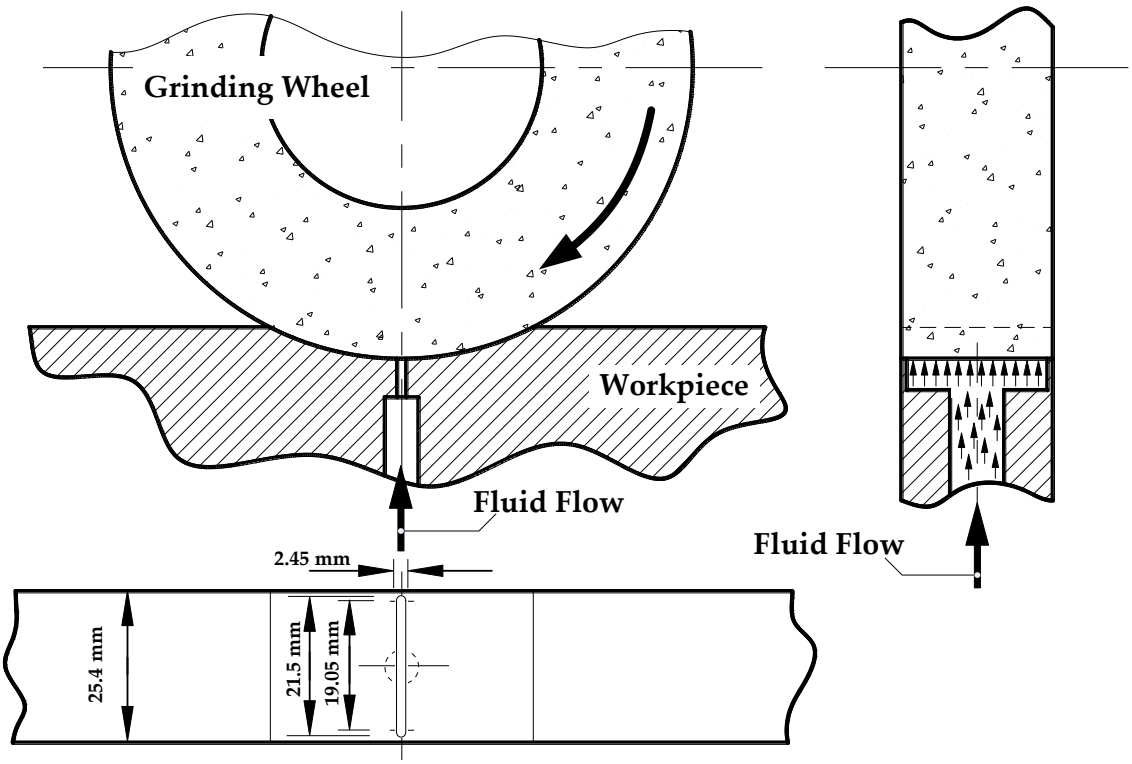

Figure 7.27: Coolant exit geometry at workpiece wheel contact

7.3.1 Flow Measurements Results

Figure 7.28 summarizes the applied input pressure verses the flow rate results. The symbol plus (+) represents the flow results without a grinding wheel. The results represented by the filled dark symbols with the solid lines correspond to the flow measurements when using the regular non-grooved grinding wheel, and the results represented by the empty or non-filled symbols with the dashed lines are for the flow measurements when using a circumferentially-grooved grinding wheel. As can be seen in Figure 7.28, an increase in the input pressure resulted in an increase in the flow. It was also observed that an increase in grinding wheel speed resulted in an increases in the flow rate. Additionally, in the case of the circumferentially-grooved grinding wheel, the resulting flow rate increased by an average of 56.5% in comparison to the flow results from the non-grooved wheel.

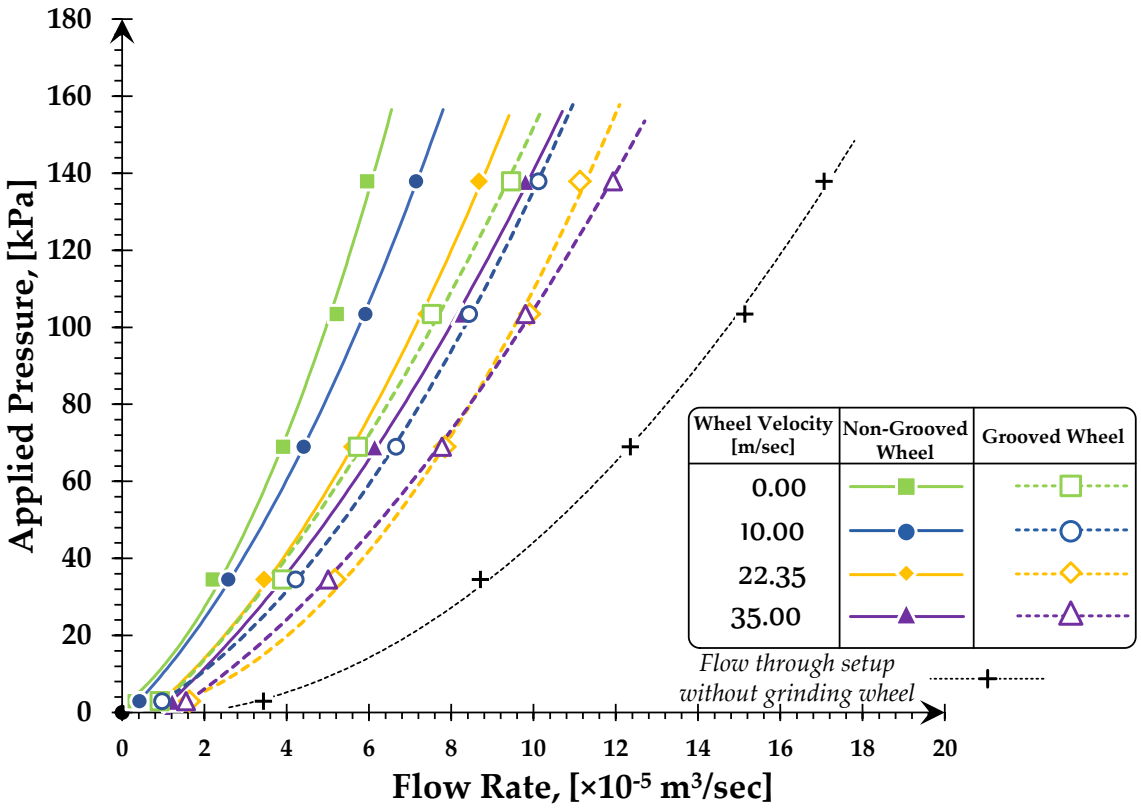

Figure 7.28: Flow rate verses applied input pressure

7.3.2 Flow Measurements Analysis & Discussion

The main objective of this discussion is to obtain the drop in the pressure at the contact zone and correlate the change in the flow rates to the change in the grinding wheel surface topography via grooving. In order to analyse the results shown in Figure 7.28, the energy form of Bernoulli's equation without losses is applied:

$$P_1 + \rho g\, z_1 + \frac{1}{2}\rho V_1^2 = P_2 + \rho g\, z_2 + \frac{1}{2}\rho V_2^2 \qquad (7.7)$$

where P, V, z, and ρ are the pressure, velocity, height, and density of the grinding fluid and the subscripts are the location of interest shown in Figure 7.25. Now, re-writing Equation (7.7) and adding friction losses, Equation (7.7) becomes:

$$P_1 + \rho g\, z_1 + \frac{1}{2}\rho V_1^2 = P_2 + \rho g\, z_2 + \frac{1}{2}\rho\,(\Sigma K + 1)\, V_2^2 \tag{7.8}$$

The lumped loss coefficient K in Equation (7.8) corresponds to the sum of the component system losses from pipe and fitting friction, the workpiece, and the grinding wheel. By Omitting V_1 (as it is assumed to be much smaller than V_2) and establishing z_2 = 0 at plane 2 as the datum, Equation (7.8) is rearranged for the system without a grinding wheel as:

$$P_{c_0} = \frac{1}{2}\rho\,(K_{wp} + 1)\, V_2^2 - \rho g\, z_1 \tag{7.9}$$

where P_{c_o} is the unknown pressure difference ($P_1 - P_2$ in Equation (7.7)) for the case where no grinding wheel was applied and K_{wp} refers to the system losses upstream of the grinding wheel (i.e., workpiece, pipe, and fitting friction). In the same manner, the following equation represents the system including the presence of a grinding wheel,

$$P_{c_s} = \frac{1}{2}\rho\,(K_{wp} + K_s + 1)\, V_2^2 - \rho g\, z_1 \tag{7.10}$$

where P_{c_s} is the unknown pressure differences ($P_1 - P_2$ values in Equation (7.7)) for the case where a grinding wheel (non-grooved or grooved) was applied and the additional parameter K_s is the loss coefficient due to the grinding wheel. Now, subtracting Equation (7.9) from Equation (7.10) results in the pressure drop across the contact zone between the grinding wheel and workpiece, as:

$$P_{\text{Drop}} = P_{c_s} - P_{c_0} = \frac{1}{2}\rho\, K_s\, V_2^2 \tag{7.11}$$

The mean velocity described in the above equations is defined in terms of the volumetric flow rate Q_f in m^3/sec and cross-section area A_f in mm^2 as:

$$V = \frac{Q_f}{A_{f_c}} \tag{7.12}$$

Substituting Equation (7.12) into Equation (7.11) yields:

$$P_{\text{DROP}} = \frac{\rho\, K_s}{2\, A_f^2}\, Q_f^2 \tag{7.13}$$

It is noticed in Equation (7.13) that the pressure drop P_{DROP} is a function of the squared volumetric flow. To simplify the flow analysis, this equation could be represented in a linear form as, for example, $P_{\text{DROP}} = a\,x$, where x denotes the squared flow rate Q_f^2 and a denotes the slope of this line. Therefore, from Figure 7.28, the flow rate verses input pressure results were linearized by squaring the volumetric flow rate and the resulting straight lines are shown in Figure 7.29.

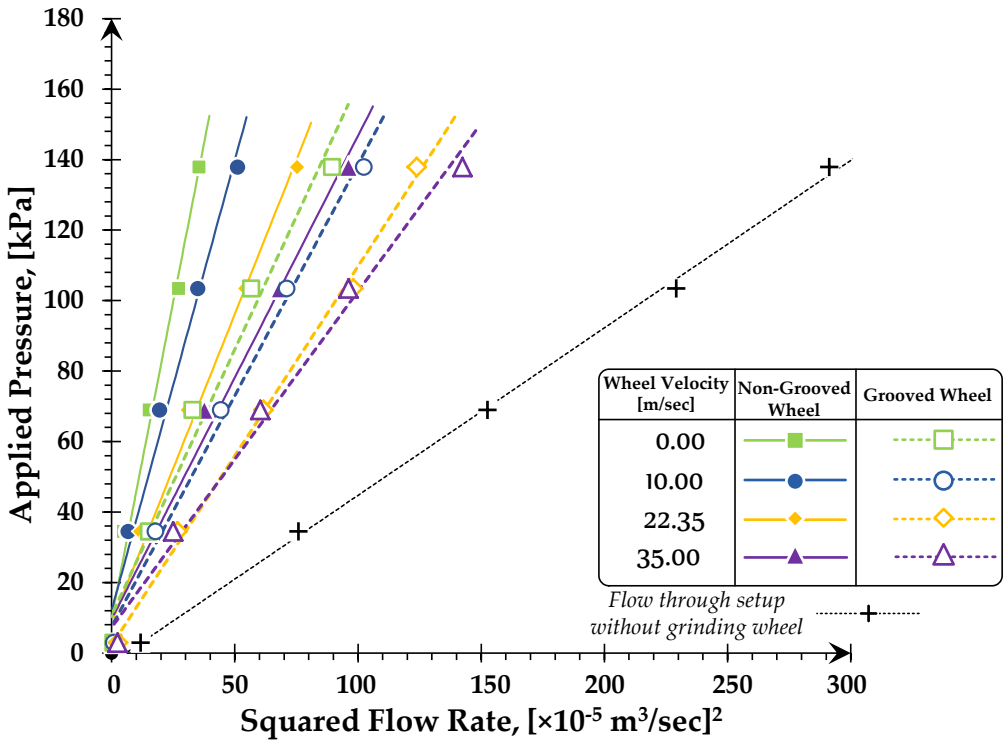

Figure 7.29: The squared flow rate verses applied input pressure

Obtaining the pressure drop in the contact zone between the grinding wheel and the workpiece was found by subtracting the linear curve fit corresponding to the measured flow for the case where no grinding wheel was present, from the linear curve fit corresponding to the measured flow for the cases where grinding wheels were present. The procedure corresponding to these mathematical steps is shown in Figure 7.30. Figure 7.30(a) shows, as an example, two selected sets of results (one of which is related to the flow measurements when no grinding wheel was present). Figure 7.30(b) shows the linearization plot of these selected sets of results and Figure 7.30(c) shows the pressure drop obtained from the subtraction shown in Figure 7.30(b).

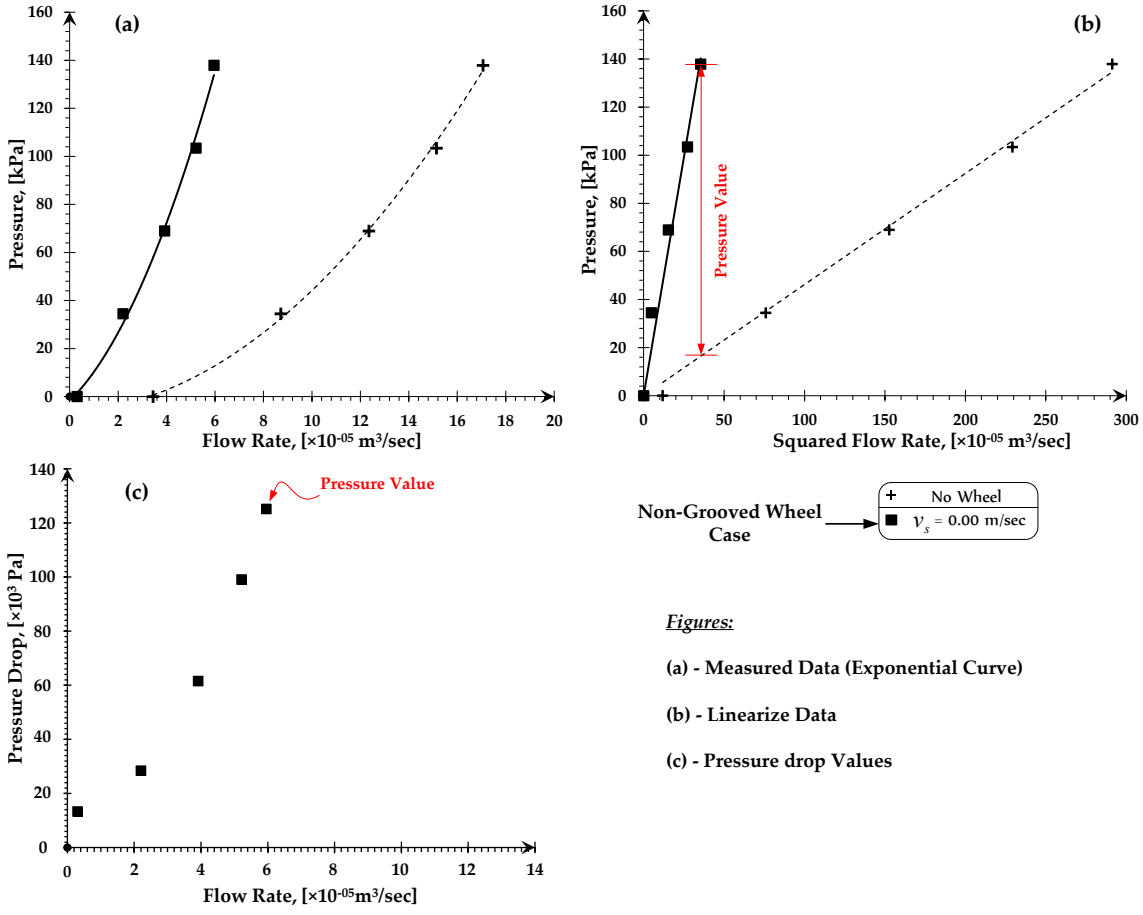

Figure 7.30: Example of steps to obtain pressure drop

Figure 7.31 depicts the resulting pressure drop verses the volumetric flow rate. Again, it can be seen that the flow rates for the grooved wheel cases are higher than for the non-grooved wheel indicating, regardless of wheel speed, that more fluid flows through the contact area resulting in better lubrication and cooling for the process.

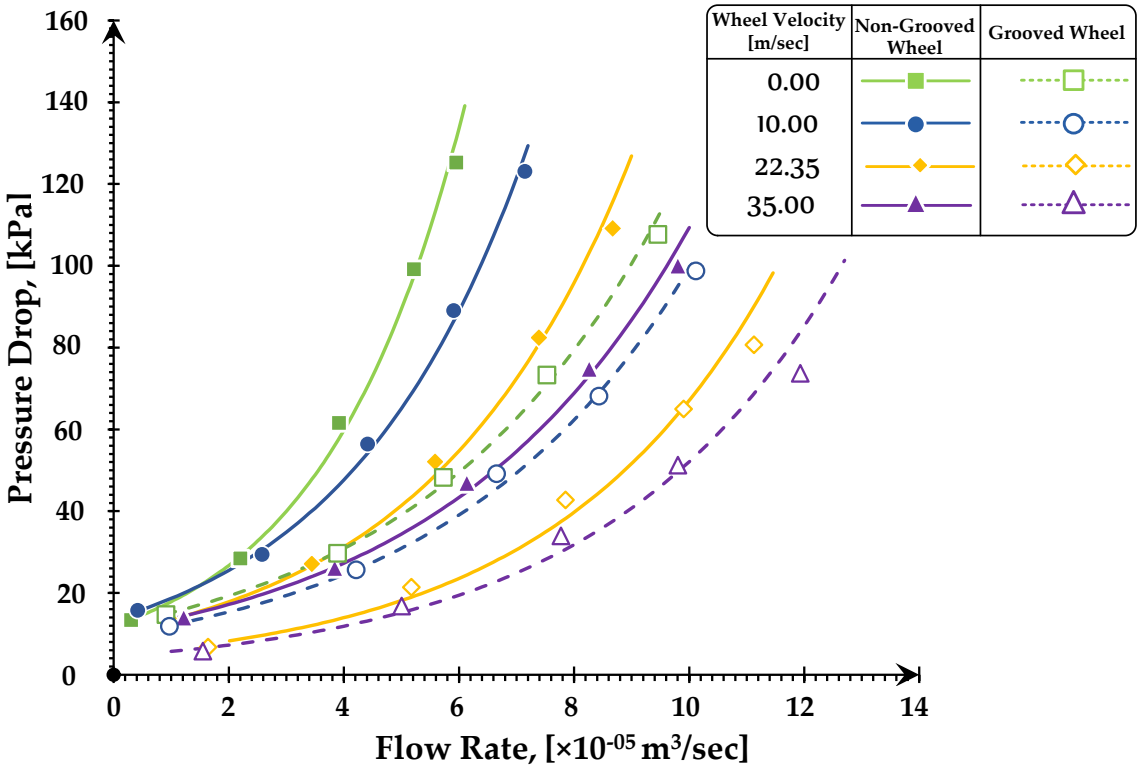

Figure 7.31: Resulted pressure drop at workpiece-wheel contact

For the purpose of examining the results shown in Figure 7.31, one can note that the resulting pressure drop verses the flow rate follows a quadratic trend. Therefore, squaring the flow rate values result in linear curves as shown in Figure 7.32. The slopes (the rate of flow change) ψ of these trend lines for each set of grinding wheel speeds were then obtained. These slopes represent the loss coefficient per squared area as introduced in the pressure drop Equation (7.13), such that:

$$\psi = \frac{\rho K_s}{2 A_f^2} \tag{7.14}$$

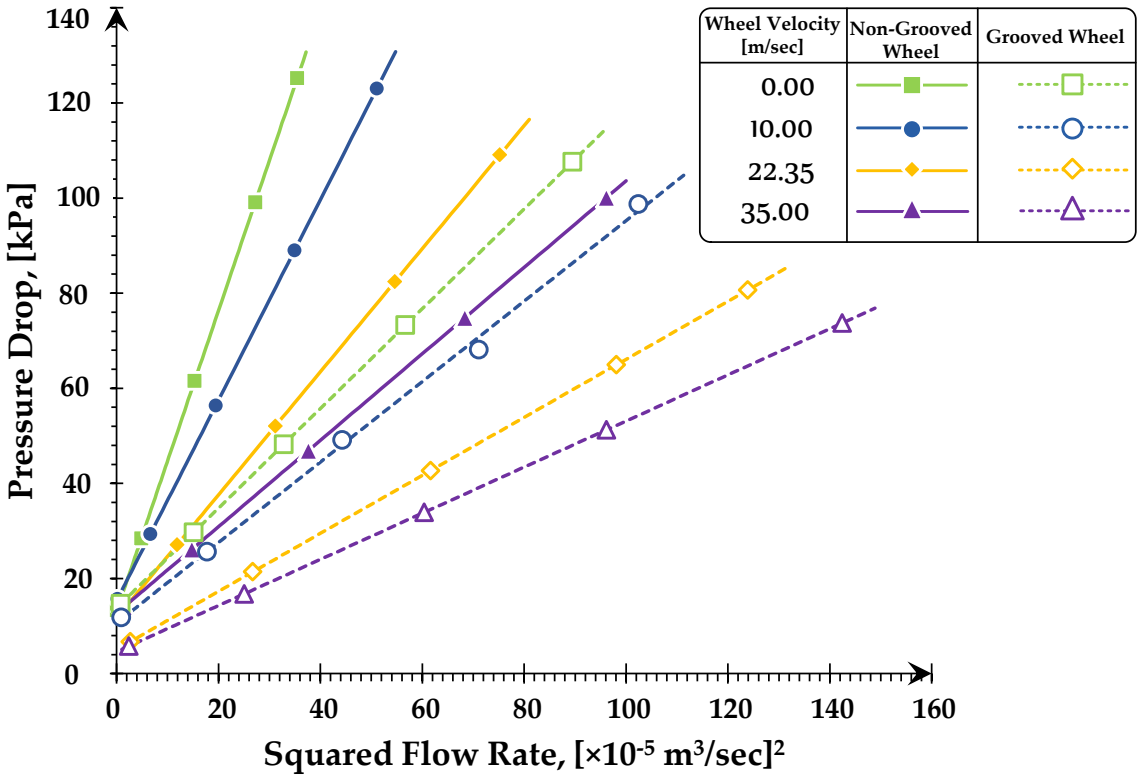

Figure 7.32: Pressure drop at workpiece-wheel contact verses squared flow rate

The slope ψ obtained from each trend line verses the grinding wheel speed is presented in Figure 7.33. It can be seen from this figure that the rate of change of the loss coefficient in relation to the wheel speed is less for the case of the circumferentially-grooved wheel than it is for the case of the regular non-grooved wheel. Due to the complexity of determining the exact value of both K_s and A_f, an approach of assuming one parameter to be a constant and investigating the effect of the other parameter was followed. First, assuming that the area parameter A_f is constant, the increase in the

slope ψ is due to the increase in the grinding wheel loss coefficient parameter K_s. Therefore, the grooved grinding wheel has a lower grinding wheel loss coefficient as it resulted in a smaller value of ψ. Now, should one assume that the grinding wheel loss coefficient parameter K_s is constant, then the decrease in the slop ψ is due to the increase in the flow area A_f. Therefore, one can state that the use of circumferentially-grooved grinding wheels result in larger flow through the contact zone between the wheel and the workpiece.

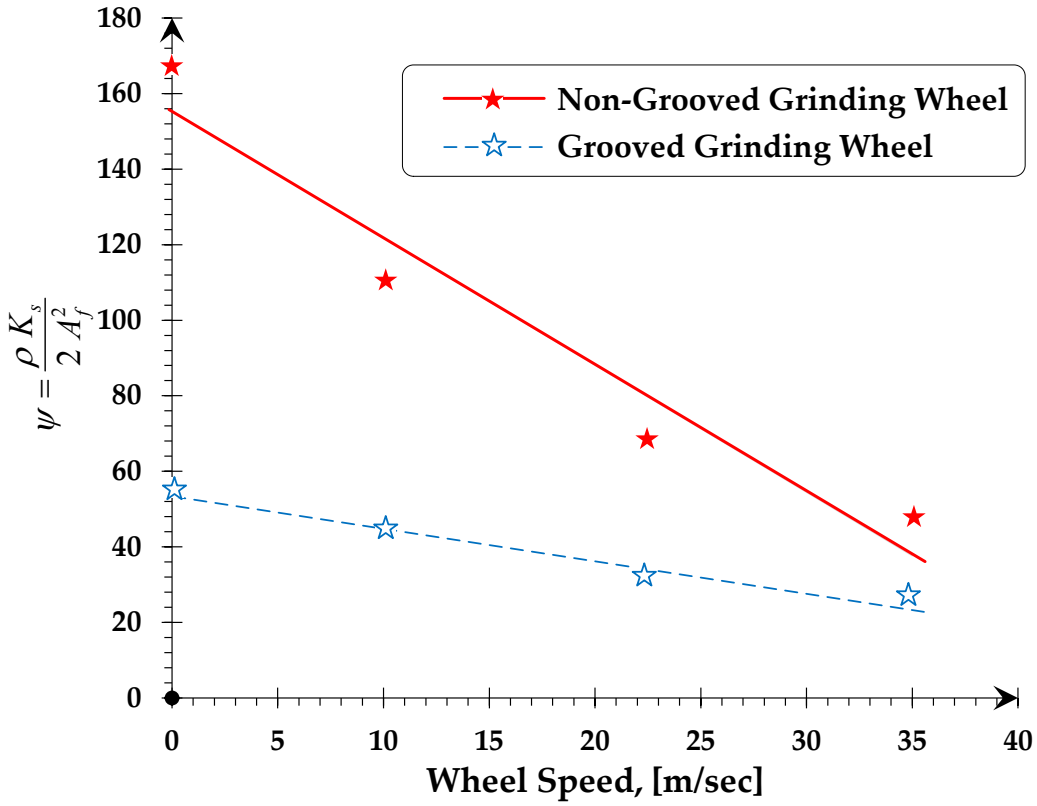

Figure 7.33: Effect of loss coefficient per squired area

7.4 Summary

In this chapter, extensive experimental investigations were carried out to provide a clear explanation of why grooved grinding wheels perform better than regular non-grooved wheels. Evidently, from the dry and wet grinding experiments, the two main parameters that affect the grinding process proved to be due to the increase in undeformed chip thickness and fluid delivery through the grinding zone. The experiments showed that the specific energy dropped by 30.5% and 40% for dry and wet experiments, respectively. SEM images of the resulting grinding chips revealed that the circumferentially-grooved grinding wheel resulted in chips that were 6-8 times larger in width than the chips resulting from the use of the regular non-grooved wheel. Additionally, experiments of fluid flow through the grinding contact zone showed that greater grinding fluid was delivered into the contact zone when utilizing the circumferentially-grooved grinding wheel than the regular non-grooved wheel and the pressure drop was much less. This increase in the flow, when using grooved wheels, was due to either an increase in the of the flow area in the contact zone or a decrease in the loss coefficient causing a better grinding performance.

Chapter 8. Conclusions

Previous chapters showed that the objectives of this thesis have been met.

A single-point diamond dressing tool was successfully used to create circumferential groove patterns on the cutting surface of aluminum oxide grinding wheels. Based on a literature review related to the topic of wheel grooving, the method of using a single-point diamond for the purpose of grooving grinding wheels was not previously studied. The resulting circumferentially-grooved wheels were validated experimentally and the results showed significant grinding improvements in comparison to a regular non-grooved wheel.

It was observed that the use of a circumferentially-grooved grinding wheel, for the creep-feed grinding conditions tested in this research, could increase the achievable depth of cut by up to 120% and reduce the power required by up to 64% when compared with the regular non-grooved grinding wheel. Additionally, for the range of depth of cut achieved by the regular non-grooved wheel, the measured surface

roughness of the ground workpiece surface finish using a circumferentially-grooved grinding wheel was similar to the surface roughness achieved with a non-grooved wheel. Yet, beyond this range of depth of cut where the grooved grinding wheel was able to cut, the surface roughness slightly increased. However, the surface roughness results still maintained in the range of an "average quality" surface finish. From the acquired experiments, it was concluded that 50% groove factor was the most efficient. A corresponding wear study showed that circumferentially-grooved wheels can remove twice as much material as a non-grooved wheel; indicating that wheels with grooves wear slower than non-grooved wheels.

In this thesis work, a novel practical wheel grooving system was successfully designed, developed and experimentally validated. This grooving system is based on the synchronization between the rotational motion of the grinding wheel and the linear motion, parallel to the grinding wheel axis, of the grooving unit (single-point diamond tool). These two motions cause interaction between the diamond tip and the surface of the grinding wheel resulting in the forming of circumferential grooves. The motion synchronization is based on monitoring signals from encoders that that are mounted on the grinding machine's spindle motor as well as on the grooving system's motorized linear stage. Testing the system exhibited high accuracy and repeatability. For exampling, when performing ten consecutively cut grooves, the resulting maximum differences in the groove depth and width were found to be 0.013 mm and 0.015 mm, respectively. These small discrepancies are believed to be because of the brittle fracture mechanism of the aluminum oxide abrasives. Besides its ability to groove and re-groove the grinding wheel, the developed system can be used as dressing device for conditioning the grinding wheel surface after it wears. Also, the wheel grooving system has the ability to groove and re-groove different groove patterns including circumferential, helical (with various helix angles), and sinusoidal patterns.

Analysis and discussion of the cutting mechanics of the regular non-grooved and grooved grinding wheels were explored. A study using scanning electron microscope (SEM) images of grinding chips showed that the circumferentially-grooved grinding wheel resulted in chips that were 6-8 times larger in width than the chips resulting from the use of the regular non-grooved wheel. Due to this variation in the chip size and unique cutting mechanism of the grooved grinding wheel, the resulting ground surface of the workpieces was also investigated. Measurements of workpiece surface profiles showed that the grooved grinding wheel resulted in a ground surface similar to the one resulting from the regular non-grooved wheel. A Fast Fourier Transform (FFT) analysis showed that no surface waviness or marks were left on the ground surface of the workpiece. Also, extensive experimental investigations including both shallow dry and wet grinding experiments showed that the improvement in the grinding performance when using the grooved grinding wheel is due to the size effect phenomenon as well as the fact that more grinding fluid is delivered to the grinding wheel-workpiece contact zone. The experimental results showed that the specific energy dropped by 30.6% and 41.3% for dry and wet experiments, respectively. The improvement in the results for the dry grinding experiments was due to the size effect, while the improvement in the results for the wet grinding experiments was due to a combination of both the size effect and coolant effect. Finally, in order to support the findings of the coolant effect, experiments to measure the fluid flow through the grinding contact zone were performed. The results of these experiments showed that more grinding fluid was delivered at the contact zone when using the circumferentially-grooved grinding wheel than the regular non-grooved wheel. Two factors might have led to the fluid improvement when using a circumferentially-grooved grinding wheel; they are the decrease in loss coefficient parameter of the grinding wheel and/or the increase in the flow area.

Finally, the following lists the main contributions resulting from this thesis work:

- Development of a novel and practical system for grooving and re-grooving grinding wheels. This system can be used on both conventional and CNC grinding machines making it easily transferable to industry.
- Identified the effect of different groove factors and geometries on the creep feed grinding process.
- Established an understanding of why the circumferentially-grooved grinding wheel performs better than the regular non-grooved wheel in terms of efficiency and productivity due to a combination of the size effect and the coolant effect.

8.1 Recommendations for Future Work

There are several significant future applications that could be explored to continue the work presented in this thesis. The methodology followed in grooving the grinding wheel and also the developed grooving system could be utilized in the following suggested research areas:

- Investigating the wear flats characteristics for individual abrasive grains of the circumferentially-grooved grinding wheels (i.e. the ones which are located at the edge of the circumferential groove). This study will help in evaluating the grooved grinding wheel's wear and to determine the tool life and the appropriate time for conditioning it.
- Testing and comparing the effect of grooving for a wider range of grinding wheels types such as CBN, abrasive size, and porosities. This study would help in maximizing the grinding wheel performance where the goal is to achieve the highest removal rates that the grooved wheel could achieve without wearing the grinding wheel out too quickly.
- Examining the circumferentially-grooved grinding wheel, in grinding special alloys such as ceramics (for creep-feed grinding investigation) and material that

are plated with hard material (for surface grinding investigation). Performing grinding on these special materials examines the grindability under extreme grinding conditions in terms of forces and energy that cause a high rise in grinding temperatures. This study could help in determining the heat partitions associated with the use of grooved grinding wheels.

- Testing the grinding fluid flow through the circumferentially-grooved grinding wheel with a wide range of grooved factors. This study could assists in providing a model that can describe the flow characteristics through the contact zone when using the grooved grinding wheel.
- Testing different groove patterns and geometries.

References

[1] Anderson, David J. (2010), *Experimental and Numerical Investigations of Single Abrasive-Grain Cutting*, Doctoral Thesis, Dalhousie University, Canada.

[2] U.S. Department of Commerce. (2004), *Manufacturing in America. A Comprehensive Strategy to Address the Challenges to U.S. Manufacturers*. Washington, D.C.

[3] Malkin, S. and Guo, C. (2008), *Grinding Technology and Applications of Machining with Abrasives*. 2nd Edition, Society of Manufacturing Engineers.

[4] World Bank. (2014), *Total GDP 2013*. World Development Indicators Database.

[5] Schneider, George Jr. (2002), *Cutting Tool Application*, Nokomis, FL: Nelson Pub.

[6] American National Standards Institute ANSI B74.13 (1982), *Markings for Identifying Grinding Wheels and Other Bonded Abrasives*, American National Standards Institute, New York.

[7] Malkin, Stephan (1989) *Grinding Technology and Applications of Machining with Abrasives*. Dearborn: Society of Manufacturing Engineers.

[8] Marinescu, I. D., Rowe, W. B., Dimitrov, B., and Inasaki, I. (2004), *Tribology of Abrasive Machining Processes*, William Andrew Publishing, Norwich, New York.

[9] Marinescu, I. D., Hitchiner,M. P., Uhlmann, E., Rowe, W. B., and Inasaki, I. (2006), *Handbook of Machining with Grinding Wheels*, CPC Press.

[10] Chen, H., Rowe, W. B., Mills, B., and Allanson, D. R. (1998), *Analysis and Simulation of the Grinding Process – Part IV: Effects of Wheel Wear*, International Journal of Machine Tools and Manufacturing, v. 38, n 1-2, pp. 41-49.

[11] Malkin, S. and Cook, N. H. (1971), *The Wear of Grinding Wheels – Part 1: Attritious Wear*, Transactions of ASME: Journal of Engineering for Industry, 93, pp. 1120-1128.

[12] Malkin, S. and Cook, N. H. (1971), *The Wear of Grinding Wheels – Part 2: Fracture Wear*, Transactions of ASME: Journal of Engineering for Industry, 93, pp. 1120-1133.

[13] Salmon, Stuart C. (1992), *Modern Grinding Process Technology*, McGraw-Hill Publishing.

[14] Brach, K., Pai, D. M., Ratterman, E., and Shaw, M. C. (1988), *Grinding Forces and Energy*, Transactions of ASME: Journal of Engineering for Industry, v. 110, pp. 25-31.

[15] Guo, C., Krishnan, N., and Malkin, S. (1993), *Matching Forces and Power in Creep-feed Grinding*, Society of Manufacturing Engineers, MR, pp.1-10

[16] Row, W. B., Morgan, M.N., Batako, A., and Jin, T. (2003), *Energy and Temperature Analysis in Grinding*, Laser Metrology and Machine Performance VI, pp.3-23.

[17] Hahn, R. S. (1962), *On The Nature of The Grinding Process*, Proc. 3rd Machine Tool Design Research Conf., pp. 129-154.

[18] Hahn, R. S. (1966), *On the Mechanics of The Grinding Process Under Plunge Cut Conditions*, Transactions of ASME: J Engineering Industry, pp. 70-80.

[19] Kannapan, S. and Malkin, S. (1972), *Effect of Grain Size and Operating Parameters on the Mechanics of Grinding*, Transactions of ASME: Journal of Engineering for Industry, 94, pp. 833-842.

[20] Toenshoff, H. B. and Denkena, B. (2013), *Basic of Cutting and Abrasive processes*, Springer-Verlag Belin Heidelberg.

[21] Lavine, A. S. and Malkin, S. (1990), *The Role of Cooling in Creep Feed Grinding*, The International Journal of Advanced Manufacturing Technology, v. 5, Issue 2, pp 97-111.

[22] Webster, J. (1995) *Selection of Coolant Type and Application Technique in Grinding*, supergrind, pp. 205-218.

[23] Webster. J., Brinksmeier, E., Heinzel, C., Wittmann, M., and Thoens, K. (???) *Assessment of Grinding Fluid Effectiveness in Continuous-Dress Creep Feed Grinding*, CIRP Annals – Manufacturing Technology, v. 51, n 1, pp.235-240.

[24] Guo, C. (1999*), Energy Partition and Cooling During Grinding*, Proc. Of 3rd Int. Machining and Grinding Conference, SME, Ohio.

[25] Whitehouse, David (2012), *Surfaces and their Measurement*, Boston: Butterworth-Heinemann.

[26] Nakayama, K., Takagi, J., and Abe, T. (1977), *Grinding Wheel with Helical Grooves – An Attempt to Improve the Grinding Performance*, Manufacturing Technology, 27th Gen Assem. of CIRP, v. 25(1), pp. 133-138.

[27] Verkerk, J. (1979), *Slotted Wheels to Avoid Cracks in Precision Grinding*, Annual Abrasive Engineering Society Conference/Exhibition, Pittsburg, Pennsylvania, May 14-16, pp. 75-81.

[28] Matsui, S., Syoji, K., and Kuriyagawa, T. (1986), *Grinding Characteristics of Segmental Wheel – Studies on Creep Feed Grinding*, 4th report, Journal of The Japanese Society of Precision Engineering, v. 52, No. 11, pp.35-41.

[29] Suto, T., Waida, T., Noguchi, H., and Inoue, H. (1990), *High Performance Creep Feed Grinding of Difficult-to-Machine Materials with New-Type Wheels*, Bulletin of the Japan Society of Precision Engineering, v. 24, n 1, pp. 39-44.

[30] Zhang, L. C., Suto, T., Noguchi, H., and Waida, T. (1995) *A Study of Creep-Feed Grinding of Metallic and Ceramic Materials*, Journal of Materials Processing Technology, v 48, n 1-4, pp. 267-274.

[31] Okuyama, S., Nakamura, Y., and Kawamura, S. (1993), *Cooling Action of Grinding Fluid in Shallow Grinding*, International Journal of Machine Tools and Manufacture, 33, pp. 13-23.

[32] Zheng, H. W., and Gao, H. (1994), *A General Thermal Model for Grinding with Slotted or Segmented Wheel*, CIRP Annals - Manufacturing Technology, 43(1), pp. 287-290.

[33] Jaeger, J. C. (1942), *Moving Sources of Heat and Temperature at Sliding Contacts*, Proc. of the Royal Society of New South Wales, v. 79, pp. 203-224.

[34] DesRuisseaux, N. R., and Zerkle, R. B. (1970), *Temperature in Semi-Infinite and Cylindrical Bodies Subjected to Moving Heat Sources and Surface cooling*, ASME: Journal of Heat Transfer, v. 92, pp. 456.

[35] Kim, J.-D., Kang, Y.-H., Jin, D.-X., and Lee, Y.-S. (1997), *Development of Discontinuous Grinding Wheel with Multi-porous Grooves*, International Journal of Machine Tools and Manufacturer, v. 37 (11), pp. 1611-1624.

[36] Kwak, J.-S. and Ha, M.-K. (2001), *Force Modeling and Machining Characteristics of the Intermittent Grinding Wheels*, KSME international journal; v. 15; n 3, pp. 351-356.

[37] Fu, Y. C., Xu, H. J., and Xu, J. H. (2002), *Optimization Design of Grinding Wheel Topography for High Efficiency Grinding*, Journal of Material Processing Technology, V. 129, n (1-3), pp. 118-122.

[38] Nguyen, T. and Zhang, L. C. (2005), *Modelling of the Mist Formation in a Segmented Grinding Wheel System*, International Journal of Machine Tools & Manufacture, v. 45 (1), January, pp. 21-28.

[39] Nguyen, T. and Zhang, L. C. (2005), *The Coolant Penetration in Grinding with Segmented Wheels – Part 1: Mechanism and Comparison with Conventional Wheels*, International Journal of Machine Tools & Manufacture, v. 45 (12-13), pp. 1412-1420.

[40] Nguyen, T. and Zhang, L. C. (2006), *The Coolant Penetration in Grinding with a Segmented Wheel – Part 2: Quantitative Analysis*, International Journal of Machine Tools & Manufacture, v. 46 (2), pp. 114-121.

[41] Nguyen, T. and Zhang, L. C. (2009), *Performance of a New Segmented Grinding Wheel System*, International Journal of Machine Tools & Manufacture, v. 49 (3-4), pp. 291-296.

[42] Jackson, M.J. (2008), *Design of Slotted Grinding Wheels*, International Journal of Nanoparticles, v. 1, No. 4, pp. 334-352.

[43] Köklü, Uğur (2012), *Grinding with Helically Grooved Wheels*, Journal of Process Mechanical Engineering, pp. 1-10.

[44] Fang, C. and Xu, X. (2014), *Analysis of Temperature Distributions in Surface Grinding with Intermittent Wheels*, The International Journal of Advanced Manufacturing Technology, v. 71 (1-4), pp. 23-31.

[45] Davis, J. R. ASM International Handbook Committee (2010), *ASM Handbook, Volume 16 – Machining*, ASM International.

[46] Anderson, D., Warkentin, A., and Bauer, R. (2011), *Experimental and Numerical Investigations of Single-grain Cutting*, International Journal of Machine Tools and Manufacture, 51, pp. 898-910.

[47] Darafon, A., Warkentin, A., and Bauer, R. (2013), *Characterization of Grinding Wheel Topography Using a White Chromatic Sensor*," International Journal of Machine Tools and Manufacture, v. 70, pp. 22-31.

[48] Darafon, A. (2013), *Measuring and Modeling of Grinding Wheel Topography*, Doctoral Thesis, Dalhousie University, Canada.

[49] Backer, W. R., Marshall, E. R., and Show, M. C. (1952), *The Size Effect in Metal Cutting*, Transactions of the ASME, 74:61-72.

[50] Nishioka, T., Mochida, Y., Yamamoto, T., and Yamakawa, A. (1998), *Effects of Grinding Conditions and Grinding Wheel Structure on the Grinding Mechanism of Fine Ceramics*, SEI Technical Review, Publisher: Sumitomo Electr Ind Ltd, n 45 (Jan), pp. 130-136.

[51] Verkerk, J. (1976), *Kinematical Approach to the Effect of Wheel Dressing Conditions on the Grinding Process*, Annals of the CIRP, v. 25, n1, pp. 209-214.

[52] Cai, R., Rowe, W. B., and Morgan, M. N. (2003), *The Effect of Porosity on the Grinding Performance of Vitrified CBN Wheels*, Key Engineering Materials, Trans Tech Publications Ltd, v. 238-239, pp. 295-300.

[53] Rowe, W. Brian and Chen, Xun (1997), *Characterization of the Size Effect in Grinding and the Sliced Bread Analogy*, International Journal of Production Research, 35 (3), pp. 887-899.

[54] Kannapan, S. and Malkin, S. (1972), *Effective of Grain Size and Operating Parameters on the Mechanics of Grinding*, Trans. ASME: Journal of Engineering for Industry, 94, P. 833.

[55] Malkin, S. (1975), *Specific Energy and Mechanisms in Abrasive Processes*, Proceedings: Third North America Metalworking Research Conference, Carnegie Press, P. 453.

[56] Malkin, S. (1976), *Selection of Operating Parameters in Surface Grinding of Steels*, Transactions of the ASME: Journal of Engineering for Industry, 98, P. 56.

[57] Rowe, W. Brian (2014), *Principles of Modern Grinding Technology*, Second Edition, 2014, Elsevier Inc., Publisher : William Andrew.

[58] Gviniashvili, V. K., Woolley, N. H., and Rowe, W. B. (2004), *Useful Coolant Flowrate in Grinding*, International Journal of Machine Tools and Manufacture, 44, pp. 629-636.

[59] Akiyama, T., Shibata, J., and Yonetsu, S. (1984), *Behavior of Grinding Fluid in the Gap of the Contact Area Between a Grinding Wheel and a Workpiece – a Study on Delivery of the Grinding Fluid*, Proceeding of 5th International Conference of Production Engineering, Tokyo 1984, pp. 52-57.

[60] Chang, C. C., Wang, S. H., and Szeri, A. Z. (1996), *On the Mechanism of Fluid Transport Across the Grinding Zone*, Journal of manufacturing Science and Engineering, 118, pp. 332-338.

[61] Schumack, M. R., Chung, J. B., Schultz, W. W., and Kannatey-Asibu, E. (1991), *Analysis of Fluid Flow Under a Grinding Wheel*, ASME Journal of Engineering for Industry, v. 133, pp. 190-197.

[62] Engineer, F., Guo, C., and Malkin, S. (1992), *Experimental Measurements of Fluid Flow Through the Grinding Zone,* Transactions of the ASME: Journal of Engineering for Industry, 114:61-66, Feb.

[63] Li, C. H., Hou, Y. L., Ding, Y. C., and Lu, B. H. (2009), *Analysis and Measurement of Effective Flow-rate in Flood Grinding*, Advances in Materials Manufacturing Science and Technology XIII: Advanced Manufacturing Technology and Equipment, and Manufacturing Systems and Automation : Materials Science Forum 2009, v. 626-627, pp. 159-164.

[64] Subhash, G. and Zhang, W. (2002), *Investigation of the Overall Friction Coefficient in Single-pass Scratch Test*, Wear, v. 252(1-2), pp. 123-134.

[65] Cai, G. Q., Feng, B. F., Jin, T., and Gong, Y. D. (2002), *Study on the Friction Coefficient in Grinding*, Journal of Materials Processing Technology, v. 129,(1–3), pp. 25-29.

[66] Anderson, D., Warkentin, A., and Bauer, R. (2012), *Comparison of Spherical and Truncated Cone Geometries for Single Abrasive-grain Cutting*, Journal of Materials Processing Technology, 212, pp. 1946-1953.

Appendix A

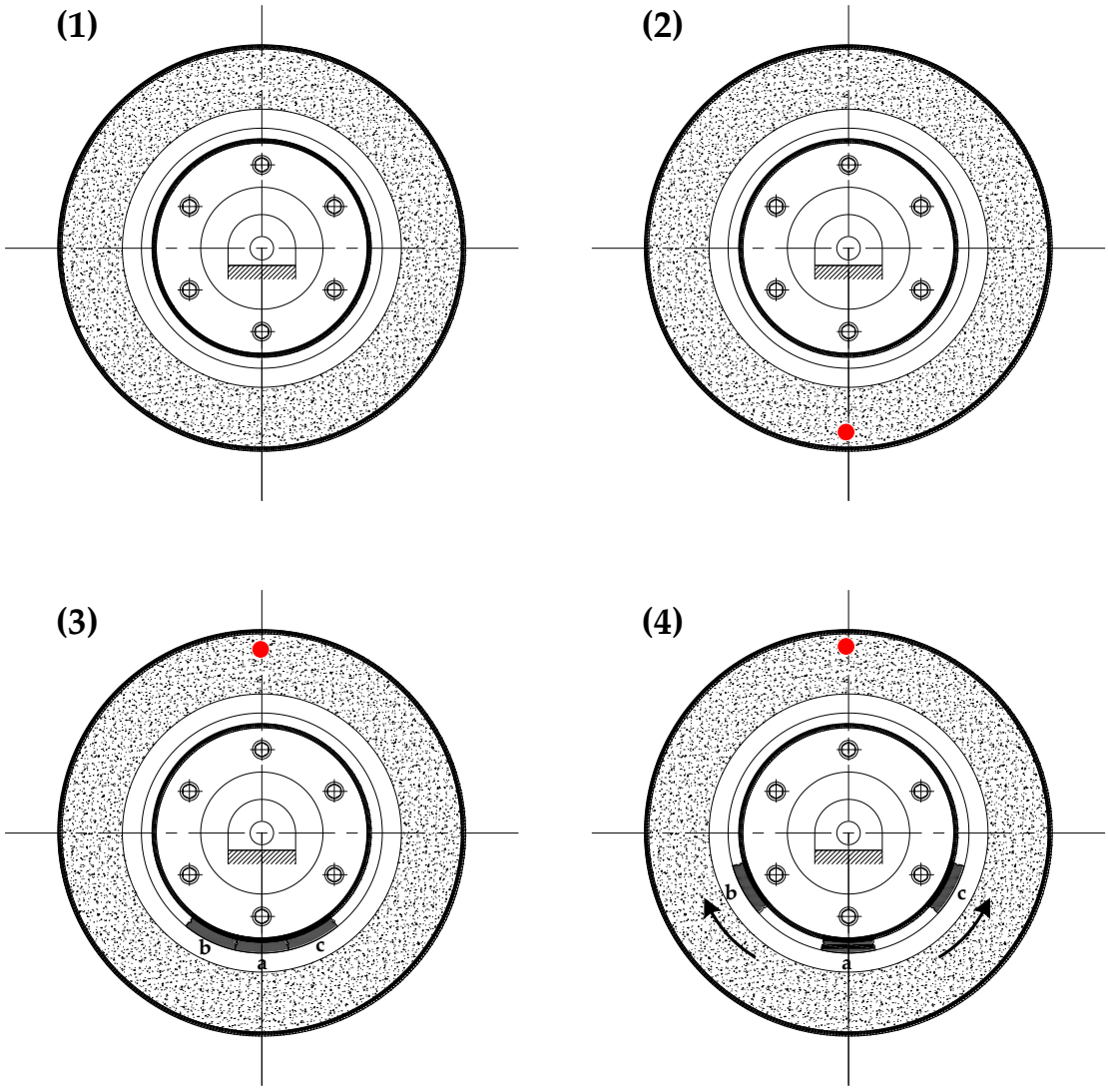

Figure A: Static balancing of grinding wheel

(1) True and dress grinding wheel. (2) Place it on two knife edges support and allow to settle to its heavy point. Mark the heavy spot of the wheel. (3) Mount three masses opposite side of the marked heavy point. (4) Move masses a and b similarly till total balancing achieved.

Appendix B

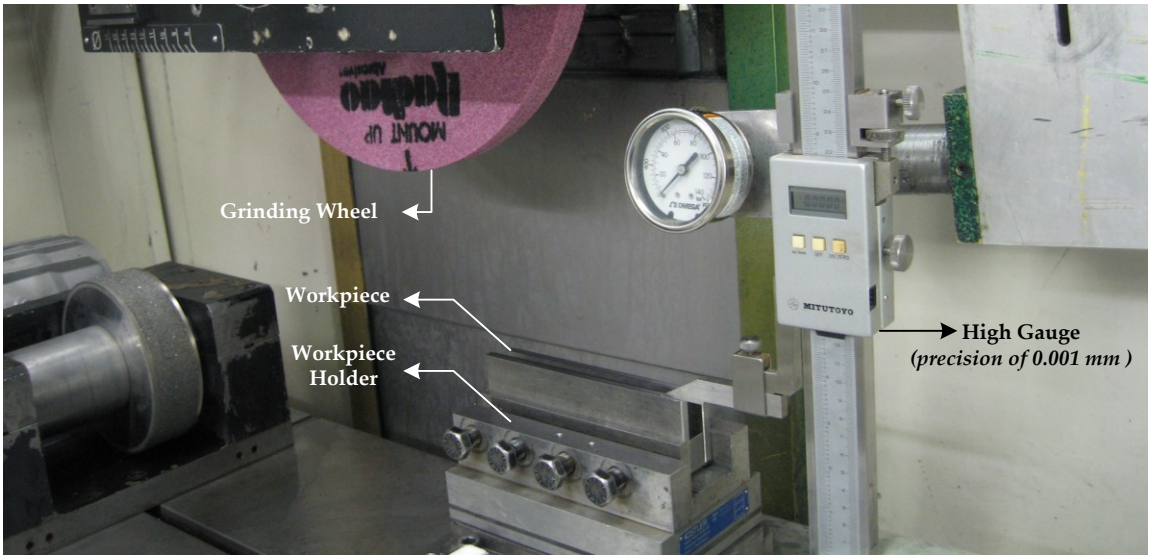

Figure B: Examining of grinding the desired depth of cut along the workpiece

Appendix C

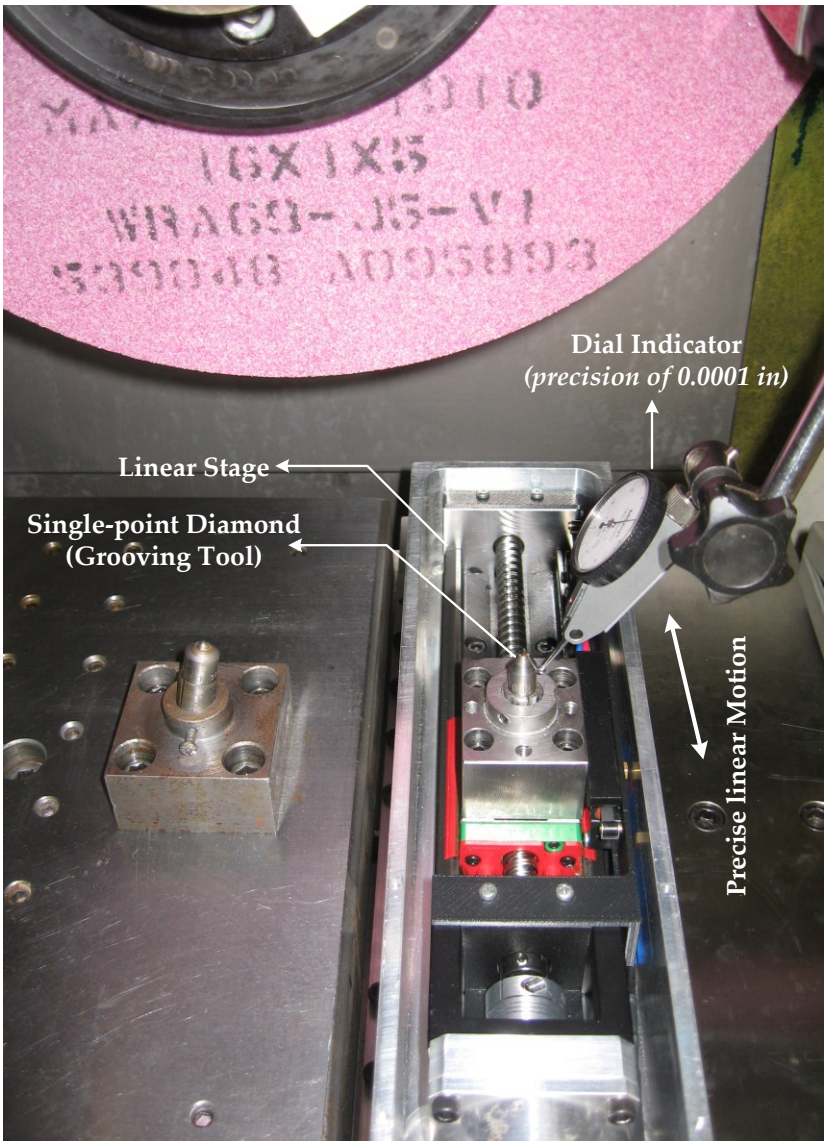

Figure C: Adjusting and mounting the grooving system on the grinding machine table to ensure the linear motion of the grooving tool is precisely parallel to the grinding wheel axis

Appendix D

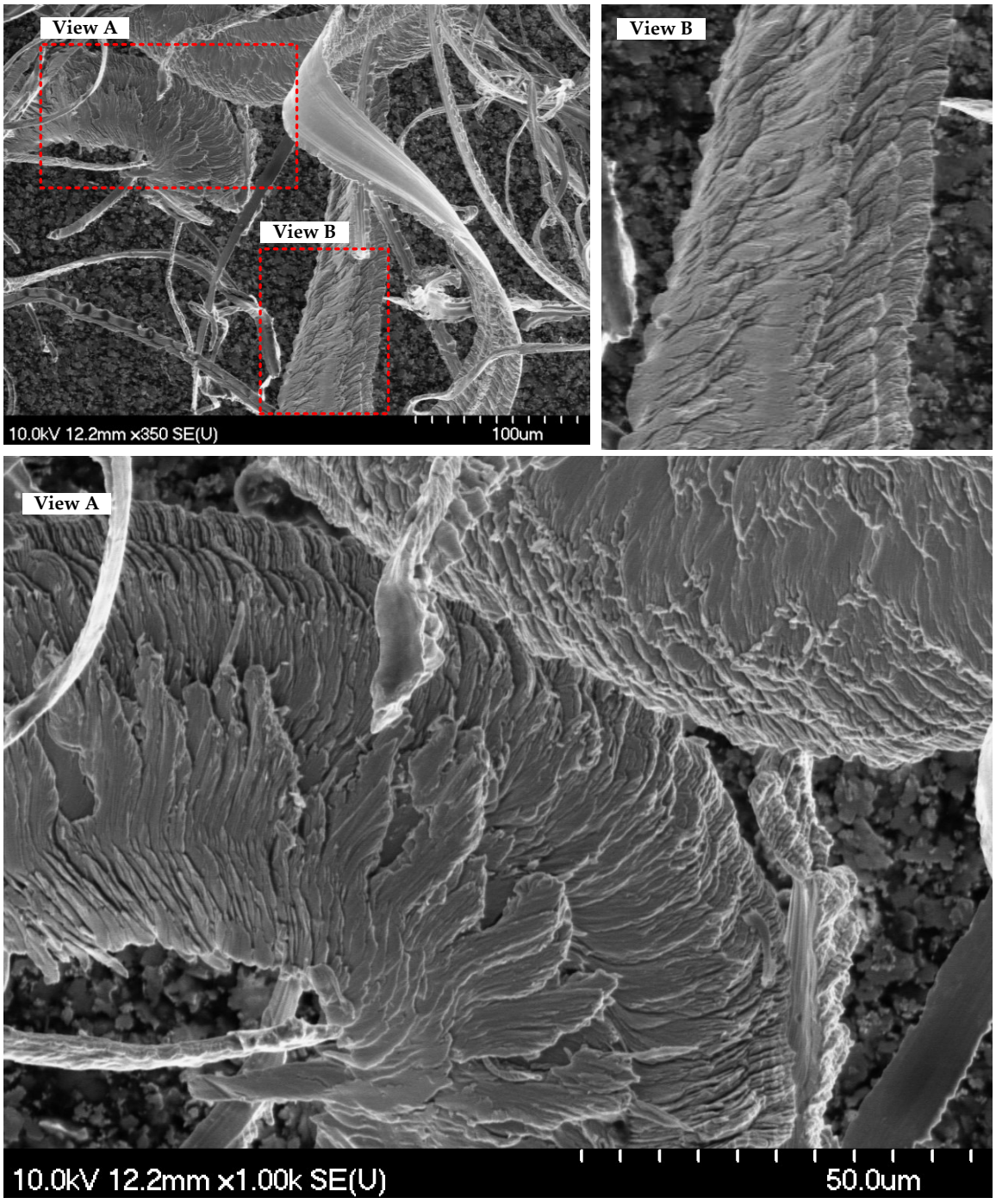

Figure D.1: Wide chip formation build up in a unique multi-layers

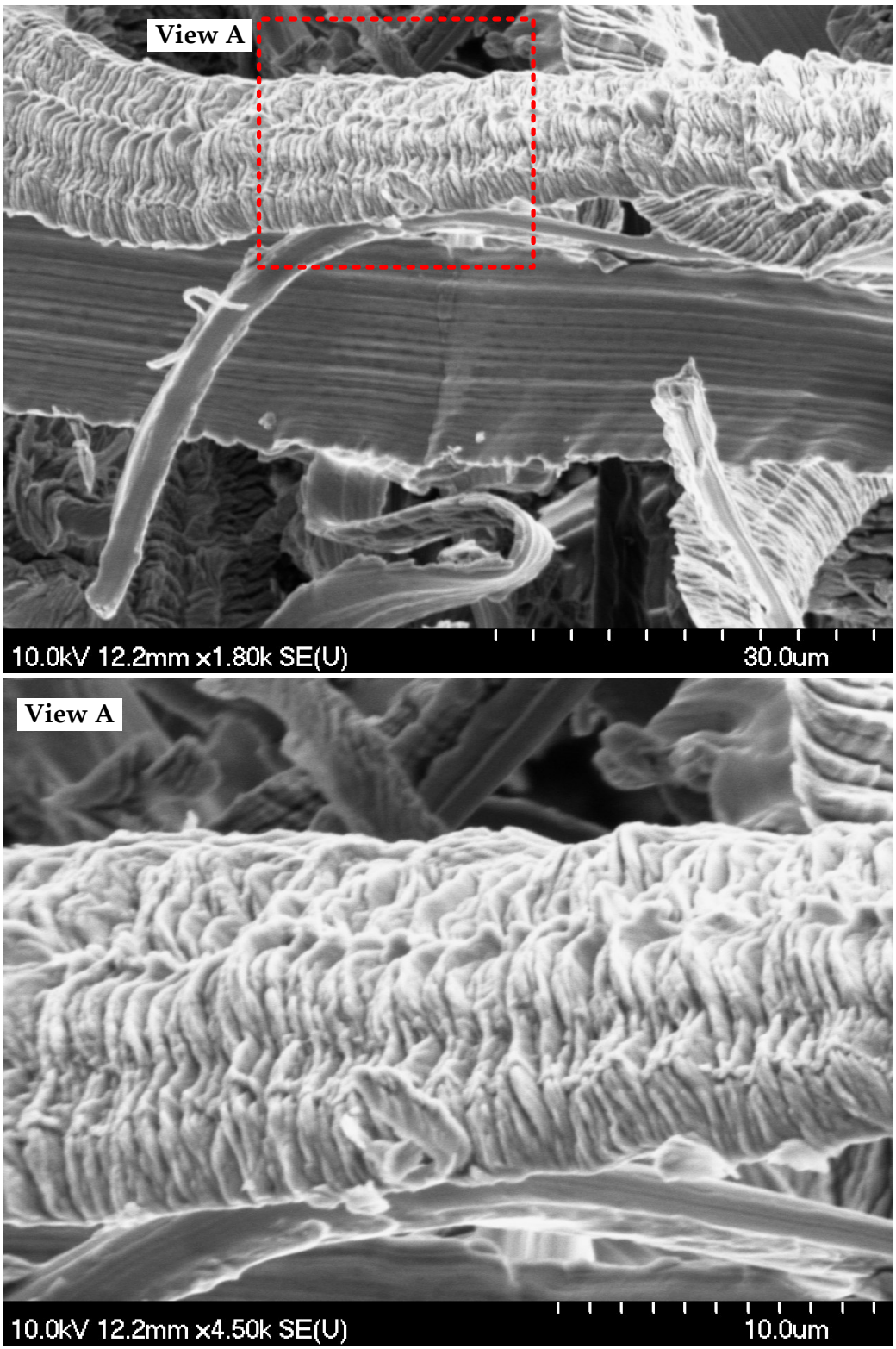

Figure D.2: View of lamella structure with various lamella thicknesses

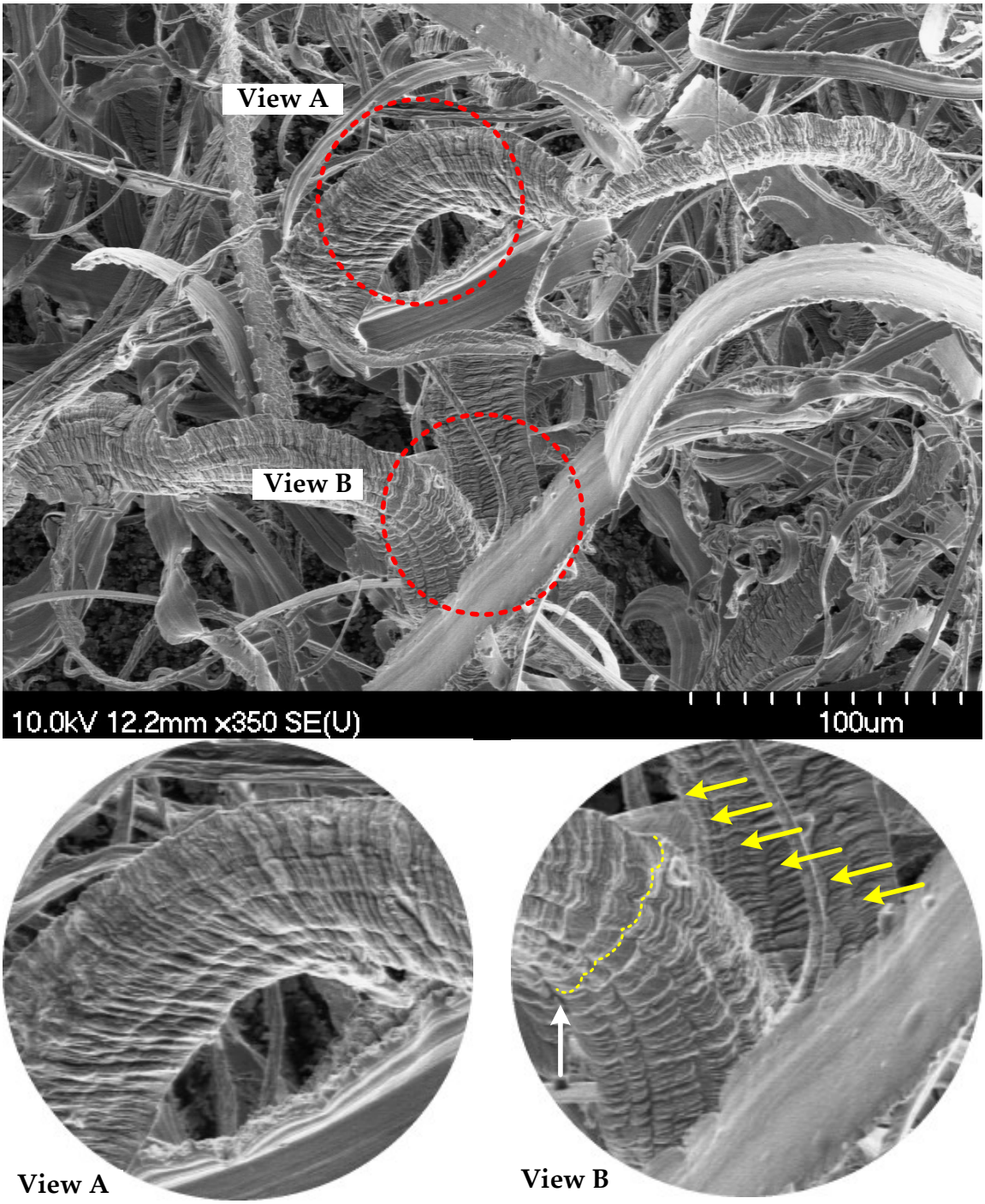

Figure D.3: Illustration of wider chips with different formation